Radio wave activated chemotherapy



Benjamin David White

St Edmund Hall, University of Oxford

Department of Engineering Science

A thesis submitted for the degree of

Doctor of Philosophy

Michaelmas 2022

Acknowledgements

I would like to thank my supervisor, Professor Helen Townley, for giving me the opportunity to carry out the work contained within this thesis. The advice and support she has provided to me during this project, and many others, has moulded me into the researcher I am today. She has always delighted me with the knowledge, vison, and positive attitude she brings to everyone in her research group.

In particular, I would like to thank my lab partner and close friend Chengchen Duan. Not only did he support me in this project, but we had many fantastic times together and made some brilliant memories. I would also like to thank Joseph Kennerly, Rob Habgood and everyone in the Townley lab and the Chemical Engineering research group. Not just for their support, but for the fantastic and fun community we formed.

I certainly would not have made it through the last four years without the support of family. My Mum, Dad, Georgie and Thea have been the best family anyone could ask for. During this time the love and cuddles from Toby, Bella and Walter have made my life ever richer.

I have had so much fun and made so many great friends in the last four years in Oxford, especially in Teddy Hall. There are far too many people to name here, but without whom my life would have been considerably less enjoyable. Particularly, I must mention the boys, Callum, Mark, Jack, and Andrew. These are some of the finest blokes I have ever met, and I cannot put into words how much better my life has been since I met them. Despite donating my sternum and both my ankles to the club, it has been my honour to play with the lads at SEHRFC over the last four years. Thank you to all the men and women at the Oxford University mixed martial arts society who it has been a pleasure to train with.

I also would like to thank the Williams fund for partially funding this research.

Abstract

As one of the most common cancer treatments used in treating patients, chemotherapy has saved countless lives. However, due to the lack of specificity provided by conventional chemotherapy, healthy tissue as well as tumour tissue is destroyed as a result of collateral damage. The side-affects reduce the quality of life of patients so much so, that in some cases, they refuse the potentially lifesaving treatment altogether. The underlying problem with conventional chemotherapy lies in the fact it is not discriminant enough in targeting cancerous cells.

This thesis presents a nanoparticle copolymer complex that is capable of actively targeting cancer cells and limiting drug release until an external stimulus "activates" the complex. The targeting manifests itself through the enhanced permeation and retention effect between nanoparticles and cancer cells, and magnetic localisation at the target location *in vivo*. Activation is triggered by radio wave induced inductive heating of an iron oxide nanoparticle core that causes a structure change in the grafted copolymer, releasing drug bearing proteins. The novel grafted copolymer has been meticulously designed to reversibly immobilise drug bearing proteins and undergo a structure change at a temperature of 42.5 °C, above that of human body temperature, but below that of hyperthermic temperatures.

Ultimately, this nanoparticle copolymer complex would be administered to patients via injection or consumption, magnetically localised in tumour locations within the body using external magnets, and selectively taken up by cancer cells due to the EPR effect. When particles have accumulated in the desired site, a harmless alternating magnetic field would be induced in target areas around the body and the drugs released. If successful, this complex treatment could provide an effective delivery system for many types of chemotherapy molecules while eliminating side effects of treatment completely.

Foreword

Time is precious, and how we use it reflects what matters to us. I appreciate any time you, the reader, are willing to devote to my work. I put a lot of time into writing it, after all, because your experience when reading it matters to me. I want you to be able to enjoy what you read here, and to feel excited by the things I've built. I was once told, by a fellow academic, that composing a thesis is "the hardest you will ever work for something nobody will ever fully read." I am not cynical enough to subscribe completely to this notion, but there is a truth here to acknowledge: academics, like most people, are busy. There is a lot of information in this thesis, and this foreword aims to help you catch the most important bits. First though, if you haven't already, please read the abstract. You may need some context for this next part.

Unsurprisingly this guide to the thesis begins in Chapter 1. This gives an overview of the problem of cancer in the modern world and the advantages of using nanotechnology in treating cancer. Importantly, figure 1.10 summarises how the system I have built works and exhibits its physical assembly.

Chapter 2 details the synthesis of the SPION core of the complex, and the construction of a device capable of heating them. Chapter 3 details the steps in the journey of creating a copolymer capable of immobilising proteins but also undergoing a phase change at the desired temperature. If you are interested in the structure of the novel copolymer, see figure 3.12. Upon looking through chapter 4, familiarise yourself with the chemotherapy agents chosen for delivery, and their effect on the cell lines tested in the lab.

Chapter 5 exhibits the construction and structure of the overall nanoparticle copolymer complex and its physical functions. Chapter 6 demonstrates a proof-of-concept test of what the system was designed to do

with figures 6.3, 6.4 and 6.5 demonstrating this. It also discusses the developed technology in comparison to literature, which is important context for the conclusion in chapter 8.

Chapter 7 describes the development of a computational model designed to predict the times taken to activate particles dependent on induction heating parameters. A graphical representation of the capability of the model is shown in figure 7.3. Chapter 8 summarises the work of the project and prospective future experiments should they be carried out.

This thesis, like most others, will not be understandable to all audiences. I do, however, hope that it will be both understandable and valuable to a large readership. Ultimately, it was written for everyone, including academics, businesspeople, professionals, laypeople, my examiners, my co-workers, friends, and you. Thank you for reading.

Publications from this project

White BD, Townley H E, Radio wave activated chemotherapy – A novel nanoparticle, thermosensitive copolymer drug delivery platform. *MDPI* , 02 2023.

ACTIVE AGENT RELEASE PARTICLE, Applicants: Oxford University Innovation limited. Inventors; White, Benjamin. Townley, Helen Elizabeth. International Application No: PCT/GB2021/052104. Status of application: Patent Pending

White, B.D.; Duan, C.; Townley, H.E. Nanoparticle Activation Methods in Cancer Treatment. *Biomolecules* **2019**, *9*, 202

Parts of Chapter 5 and 6 are under preparation for publication:

White BD, Townley H E, A new strategy for treatment of metastatic liver cancer with localised paracetamol and acetylcysteine delivery.

Other publications

White BD, Evison A, Dombi E, Townley HE, *Improved delivery of the anticancer agent citral using BSA nanoparticles and polymeric wafers.* Nanotechnology science and applications, 2018, 10

Victor M. Lu, Felicity Crawshay-Williams, Benjamin White, Amy Elliot, Mark A. Hill & Helen E. Townley (2019) *Cytotoxicity, dose-enhancement and radiosensitization of glioblastoma cells with rare earth nanoparticles, Artificial Cells,* Nanomedicine, and Biotechnology, 47:1, 132-143

Contents

Abbreviations and acronyms XI
List of Figures XIII
Chapter 1: Literature review 1
1.1 Cancer treatment and chemotherapy 1
1.1.1 Chemotherapy 2
1.2 Nanoparticles and nanotechnology in oncology 4
1.2.1 Nanoparticle effects *in vivo* 6
1.2.2 Advantages and enhancements of nanoparticles in drug delivery 11
1.2.3 Active targeting strategies of nanoparticles 14
1.3 Iron oxide nanoparticles and inductive heating 16
1.3.1 The nature of ferrimagnetic, ferromagnetic and superparamagnetic particles 16
1.3.2 Induction heating of bulk materials 20
1.3.3 Induction heating of iron oxide nanoparticles 22
1.4 Thermoresponsive polymers and their use in medicine 23
1.5 Extrinsic activation methods within oncology 25
1.5.1 Ultrasound stimulated systems for cancer treatment 25
1.5.2 Ultraviolet-Visible light activation and photodynamic therapy 30
1.5.3 Alternating magnetic field stimulated systems 37
1.6 Research gap and aims of the thesis 41
Chapter 2: SPION synthesis and inductive heating. 44
2.1 Introduction 44
2.1.1 Nanoparticle properties and synthesis routes 44
2.1.2 Induction heating and induction heaters 47
2.1.3 Induction heating of iron oxide nanoparticles 47
2.2 Materials and Methods 48
2.2.1 LA-ION and DD-ION synthesis 48
2.2.2 Inductive Heating Equipment 49
2.2.3 Characterisation techniques 49
2.3 Results 51
2.3.1 Lauric acid stabilised iron oxide nanoparticles: 51
2.3.2 DDMAT stabilised iron oxide nanoparticles 55
2.3.3 Magnetisation values of Particles 60
2.3.4 Induction heating design and assembly 61

2.3.5 Initial particle heating tests....67
2.4 Discussion....69
2.4.1 Physicochemical characteristics of stabilised SPIONs....69
2.4.2 Design and operation of the induction heating device....71
2.4.3 Induction heating of SPIONs....73
2.5 Conclusion....74
Chapter 3: Copolymer design synthesis and analysis. 76
3.1 Introduction 76
3.1.1 Poly-N-isopropylacrylamide as a thermoresponsive polymer....76
3.1.2 RAFT as a polymerisation technique and chain transfer agents....78
3.1.3 Radical copolymerisation....82
3.2 Materials and methods....84
3.2.1 RAFT polymerisation of unbound polymers 84
3.2.2 Poly–(methacrolein-b-(NIPAM-co-acylamide) synthesis 85
3.2.3 Analysis methods 85
3.3 Results....87
3.3.1 Poly-N-isopropylacrylamide synthesis and analysis 87
3.3.2 Copolymerisation of NIPAM-Acrylic Acid....92
3.3.3 Copolymerisation of NIPAM and Acrolein 94
3.3.4 Copolymerisation of NIPAM, acrylic acid and Acrolein....96
3.3.5 Copolymerisation of NIPAM and acrylamide....100
3.3.6 Copolymerisation of NIPAM-Acrylamide-Allyl Thiol 103
3.3.7 Copolymerisation of NIPAM, Acrylamide and Methacrolein....105
3.4 Discussion....116
3.4.1 DDMAT as a chain transfer agent 116
3.4.2 PNIPAM synthesis and characterisation 116
3.4.3 Synthesis of PNIPAM-co-Acrolein 117
3.4.4 Synthesis of PNIPAM-co-acrolein-co-acrylic acid....117
3.4.5 Synthesis of PNIPAM-co-acrylamide....119
3.4.6 Synthesis of PNIPAM-co-acrylamide-co-Allyl thiol 119
3.4.7 Synthesis of PNIPAM-co-Acrylamide-co-Methacrolein 120
3.5 Conclusion....123
Chapter 4: Model drugs for delivery....125
4.1 Introduction 125
4.1.1 Sarcoma, brain, breast, and liver cancer cell lines....125
4.1.2 Bovine serum albumin as a drug carrying vehicle 127

4.1.3 Paclitaxel, vinblastine and paracetamol as model drugs for delivery 127
4.2 Materials and methods 130
4.2.1 Drug binding to BSA 130
4.2.2 Protein immobilisation on copolymers 130
4.2.3 Cell lines 131
4.2.4 Analysis methods 133
4.3 Results 134
4.3.1 Effect of chemotherapy agents on cell lines 134
4.3.2 Binding chemotherapy agents to bovine serum albumin 137
4.3.3 Immobilising BSA-Pac on synthesised copolymers 142
4.4 Discussion 145
4.4.1 Effect of chemotherapy agents on cell lines 145
4.4.2 Binding chemotherapy agents to bovine serum albumin 146
4.4.3 Uptake and release of BSA onto the (poly-b-(NIPAM-co-acrylamide)-b-methacrolein copolymer 149
4.5 Conclusions 150
Chapter 5: Nanoparticle-polymer complex assembly 152
5.1 Introduction 152
5.2 Materials and methods 153
5.2.1 Superparamagnetic iron oxide nanoparticle poly–(methacrolein-b-(NIPAM-co-acrylamide) synthesis 153
5.2.2 Induction heating of the NCC 156
5.2.3 Analysis techniques 156
5.3 Results 157
5.3.1 Poly-N-isopropylacrylamide stabilised iron oxide nanoparticles 157
5.3.2 Nanoparticle copolymer complex synthesis and analysis 158
5.3.3 Radio wave stimulated release of BSA from the Nanoparticle copolymer complex and FITC attachment 172
5.4 Discussion 176
5.4.1 SPION surface synthesised poly-N-isopropylacrylamide 176
5.4.2 Nanoparticle copolymer complex synthesis and analysis 177
5.4.3 Protein immobilisation and release from the nanoparticle copolymer complex 180
5.4.4 Comparison to other protein release methods reported in literature 182
5.5 Conclusions 183
Chapter 6: Selective cell death in cell lines 185
6.1 Introduction 185

6.2 Materials and methods 187
6.2.1 Cell culture and viability experiments 187
6.2.1 Spheroid experimentation 188
6.2.2 Magnetic directing capacity of ION-Polymer complex 189
6.3 Results 192
6.3.1 Haemolysis effects of the nanoparticle copolymer complex 192
6.3.2 Initial cell viability assessment 193
6.3.3 Effect of NCC activation on cell viability 195
6.3.4 Effect of NCC drug delivery on spheroids 201
6.3.5 Magnetic dictation of cells as a demonstration of magnetic direction capabilities 205
6.4 Discussion 207
6.4.1 Haemolysis effects of the nanoparticle copolymer complex 207
6.4.2 Enhanced cell death with radio wave stimulation of the NCC 208
6.4.4 Effect of drug delivery to cell spheroids 214
6.4.5 Magnetic localisation of cells and nanoparticles 215
6.5 Conclusion 215
Chapter 7: Computational modelling of induction heating parameters 217
7.1 Introduction 217
7. 2 Materials and methods 218
7.21 Script language used 218
7.2.2 Constant values 218
7.2.3 Variables 219
7.3 Results 219
7.3.1 Model design and calculations 219
7.3.2 Study of parameters affecting activation heating times 225
7.3.3 Study of parameters affecting linear heating rates (SAR) 227
7.3.4 Study of parameters affecting power produced per particle 229
7.4 Discussion 229
7.4.1 Linear response theory calculations 229
7.4.2 Field effects 231
7.4.3 Frequency effects 231
7.4.4 Diameter effects 233
7.4.5 Comparison to specific absorption rates observed 233
7.4.6 Assumptions and limitations of the model 234
7.5.7 Other factors that would affect heating rates *in vivo* 235
7.5.8 Further work and adaptations 236

7.5 Conclusions 237
Chapter 8: Conclusion and future directions 238
8.1 Summary of findings and limitations 238
8.2 Future work 242
8.3 Impact in oncology 245
8.4 Closing remarks 245
Appendix 247
Bibliography 256

Abbreviations and acronyms

AA	Acrylic acid
AC	Differential centrifugal sedimentation
ACR	Acrolein
AIBN	Azobisisobutyronitrile
AM	Acrylamide
AMF	Alternating magnetic field
AT	Allyl thiol
AU	Arbitrary units
BSA	Gel permeation chromatography
Cp	Specific heat capacity
CPS	Centrifugal sedimentation
CT	Computerized tomography
DC	Direct current
DD-ION	2-(Dodecylthiocarbonothioylthio)-2-methylpropionic acid stabilised iron oxide nanoparticles.
DDMAT	2-(Dodecylthiocarbonothioylthio)-2-methylpropionic acid
DMF	Dimethylformamide
DNA	Deoxyribonucleic acid
DSC	Differential scanning calorimetry
EPR	Enhanced permeation and retention
FID	Transmission electron microscope
FITC	Fluorescein isothiocyanate
FT-IR	Fourier transform – infrared (spectroscopy)
GC	Gas chromatography
GPC	Gel permeation chromatography
HPLC	High-performance liquid chromatography
HSA	Human serum albumin

ION	Iron oxide nanoparticles
LA	Lauric acid
LA-ION	Lauric acid stabilised iron oxide nanoparticles.
LCST	Lower critical solution phase transition temperature
LRT	Linear response theory
MA	Methacrolein
MN	Number average molecular weight
MOSFET	Metal – oxide – semiconductor field-effect transistor
MP	Molecular weight of peak maxima
MRI	Magnetic resonance imaging
MV	Viscosity molecular weight
MW	Weight average molecular weight
MZ	Size average molecular weight
NAPQI	N-acetyl-p-benzoquinone imine
NCC	Nanoparticle copolymer complex
NMR	Nuclear magnetic resonance
NPs	Nanoparticles
PBS	Phosphate buffered saline
PCB	Printed circuit board
PDI	Poly dispersity index
PDT	Photodynamic therapy
PLIN	Power generated (by linear response model)
PN-ION	Poly(N-isopropylacrylamide) stabilised iron oxide nanoparticle
PNIPAM	Poly(N-isopropylacrylamide)
PPP	Power per particle
PS	Photo sensitiser
RAFT	Reversible addition-fragmentation chain transfer polymerisation
RMS	Rhabdomyosarcoma
SAR	Specific absorption rate
SD	Standard Deviation
SEM	Scanning electron microscopy
SPIONs	Superparamagnetic iron oxide nanoparticles
TEM	Transmission electron microscopy
THF	Tetrahydrofuran
UV-VIS	Ultraviolet – Visible light spectrum (spectroscopy)

List of Figures

Figure 1. 1: Five-year cancer survival rates in the USA. 1
Figure 1. 2: Schematic demonstrating the enhanced permeation and retention effect. 6
Figure 1. 3: Drainage of nanoparticles through different organs according to their properties. 8
Figure 1. 4: Nanoparticle properties and features that can be adjusted to aid in specific uptake to cancer cells. 13
Figure 1. 5: Active targeting strategies for nanoparticles. 14
Figure 1. 6: Magnetic configuration of ferrimagnetic and superparamagnetic materials. 16
Figure 1. 7: Field effects of an electromagnet and the mechanism of joule heating. 21
Figure 1. 8: An example of ultrasound stimulated treatment. 28
Figure 1. 9: An example of a dual functional NIR stimulated therapeutic system. 35
Figure 1. 10: Overall nanoparticle polymer complex design, stimulation technique and general treatment method which this project has created, graphically explained.. 42

Figure 2. 1: The unit cell structures in the crystals of (A) magnetite and (B) maghemite. 46
Figure 2. 2: Typical TEM images of LA-ION synthesised particles. 52
Figure 2. 3: Measured particle diameters of LA-ION and DD-ION. 53
Figure 2. 4: FT-IR spectrum of LA-ION (Blue) and DD-ION (purple). 54
Figure 2. 5: Zeta potential of stabilised SPIONs. 55
Figure 2. 6: Gas chromatography spectrum of DDMAT obtained from the surface of DD-ION particles. 57
Figure 2.7: Typical TEM images of DD-ION synthesised particles. 59
Figure 2. 8: Thermal gravimetric analysis data of Lauric acid stabilised iron oxide nanoparticles. 61
Figure 2. 9: Initial induction heater circuit design. 62
Figure 2. 10: Final induction heater circuit design. 64
Figure 2. 11: Images of the constructed induction heating device. 65
Figure 2. 12: Heating capabilities of the induction heating device. 68

Figure 3. 1: Structure of poly N-isopropylacrylamide (PNIPAM) and the phase change that occurs at the LCST. 77
Figure 3. 2: The reaction scheme of a typical RAFT polymerisation reaction. 80
Figure 3. 3: Exchange reaction on the surface of Iron oxide nanoparticles. Lauric acid ligands on the surface are exchanged with excess DDMAT molecules present in solution. 82
Figure 3. 4: Polymerisation of n molecules of NIPAM, initiated by AIBN to form PNIPAM. 88
Figure 3. 5: Identification of the structure of PNIPAM by spectroscopy methods. 89
Figure 3. 6: Determination oof the LCST of PNIPAM. 92
Figure 3. 7: Reaction scheme for the RAFT copolymerisation of NIPAM and Acrylic acid (A) and the FT-IR spectrum of the resultant product (B). 93
Figure 3. 8: Reaction scheme for the RAFT copolymerisation of NIPAM and Acrolein (A) and the FT-IR spectrum of the Poly-Acrolein-NIPAM product (B) 95
Figure 3. 9: Reaction scheme for the copolymerisation of NIPAM, acrylic acid and Acrolein and identification of the structure by spectroscopy methods.. 97
Figure 3. 10: Copolymerisation of NIAPM and acrylamide analysis and polymerisation.. 101
Figure 3. 11: Reaction scheme and analysis of copolymerised NIPAM, acrylamide and allyl thiol. 103

Figure 3. 12: Reaction scheme and product analysis of the copolymerisation of NIPAM, Acrylamide and Methacrolein.....106
Figure 3. 13: NMR analysis of the product from the copolymerisation of NIPAM, Acrylamide, and Methacrolein..
.....109
Figure 3. 14: Thermodynamic and physical data of PNIPAM and copolymerised NIPAM, Acrylamide, and Methacrolein.....112
Figure 3. 15: The simulated three dimensional structure of the synthesised Poly-b-Methacrolein-b-NIPAM-co-acrylamide copolymer in its hydrophilic coil like state.....115

Figure 4. 1: The effect of varying paclitaxel concentrations on the cell viability of RD cells (A) and RH30 cells (B). 135
Figure 4. 2: The effect of Vinblastine on the cell viability of U87-MG (A) and MCF-7 (B) Cells. 136
Figure 4. 3: The effect of Paracetamol on the cell viability of HEP-G2 cells.....137
Figure 4. 4: HPLC chromatogram demonstrating the Paclitaxel detection.....138
Figure 4. 5: HPLC chromatogram demonstrating vinblastine detection.....139
Figure 4. 6: HPLC chromatogram demonstrating paracetamol detection.....141
Figure 4. 7: The cycled release of BSA from the copolymer.. 143
Figure 4. 8: The cycled release of BSA- drug proteins from the synthesised copolymer.....144

Figure 5. 1: Spectroscopy of SPION synthesised polymers.....160
Figure 5. 2: The spectroscopic analysis of the NCC 162
Figure 5. 3: Thermodynamic analysis of the NCC. 164
Figure 5. 4: Hydrodynamic diameter measurements of the NCC.....166
Figure 5. 5: Electron microscopy images of the NCC particles splutter coated in a gold-palladium alloy. 167
Figure 5. 6: Schematic diagram illustrating the physiological mechanism of protein-bearing drug release from the NCC upon reaching the LCST.....169
Figure 5. 7: Imgaes of the NCC (Copolymer ratio PNIPAM-Acrylamide-Methacrolein 45:45:10) below and above the lower critical phase transition temperature of the complex, and indcution heating of the NCC.....171
Figure 5. 8: Release profile of BSA from protein loaded NCC as measured by Bradford protein assay.....173
Figure 5. 9: Fluorescence tagging reaction and fluorescence of the resulting NCC-fluorophore.. 175
Figure 5. 10: Fluorescence effects of binding a fluorophore to the nanoparticle complex.....176

Figure 6. 1: Haemolysis percentages highlighting the biocompatibility of the unloaded NCC. PBS was used as a negative control and water as a positive control to indicate haemolysis. Standard deviation is given as error bars P value significance indicators, ***=p<0.01, **= 0.05<p>0.01, *=0.5<p>0.05.....192
Figure 6. 2: Qualitative images demonstrating stimulated cell death by radio wave activation. 194
Figure 6. 3: Effects of NCC assisted delivery of Paclitaxel to cancer cells.....196
Figure 6. 4: Cell viability was assessed by delivering vinblastine via the NCC to cells in vitro to U87-MG cells (A) and MCF-7 cells (B). 198
Figure 6. 5: Cell viability was assessed by delivering paracetamol via the NCC to HEP-G2 cells in vitro.....200
Figure 6. 6: The effect of drug delivery by the NCC on spheroid models 202
Figure 6. 7: The effect of paracetamol delivery by the NCC on HEP-G2 spheroid models.....204
Figure 6. 8: The 6 well plate setup for the demonstration of magnetic dictation of cells by NCC-FITC. The black circles represent the position of the neodymium magnets below the plate. 205
Figure 6. 9: Magnetic localisation of cells in vitro.. 206

Figure 7. 1: Overall model flow chart design for use in the clinic 220
Figure 7. 2: Pilot model design.....221
Figure 7. 3: Predicted heating times required for activation of the NCC dependent on induction heating and particle parameters.....224
Figure 7. 4: SAR or Power generated by NCC particles from the linear response model (PLIN) In Wm^{-3}.....226
Figure 7. 5: Power generated per particle from the linear response model (PPP).....228

Table 1. 1: Clinically approved nanomedicines and the cancer types approved for treatment, as of 2017. Adapted from Tran et al.[30] 5

Table 2. 1: Quantification of loading of DDMAT on DD-ION by the different investigated synthesis methods 57

Table 3. 1: Examples of free Radical monomer reactivity ratios.[214].....83
Table 3. 2 : Depiction of the LCST of each type of copolymer created, based on the molar ratios of the constitute monomers at the start of the polymerisation process. Not necessarily the resultant molar ratio in the synthesised product. 99
Table 3. 3: Effect on the LCST of a synthesised copolymer with increasing content of acrylamide in the starting reagents. 102
Table 3. 4: Effect on the LCST of a synthesised copolymer with increasing content of allyl thiol in the starting reagents. 104
Table 3. 5: Effect on the LCST of a synthesised copolymer with varying content of NIPAM, acrylamide and methacrolein in the starting reagents. 111
Table 3. 6: Calculated dispersity and molecular values for synthesised polymers 114

Table 4. 1: The loading ratios of chemotherapeutic agents to BSA. Ratios are given as molecules loaded onto each BSA protein.....141

Table 5. 1: Calculated dispersity and molecular values for synthesised NIPAM-Acrylamide-Methacrolein copolymer synthesised at a starting molar ratio of 45:45:10 respectively on the surface of SPIONs 164
Table 5. 2: Effect on the LCST of the synthesised NCC with varying content of NIPAM, acrylamide and methacrolein in the starting reagents. 169

Chapter 1: Literature review

1.1 Cancer treatment and chemotherapy

Cancer is the second biggest killer in the world by any measure.[1] Around 9.6 million people die each year as a result of cancer all across the globe.[2] Cancer is not just a burden in terms of illness and loss of life, but carries a heavy financial toll as well with over $200 billion spent on in the US on cancer treatment in 2020.[3] Although survival rates are better now than they have ever been, research to improve treatment is ongoing (Figure 1.1). Cancer is one of the biggest challenges facing scientists and clinicians in the 21st century, and there is political, social and economic pressure for scientists to develop new innovative and effective treatment methods.

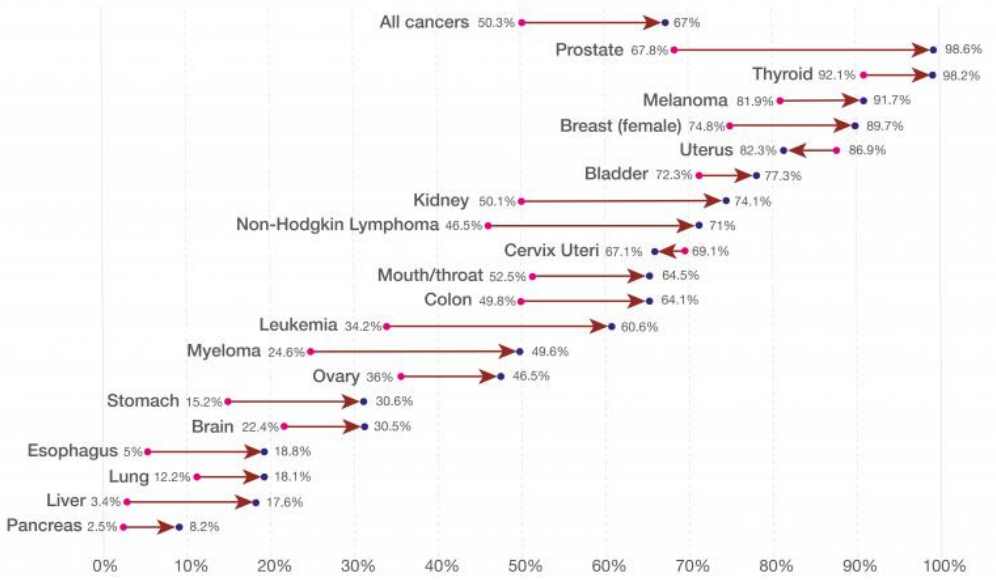


Figure 1. 1: Five-year cancer survival rates in the USA. The average survival rate for each type of cancer from 1970-77 is represented by the pink dots, the survival rate from 2007-13 is represented by the blue dots. Taken from the national cancer institute.[4]

Cancer cells develop and proliferate quickly and continuously. In healthy somatic cells, a number of growth factors and cell signalling precisely control cell growth and proliferation cycles to preserve homeostasis in

cell number and function. Cancer cells lose such homeostasis as a result of stimulatory proliferative signals (from intrinsic cells or nearby non-cancerous cells) and the deregulation of anti-proliferative signals. Apoptosis-inducing capacity is also permanently lost or deregulated.[5,6] These phenomena lead to an aberrant cell cycle, cell immortality and limitless proliferation in cancers.

The connection or adhesion between cells is reported to be diminished or blocked in many aggressive malignancies, which increases cellular mobility, tumour metastasis, and invasion.[7–9] Due to the down-regulation of some cell-cell adhesion molecules (such as cadherins, radixin), the degradation of extracellular matrix, and the up-regulation of lamellipodia formation, cancer cells can leave the primary tissue sites and migrate to nearby, or even distant tissues, via the circulatory and/or lymphatic systems.[10,11]

The microenvironment of tumour cells differs greatly from that of healthy cells as a result of abnormal cellular metabolic processes and faulty angiogenesis. The oxygen supply to tumours is never adequate (particularly in the core), which results in hypoxia. This is because tumours grow quickly and without limit, consuming a lot of oxygen through aerobic glycolysis.[12] Furthermore, defective angiogenesis causes the accumulation of acidic molecules (e.g. CO_2 , lactic acid), resulting in an acidic microenvironment with a pH as low as 6.5.[13] This has broad ramifications because effective anti-cancer drugs must function in the tumours acidic and hypoxic microenvironment. Hypoxia is a state in which oxygen is not available in sufficient amounts at the tissue level to maintain adequate homeostasis, resulting in cellular death.[14]

1.1.1 Chemotherapy

One of the most common forms of cancer treatment is chemotherapy.[2,15] This is a method of treating cancer by the administration of therapeutic drugs that destroy cancer cells and these drugs, whether natural or

synthetic, are known as chemotherapy agents. Chemotherapy agents can be administered by several methods including injections, oral consumption and embedment in a biodegradable device.[16] Although chemotherapy has no doubt saved many lives and is hugely effective in the majority of cases (Figure 1.1), the fundamental problem is the lack of specificity when targeting cancerous tissue.[16] This undiscerning destruction of cells leads to many adverse side effects including, but not limited to, hair loss, fatigue, decrease of libido, weight loss and breakdown of the immune system.[17] Surgery, radiotherapy, and/or other forms of chemotherapies are frequently combined with the administration of a chemotherapeutic. Chemotherapeutics can be roughly divided into molecularly focused therapy, hormonal therapies, and cytotoxic chemotherapeutics.

The most traditional and often used chemotherapeutics to date are cytotoxic agents. Through various methods, including as preventing mitosis or interfering with DNA synthesis, they harm and destroy rapidly dividing and expanding cells. The most well-known and frequently used examples include Camptothecin (inhibiting DNA topoisomerase activities, preventing DNA re-ligation, causing DNA damage and cell death), Paclitaxel (restraining mitosis by inducing microtubule polymerization and inhibiting the formation of the mitotic spindle), and Doxorubicin (intercalating DNA).[18–20] Cytotoxic chemotherapeutics can effectively accumulate in and destroy tumours since most cancer cells multiply far more quickly than healthy cells. However, they also cause significant harm to healthy cells that divide quickly, such as bone marrow stem cells. As a result, they may cause serious adverse effects such decreased blood cell formation, epilation, and infertility.[17] Epilation refers to the loss or removal of hair.[21]

Molecular targeted treatments can target particular enzymes (like some kinases) or oncogenes that are linked to tumour growth and/or carcinogenesis rather than disrupting all rapidly proliferating cells. There have

been numerous studies on therapies that target poly-ADP-ribose polymerase, the folate receptor, and epidermal growth factor, with some of these making it to the clinical trial stage.[22] Therapeutics targeting cell growth, apoptosis evasion, and mis-regulated metabolism pathways are being considered as promising anti-cancer agents to treat many cancers.[22,23]

Some malignancies, such as some breast and ovarian cancers, are hormone-dependent. A method of treating these tumours is by altering (or disrupting) the endocrine system, slowing tumour growth or even causing cancer cells to die.[24] This is known as hormone therapy.

In practice, chemotherapy for human solid tumors is by no means adequate, despite the discovery and synthesis of hundreds of thousands of anticancer compounds targeting various crucial units in cancer cell proliferation and metabolism. The main issue is the lack of targeted delivery of these compounds into solid tumour tissue, this is important to maintain an effective concentration level for a certain amount of time for drug-tumour interaction to carry out anticancer activities.

1.2 Nanoparticles and nanotechnology in oncology

Nanoparticles are defined as being particles with a diameter between 1-1000 nm.[25] In the last 30 years nanotechnology has become a huge area of interest in almost every area of science research. Nanoparticles possess very advantageous inherent properties compared to bulk material of the same substance. These include; an extremely high surface area to volume ratio, single domain magnetism, quantum surface effects and the enhanced permeation and retention (EPR) effect with cancer tissue.[15,26–28] The EPR effect is an example of passive targeting of cancer cells by nanoparticles.[29]

Nanomedicine, a contemporary field in nanotechnology, has the potential to solve this fundamental flaw in conventional chemotherapy. As of 2017 there were 13 clinically available nanomedicines for cancer treatment.[30]

Table 1. 1: Clinically approved nanomedicines and the cancer types approved for treatment, as of 2017. Adapted from Tran et al.[30]

Year approved	Name	Type	Active drug	Type of cancer
Japan (1994)	Zinostatin stimalamer	Polymer protein conjugate	Styrene maleic anhydride neocarzinostatin (SMANCS)	Renal cancer
FDA (1995) EMA (1996)	Doxil/caelyx	Liposome (PEGylated)	Doxorubicin	HIV-associated Kaposi's sarcoma, ovarian cancer, metastatic breast cancer, multiple myeloma
FDA (1996)	DaunoXome	Liposome (non-PEGylated)	Daunorubicin	HIV-associated Kaposi's sarcoma
Taiwan (1998)	Lipo-Dox	Liposome	Doxorubicin	Kaposi's sarcoma, breast and ovarian cancer
FDA (1999)	DepoCyt	Liposome	Cytosine arabinoside (cytarabine)	Neoplastic meningitis
EMA (2000)	Myocet	Liposome	Doxorubicin	Breast cancer
FDA (2005) EMA (2008)	Abraxane	Nanoparticle albumin bound	Paclitaxel	Advanced non-small-cell lung cancer, metastatic pancreatic cancer, metastatic breast cancer
FDA (2006)	Oncaspar	PEG protein conjugate	L-Asparaginase	Leukemia
South Korea (2007)	Genexol-PM	PEG-PLA polymeric micelle	Paclitaxel	Breast cancer, Lung cancer, Ovarian cancer [126]
EMA (2009)	MEPACT	Liposome (non-PEGylated)	Mifamurtide	Osteosarcoma
EMA (2010)	NanoTherm	Iron oxide nanoparticle	–	Thermal ablation glioblastoma
FDA (2012)	Marqibo	Liposome (non-PEGylated)	Vincristine	Philadelphia chromosome negative acute lymphoblastic leukemia
FDA (2015)	MM-398 (Onivyde)	Liposome (PEGylated)	Irinotecan	Metastatic pancreatic cancer (2nd line)

There are several properties of nanoparticles which make them ideal as carriers of drugs to tumor sites or as therapeutic complexes themselves. The enhanced permeation and retention effect means nanoparticles will passively accumulate in cancer cells at a higher proportion than healthy tissue (Figure 1.2).[29] Leaky tumour blood vasculature allows nanoparticles to be taken up at higher rates by tumour tissue, and poor lymphatic drainage also prevents nanoparticles from being secreted.[31] Drug circulation times are also massively

increased by attachment or encapsulation with nanoparticles, improving drug half-life and allowing smaller doses to be used.[32] Size, shape and charge can also be precisely controlled in nanoparticle synthesis and all can be used to increase uptake in cancerous tissue. Drugs with poor aqueous solubility and therefore a short half-life can be bound to nanoparticles as a transport vehicle.[33 – 35] Particles can also be coated in ligands targeting proteins or membrane features specific to cancer cells. Highlighted in this project, nanoparticles allow the creation of controlled payload release systems, under activation from an external stimulus.[30]

1.2.1 Nanoparticle effects *in vivo*

Since the strength of the EPR effect varies depending on the type and location of tumours, the state of blood perfusion in tumours, and the physical-chemical properties of macromolecular anticancer medicines, targeting therapy by the EPR effect is not always successful in practical use in the clinic.

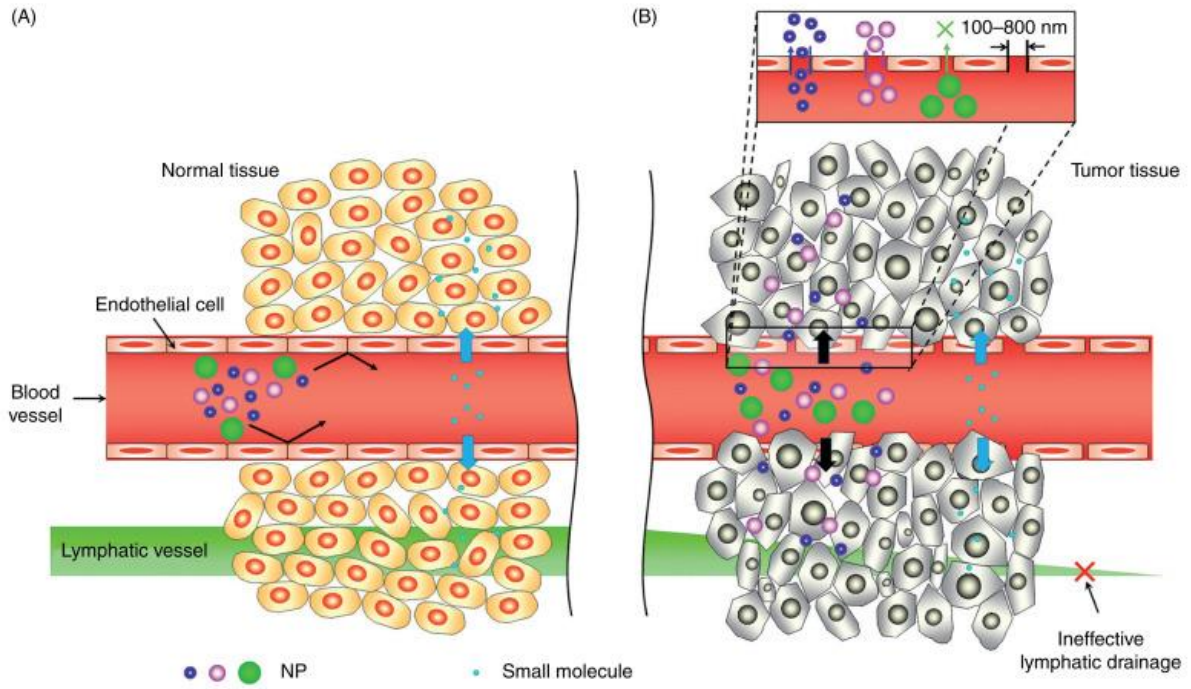


Figure 1. 2: Schematic demonstrating the enhanced permeation and retention effect. Transfer pathways of nanoparticles and molecular drugs from blood vessels into healthy tissue (A) and from abhorrently formed blood

vessels into tumour tissue (B). Also demonstrated is the capacity of the lymphatic drainage of each tissue. Taken from Neda Alasvand et al. [36]

The EPR effect is widely acknowledged as one of the universal pathophysiological properties of solid tumours and serves as a core design basis for anticancer drug delivery systems that target specific tumours.[37,38] However, gaining enough therapeutic benefits in clinical practice has long been a challenge for the development of nanomedicine. Thus, there has been disagreement over the presence and strength of the EPR effect in situations involving human solid tumours.[39,40] For instance, it is thought that the EPR effect is more relevant in small animal tumour models used in research than it is in human malignancies. In comparison to animal tumour models, the delivery efficacy of nanoparticles into human tumour tissue is quite poor. The spaces between endothelial cells in the tumour vasculature vary between tumour types, and vesiculo-vacuolar organelles that also play a role in the extravasation of nanoparticles into tumours, behave very differently between tissues.[41] In 2016 the Warren Chan group found that only 0.7% (median) of the injected nanoparticle dose is found to be delivered to a solid tumour.[42] Furthermore, in 2020 the Chan group used three different human tumour xenograft models in mice to demonstrate that the main route (97%) of particles enter tumour tissue not through the large fenestrations in tumour blood vessels, but by active transcytosis through the endothelial cells themselves.[43] The conclusion of this study suggested future research should aim at refining and manipulating the specific active mechanisms of transport across endothelial cells. In addition, future work should also study surface adsorbed proteins on nanoparticles and their interaction with tumour endothelial cells. Research in these areas could help increase rates of nanoparticle accumulation in target sites. However, at this current point in time it cannot be guaranteed that the EPR effect will have a considerable impact on efficacy of nanoparticle delivery.

Utilizing the EPR effect to create and enhance the therapeutic efficacy of nanomedicine is the true problem. Optimal size and surface charge, clever drug release mechanisms, and administration kinetics are only a few of the enhancement techniques that might increase delivery and accumulation efficacies. The accumulating performance of nanoparticles in tumour tissues may not always be the same as with other macromolecules like linear polymers and biological macromolecules like albumins, due to their hard structure properties (in this context hard refers to particles that are dense and incompressible, usually solid inorganic particles). It may be necessary to further modify nanoparticles with polymers in order to increase their affinity for tumour-related endothelial cells.[29]

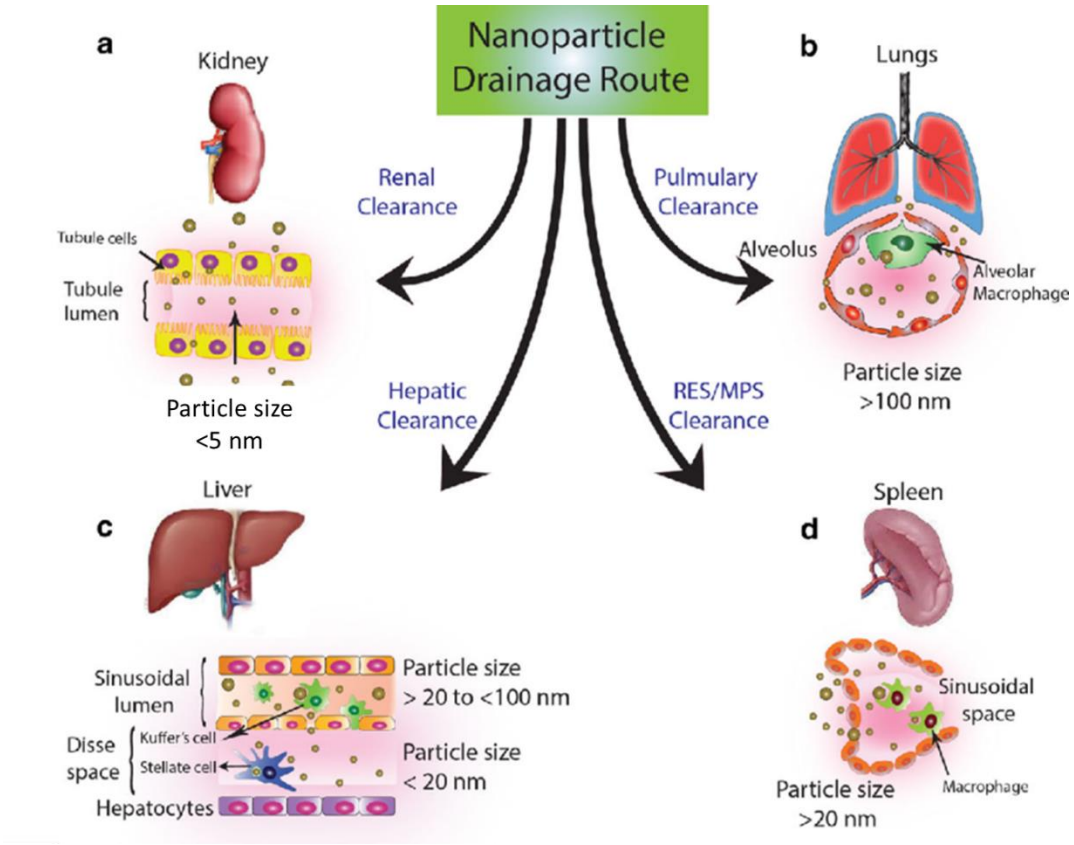


Figure 1. 3: Drainage of nanoparticles through different organs according to their properties. (A) The Kidney is the most common drainage system eliminating the particles and the particles are easily eliminated from the blood. Although the lungs (B) is not a conventional eliminatory system, it can help in filtering aerosolic nanoparticles for elimination. A second level of elimination is done through the liver (C). The larger particles (200 nm) which are not eliminated through the kidney or liver are eventually eliminated by the RES (D). Taken from Bose et al.[44]

The effectiveness of cellular absorption and the potential toxicity of nanoparticles to living cells are both significantly influenced by its size. [45,46] Furthermore, it was discovered that the size of nanoparticles also had a significant impact on the absorption pathway. Pino- or macropinocytosis is the mechanism through which small nanoparticles with diameters ranging from a few to several hundred nanometres enter the cells. Nanoparticles with a size between 120 and 150 nm are internalised through clathrin- or caveolin-mediated endocytosis, whilst NPs with a size between 250 nm and 3 μm have been demonstrated to have the best *in vitro* phagocytosis.[47,48 – 50]

Due to nonspecific uptake of nanoparticles in healthy organs, the main drawback of nanotherapeutic delivery is its inability to provide therapeutic doses of medicines at disease locations. Nanoparticles are promptly captured by the mononuclear phagocyte system (MPS), which is a network of phagocytic cells, primarily resident macrophages, located in the spleen, lymph nodes, and liver.[51] Opsonization of nanoparticles, which involves the adsorption of plasma proteins, such as serum albumin, apolipoproteins, complement-building blocks, and immunoglobulins onto the surface of moving nanoparticles, is the first step in the sequestration process.[52] PEGylation is the process of attaching polyethylene glycol (PEG) to the surface of nanoparticles, where the ethylene glycol units make close bonds with water molecules to create a hydrating layer. This hydrating layer in turn hinders protein adsorption and subsequent clearance by the MPS.[53]

One of the main goals in delivering drugs using nanotechnology is increasing the circulation times of drugs. In order to achieve this, it is important to consider the clearance routes of nanoparticles from the body

(Figure 1.3). Two of the major routes of nanoparticle clearance from the body is renal and hepatic clearance.[54]

Renal clearance of intravascular agents is a multifaceted process involving glomerular filtration, tubular secretion, and finally elimination of the molecule through urinary excretion.[54] Taking into consideration, the combined effects of each layer of the capillary wall, the functional pore size is significantly small, only 4.5-5 nm in diameter (Figure 1.3A). Therefore, to undergo primarily renal clearance, NPs should be smaller than the kidney filtration threshold of ~5 nm while simultaneously avoiding sequestration by the MPS. NP recognition by phagocytes is mediated through protein opsonisation.[55] This means that the formation and composition of an NP's corona greatly determines its uptake by the MPS. The conventional approach to reducing phagocyte recognition involves the use of antifouling and hydrophilic polymers.[56]

In the hepatic route, NPs are captured by the mononuclear phagocyte system (MPS) or tissue-resident phagocytes, leading to their accumulation in the liver and spleen. Subsequently, NPs are subject to biliary elimination and excretion via the stools. One of the physiologic functions of the liver is to efficiently capture and eliminate particles on the scale of 10-20 nm for the clearance of viruses and other small particles.[57] As a result of this adaptation, agents within this size range often undergo rapid liver uptake. It is worth noting however, that the size of liver fenestrations varies between mice and humans.[58] It has been measured at 107 ± 1.5 nm (mean $\pm$ SEM) in the human liver, while for the mouse liver an average diameter of 141 ± 5.4 nm.[59] This size difference means hepatic clearance of particles will differ between mouse and human experiments and must be considered when analysing results.

Pulmonary clearance is also a clearance route for particles in the near tissue vicinity of the lungs (Figure 1.3 B).[44] *In vivo* clearance of nanoparticles by transcytosis across alveolar epithelial cells has been shown in mice.[60]

Lower clearance rates of particles could increase the efficiency of delivery but also potentially harm other organs or tissues particles accumulate in. For effective treatment, a careful balance between the two must be established.

1.2.2 Advantages and enhancements of nanoparticles in drug delivery

Nanoparticles are used in many different ways for diagnostics, both within and outside oncology. In magnetic resonance imaging (MRI), superparamagnetic iron oxide nanoparticles (SPION) and Galodinium contained within paramagnetic liposomes, are used as contrast agents to help improve *in vivo* imaging.[61–63] Micro and nano gas bubbles can assist in ultrasound to improve temporal and spatial imaging.[64,65] Iodine based micelles, barium and gold nanoparticles are used as contrast agents in CT scans.[66–68] Optical imaging is also improved with the use of quantum dots and fluorescent nanoparticles.[69–71]

Nanoparticle-based radio sensitization is a technique of using nanoparticles to increase the susceptibility of tumour cells to ionizing radiation to achieve a higher radiotherapeutic ratio. Nanoparticles can act as photosensitiser carriers or photosensitisers themselves.[72–74] Therapeutic NPs (e.g., cisplatin, oxaliplatin or carboplatin containing particles) can sensitize and kill cancerous cells without input of ionizing radiation. They can also act in a dual manner as radiosensitizers to increase the therapeutic ratio when combined with ionizing radiation exposure due to inclusion of high atomic number elements such as platinum.[75]

Photo dynamic therapy (PDT) can also be enhanced using nanoparticles as photosensitiser carriers or photosensitisers themselves. Two different strategies are often adopted as nanoparticle carriers for PDT. The first is biodegradable nanoparticles (natural or synthetic polymer-based nanoparticles) carrying the photosensitiser (PS) payload, which could undergo enzymatic or hydrolytic degradation and thereby excreted out, minimizing long-term accumulation of carriers in biological system.[76] The second is nonbiodegradable nanoparticles (ceramic- or metal-based nanoparticles), which do not readily degrade in the biological system, but quite often offer in-built multiple functionalities that make them valuable as theranostic agents. When subjected to radiotherapy wavelengths, these particles can generate reactive oxygen species (ROS) to enhance the therapeutic effect.[77] Nanoparticles can also act as Energy Transducers, transferring absorbed light onto conjugated photosensitisers. Generally, the energy harnessed from light is transferred to the PS associated with the particle, thereby offering the possibility of indirectly activating the PS using light at wavelengths that it normally does not absorb. Thus, reducing the possibility of off target effects.[78]

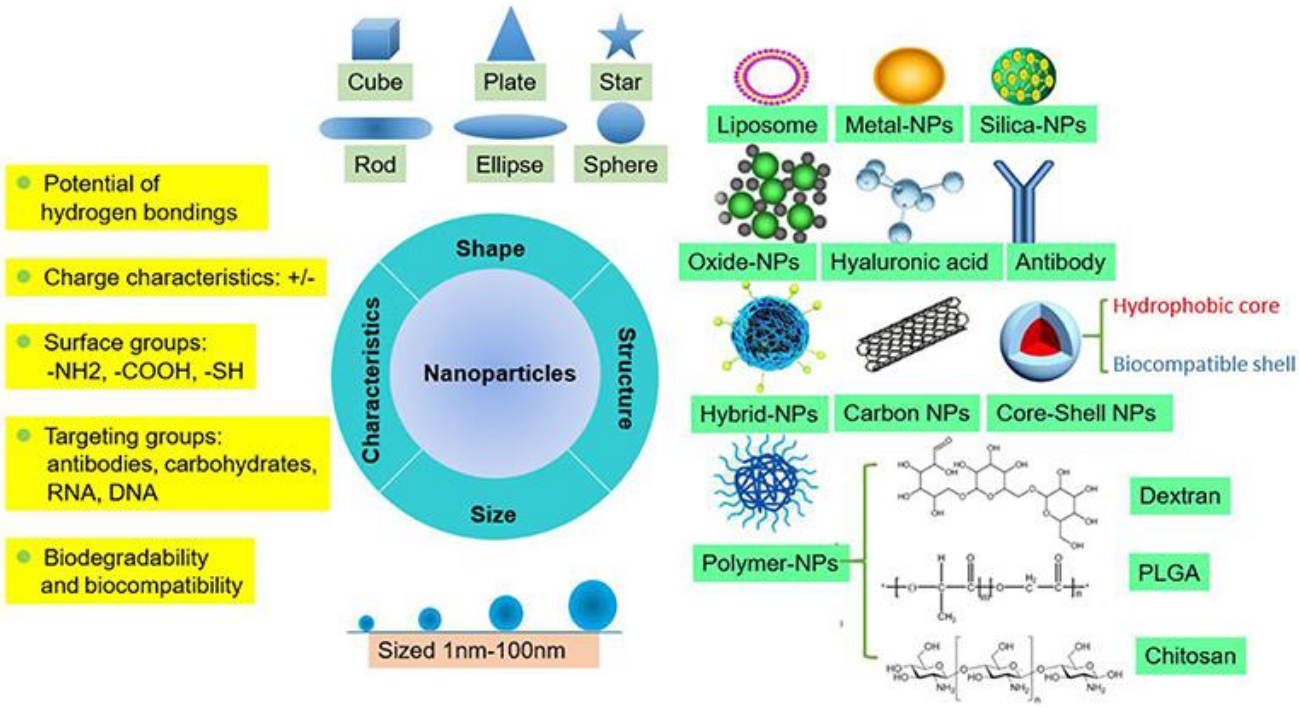


Figure 1. 4: Nanoparticle properties and features that can be adjusted to aid in specific uptake to cancer cells. Schematic showing the different nanoparticle properties and functions which can be controlled during the production of nanoparticle-based drug delivery systems. Taken from Hu, G. et al[79]

Nanoparticles are used extensively as vesicles for targeted drug delivery. Metallic, organic, inorganic and polymeric nanostructures, including dendrimers, micelles, and liposomes are frequently considered in designing the target-specific drug delivery systems (Figure 1.4).[30,80] Nanoparticles typically have longer circulation times than small drug molecules when administered intravenously, given that they are large enough not to be excreted by the kidneys or too large to be trapped by the reticuloendothelial system.[29] The therapeutic effect of hydrophobic drugs in particular is massively increased, due to the removal of the harmful solvents previously needed.[81] The efficacy of these nanostructures as drug delivery vehicles varies depending on the size, shape, and other inherent biophysical/chemical characteristics.[82–84] For example, polymeric nanomaterials with diameters ranging from 10 to 1000 nm, possess properties that make them ideal for drug delivery. Polymeric nanoparticles can be categorized into nanospheres and nanocapsules, both of which are excellent drug delivery systems. Examples of dual phase, hydrophilic-hydrophobic drug

encapsulation has been shown in polymeric nanocapsules. Similarly, lipid nanostructures and phospholipids including liposomes and micelles are very useful in targeted drug delivery.[85] In the 1980s the first passively targeted nanocarriers reached clinical trials, while in the mid-1990s the first products based on liposomes and polymer-protein conjugates were approved for clinical use.[86] Nanoparticles have also been used in combination with natural products to further lower observed toxicity.[87,31] Thus, nanotechnology offers a plethora of benefits in treating chronic human diseases by site-specific, and target-oriented delivery of medicines.

1.2.3 Active targeting strategies of nanoparticles

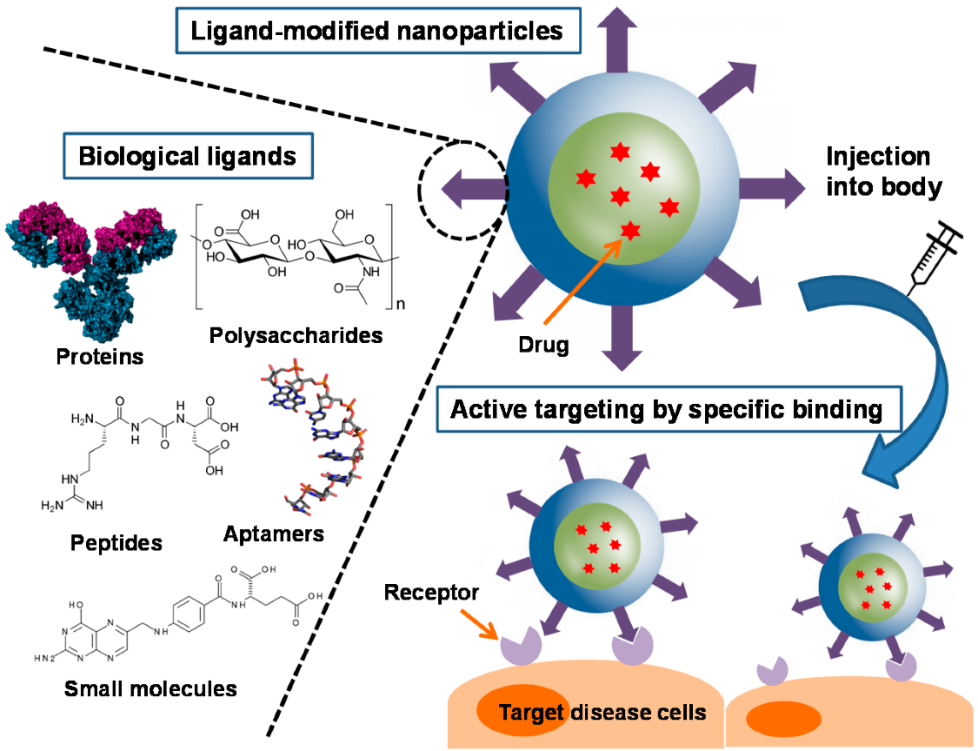


Figure 1. 5: Active targeting strategies for nanoparticles. Schematic detailing how ligands on the exterior of particles can bind to receptors on cells to aid nanoparticle uptake. Taken from Yoo et al.[88]

A type of active targeting involves the use of conjugating ligands onto the surface of nanoparticles which specifically increases the retention and uptake of the nanoparticles within cancer tissue (Figure 1.5). Ligands

are selected to bind to specific proteins or molecules that are overexpressed on cancer cell membranes. Characteristic ligands include antibodies, proteins, aptamers and nanobodies.[89]

In contemporary medicine, antibodies are well-established target-specific reagents used for both therapeutic and diagnostic purposes. Antibodies were among the first agents employed to direct nanovehicles to particular cell types based on the antigens on their surface.[90] Due to the availability of two epitope binding sites in a single molecule, antibodies exhibit extremely high selectivity and binding affinity when used as targeting agents.[91] There are now many monoclonal antibody medicines that have received FDA approval, and hundreds more are undergoing clinical studies. Common targets for nanoparticle delivery are; human epidermal growth factor receptor 2, epidermal growth factor receptor, transferrin receptor, and prostate-specific membrane antigens.[92]

Aptamers are short single-stranded DNA or RNA molecules with defined three-dimensional structures that can selectively bind to target molecules with high affinity.[93] Aptamers are one of the greatest options for the particular ligands of nanoparticle functionalization due to their high specificity and affinity, small size, very low immunogenicity, relatively low production cost, and ease of storage.[94]

The use of targeting moieties to aid in uptake of nanoparticles to specific types of cancer cells has been shown to significantly reduce systemic toxicity in pre-clinical models.[95] However, binding these ligands to a nanoparticle construct adds another step in synthesis, adding cost and time to any creation process. Moreover, ligands may adversely affect the action of the nanoparticle, or may be degraded or altered and not effectively bind to the target.

1.3 Iron oxide nanoparticles and inductive heating

1.3.1 The nature of ferrimagnetic, ferromagnetic and superparamagnetic particles

For the last two decades the synthesis of super paramagnetic and ferrimagnetic iron oxide nanoparticles (ION) has been intensively developed. The research in this field spans across almost all aspects of science, partly due to fundamental scientific interest, but mainly owing to the vast array of applications that iron oxide nanoparticles possess: Magnetic resonance imaging, tissue repair, immunoassay techniques, detoxification of biological fluids, hyperthermia, drug delivery and cell separation all utilise iron oxide nanoparticles.[61,96 – 98]

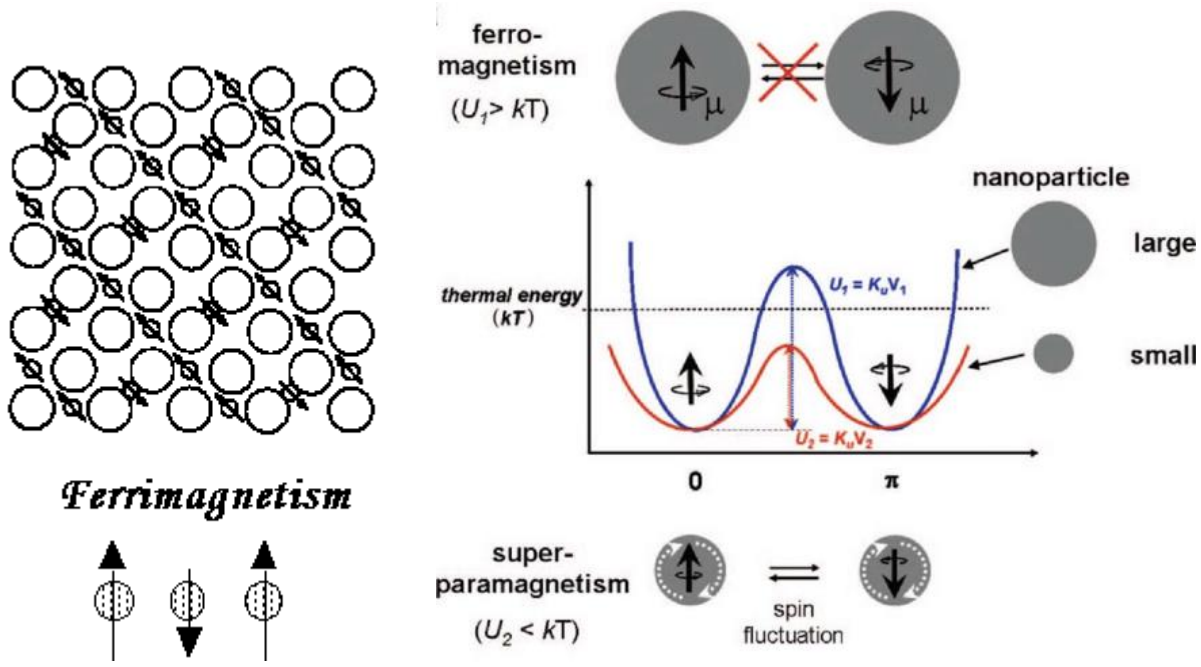


Figure 1. 6: Magnetic configuration of ferrimagnetic and superparamagnetic materials. Depiction of the electron spin system in ferrimagnetic materials, highlighting the imbalance in the number of opposing spins, resulting in an overall magnetic moment. [99] *Depiction of the energy barrier for magnetic domain flip in ferrimagnetic and superparamagnetic magnetic systems. In superparamagnetic particles the energy barrier is sufficiently small to allow a spontaneous change in magnetic domain orientation. Adapted from Yoon Kim.*[100]

Magnetic materials contain distinct magnetic regions within them called magnetic domains. Within these domains the magnetization of the material is in a uniform direction. This means that the individual magnetic moments of the atoms are aligned with one another, and they point in the same direction. The magnetic moment of an atom is dictated by the spin direction of unpaired electrons.[99] The magnetization within each domain points in a uniform direction, but the magnetization of different domains may point in different directions. Magnetic domains typically exist within the boundaries of individual crystals of a material.[101]

Ferromagnetism is a property of a material in which all electron spins are aligned within a magnetic moment. Ferrimagnetism, not to be confused with ferromagnetism, describes a material in which electron spins are aligned along one axis within a magnetic domain, but adjacent rows of electron spins are opposite to one another (Figure 1.6). The overall magnetism of a domain is a result of one spin system having a greater strength than the opposing spin system, thus generating an overall magnetic moment.[101] In nature Fe_3O_4 is found as a mineral called magnetite and exhibits magnetism due to its ferrimagnetic arrangement of electrons below its curie temperature.[102,103] A materials curie temperature is the temperature at which the magnetic orientation of atoms within the material can spontaneously flip and thus magnetic order is lost.

Magnetic domains located near each other will influence the direction of neighbouring domains, but typically the energy barrier to change a neighbouring spin is too great.[104] Thus, neighbouring domains are commonly orientated randomly and so their fields are not aligned, this results in a negligible or no overall field for a large sample of material. However, when a strong external field is applied, domains will align along the axis of the applied field. If the materiel is heated up above its curie temperature, and an externally applied field is strong enough, all magnetic moments will align in one direction and the material becomes magnetised.[15,104,105]

A key property of Fe_3O_4 nanoparticles is their superparamagnetism.[96] When a ferrimagnet or ferromagnet is suitably small, its magnetism behaves as a single magnetic spin that is subject to Brownian motion, thus giving magnetite nanoparticles greatly enhanced paramagnetisim.[106] At this size, the particles or the substance has one single magnetic domain, that is a sum of the individual magnetic domains of the atoms in the particle or substance.[15,107 – 110]

The definition of a superparamagnetic particle is defined as when the time taken to measure the magnetic moment of a particle is greater than that of the Neel relaxation time. The Neel relaxation time of a magnetic material is the time taken for a spontaneous magnetic orientation flip of a single magnetic domain (Figure 1.6).[111] Essentially, this definition explains that if a particles magnetic domain can change in the time a measurement is taken, then the overall value of magnetism recorded will be zero, despite the substance having a magnetic moment. Normally, any ferromagnetic or ferrimagnetic material undergoes a transition to a paramagnetic state above its Curie temperature. Superparamagnetism is different from this standard transition since it occurs below the Curie temperature of the material.[111] Particles in this state show no overall magnetic field, but are incredibly susceptible to an applied field, hence the term "superparamagnetic". In the case of iron oxide (Fe_3O_4), when nanoparticles are <15nm in diameter, they exhibit superparamagnetism.[112] Using magnetic fields, magnetite particles can be easily extracted from solution and reused, making them efficient particles for homogenous catalysis and in water purification.[113,114] Synthesis on a large scale is also aided by this convenient and cheap extraction method. Most notably, and of the upmost importance to this project, this superparamagnetic feature allows the efficient inductive heating effect of iron oxide nanoparticles when subject to a high frequency alternating magnetic field.[115,116]

In current medical practices magnetic resonance imaging (MRI) makes use of iron oxide nanoparticles as contrast agents.[61] In typical MRI scans, the hydrogen nuclear magnetic resonance spectrum of water is observed within the body in a 3-dimensional field, this data is then used to create a detailed image of the patient's body.[62] Due to its non-invasive nature, high spatial resolution and ease of use, MRI has become one of the most powerful and widely used clinical diagnostic techniques in modern medicine. The signal intensity of water protons within the body is proportional to the number of scans taken of the patient. More scans are possible if the if the relaxation times of protons are reduced, the two possible relaxation pathways, spin lattice (T1) and spin-spin (T2), dictate the rate of relaxation and in-turn the number of scans possible in any given period.[117] Addition of superparamagnetic agents into a sample or patient vastly reduces T1 and T2 creating hyperintense and hypointense signals, giving greater contrast in the different signals than in a standard MRI scan. The decrease in relaxation times also allows for a higher scan rate, increasing the signal to noise ratio of the scan. Addition of superparamagnetic iron oxide nanoparticles is now a common procedure in MRI scans, the enhanced signal has no doubt aided in the diagnosis of many patients and by extension has saved many lives.[61]

In order to form nanoparticles that remain stable, they must have a means of stabilisation to prevent aggregation of particles. Without stabilisation, the particles would simply coagulate and produce unwanted products such as macroparticles or would simply drop out of solution. In nanotechnology there are two primary methods for forming a stable colloidal suspension; electrostatic stabilisation or steric stabilisation.

Electrostatic stabilisation is a common method used to stabilise many types of nanoparticle solutions; it relies on the forces of electrostatic repulsion from the ‘like-charges’ on particle surfaces. The counter ion layer that forms between the two particles is vital to the stability of the solution.[118] When forming a charged

surface, counter ions are always present in solution. However, if the counter ion layer has a high concentration, the attractive forces between this layer and nearby particles will overcome the repulsive like charge forces between the particles and the particles will aggregate.[98]

The second method, steric stabilisation, is also widely used in colloidal chemistry. Typically, ligands, polymers or surfactants are grafted onto the surface of nanoparticles and act as stabilisation agents.[98] Functionalised molecules or polymers are usually synthesised from the surface, or bound during a ligand exchange reaction.[96] Stabilisation ligands are added stereotypically in situ during emulsion and desolation methods, then exchanged with functional ligands in more sensitive conditions.[119,120]

In the case of iron oxide nanoparticles, a huge number of functional ligands and polymers have been grafted onto the surface of the particles for a variety of different purposes. Most commonly used are; dextran, polyethylene glycol, starch, styrene and polyvinyl chains.[96] Iron oxide is a relatively strong Lewis acid, allowing Lewis bases to act as strongly binding ligands, for example carboxylate ions have a very high affinity for iron oxide surfaces. This method of surface attachment allows molecules such as radical polymerisation chain transfer agents to act as stabilizing ligands.

1.3.2 Induction heating of bulk materials

Induction heating is a contactless method of heating electrically conductive materials by electromagnetic induction. Heat is generated within the conductive material itself by a penetrating alternating magnetic field generating eddy currents within the material and causing joule heating.[121] Example of materials that can be inductively heated are steel, copper, brass, graphite, gold, silver, aluminium, and carbide.[121,122]An induction heater consists of a high frequency alternating current (AC) 1kHz-1MHz passing through a working coil

that generates a high frequency electromagnet. The rapidly alternating magnetic field penetrates the object, generating electric currents inside the conductor, called eddy currents (Figure 1.7 B). The eddy currents flow through the resistance of the material and heat it by joule heating. In ferromagnetic and ferrimagnetic materials heating efficiency is increased by magnetic hysteresis losses.[123]

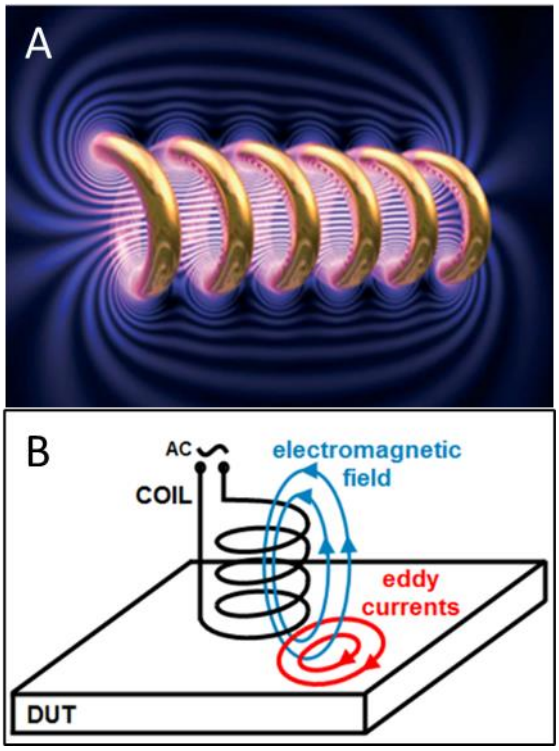


Figure 1. 7: Field effects of an electromagnet and the mechanism of joule heating. (A) Depiction of the magnetic field boundaries exhibited by a conductive coil setup in an electromagnet, demonstrating the field orientation in 3D. (B) Illustration of the induction of eddy currents in a conductive material within the field of the coil, note the direction of the induced current is perpendicular to that of the coil's magnetic field.

Typically, the inductive heating of a material takes place inside or around the coil of a high frequency electromagnet. The high frequency current through the coil generates a strong magnetic field within the coil itself, this field can penetrate almost any material with few exceptions.[122] The advantage of inducing heat in a material without any physical contact with material itself could be very applicable in biomedical applications, since it is non-invasive and therefore does not risk infection.[124] This effect has provided the grounding for a non-ionizing and harmless *in vivo* stimulus method.[125]

In ferrimagnetic materials such as iron or steel, another more considerable heating mechanism occurs; this is known as hysteresis loss heating.[126] Hysteresis loss states that this is caused by friction between magnetic domains when the material is magnetized first in one direction, and then in the other, as well as heat released as a result of relaxation. The molecules may be regarded as small magnets which turn around with each reversal of direction of the magnetic field.[127] The strong applied field on the magnetic material results in alignment of the magnetic domains of the material in the direction of the field. The friction of the rotating magnetic domains with their neighbours generates heat, and due to the rapidly alternating direction of the field, provided by the AC circuit, a large amount of energy is dissipated within the material due to hysteresis loss heating.[128] The result is a drastic increase in heating efficiencies of ferromagnetic materials compared to non-ferromagnetic materials.

1.3.3 Induction heating of iron oxide nanoparticles

At low and medium radio frequencies, iron oxide nanoparticles (ION) absorb electromagnetic energy as thermal energy while in solution. This effect is explained by the dissipation relationships of rotational relaxation of single domain magnetic particles dispersed in a liquid medium.[129] The extent of heating is dictated by a number of factors including; intensity of radiation, environment of particles, size and the morphology of particles.[107] Since the majority of tissues in the body have no absorption in the radio wave spectrum, heating particles *in vivo* has many potential biomedical applications.[15]

The specific adsorption rate (SAR) establishes how efficiently nanoparticles generate heat when exposed to an alternating magnetic field. The SAR is the most important property for the use of superparamagnetic iron oxide nanoparticles for triggering the release of cargo encapsulated in thermoresponsive drug delivery

vehicles, or when trying to reach hyperthermic temperatures. For superparamagnetic particles the SAR at a fixed frequency is dependent on the relaxation time of the nanoparticles. This increases with increasing nanoparticle diameter. Therefore, the SAR increases with increasing NP size up to a critical core diameter, when the Neel and/or Brownian relaxations of NPs cannot follow the alternating magnetic field and thus the SAR then rapidly drops off.[130] In layman's terms: above this critical diameter it takes longer for the magnetic domain to align with the field than the direction of the field itself lasts before flipping. Particles are most efficiently heated in an alternating magnetic field when the lifetime of the particles matches the lifetime of the applied field. For particles that possess superparamagnetic properties, this occurs in fields at a frequency between 300-800 kHz.

1.4 Thermoresponsive polymers and their use in medicine

Thermoresponsive polymers, also known as temperature-responsive polymers, show a sharp and abrupt change in their physical properties at a characteristic temperature.[131] The phrase is frequently used to refer to a property's solubility and structure in a particular solvent, but it can also be used to refer to other qualities that are impacted. In contrast to temperature-sensitive (also known as thermosensitive) materials, which continually change their characteristics with ambient circumstances, thermoresponsive polymers are part of the class of stimuli-responsive materials. In a more formal sense, the temperature-composition diagram of thermoresponsive polymers exhibits a miscibility change. The response of these polymers is known as a lower critical solution temperature phase change (LCST). In solution, thermoresponsive polymer chains take on the shape of an extended coil, when the temperature of phase separation is reached, they transform into compact globuli. When there are no mechanisms to lower surface tension, the globules collect, which leads to turbidity and the production of visible precipitation.[132]

Given that water is an inexpensive, secure, and biologically relevant solvent, polymer solutions that exhibit thermoresponsivity in water are particularly useful. Water-based applications such medication delivery systems, tissue engineering, and bioseparation are the focus of current research. There are many polymers that have LCST in water.[133] Polymers that have been studied the most include (N-isopropylacrylamide), Poly[2-(dimethylamino)ethyl methacrylate (pDMAEMA), Poly(vinylcaprolactame), hydroxypropylcellulose, poly-2-isopropyl-2-oxazoline, and hydroxypropylcellulose polyvinyl methyl ether. [134]

Since they are insoluble, three-dimensional covalently linked polymer networks merely swell in suitable solvents; this is useful for some applications but generally not desired in biomedical design.[135] Tissue engineering has employed thermoresponsive physical gels for tissue repair or manipulation. This entails combining cells and the thermoresponsive polymer in solution at room temperature before injecting the resulting mixture into the body.[136,137] The polymer turns into a physical gel as a result of the temperature rise (to body temperature), cells are enclosed in the actual gel itself and are thus given a framework to multiply and generate tissue. However, it can be difficult to regulate the temperature at which the polymer solution gels since it depends on a variety of parameters, such as the composition of the polymer.

Thermoresponsive polymers in aqueous solutions are the main subject of research. However, there are only a select few commercial uses, including cell culture plates covered with an LCST-polymer, medication delivery, bio separation, tissue engineering, and liquid chromatography. [134,138 – 140]

1.5 Extrinsic activation methods within oncology

By focusing treatment locally, activation or release of a substance at a tumour site can lessen the negative effects frequently associated with cancer treatment. Furthermore, localised action may enable the use of higher therapeutic doses at the site of the tumour that would not be tolerated if given systemically. However, designing intelligent systems is necessary to manage a compounds release or the activity of a molecule or nanoparticle. Such mechanisms may be influenced by distinctions between malignant and healthy cells or by activation from an external source.

1.5.1 Ultrasound stimulated systems for cancer treatment

Due to the non-invasive, non-ionizing, and minimal adverse effects, ultrasound (US) has been utilised in medicine for decades for both diagnostic and therapeutic purposes. As a result, numerous remote activation initiatives have shown interest in ultrasound.

US irradiation behaves exactly like soundwaves that humans can hear; the positive and negative pressures of the waves result in mechanical friction that has both thermal and non-thermal effects.[141] The thermal and mechanical processes can be used to improve nanoparticle delivery, These processes can be used to enhance nanoparticle delivery and work in conjunction with the enhanced permeation and retention effect (EPR). The US could also serve as a stimulant to activate nanoparticles.

Sonoporation, a phenomenon caused by US applied to cells, increases cell poration; this action is further exacerbated when microbubbles are present. Although theories about the precise mechanism differ, it is thought that the microbubbles' enhanced absorption is the result of inertial or stable cavitation.[142] A microbubble oscillates during stable cavitation under alternate US pressure, which results in fluid streaming

around the bubble. The microbubble is not damaged, but the cell membrane is sheared and fractured, leading to increased porosity. However, during inertial cavitation, the bubble collapses under the alternating pressure, causing microjets and shockwaves to be produced, which then causes pores to form. Permanent porosity will eventually result in cell death, however this type of cell death is typically uncontrollable and undesirable in distant activation of nanoparticles. These induced pores can either be transitory or permanent.[143] Microbubbles typically have a perfluorocarbon gaseous interior and a biocompatible polymer or protein exterior.

The administration of nanoparticles using microbubble attachment has been shown to increase nanoparticle uptake by between 40-670 fold in mouse adductor muscles in a model of hind-limb arterial insufficiency.[144,142] Gas filled microbubbles can be used for the delivery of nanoparticles by chemical attachment or encapsulation on or within the microbubble, followed by US irradiation.[142,145] The localised breakdown of microbubbles inside the tumour blood artery and the subsequent dissemination of the bound nanoparticles to the surrounding tumour tissue are necessary for enhanced delivery of nanoparticles.[146 – 149] Using this effect, hundreds of micrometres were added to the effective depth of nanoparticle penetration in tissue.[149,150,151,148] US assisted delivery has been utilised to distribute substances like the hydrophilic medication doxorubicin where the drug is encapsulated by liposomes using an emulsion approach.[152,153] When the shell is ruptured by US irradiation, the drug is released into the tissue. Due to the low loading capacity of doxorubicin in these bubbles, paclitaxel, an exceptionally potent microtubule stabilising drug, was encapsulated as an alternative chemotherapy agent using this technology.[152,154]

Recently, nano-cones and nano-cups have been developed that maintain cavitation times while quadrupling the circulation times of nanoparticles. An unstable nanobubble is created and maintained

inside the single cavity of the nano-cones and nano-cups. The particles are launched into the surrounding tissue after being exposed to US radiation, cavitation and subsequent sonoporation help with uptake once more. IgG mouse antibody has been delivered *in vivo* using gold particles of this kind, extending delivery distances from blood arteries to hundreds of micrometres.[150,151] When ultrasound is utilised as an activating stimulus, mRNA-lipoplex laden microbubbles have also been demonstrated to boost dendritic cell transfection from insignificant quantities to 50%.[145]

An innovative combinatorial mechanism has been developed utilising the anti-proliferative effect of sonodynamic therapy together with a pH-activated chemotherapeutic action.[155] TiO_2 particles doped with Gadolinium served as a sonosensitiser and a nanocarrier for the delivery of doxorubicin, a potent anticancer drug.[18] US irradiation at the tumour site generated the creation of reactive oxygen species (ROS), which was catalysed by the Gd doped surface of the nanoparticles, which were then metabolised and the drug payload released as a function of pH. The outcome is a two-pronged strategy that can only selectively start cell death within the diseased tissue.

Calcium carbonate nanoparticles have been used in conjunction with ultrasound for enhanced activity. pH sensitive calcium carbonate was encapsulated within a poly(D-L-lactide-co-glycolide) coating. The surface was modified with rabies virus glycoprotein which was shown to actively target the particles to neuroblastoma cells in tumour bearing mouse models. In the low pH environment of tumour tissue, the calcium carbonate dissolves to form carbon dioxide gas; this can assist US imaging. In addition to increasing imaging capability, the nanoparticles and ultrasound in combination slowed the growth of the tumours (to a much greater extent than either US or the particles alone). [156]

With lipid (DPPE-PEG) coated, perfluorocarbon packed particles created as nanoscale lipid droplets, activated imaging has also been accomplished. The droplets are vaporised into gaseous microbubbles for imaging and treatment upon US stimulation. Additionally, fluorescent dyes in the lipid layer's outer shell allow for microscopic imaging and tracking of the molecules' phase changes.[157] To specifically target the MDA-MB-231 and MCF7 breast cancer cell lines, folate receptors were added to the construct. The phase change following activation demonstrated great absorption of the contrast agents and strong imaging capabilities.

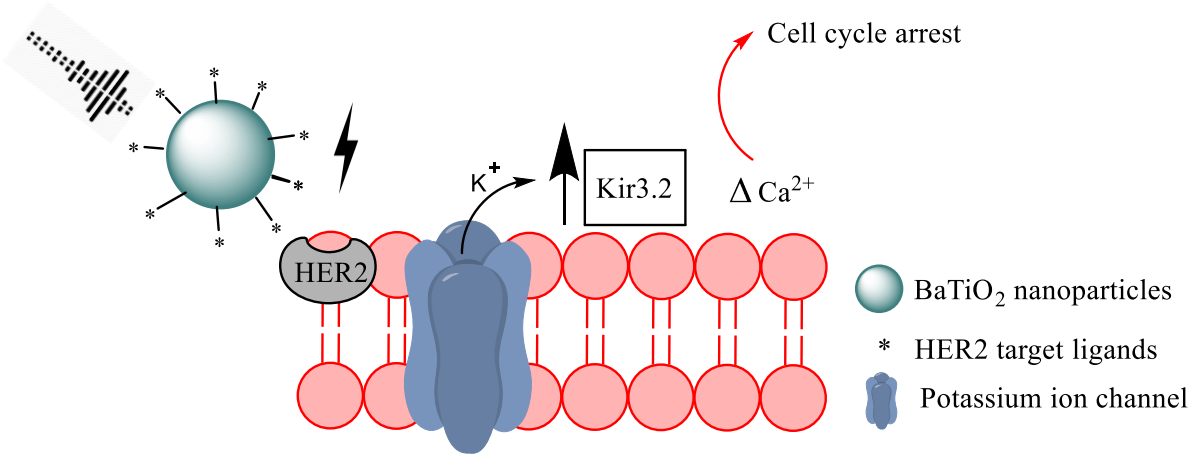


Figure 1. 8: An example of ultrasound stimulated treatment. Graphic representation of ultrasound stimulated piezoelectric stimulation of breast cancer cells. Upon ultrasound induced deformation, barium titanate nanoparticles create a potential difference that interferes with Ca^{2+} homeostasis and upregulates the Kir3.2 gene. Taken from White et al.[158]

When mechanically deformed, piezoelectric nanoparticles are known to exhibit an electric potential difference on their surface. A piezoelectric semiconducting coupling technique transforms mechanical energy into an electric potential in response to US radiation (Figure 1.8).[159] This potential difference can disrupt cell division by affecting K^+ channels.[160] Further functionalized with the anti-HER2 antibody, barium titanate piezoelectric nanoparticles have been shown to successfully stop breast cancer (SK-BR-3 cell line) cell proliferation when exposed to US stimulation for *in vitro* cells.[161]

Constructs have displayed minimal cytotoxicity in the absence of US stimulation, demonstrating the selectivity of activation. Without impacting the viability and functionality of healthy cells, these US-developed approaches effectively suppress and even destroy tumour tissue. However, there are restrictions to using ultrasound as a technique of activation. Since ultrasound has relatively weak penetration through bone and air, trying to activate molecules near organs like the lungs or ribs would result in only minimal activation of the target particles. Since the particles need to be close to the nearest blood vessel for successful treatment, tumours with low vascularity would likewise not respond well. More seriously, because of the risk of inertial cavitation leading to petechial haemorrhage, specific US frequencies could not be used to treat cerebral tumours.[149] The significant decrease in *in vivo* circulation time is another disadvantage of adhering nanoparticles to microbubbles.

Additionally, enhanced poration caused by sonoporation, especially when done near vascular tissue, results in the accumulation of therapeutic molecules in undesirable tissues and organs.[142] When providing medications that frequently result in necrosis, this would have negative side effects. This ultimately goes against the selective uptake benefit of employing US, but it's not a problem that can't be resolved with more research and precise US setup optimization.

Ultrasound technology offers a number of appealing uses both *in vitro* and, more significantly, *in vivo*. The frequencies and amplitudes required for activation are feasible with currently available medical equipment. Results from pre-clinical studies indicate that using US as an activation technique in cancer treatment has a bright future. However, without the necessary adjustments to prevent the US-caused build-up of medicines in specific organs, more focus on researching the impact of cavitation on brain tissue, and a restriction to only US-accessible tissues.

1.5.2 Ultraviolet-Visible light activation and photodynamic therapy

Photodynamic therapy uses a drug that is activated by light, called a photosensitizer or photosensitizing agent, to kill cancer cells. Since its first modern application in 1975, photodynamic treatment (PDT) has advanced quickly.[162] Unlike chemotherapy and radiotherapy, PDT has relatively minimal systemic toxicity. In order to increase the effectiveness, localization, and penetration depth of traditional PDT, nanotechnology has found a role in PDT treatment. PDT has advanced thanks in large part to upconversion nanoparticles (UCN). In photon upconversion, two or more photons are sequentially absorbed, leading to the emission of light with a shorter wavelength than the excitation wavelength. As a result, visible light frequencies can be used to excite UCNs and produce ultraviolet light. Because of its greater penetration depths and minimal tissue interaction, near infrared light can also be employed as the excitation source. Typically, the upconversion material comprises crystals of $NaYF_4$ doped with either Yb/Er or Yb/Tm; the choice of activator dopant is influenced by comparative energy levels.[163]

Numerous approaches to visible or near-infrared light assisted chemotherapy have been devised using the principles of UCN and conventional PDT. Localized release, reduced incidence light effects, and synergistic treatments have all been made possible by the use of visible light as a stimulation mechanism. An efficient, non-invasive method of treatment is provided by the illumination of photosensitizers within the patient, which produces reactive oxygen species (ROS) and leads to the elimination of the tumour.

Since the development of upconverting nanomaterials, near infrared light (NIR), specifically 700 – 1200 nm, has been employed as a stimulus for PDT.[164] Visible light can only enter bodily tissue to a depth of 1 cm, and continuous, strong exposure will result in burns and lesions.[162,165] NIR has substantially enhanced

penetration depths (up to 4 cm) while decreasing the likelihood of harming healthy tissue.[166 – 169, 170] Gold nano clusters have been created to image, help with gene transport, and enable PDT in HeLa cells in response to NIR activation. Red fluorescence imaging with TAT-peptide gold nanoclusters has been demonstrated to be possible both *in vitro* and *in vivo*. The peptide produces singlet oxygen and acts as a DNA delivery medium in addition to imaging, providing extremely high uptake (90%) and transfection (80%).[169]

Additionally, imaging has been done using poly latic acid-poly ethylene glycol -folic acid polymers that contain a boron-dipyrromethene photosensitizer that is NIR sensitive and substituted with a carbazole. When these tiny, biocompatible organic nanoparticles were combined with an ultralow power laser (670 – 800 nm), the tumour volume in mice receiving a subcutaneous 4T1 tumour xenograft was reduced by an average of 80%.[168] Photosensitizer TiO_2 particles have been engineered to react to NIR light. The addition of a $NaYF_4$:Tm upconverting shell makes it possible for NIR light activation and a PEG coating made the particles hydrophilic and biocompatible. Stimulation with NIR irradiation caused >70% of OSCC (Oral squamous cell carcinoma) cells to die.[166]

NIR can also be employed for medication release under control. Black phosphorous nanosheets and a low melting point agarose hydrogel matrix were used in a novel method that demonstrated completely regulated drug release. The black phosphorous nanosheets exhibit a very high photothermal conversion under NIR, causing the breakdown of the hydrogel and the release of the therapeutic compounds. The ability to regulate the rate of medication release (by light intensity and exposure period) and the biocompatibility of the breakdown products are critical component of this technology.[171] Gold nanorods covered in a mesoporous silica shell have been used to demonstrate the release of doxorubicin via NIR. The phase-changing molecule

1-tetradecanol was used to seal pores in the silica, and when the gold nanorods were heated by NIR, the chemical caps changed phase, allowing the pores to open and release the medication. Under strong NIR, the nanorods were also able to cause the tumours to overheat in addition to doxorubicin release. KB cells, a sub-line of the cervical cancer HeLa cell line, were used to test the nanoparticles, and the results showed resulting in a total of 50-fold decrease in IC50 value response to NIR exposure compared to the drug alone.[172] $NaGdF_4$:Yb,Tm:NaGdF is another example of an NIR responsive with a mesoporous silica shell. In this technology photocleavable platinum (IV) complexes keep doxorubicin from escaping the porous shell. The platinum(IV) complex disintegrates into a chemotherapeutic platinum(II) complex with NIR exposure, which also causes the material to upconvert to visible light photons, opening the pores and releasing doxorubicin.[167] The use of nanoparticles with a polymer core containing the chemotherapeutic drug cisplatin and an ordered asymmetrical shell made of cholesterol, PEG, and the photosensitizer pyrolipid allowed for the combination of PDT and chemotherapy. In addition to the ROS produced by the photosensitizer, the therapeutic chemical is released when the lipid layer is ruptured by 600 nm light.[173]

Hypoxia, however, can occasionally be brought on by PDT. Localised hypoxia in tissue is usually caused by reduced perfusion to that organ or limb. A locally reduced perfusion is generally caused by an increased resistance to flow through the blood vessels of the affected area.[174]

Tumour hypoxia is the situation where tumour cells have been deprived of oxygen. As a tumour grows, it rapidly outgrows its blood supply, leaving portions of the tumour with regions where the oxygen concentration is significantly lower than in healthy tissues.[175] Hypoxic microenvironements in solid tumours are a result of available oxygen being consumed within 70 to 150 μm of tumour vasculature by rapidly proliferating tumour cells thus limiting the amount of oxygen available to diffuse further into the tumour

tissue.[176] Hypoxia is a crucial factor in cancer relapse because of its effects on the regulation of the cell cycle and evasion of apoptosis. For this reason hypoxia-active nanoparticles have been intensively investigated and have demonstrated advanced effects on targeting tumour hypoxia. Hypoxia-active fluorescence nanoparticles containing azobenzene compounds have been developed to fluorescently image hypoxic environments.[177] In addition to this, hypoxic-active nanoparticles as radiosensitizers containing nitroimidazoles, and hypoxia-active nanoparticles for chemotherapy containing azobenzene or quinone have been shown to aid in the destruction of hypoxic tumour environments. [178]

A clever system that includes 2-nitroimidazole-grafted conjugated polymer (CP-NI), polyvinyl alcohol-based surface coatings, and encapsulated doxorubicin hydrochloride was developed to address this issue. When exposed to NIR, the polymer shell will produce ROS, which will kill cells or may cause hypoxia. As a result, the nanoparticle will break, releasing the doxorubicin that has been encapsulated.[179] To increase selectivity, targeting has also been heavily included into nanoparticle systems. One such example employs a -$NaGdF_4$:Yb,Tm:NaGdF core to generate ROS together with the photosensitizer PC70, and a chain-capped folic acid PEG coating. The nanoparticles were evaluated *in vivo* in female mice and *in vitro* on HeLa-luc cells; in both cases, tumours were entirely eliminated with little detectable side effects.[180]

Other metals have been utilised in light-activated systems, while rare earth elements are more frequently used because of their functions in upconversion systems. A polymer nanoparticle with a mitochondrial targeting moiety has been created using zinc phthalocyanine, which is a well-known photosensitizer. Camptothecin is liberated from modified PEG with thioketal linkers upon ROS formation. By adding triphenylphosphine cations to the particle surface, mitochondrial targeting was made possible. Using 633 nm light to treat mouse NCI-H460 (lung derived) tumours resulted in a significant remission.[181] Nano metal organic frameworks

have also seen use as a means of delivering and increasing the photosensitizer effect of Ce6. $Hf_6(u_3\text{-}O)_4(u_3\text{-}OH)_4$ frame points and 5,15-di(pmethylbenzoato)chlorin linkers show high efficiencies in treating xenografted colon cancer in mice with PDT.[182] Another technique to address the issues caused by hypoxia in conventional PDT is the use of manganese ferrite nanoparticles anchored to the surface of mesoporous silica nanoparticles. The Fenton reaction is used (H_2O_2 conversion into O_2 by an Fe catalyst)[183] and the high concentration of H_2O_2 in cancer microenvironments these nanoparticles can produce a continuous source of O_2 within tumours. By increasing ROS creation and preventing hypoxia, the Ce6 photosensitizer included in the silica nanoparticles can improve oxygen production.[184] Using iron oxide nanocubes, an inventive combined photothermal and magneto-thermal treatment has been developed. Specific loss heating powers of 5000 W/g, or a 15-fold increase in the inductive heating effect alone, were seen in aqueous suspension under an NIR light of 808nm and an AMF. *In vivo*, full tumour regression was observed in SKOV3, PC3 and A431 xenograft mouse models.[185] Although the potential to harm healthy tissue is still a significant limitation, this dual heating technique does demonstrate extraordinary ability to produce substantial levels of apoptosis in tumour tissue.

Nucleotide sequences can be added to the nanoparticulate systems to increase their functionality. For the treatment of triple-negative breast cancer, one example of a nucleotide integrating smart release system has been devised. Docetaxel as a chemotherapeutic agent, anti-twist siRNA as a gene therapy agent, and chlorin e6 (Ce6) as a photosensitizer have all been included in polymeric (DSPE - PEG) nanoparticles. The majority of cell death occurs during photodynamic therapy at low penetration depths because of the Ce6 photosensitizer. However, chemotherapy and gene therapy promoted cell death in circumstances simulating deep tissue tumours and dim lighting (Figure 1.9). The TWIST gene, which encourages the

epithelial-mesenchymal transition and metastasis, was silenced here using siRNA. Chemotherapy and gene therapy were activated with the help of light-assisted endolysosomal escape.[165]

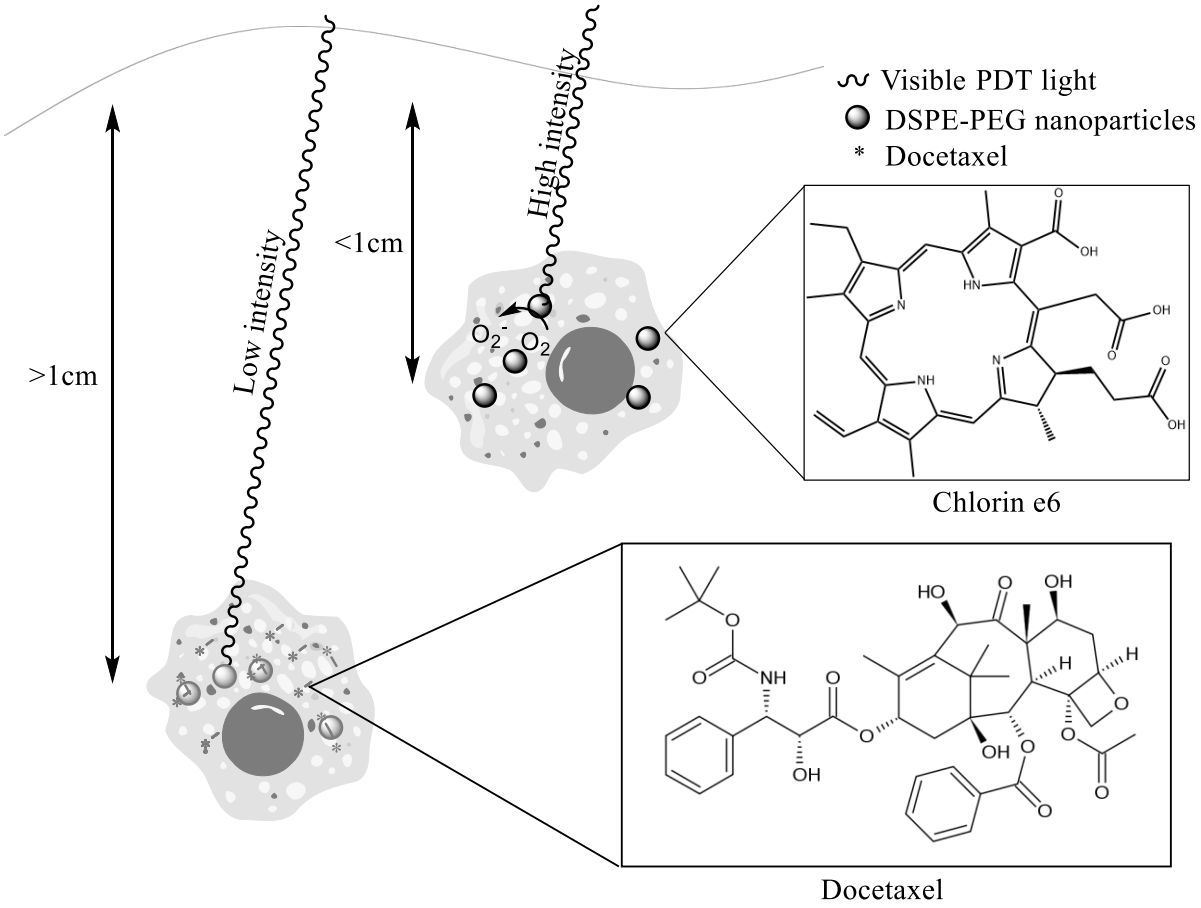


Figure 1. 9: An example of a dual functional NIR stimulated therapeutic system. Cell death mechanisms utilising different intensities of near infrared radiation (NIR) light for treating tumours at differing depths. At low penetration depths cell death is caused by reactive oxygen species (ROS) generated by Ce6 as photodynamic therapy (PDT). At high penetration depths and low light intensity cell death is caused by the release of docetaxel. Taken from White et al.[158]

Doxorubicin and HER2-targeted lapatinib can be released from gold-shelled silica nanoparticles with the use of a smart light responsive drug delivery complex. By conjugation to thiolated dsDNA, doxorubicin was attached to the surface of the core-shell nanoparticles. The thiol bonds break down as a result of NIR heating of the gold, releasing the drug. In addition, lapatinib was conjugated to immobilised Human Serum Albumin, and this albumin was released as a result of the photothermal effect.[186] This showed a way to load

multiple hydrophobic drug molecules as well as a synergistic impact between hyperthermia and active drug delivery, causing enormous cytotoxicity in breast cancer cell lines. Another method of increasing the targeting specificity of aptamers is by masking them with DNA. A complementary DNA sequence was used to hybridise to the aptamers on single walled carbon nanotubes that contained doxorubicin and were capped with sgc8 targeting aptamers. In order to target and bind to cancer-specific cells, double-stranded DNA must be dehybridized by photothermal heating of the nanotubes with NIR.[187]

The first demonstration of X-ray induced PDT in addition to visible and NIR light was in 2015. Under X-ray stimulation, it has been demonstrated that nanoparticles with a $Sr_2Al_2O_4:Eu^{2+}$ upconverting core and a mesoporous silica membrane containing the photosensitizer MC540 effectively decrease tumours. The treatment of U87-MG tumour-bearing mice reached tumour depths of several centimetres (addition tissue depth created by placement of pork flesh between x-ray source and mouse), which is beyond the scope of standard PDT. The mice also showed barely detectable damage in the body's essential organs, demonstrating the treatment's broad spectrum of therapeutic effects.[188] The therapy window for surface-dwelling tumours is no longer limited by X-rays, which may penetrate deep into tissue unlike NIR and visible light. Additionally, the X-rays utilised for stimulation are calibrated to cause nearly no off-target harm and can be produced using already-in-use medical equipment. The most widely used radiotracer in PET, fluorodeoxyglucose (FDG), has also been employed as a source of photoelectronic energy. To specifically target the GLUT1 glucose transporter protein, nano micelles containing the photosensitizer titanocene were created. Nano micelles with FDG delivery caused a significant amount of cell death in the metastatic breast cancer cell lines (PyMT-TC). However, because of the very short circulation half-life—2 hours—of micro

micelles, their clinical use might be constrained. Additionally, resistance in tiny groups of cancer cells was seen. [189]

The use of NIR activated complexes has been made possible by the expansion of UCN's application in PDT and light-activated chemotherapy. As mentioned, these particles offer a particular, controlled, and extremely effective method of killing malignant cells. NIR has produced a stimulus method that is affordable, reliable, and minimally harmful to healthy tissue. The problem of medication administration and permeability has been partially resolved with the introduction of more soluble photosensitizing compounds using UCN cores. The main disadvantage of using visible light as a stimulus, however, continues to be the depth of penetration into tissue. Despite being effective in treating tumours that are less than 1cm from the skin's surface, PDT exhibits very low cytotoxicity. New systems using X-ray energy to activate PDT may be able to address this issue.

1.5.3 Alternating magnetic field stimulated systems

Alternating magnetic fields are carried by electromagnetic radiation in the form of radio waves. Radio waves are not considered to interact with body tissues at frequencies below 3 GHz. This minimal interaction allows for stimulation of particles in any location of the body with no off-target effects. Typical wavelengths used for stimulation are 1-800 kHz.[130] It also prevents any potential reduction in stimulation of particles due to tissue absorption.

Iron oxide nanoparticles can be stimulated by radio waves by a number of different methods to produce different therapeutic effects; one being hyperthermia. When used in combination with radiotherapy, hyperthermia treatment has shown excellent results in a variety of cell lines.[190] Iron oxide nanoparticles

(ION) have a very high specific absorption rate, which has substantially boosted the effectiveness and specificity of subsequent hyperthermia research, leading to the first clinical trials in 2009.[191] The inductive heating effect of IONs is caused when an alternating magnetic field (AMF) constantly flips the magnetic orientation of superparamagnetic magnetite particles which results in heat generation. After cell internalization cell death will occur when temperatures exceed 43°C.[191,192] Magforce has developed the NanoTherm™ therapy for treating brain tumours. The technology was tried in clinical trials for glioblastoma and used in conjunction with radiotherapy. In comparison, the 59 patients who received this hyperthermia treatment had a median survival time of 13.4 months, vs patients receiving conventional care, who had a median survival time of 6.2 months. However, this method has two drawbacks: first, all metal (for example, dental work) must be removed from within 40cm from the treatment area, and second, MRI cannot ever be used again, including for the detection of tumour growth.[193,194] In addition to this, due to hyperthermia's action to the immediate tissue, NanoTherm™ treatment application is limited by its reliance on localised delivery.

Magnetite-based nanoparticle delivery systems can be used to enhance chemical localisation and uptake by tumours. Fe_3O_4 core nanoparticles with a poly(N-(1-1-butyric acid))aniline shell have demonstrated active targeting in directed magnetic fields, improved Carmustine delivery from within the polymer, and simultaneously function as a contrast agent for MRI imaging. Additionally, compared to administering the medicine alone, the nanocarrier increased the drug's half-life from 18 to 62 hours and increased mouse glioma model survival rates by 20%.[195,196] Doxorubicin-loaded cationic, biocompatible peptide dendrimers are grafted onto the surface of IONs in another combinational treatment approach. The "best of both worlds" treatment is provided by an applied AMF, which causes hyperthermia in cells and encourages the

release of the chemotherapy medication. In the HeLa (cervical cancer), PC-3 (prostate cancer), MCF-7 (breast cancer), and KB (HeLa derived cells) cell lines, these particles caused significant amounts of cell death.[197] By utilising magnetic field-enforced cellular transport mechanisms, magnetofection has been used as a potent method to increase gene transfection efficiency. This research involved development of cross-linked polyethyleneimine and magnetite nanocrystal clusters for the magnetic delivery of tiny interfering RNA into cells.[198]

With the aid of antibody-coated IONs and a modified temperature-sensitive TRPV1 channel, a proof-of-concept system for boosting insulin release has been created. Anti-histidine (His) was applied to IONs, and His bound to an extracellular His epitope tag on the altered TRPV1 channel. The IONs were inductively heated by the application of the AMF, which caused the temperature-sensitive TRPV1 channel to produce a calcium current. In turn, this stimulated the human insulin reporter genes Ca^{2+}-sensitive promoter.[97]

Without being triggered by an AMF, core shell shaped nanoparticles offer an almost "zero release" profile of medicines. As an example of a modern formulation a PVA-ION-hydrophobic drug core is surrounded by a thin film of silica, which can help control the release pattern. When the inner core disintegrates as a result of the AMF's inductive heating effect, there is a burst release.[199] A core shell system that has an iron oxide crystal shell around a silica core that contains drugs has been developed in a manner that is similar to this. Once more, substantial release is only visible after applying an external field.[200] Methylene blue for fluorescence imaging and ION were trapped inside the holes of functionalized mesoporous silica nanoparticles approximately 100 nm in diameter. The pores were then sealed using a lipid bi-layer. AMF stimulation causes the bi-layer to break, releasing the payload of the pores, followed by ION inductive

heating.[201] If the payload is optimised to carry therapeutic drugs and the bilayer surface is engineered with receptor targeting ligands, this novel design has the potential to have an even greater impact.

In an inventive nanodevice that was created to selectively release DNA and vitamin B12 in a pulsed or burst way, magnetite particles were used as a pore-blocking tool. When the direction of an external magnetic field was changed, a biodegradable polymer (poly lactic acid) multi-reservoir device that allows reversible drug release from inside the polymer material itself is triggered. The magnetite particles function as a blocking mechanism while the switch is off, preventing the release of pharmaceuticals from the reservoir. Upon application of an external field, the particles are drawn to the bottom of the wells and the medications released. The magnetic field direction can be changed, and the pores can be sealed, after the desired release concentration has been reached.[202]

In a mesoporous silica shell with zinc doped iron oxide nanocrystals, a comparable "gate keeping" releasing system has been achieved. Doxorubicin is released when the nano-valves enclosing the pores in the interstitial ION separate because of inductive heating. N-(6-N-Aminohexyl)aminomethyltriethoxysilane, which is then capped with cucurbituril, makes up the smart nano-valve used to shut the pores. When the temperature rises, the electrostatic bonds between the silica surface and the valve are broken and the drugs can be released.[203]

In truth, the conversion of nanomedicine research into clinical/ commercial use has been very poor. The total number of published articles containing the word “nano” and “tumour” up to the year 2016 is 20,251, however by 2017 there were only 13 clinically approved nanomedicines.[30,204] The poor conversion can be partially attributed to some of the assumptions of nanomedicine not being completely validated, for

example, the EPR effect (discussed in section 1.2.1). Factors like the EPR effect and increased circulation times often lead researchers to assume drug efficacy will be improved when delivered by nanoparticles, when in reality these effects could only take place in the conditions in which they were derived e.g. certain mouse models.[204] It is important not to make these assumptions when designing drug delivery systems since when they are made, clinical relevance of nanotechnology research can be reduced.

1.6 Research gap and aims of the thesis

Nanoparticles can improve drug delivery by a number of methods, passive and active. Increased efficiency in crossing cell membranes and the EPR effect are both passive advantages of nanoparticle assisted drug delivery. Active targeting in the form of aptamers, antibodies, and nanobodies can also improve the specificity and efficiency of uptake, although none of these approaches yet features in a clinically approved product. This is primarily due to incomplete consideration of the true tissue selectivity and internalisation capacity of target receptors, the impact of opsonisation and corona formation, RES capture, and adherance to the dogma of the EPR effect. Furthermore, the general unguided nature of these delivery devices results in the possibility of remaining systemic toxicity. The development of systems that minimize toxic effects until activated by a stimulus offer the potential of removing off target effects.

Near infrared – visible light and ultrasound activation systems have fundamental drawbacks. Alternating magnetic fields, transmitted by radio waves, are an alternative activation method that is highly penetrating but non-ionizing. It has a clear benefit in that it can reach parts of the body where other stimuli frequently fail. Alternating magnetic fields can also be directed at specific body parts while having little to no negative impact on the tissue around it.

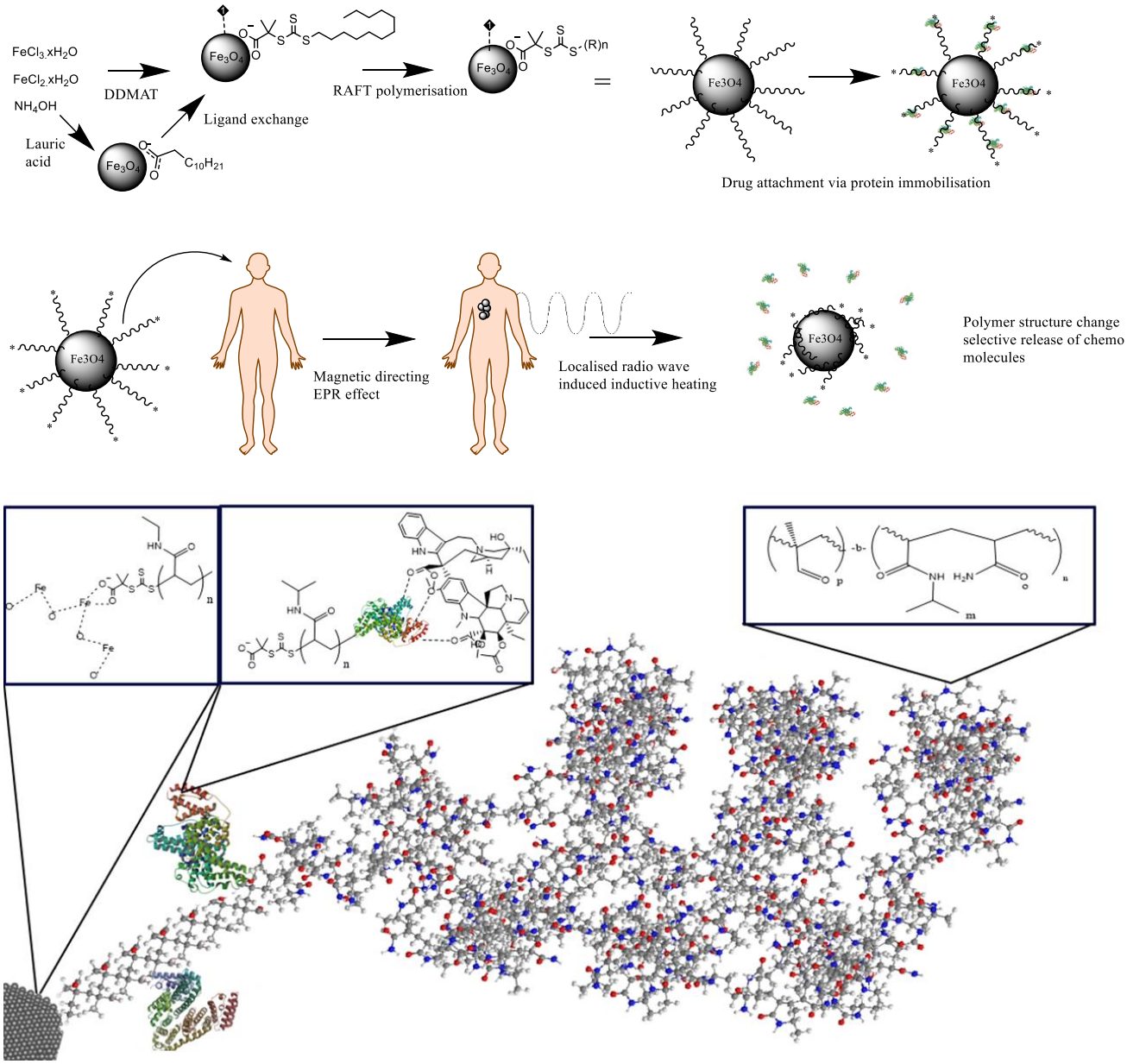


Figure 1. 10: Overall nanoparticle polymer complex design, stimulation technique and general treatment method which this project has created, graphically explained. Including the demonstration of magnetic localisation and the fine structure of the nanoparticle copolymer complex developed.

The research described in this thesis bridges this research gap by the design and creation of a novel nanoparticle-copolymer-protein complex that is capable of actively and passively targeting cancer cells over healthy tissue (Figure 1.10). The nanoparticle complex is capable of transporting a chemotherapy drug to a target site while minimising toxic effects until the stimulation to release the drug is triggered by a non-

ionising, harmless, alternating magnetic field in the form of radio waves. The specific aims of the project were as follows:

- Synthesise, characterise, and analyse superparamagnetic iron oxide nanoparticles that could be efficiently inductively heated in a medium mimicking that of the human body.
- The creation of an induction heater that could efficiently heat the synthesised particles over an extended period of time, and to high temperatures.
- Design and successfully synthesise a copolymer able to immobilise serum proteins and undergo a phase transition between 40-43 °C.
- Graft synthesised polymers to the surface of iron oxide nanoparticles and demonstrate the inductive heating induced phase change.
- Immobilise drug carrying moieties such as bovine serum albumin on grafted polymers and demonstrate the release of these carrying moieties by radio wave activation.
- Show this nanoparticle copolymer complex can release of a number of different chemotherapy agents bound to carrying proteins.
- Exhibit discriminant and selective cell death in cancer cell lines when the complex is activated by radio-waves from an alternating magnetic field.
- Demonstrate the regional localisation of the created nanoparticle system by magnetic field guidance.
- Optimise inductive heating parameters for activation of the complex in a simulated clinical environment.

Chapter 2: SPION synthesis and inductive heating.

2.1 Introduction

2.1.1 Nanoparticle properties and synthesis routes

The two main forms of iron oxide are maghemite (Fe_2O_3) and magnetite (Fe_3O_4), with the former being a fully oxidised version of the latter. The bulk material of maghemite is ferromagnetic and magnetite ferrimagnetic, giving both substances magnetic susceptibility.[96,109,205] While many of the bulk materials properties are similar, maghemite is a white material and magnetite is a black material. This can allow visual distinction between particles and polymer, a contributary reason for use in this study. Nanoparticle forms of both materials have attracted extensive interest due to their superparamagnetic properties and their potential applications in many fields.[49,61,106,205,206] Nickel, cobalt and heavy metal alloys exhibit superparamagnetic properties, but they are toxic and are oxidised under physiological conditions.[207]

Contemporary applications of iron oxide nanoparticles include but are not limited to; terabit magnetic storage devices, catalysis, electrical and biomedical sensors, high-sensitivity biomolecular MRI, magnetic particle imaging, magnetic fluid hyperthermia, separation of biomolecules, and targeted drug and gene delivery for medical diagnosis and therapeutics.[112]

A key feature of sub 15 nm magnetite particles is their superparamagnetism. This property is a result of the single crystal nature of particles containing only a single magnetic domain. This single magnetic domain allows the relaxation time of the particles to be sufficiently short to fulfil the definition of

superparamagnetism (Chapter 1). Superparamagnetism is necessary for efficient induction heating of particles in a mobile solution.[208]

Bottom-up, or self-assembly, methods of nanofabrication combine fundamental units into more complex ones using chemical or physical forces that act at the nanoscale. In a top-down method, the bulk material is broken down into nanoscale structures or particles. Top-down synthesis methods are an extension of those that have been utilised to create micro particles.

There are several widely used bottom-up synthesis routes for magnetite particles. The ideal synthesis route depends on the desired size, shape, and charge of the particles, as well as any desired surface functionalisation. Coprecipitation is the most common method of synthesis for metal oxide nanoparticles.[110] Typically for magnetite particles, a synthesis involves a 1:2 stoichiometric molar ratio of Fe^{2+} and Fe^{3+} in a ferrous hydroxide suspension, these are then partially oxidized with different oxidizing agents. The following oxidisation reaction takes place:

$$2\,Fe^{3+} + Fe^{2+} + 8\,OH^- \rightarrow Fe_3O_4 + 4\,H_2O \qquad Equation\ 2.1$$

A non-oxidizing environment, typically N_2 gas is required since magnetite is readily transformed to maghemite in the presence of oxygen.

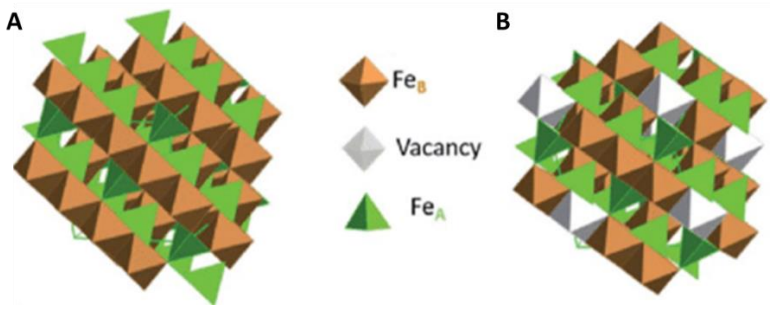


Figure 2. 1: The unit cell structures in the crystals of (A) magnetite and (B) maghemite. The diagram highlights the physical difference in the physical structure of the two magnetic forms of iron oxide.

The crystal structure of magnetite is an inverse spinel arrangement whereas, maghemite, has cationic vacancies in the octahedral positions (Figure 2.1).[109] This crystal structure difference results in a different net spontaneous magnetisation (or emu g^{-1}) of the iron particles : 92 emu g^{-1} for magnetite at 300 K, and 78 emu g^{-1} for maghemite.[130] The greater magnetic susceptibility of magnetite over maghemite is the primary reason for its use in this study. The size and shape of the nanoparticles can be controlled by adjusting pH, ionic strength, temperature, the composition of spectator salts, or the Fe^{2+}, Fe^{3+} molar ratio.[110]

A microemulsion is a stable colloidal dispersion of two immiscible substances consisting of nanosized domains of one or both liquids in the other stabilized by surfactant formed micelles. Microemulsions are generally categorised as either oil-in-water or water-in-oil. Water-in-oil is generally used more for magnetite particle synthesis. The water nanodroplets act as confined nanoparticle sized reactors for spatially controlling nanoparticle synthesis. The size of the nanoparticles will depend on the size of the water containing micelle. Thus, the size of the spherical nanoparticles can be tailored and tuned by changing the type of surfactant used.[76,110,130]

Large ball milling is a top-down approach used for the creation of many metal and metal oxide nanoparticles. Particle synthesis can be done quickly and on a large scale but produces particles with a larger

diameter deviation. It also makes stabilising particles more complicated since stabilising ligands cannot be grafted *in situ*.[209]

High-temperature decomposition of organic precursors is a more expensive synthesis method but can produce particles with good size control, narrow size distribution, good crystallinity and many different stabilisation ligands can be easily grafted. For biomedical applications like MRI, where particle size deviation plays a vital role, magnetic nanoparticles produced by this method are very useful. A combination of Xylenes and sodium dodecylbenezensulfonate as a surfactant are used to create nanoreactors where iron ions can react in controlled environments.[110,130,210]

2.1.2 Induction heating and induction heaters.

Induction heating devices consist of several main features, an inverter circuit, a tank circuit and a power driving circuit. An inverter circuit transforms DC input current to an AC current for the coil. Within the tank circuit the combination of capacitors and inductors will dictate the frequency of the current passed on to the working coil. The driver circuit will maintain a constant current and drive it through the tank circuit, within the driver circuit are metal – oxide – semiconductor field-effect transistors (MOSFETs) that manage spikes in power without damage to the circuit.

2.1.3 Induction heating of iron oxide nanoparticles

Iron oxide nanoparticles can be heated by induction heating; however, it is not through the same mechanisms as bulk materials. Nanoparticles are too small to generate heat through eddy currents and joule heating. According to the first law of thermodynamics and the principle of energy conservation, the heat

generated by iron oxide nanoparticles corresponds to the magnetic work done by the electromagnetic field to align the atomic magnetic moments with the applied field.[208] Essentially, when the magnetic field direction changes due to the change in direction of current, the particles will magnetically relax in the direction of the field, and this relaxation gives out thermal energy to the field.

2.2 Materials and Methods

2.2.1 LA-ION and DD-ION synthesis

The SPION core was synthesized using 0.56 g of Iron (II) chloride and 2.35 g of Iron(III) Chloride hexaqua dissolved in 25 mL of ddH_2O under a nitrogen atmosphere. The solution was gradually heated to 80°C, and during heating 0.1 g of lauric acid in 5 mL acetone was added. This was immediately followed with addition of 5 mL of pre-mixed 28 % (v/v) ammonium hydroxide. Once the solution had reached 80°C, 5 aliquots of 0.2 g of lauric acid in 5 mL acetone were added over 5 minutes. The solution was allowed to cool and precipitated out in 100 mL ethanol: acetone (50:50 v/v) and the product removed by magnetic decantation. Magnetic decantation involved the application of a permanent magnet to the bottom of a glass beaker to retain particles while the solvent is removed. Washing of particles was achieved by dissolution in 5 mL of THF and precipitation in 100 mL ethanol: acetone (50:50 v/v) before removal by magnetic decantation. Washing was repeated three times.

To enable ligand exchange, 50 mg of freshly synthesised lauric acid stabilised iron oxide nanoparticles were dispersed in 20 mL of 1,2-dichlorobenzene. 2-(Dodecylthiocarbonothioylthio)-2-methylpropionic acid (DDMAT; 1 g) was then added and the solution and stirred at 80 °C for 24 hours. The DDMAT stabilised nanoparticles (DD-ION) were precipitated in methanol and washed in several cycles of dispersion in Tetra

hydro furan and re-precipitation in methanol. To study the ligands present on the surface of stabilised SPIONs, ligand exchange was performed with 50 mg of Lauric acid of DDMAT stabilised SPIONs and a 40mL of a 50:50 (v/v) solution of Tetra hydro furan and glacial acetic acid.

2.2.2 Inductive Heating Equipment

Inductive Heating was carried out using a 2000 W ZVS Low Voltage induction Heating Board with a Module Tesla Coil and a Flyback Driver Heater. The working coil consisted of a copper tube wound with 10 coils and a 6-inch coil diameter. The coil was water cooled to prevent external heat input to the sample. The coil had a sufficient diameter to allow cell culture plates to fit inside the coil. The frequency of the circuit was assessed using a multimeter applied to either end of the working coil during operation. A variable laboratory power supply system was used to supply the circuit board with current and voltage. To assess heating times in cell culture and in standard solutions, preliminary tests were run in non-sterile conditions with particles dispersed in PBS. The voltage was varied by the power supply and the temperature of the solution was measured every minute using a non-mercury or non-conductive thermometer. For the activation of nanoparticles in cell culture, the plate was placed inside the inductor coil and insulated. Once the desired temperature had been reached, the plate was removed and returned to the cell culture incubator. Input voltages and heating times were dependent on the concentration of particles used as measured in non-sterile conditions.

2.2.3 Characterisation techniques

Gas chromatography:

Detection of DDMAT by gas chromatography was performed using a Shimadzu GC 2010. The samples were separated with a ZB-FFAP column (Zebron, Phenomenex, Macclesfield, Cheshire United Kingdom) and coupled to an FID detector. An optimized protocol to give a clear unmasked signal for DDMAT was as follows; temperature maintained at 100°C for 5 min, followed by ramping to 240°C at a rate of 50°C per minute, and finally held at 240°C for 5 minutes. This temperature was then maintained for 4 min to ensure complete flushing of the column. Total run time was 28 minutes and 30 s. Samples were dissolved in HPLC grade ethanol before analysis.

Zetapotential Measurements:

The zeta potential of the nanoparticles was measured using a Malvern instruments, Zetasizer Nano. Samples were run in a Disposable Folding Capillary Cuvette (DTS1070, LS Instruments AG, Fribourg, Switzerland). To determine the electrokinetic potential, or ζ potential (which represents the surface charge of a colloidal suspension), particles were suspended in PBS buffer at a concentration of 0.1 mg / mL (pH 7.4) prior to the measurement. 30 runs were read before the calculation of electrophoretic mobility, zeta potential and zeta potential distribution.

TEM imaging

TEM images were taken using a JEOL JEM-2100 Plus microscope. Samples (5 mg) were dissolved in ethanol or tetrahydrofuran depending on solubility, before dispersion on holey carbon grids (Sigma-Aldrich Merck Life Science UK Limited, Gillingham, UK). The samples were then imaged under a 200 Kv beam.

FT-IR

PerkinElmer Frontier FT-IR (Seer Green, Beaconsfield, UK) was used for the determination of surface functional groups in samples, with a scan range from 600-4000 cm^{-1}. Samples were scanned in powder form with 64 repeat measurements made per scan upon a KBr crystal disc. The obtained data was presented as transmittance spectrums and significant peaks shifts were detected.

2.3 Results

Fe_3O_4 superparamagnetic particles were synthesised and subsequently analysed by several methods. The black colour of the product indicated the identity of Fe_3O_4 particles, in contrast to white Fe_2O_3 particles. A yield of 77-86 % was typically obtained from the synthesis method after three cycles of washing in a 50:50 (v/v) mixture of acetone and ethanol and subsequent magnetic decantation.

2.3.1 Lauric acid stabilised iron oxide nanoparticles:

Fe_3O_4 superparamagnetic particles sterically stabilised with lauric acid ligands (LA-ION) were synthesised and used as a base to produce the nanoparticle complex. Lauric acid was used as a stabilising agent, due to its ready availability, ease of handling and existing literature methods.[49] To confirm the identity, size, shape and morphology of particles; TEM, FT-IR, Zeta potential and centrifugal sedimentation were used. The nanoparticle morphology is an important parameter in determining the utility of synthesised nanoparticles in drug delivery applications. They were all found to be broadly spherical in shape with an aspect ratio nearly 1:1 (Figure 2.2).

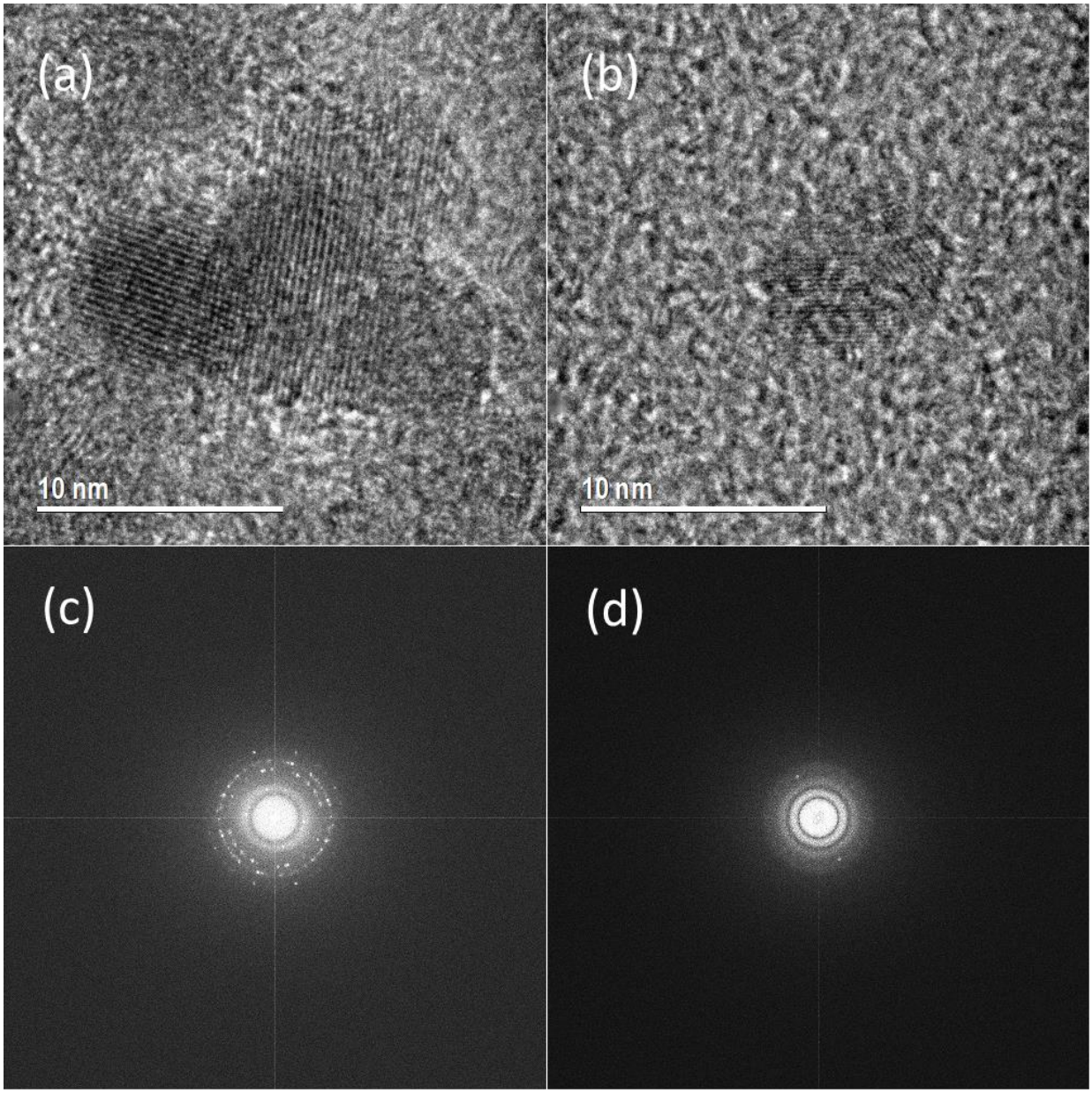


Figure 2. 2: Typical TEM images of LA-ION synthesised particles. (A) LA-ION cluster showing single crystal particles (scale bar: 10 nm); B) a single LA-ION nanoparticle exhibiting dual crystal morphism (scale bar:10nm); C) The Fourier transform from the LA-ION cluster image in (A), each pairing of dots representing distinct crystal lattice structures from individual particles; D) The Fourier transform from the single particle in (B), again each pairing of dots representing the distinct dual crystal lattice structure from the particle.

TEM imaging allowed accurate size determination of the particles to be conducted; 30 particles were measured (using Gatan 3 imaging software) for average diameter and the standard deviation calculated. From TEM images the average size was determined to be 7.74 nm (SD, +/-0.62nm) (Figure 2.3 A). The

atomic spacing can be visualised by the repeating "rows" in each crystal, representing the space between the iron atoms in the structure, occupying the holes in the fcc oxygen crystal lattice. The spacing was calculated at 2.7 Å, which is within the range expected for a magnetite crystal.[113]

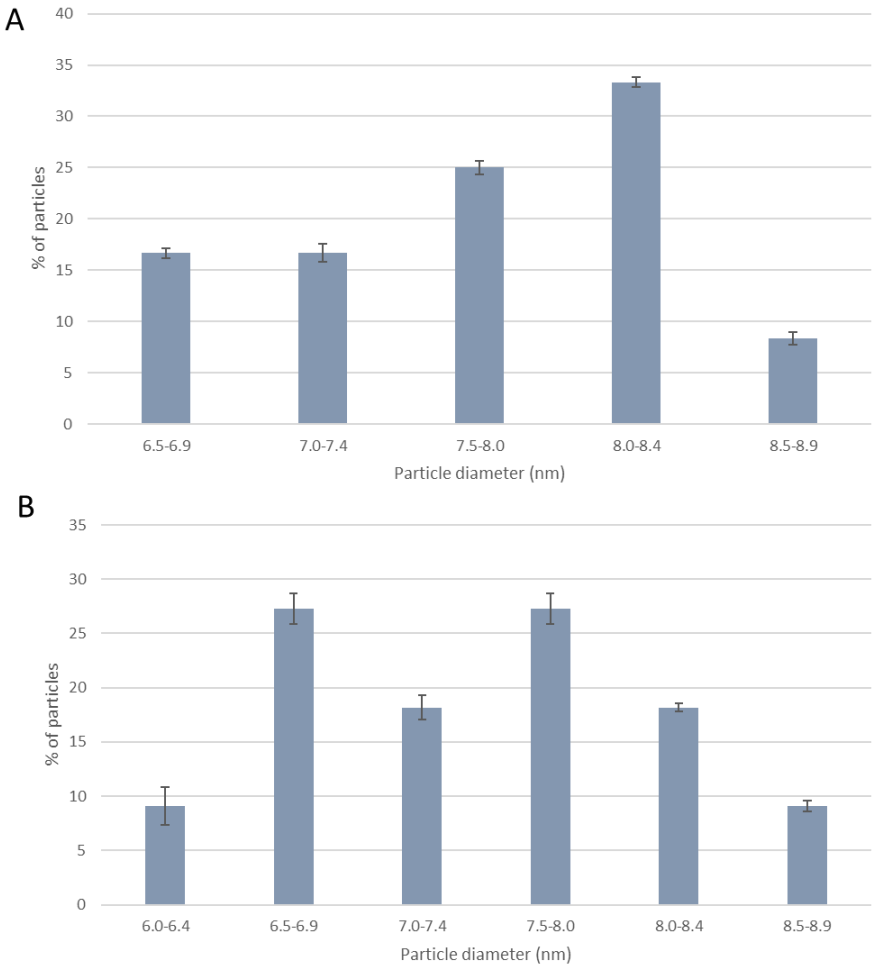
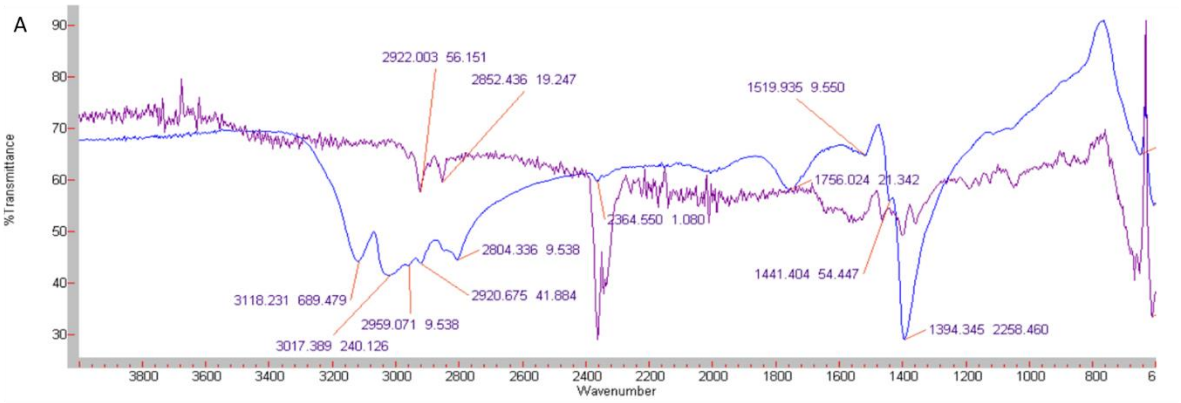


Figure 2. 3: Measured particle diameters of LA-ION (A) and DD-ION (B) from 30 randomly selected particles visualised ion TEM images repeat measurements were made. Three diameter measurements were made of each particle and an average diameter for each particle calculated. The error bars represent the standard deviation in category, n=3.

The synthesised particles were soluble in organic but not aqueous solvents, indicating an organic particle coating. For further confirmation of a successful synthesis and to verify the stability of the particles, the presence of Lauric acid as a stabilisation ligand was examined with FT-IR spectroscopy.

A



B

Wavenumber (cm^{-1})	Functional group
3118 (Broad)	O-H (Acid)
2364	C-H
1756	C=O (Acid)
1394	C-O

C

Wavenumber (cm^{-1})	Functional group
2975-2850	C-H
1637, 1535	C=O (Acid)
3300 Very broad	O-H (Acid)
1370-1350	C-H

Figure 2. 4: FT-IR spectrum of LA-ION (Blue) and DD-ION (purple) (A). The x axis represents absorbance wavenumber and the y axis represents transmittance of the signal. The FT-IR assignments of LA-ION (B) and DD-ION (C).

The peaks observed in this FT-IR (Figure 2.4) are solely a result of the stabilising ligands, in this case lauric acid, since the inorganic vibrational wavelengths of Fe_3O_4 are outside typical spectrometer wavelength range. The FT-IR spectrum was taken and the following peaks observed; The C-O stretch was present at 1081cm^{-1}, the C-H was present at 1394 cm^{-1}, further C-H stretches were observed at 2847 and 2917cm^{-1}. The O-H broad peak was observed at 2700-3500 cm^{-1}.

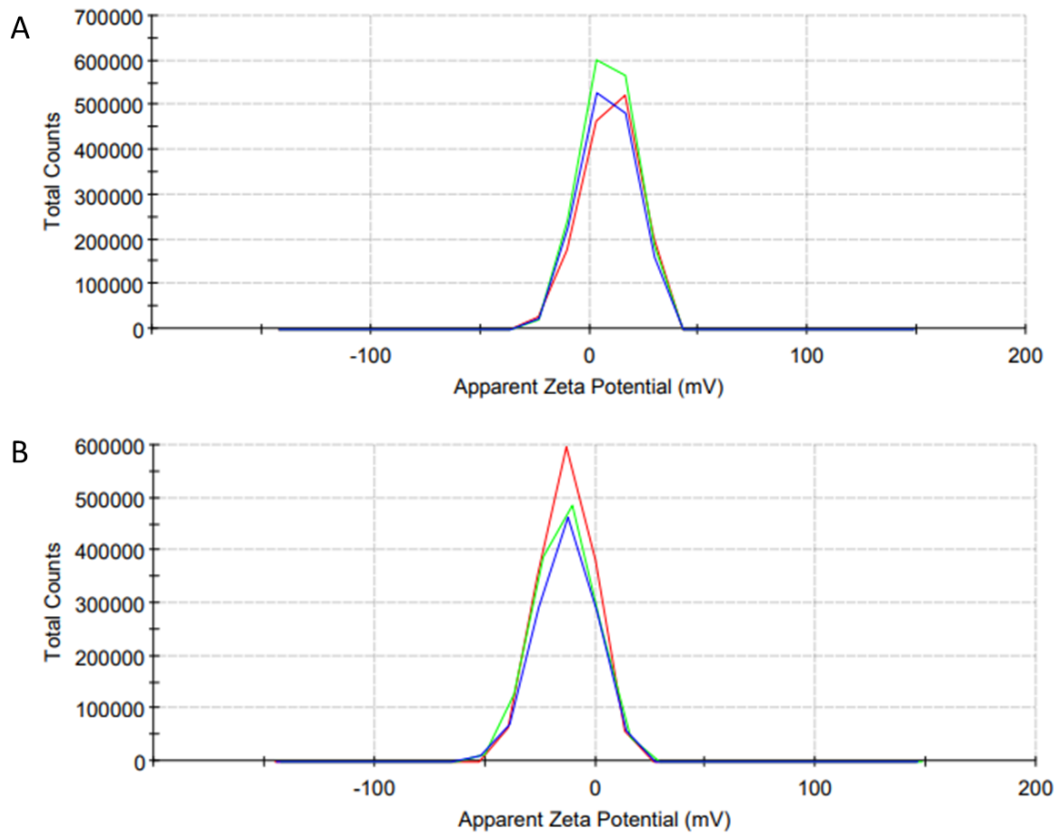


Figure 2. 5: Zeta potential of stabilised SPIONs. Triplicate zeta potential spectrum of lauric acid stabilised SPIONs (A) and DDMAT stabilised SPIONs (B).

Zeta potential measurements confirmed the neutrality of the surface of the particles (+8.79 SD=+/-0.58, figure 2.5 A), indicating a good coverage of ligands and stability. This value is expected since particles are stabilised sterically, by the long neutral tail of lauric acid molecules.

2.3.2 DDMAT stabilised iron oxide nanoparticles

Fe_3O_4 superparamagnetic particles synthesised with Lauric acid were used as the starting particle in a ligand exchange synthesis to produce DDMAT stabilised particles (DD-ION). Particles were washed in a similar fashion to that of the LA-ION synthesis procedure and analysed by the same methods. This type of synthesis method was denoted EXC-SYNT.

Yields from this synthesis were 94% when based on the recovery of nanoparticle mass, however, the excess of DDMAT used was becoming a problem due to the costs of the chemical. In order to make more efficient use of DDMAT a new synthesis method was devised. This method eliminated the need of an exchange step by using DDMAT as the stabilising ligand in the synthesis of the particles, thus reducing reaction steps and increasing uptake efficiency (denoted OUT-SYNT, table 2.1). To measure the efficiency of uptake in this new synthesis method in comparison to the literature method, the total grafted DDMAT from 100 mg particles was removed by a further ligand exchange and tested for quantitative measure by gas chromatography (GC) analysis.

Estimation of loading of DDMAT

After a ligand exchange reaction and subsequent purification of the cleaved groups from the surface, the concentration was determined against known samples from spectra run by gas chromatography (GC). A calibration curve was used to gain an accurate relationship between peak area and DDMAT concentration and samples were run against an internal standard to ensure validity.

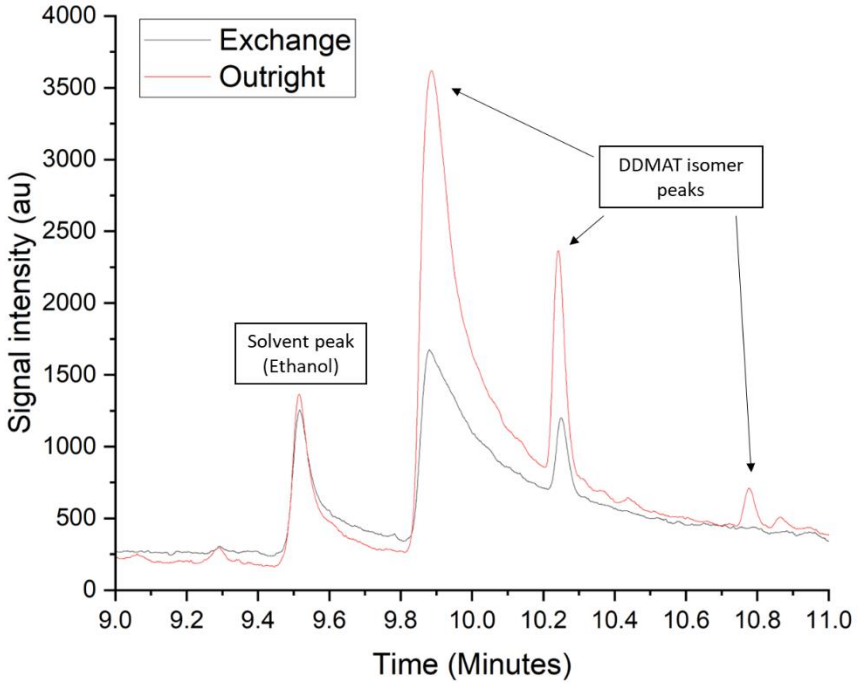


Figure 2. 6: Gas chromatography spectrum of DDMAT obtained from the surface of DD-ION particles. The DDMAT peaks observed from ligand exchange samples from DD-ION outright synthesis method (red) and the exchange method (black).The three DDMAT peaks are a result of the flame ionisation detector used in the GC, the solvent peak at 9.52 is ethanol. The content of DDMAT in each sample was detected by the integration area of the peaks at 9.91,10.25, and 10.78 minutes.

DDMAT content was measured as a concentration and converted into total mass obtained from 1 mg DD-ION particles (Figure 2.6). The total weight was compared to the total weight of the nanoparticles and presented as a percentage weight of the entire complex.

Table 2. 1: Estimation of loading of DDMAT on DD-ION by the different investigated synthesis methods

SYNTHESIS METHOD	MG DDMAT/MG PARTICLE	% WEIGHT OF DDMAT IN PARTICLE
EXCHANGE SYNTH	0.0577	5.77
OUTRIGHT SYNTH	0.143	14

By weight the new synthesis method loaded DDMAT onto the SPION cores at over double the efficiency of the initial ligand exchange method (Table 2.1). Resulting in a higher loading efficiency and a reduced overall synthesis route.

Physiochemical characteristics of DD-ION

TEM imaging was used once more to study size and morphology of particles (Figure 2.7), the size determination of DD-ION was calculated again with 30 particles from TEM images, and the average size was determined to be 7.32 nm (SD, +/-0.72 nm) (Figure 2.3 B).

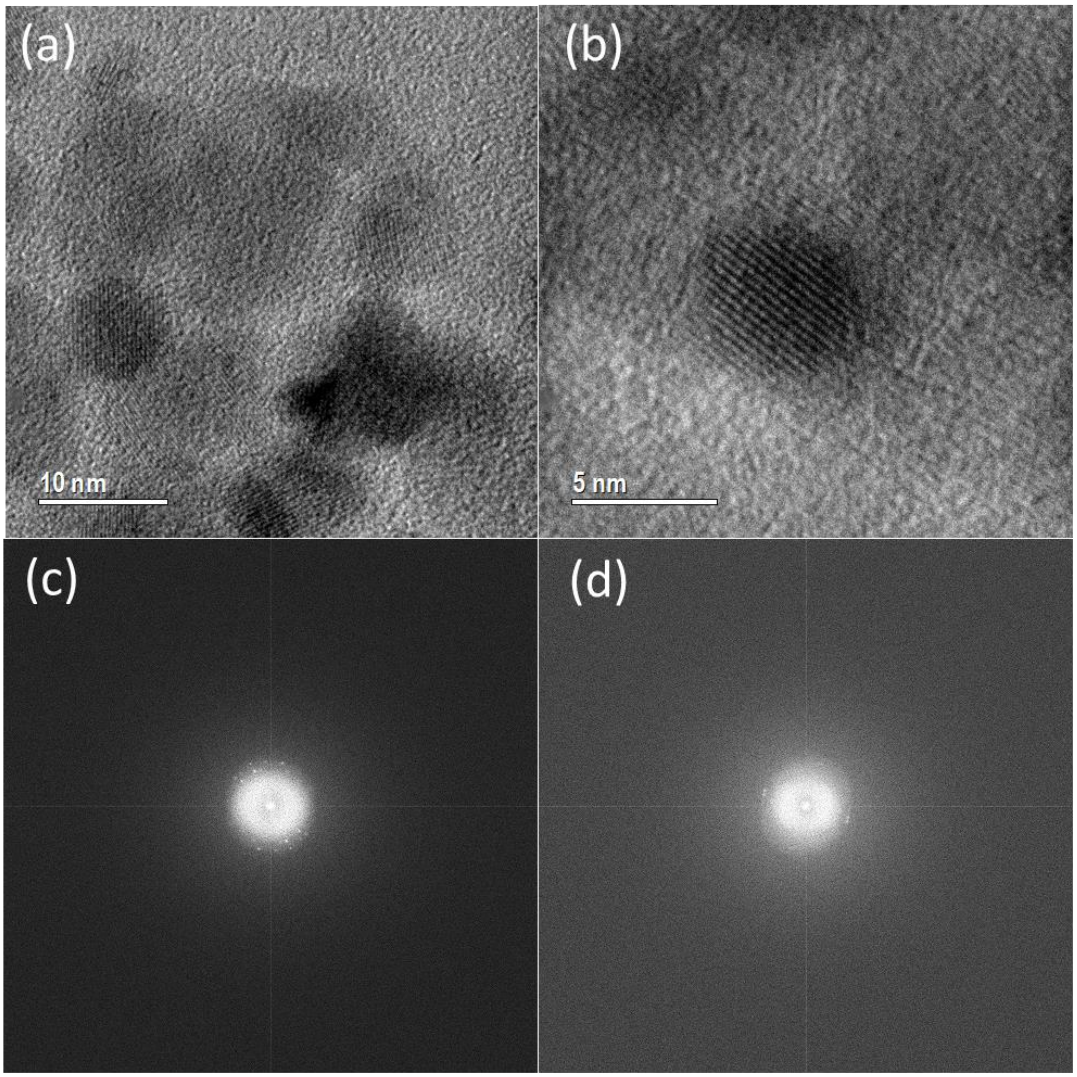


Figure 2.7: Typical TEM images of DD-ION synthesised particles: (A) DD-ION cluster showing single crystal particles (scale bar: 10 nm); (B) a single DD-ION nanoparticle exhibiting single crystal morphism (scale bar: 5 nm); (C) The Fourier transform from the DD-ION cluster image in (A) each pairing of dots representing distinct crystal lattice structures from individual particles; (D) The Fourier transform from the single particle in (B) once again, the pairing of dots representing the distinct the single crystal lattice structure from the particle.

The atomic spacing was identical to that of LA-ION and can be visualised by the repeating "rows" in each crystal particle (Figure 2.7 A and B). The morphology of the particles remained spherical in all dimensions again, with very good homogeneity. Particles were again single crystal.

The FT-IR spectrum was taken and the following peaks observed (Figure 2.4 purple); The C-O stretch was present at 1081 cm^{-1} with a reduced intensity compared to LA-ION, the C-H was present at 1354 cm^{-1} and

again greatly reduced intensity in comparison to LA-ION, further C-H stretches were observed at 2847 and 2917 cm^{-1}. The O-H broad peak was notably smaller and less pronounced. Generally, the C-H footprint was completely different to that of LA-ION. Although the sulphur bonds in DDMAT were not observable, the continued stability of the nanoparticles, combined with the clear differences in the FT-IR spectra of DD-ION and LA-ION, indicated the presence of DDMAT stabilised particles.

Zeta potential measurements confirmed a slight negative surface charge of the particles (-13.26 SD=+/-0.38, Figure 2.5 B), indicating full coverage of ligands and particle stability. The particles were sterically stabilised by DDMAT, which owing to the sulphur junction present gave a slight negative zeta ζ to the particles.[211]

2.3.3 Magnetisation values of Particles

The magnetic properties of the DDMAT stabilised SPIONs were investigated using thermal gravimetric analysis. The magnetic field dependence of the magnetization of DD-ION is shown in (Figure 2.8). As can be seen there is no retention of magnetisation in one direction when the field is reversed, therefore the superparamagnetic property is observed.[212] The magnetic measurement of DD-ION by variable magnetisation indicates superparamagnetic behaviour at room temperature and minimum temperature, (300 K and 100 K respectively) with no hysteresis and perfect Langevin behaviour.[213]

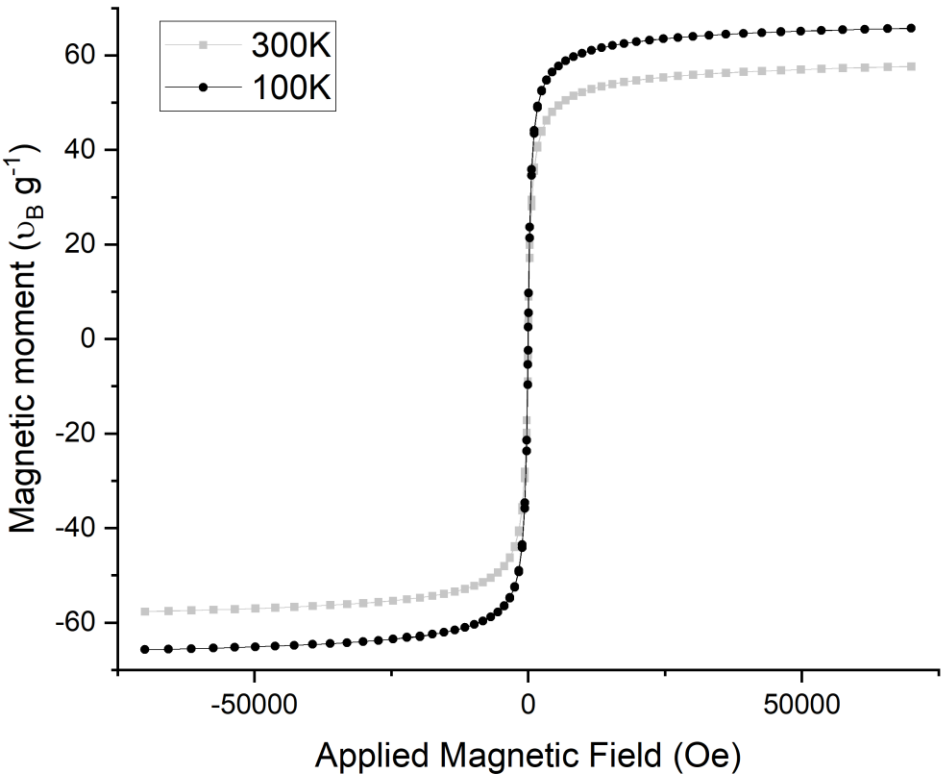


Figure 2. 8: Magnetic susceptibility data of DDMAT stabilised iron oxide nanoparticles as measured by Gouy balance. The y axis represents the magnetic moment of the particles in relation to the applied magnetic field represented on the x axis. Magnetization data was measured at 100 and 300K.

The magnetisation saturation values for the particles at 100 and 300 K were observed at 65.7 and 57.6 emu g^{-1} respectively. At 300 K the magnetization reaches 90 % of its maximum value at 100 Oe (8 kAm^{-1}), underlining the suitability of these samples for the envisaged applications.

2.3.4 Induction heating design and assembly

The induction heater designed to carry the AMF via radio waves to serve as the activation method needed to be able to continuously and effectively be able to heat particles in solution. Thus, with these objectives in mind the induction heater was designed as in Figure 2.9.

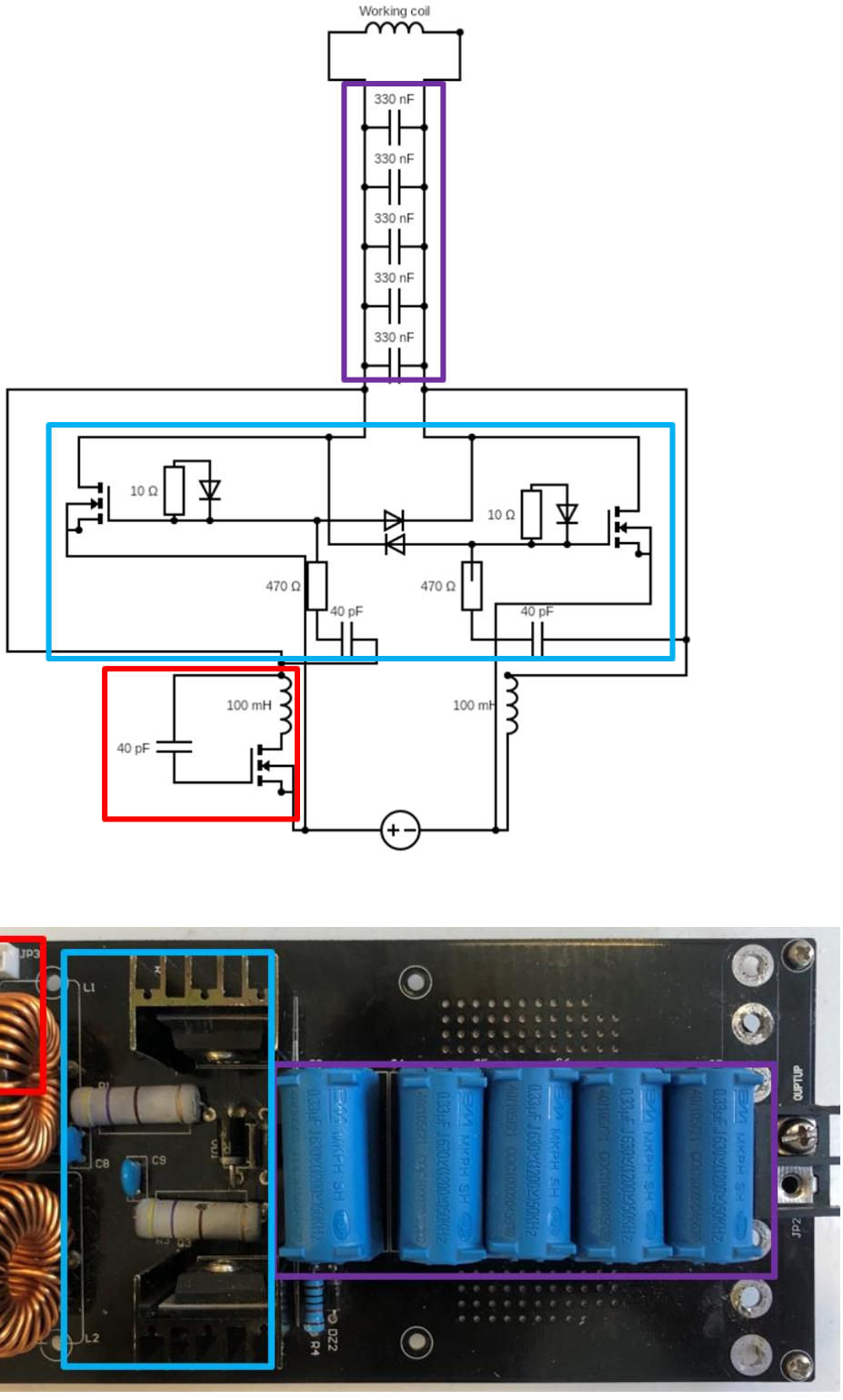


Figure 2. 9: Induction heater circuit design. Distinct feature includes the inverter circuit (red), the driver circuit (blue) and the tank circuit (purple). These features are highlighted in both the circuit diagram and the physical image of the device printed cicuit board (PCB).

The device initially used consisted of an inverter circuit, driver circuit and the tank circuit (Figure 2.9) with the working coil placed on the end of the printed circuit board (PCB), specifically soldered to the output terminals. The working coil was a hollow copper tube with a 4-inch diameter, not large enough for culture plates. The design did not allow for cooling of the working coil, which heated upon function due to joule heating in the coil itself. The initial induction heating device proved excellent at heating bulk materials, however, the rates of heating for nanoparticles was poor. In an attempt to increase heating efficiency for particles when placed in the working coil the frequency needed to increase. In the initial design, the frequency produced by the circuit was measured at 83 kHz. This is dictated by the resonant frequency in the tank circuit f_o.

$$f_o = \frac{1}{2\pi\sqrt{(LC)}} \qquad [Equation\ 2.2]$$

The frequency of the tank circuit is inversely related to the root of product of the capacitance (c) and inductance (L) in the circuit, reducing the value of capacitance therefore increases the frequency of the circuit. The capacitance of the circuit was reduced, which increased frequency. However, too much capacitance was removed with caused a catastrophic failure in the driver circuit and the device ceased to function. A new PCB was ordered of a different design, to ensure more efficient heating and allow for other desired features.

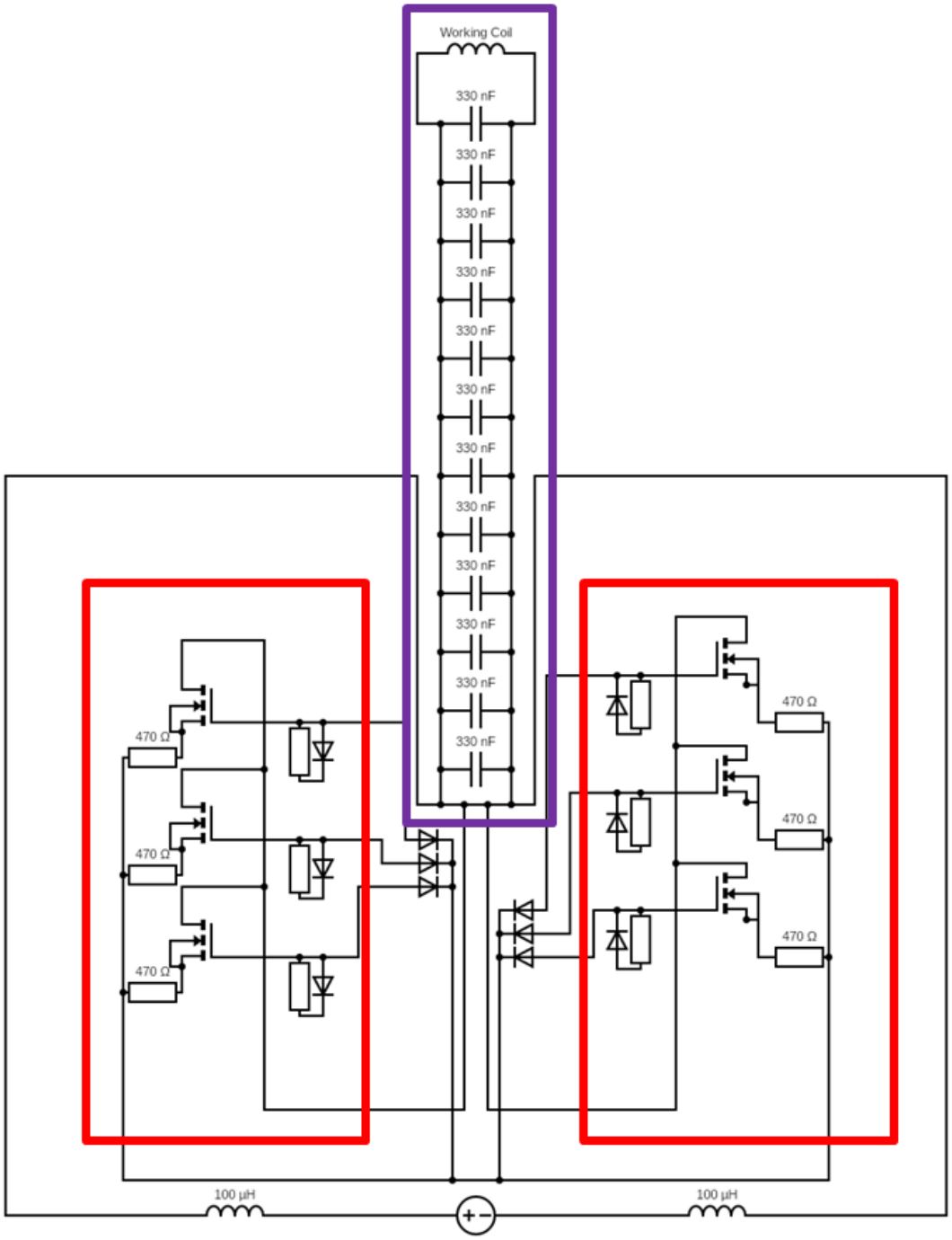


Figure 2. 10: Final induction heater circuit design. Distinct feature include the combined inverter and driver circuit (red) and the tank circuit (purple). Diagram not to scale.

The main circuit board design ensured incorporation of the vital circuit components while also minimizing device size. The inverter component and driver component were combined into the same circuit to reduce the size of the printed circuit board (Figure 2.10, red). While this reduced the device size it also resulted in

a high heat build-up in the metal – oxide – semiconductor field-effect transistor (MOSFET) transistors (Figure 2.10, red), requiring an efficient heat dissipation system. This was a sequence of six heat sinks which were positioned facing out of the circuit and were in turn cooled by external fans, fixed above the circuit board (Figure 2.11 c). The Tank circuit used to generate the resonant frequency for the coil is shown in figure 2.11 A and D. A variable voltage power input was used as a method of controlling the strength of the field produced in the working coil, thus giving control over heat generation rates in samples, but as a DC input, not AC. The DC current was converted into an AC signal by the combined driver-inverter circuit (Figure 2.10 red). This integrated driver/inverter also allowed for a greater power input from the external power source, allowing for a stronger field strength produced by the working coil.

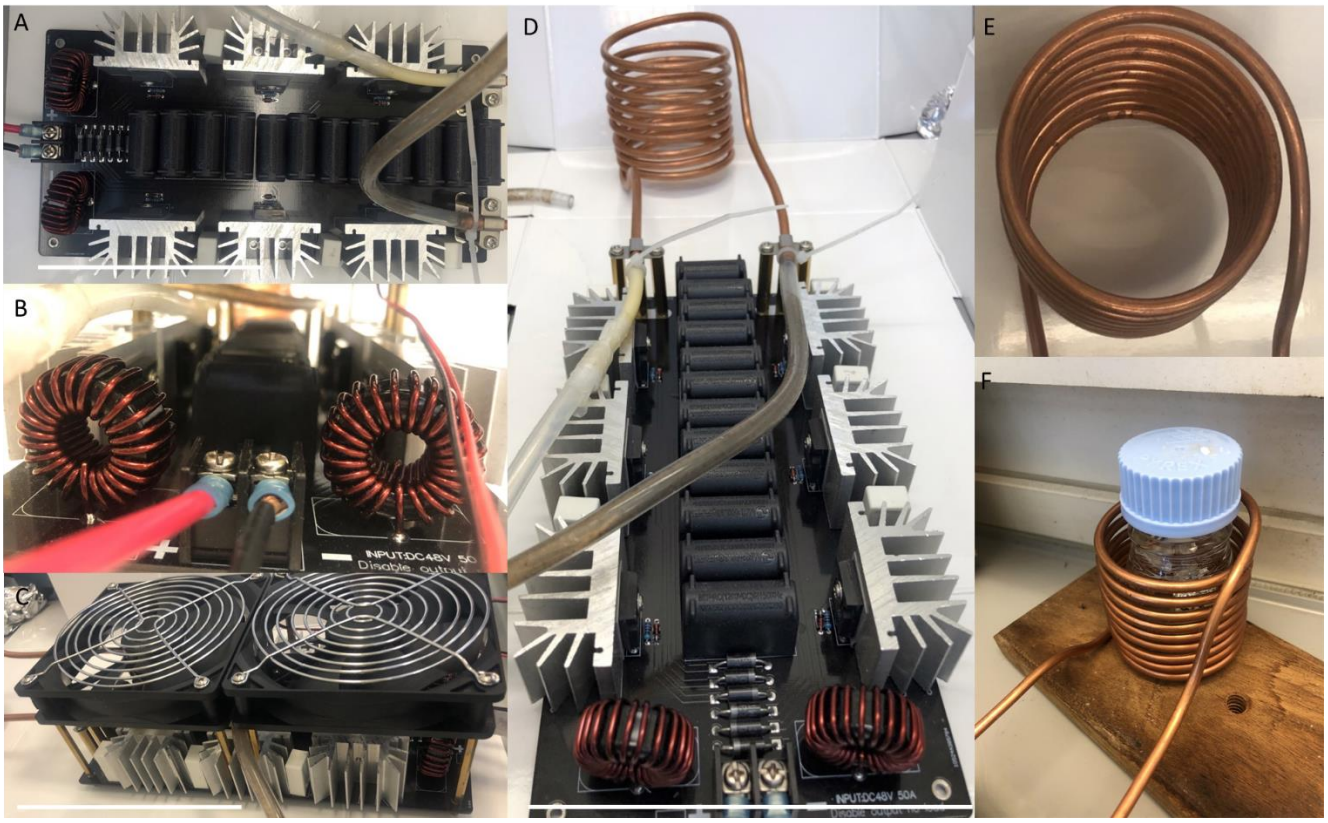


Figure 2. 11: Images of the constructed induction heating device. Top-down view of the main circuit showing the row of capacitors, diodes, MOSFETs and the outwards facing heat sinks (A), front on view of the main circuit board highlighting the capacitors and the power input terminal (B) and the position of the external cooling fans fixed to the main board when in operation (C). (D) the longways view of the induction device showing the main

circuit board and the water-cooling input/output tubes connecting with the working coil. (E) the top-down view of the working coil. (F) A sample within a sealed beaker within the working coil to prevent contamination. The scale bar is 10 cm.

The working coil (Figure 2.11 E and F) could be easily removed and replaced with a coil of differing diameter depending on the medium and holder of the sample. For cell culture plates the coil diameter needed to be at least 4 inches. The change in coil diameter slightly changes the strength of the field felt by samples, thus heating times were slightly adjusted. To ensure there was no external heat input to the sample from the working coil a water-cooling system was created (Figures 2.11 D). Water from a tap flowed through a closed system into the coil itself, throughout its length and then disposed of. The cooling system maintained constant temperature of the working coil between 19-21 ˚C throughout operation.

An alternative tank circuit was designed and integrated into the device to provide an alternative function with a higher frequency of operation, specifically to heat nanoparticles (Figures 2.10). The frequency of the circuit and therefore the induced field was confirmed with the use of external multimeters and measured at 83 kHz for the original tank circuit and 148 kHz with the alternative circuit.

Sample temperature measurement within the coil is made difficult due to the induction effect however. This lead to the use of a standard visual thermometer for measurements *in situ*, or the use of thermocouples intermittently when the coil is switched off.

Induction heating of bulk metals

To confirm successful creation of the induction heating device initial experiments were run on bulk materials as a positive qualitative control. A steel Eppendorf holder was placed inside the working coil and

a Eppendorf containing 1 mL of PBS was placed within the holder. The temperature of the PBS was raised to 65 ˚C using differing initial input voltage and maintained at that temperature for 30 minutes (Figure 2.16).

2.3.5 Initial particle heating tests

Nanoparticles were initially heated in high concentration solutions (200 mg/mL in ethanol), mimicking that of a ferro fluid. Naturally, the mass of iron oxide in these solutions was lower than that of bulk metals and therefore heating is not as rapid. However, nanoparticle solutions showed more reliable temperature control than bulk materials, demonstrated by the reduced temperature overshoot to 65 ˚C for a 200 mg solution (Figures 2.12 A and B).

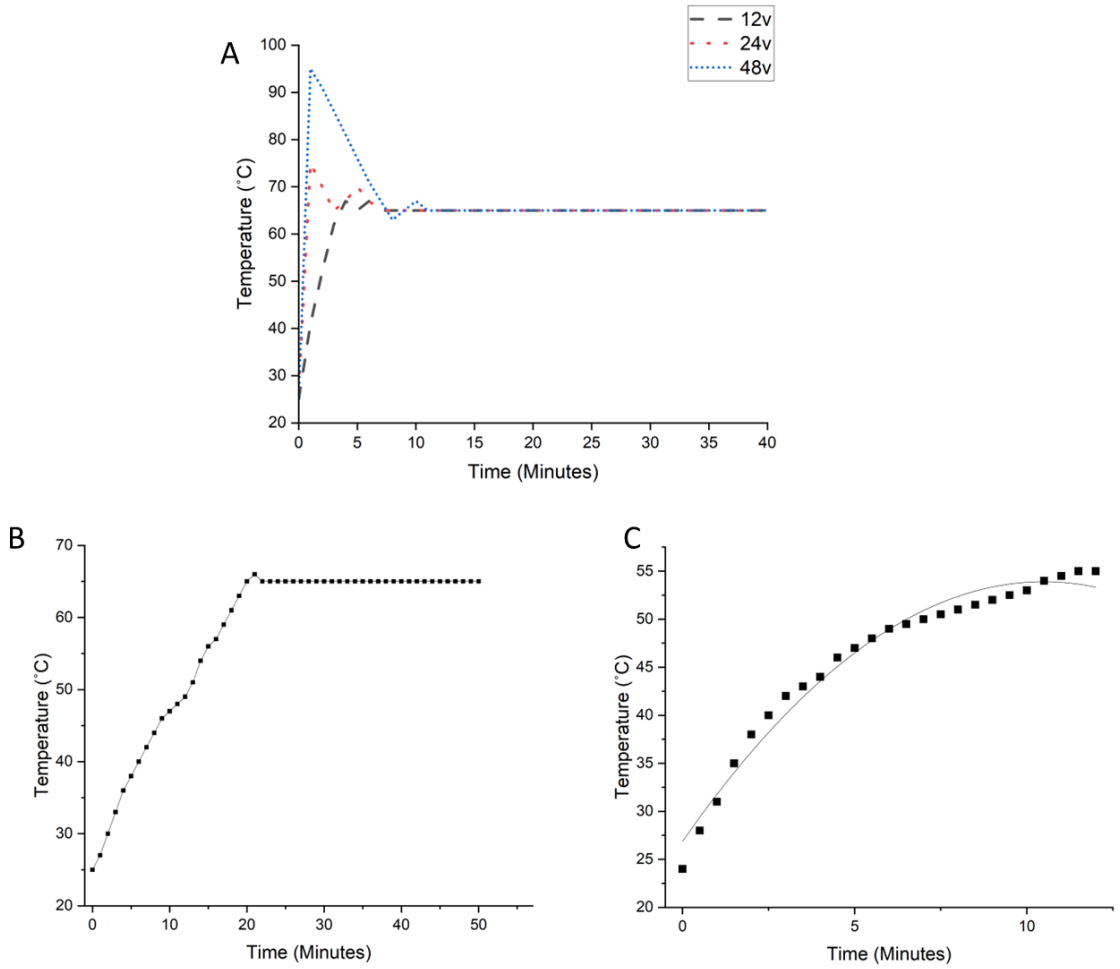


Figure 2. 12: Heating capabilities of the induction heating device. (A) Heating of 1 mL sample of PBS within a steel Eppendorf holder. The sample was heated at various input voltages through induction heating. The sample was brought up to 65 °C and then held at the temperature for 30 minutes. (B) Induction heating of a 200 mg/mL solution of LA-ION in Ethanol, the input voltage to the heater was set at 48 volts. After a temperature of 65 °C was reached the voltage was dropped and the temperature maintained. (C) Induction heating of a 100 mg/ml solution of LA-ION in Ethanol, the input voltage to the heater was set at 48 volts. The curve present is a polynomial line of best fit. $R^2 = 0.9011$.

Particle heating tests were run on LA-ION since it was not cost efficient to synthesise DD-ION when they were not used in polymer synthesis. Initial particle heating experiments involved heating of 200 mg/mL solution of LA-ION in 50:50 (v/v) ethanol water solution (Figure 2.12 B and C). Although the heat capacities for the solvent used in these tests and the medium used for *in vitro* testing (PBS/DMEM) are indeed slightly different, they are similar enough in that the experimental protocol does not need to change.

At 48 V the solution was heated at a rate of 2.42 ˚C min^{-1} up to a temperature of 65 ˚C, when this temperature was reached the voltage was reduced to 8.5 V and the temperature was maintained for 30 minutes (Figure 2.12 B). Control over the temperature of the solution was achieved easily with manipulation of the input voltages.

The initial particle heating tests were repeated with a 100 mg/mL solution. While initial heating rates were similar (2.5 ˚C min^{-1}), the heating gradient considerably reduced above 45 ˚C and began to plateau at 55 ˚C (Figure 2.12 B). The specific absorption rate (SAR) of the SPIONs was calculated using the formular:

$$SAR = \left(\frac{C_p H_2 O}{m_{SPIONs}}\right) \cdot \left(\frac{dT}{dt}\right) \quad Equation\ 2.3$$

Where m_{SPIONs} is the concentration of SPIONs, Cp H_2O is the specific heat capacity of water, and dT/dt is the slope of the linear part of the heating curve, measured in Ks^{-1} (Figure 2.12). The SAR of a 100 mg/mL solution of the SPIONs was calculated at 1.76 Wg^{-1}.

2.4 Discussion

2.4.1 Physicochemical characteristics of stabilised SPIONs

The co-precipitation method of nanoparticle synthesis was chosen as the synthesis route of SPIONs. This was due to convenient reaction conditions, high yields and the low deviation in diameter of synthesised particles.[96]

The size, shape and homogeneity are important factors in both the biological action and the induction heating of nanoparticles.[15,112,208,214] The morphology of the particles synthesised was shown to be spherical, homogenous and single crystal in nature (Figure 2.2). This is crucial to ensure the superparamagnetic

property of the particles and that a single magnetic domain is present, which is necessary for efficient inductive heating.[130,215,216] Dynamic light scattering methods were not used to determine the diameter of lauric acid and DDMAT stabilised particles since the diameter of the particles was below that of the accurate measurement rang of the equipment used.

Improved loading efficiency and physiochemical characteristics of DD-ION

Chain transfer agent (CTA) loading of nanoparticles is of the upmost importance when performing RAFT polymerisation on the surface of these particles. The content of DDMAT in the polymerisation reaction must be in excess of the number of propagating chains for proper polymer control to be established.[217,218] Naturally the greater content of DDMAT per weight of particle will provide a more controlled polymerisation and allow for increased chances of the polymer remaining grafted on the surface of the particles. The initial method of loading *via* ligand exchange was costly in terms of total use of DDMAT. Thus, to reduce wastage a new synthesis method, eliminating the need for the ligand exchange step was developed.

The total loading through the newly devised method was over twice that of the method presented in literature.[119] This gave more efficient loading and more efficient use of DDMAT in the process overall, more than doubling the initial loading rates (Table 2.1). There was no difference in the FT-IR spectra and negligible differences in the size, shape and morphology of the particles between the different synthesis methods. The reduction in costs associated with the production of DDMAT stabilised SPIONs allowed for more SPION bound polymerisations than would have been possible using literature methods.

The particles synthesised showed of DDMAT, with a novel synthesis method improving upon the loading described in literature (14 % by weight compared to 6% by weight).[119] This data indicates the synthesised DD-ION particles can serve as a good surface for RAFT mediated polymerisation, with the loaded DDMAT acting as a chain transfer agent and a means of grafting polymers to the surface of SPIONS.

The physiological properties of the SPIONs indicated they were single crystal in nature, sub ten nanometre in diameter and had magnetisation values similar to that of literature. The magnetic field dependence of the magnetization of coated Fe_3O_4 nanoparticles is shown in (Figure 2.8). As can be seen there is no retention of magnetisation in one direction when the field is reversed, indicating there is no magnetic domain interaction when relaxing to an applied field. Therefore it can be said the superparamagnetic property is observed.[212] Magnetisation saturation values were calculated at 65.7 and 57.6 emu g^{-1} at 100 and 300K respectively, this value is similar to that seen in literature (62.5[119] and 65[219]) for particles of this type.[119,220,107,221]

Between 100 and 300K there is no change in gradient to the susceptibility curve, hence it can be assumed the blocking temperature of the particles is below 100 K (Figure 2.8).[222] Using the high temperature regime, assuming it as an equilibrium state, the magnetic susceptibility follows the Curie-Weiss law (Figure 2.8) .[213] As expected the magnetic saturation for particles at 300 K is less than that of particles at 100 K, due to the increase in Brownian motion at higher temperatures.[223]

This data indicated by analysis of the synthesised particles indicated the required properties were present for the particles to be effectively inductively heated by a high frequency field.

2.4.2 Design and operation of the induction heating device

Acting as the external activation stimulus, the imposed alternating magnetic field (AMF) (carried by radio-waves) must have a strong field strength, a high frequency and high penetration depth to ensure particles can be activated. While a variety of commercial machines exist with these features available, price restrictions within the project prevented acquisition. Furthermore, the desire for a device with an adjustable working coil diameter (for cell culture plates) and coil cooling to prevent external heat input further supported the construction of a self-made device.

In comparison to what is commercially available the device designed in this thesis possess several advantageous features. The field produced is high frequency (148 kHz) sufficient to heat SPIONs.[208,224] The input power could be varied up to a maximum of 2 kW allowing for control of the input energy and therefore temperature of the sample. The cooling design of the printed circuit board (PCB) and the water-cooling system of the coil ensures the device can be operated indefinitely, without external heat input into the working coil. The working coil itself could be interchanged easily to allow for different sized samples to be heated. The device is small, easy to operate and compared to commercially available products, inexpensive, costing just £110. Commercially available products such as the "Ambrell Easy heat® 4.2" can produce a high frequency field (150-400 kHz) that has an adjustable input power, however, the working coil does not possess a cooling system and importantly, the equipment costs in excess of £3000.[225] "Solary systems" 1 kW induction heater is sold at a much lower cost (£186), however, there is no adjustable input power, the device can only be run for 120 seconds before a cooldown period of 15 minutes must commence. There is no prevention of external coil heat input into the sample and the device is not sufficient to heat nanoparticles due to its low frequency and input power.[226]

Induction heating of bulk metals

The created device showed very powerful heating rates of bulk materials and demonstrated the ability to control the temperature of a solution by changing only one external factor, circuit input voltage. Therefore, this demonstrated a working induction heating device that could carry out the desired functions. By touch measurements it was confirmed there was no heat input to the sample through the working coil, thus the water-cooling system devised was efficient.

2.4.3 Induction heating of SPIONs

Heating rates of SPIONs in solution showed linear trajectories, obeying the prediction of the liner response theory of heating.[107] At the highest input powers the rates of heating observed allowed particles to reach the activation temperature within a matter of minutes (Figure 2.12 B and C).

Furthermore, initial heating rates were the same for both 100 and 200 mg/mL concentrations of particles, indicating a saturation heating rate had been reached. Indeed this high concentration effect can be explained by the adverse interactions of magnetic domains and possible aggregation.[227]

The SAR of particles at each concentration were calculated at 1.76 Wg^{-1} for a concentration of 100 mg/mL particles in a field of frequency 148 kHz and field strength of 1.58 kAm^{-1}. Since SAR is dependent on a number of factors; field strength and frequency, coil diameter, number of coil turns, current through the coil, distance from the centre of the coil, etc, SAR cannot be directly compared between studies. However, using equation 8.7 (SAR is proportional to field strength squared) and extrapolating with an increase field strength to those used in literature (from 1.5 to 23 kAm^{-1}) the SAR of the particles is calculated to be 260 Wg^{-1} similar to the literature value of 225 Wg^{-1}.[228]

The plateau of temperature observed for a 100 mg/mL solution at 55 °C indicates that the input of energy from induction heating has become equal to the radiation of heat from the sample to the surroundings and an equilibrium has formed. Without a greater input energy or a higher frequency AMF a solution at this concentration cannot reach a higher temperature. However, this temperature was significantly above the desired temperature target for stimulated drug release.

Expected concentrations of particles for drug delivery were in the micro-milligram range, further tests for induction heating on polymer coated nanoparticles showed slightly different heating rates. Polymer – particle heating rates were less per weight particles since the polymer on the surface of the particles comprised a greater proportion of the total mass of the complex than LA-ION. For *in vitro* testing the temperature change requirement is 37.5-43 °C, and with good control to not exceed the target temperature and reach hyperthermic temperatures. Given the data from these initial tests, the constructed induction heating device was sufficient to provide this required level of heating and subsequent temperature control.

2.5 Conclusion

Superparamagnetic iron oxide nanoparticles (SPIONs) were synthesised and stabilised successfully with Lauric acid. Ligand exchange to stabilise the particles with DDMAT was successful. A new method of creating DDMAT stabilised particles was developed, this new method improved the uptake efficiency of DDMAT as a stabilisation ligand. The presence of the stabilising ligands was confirmed by FT-IR, zeta potential measurements and the size and morphology of particles by TEM imaging. From TEM images the single crystal nature of particles was observed. Magnetisation data confirmed the superparamagnetic properties of the SPIONs.

An induction heating device was constructed capable of induction heating of bulk metals and nanoparticle solutions. The device itself was designed to incorporate desirable features including an adjustable power of the induced field and a water-cooled working coil. The device was constructed at low cost and showed remarkable reliability and consistency. Synthesised SPIONs showed efficient induction heating. Temperature control of nanoparticle solutions could be achieved by adjustment of input voltages from the device. Compared to commercially available devices the constructed induction heater described is superior overall given the functions required and the constraints on costs.

The induction heating device and the synthesised particles were ideally suited to be taken forward as an extrinsic activation method for a temperature dependant release mechanism.

Chapter 3: Copolymer design synthesis and analysis.

3.1 Introduction

The action of thermoresponsive polymers undergoing a phase change has the potential to act as a release mechanism in a variety of different methods. The release mechanism in this project involves applying strain on bonds between polymers grafted on the surface of SPIONs and immobilised drug bearing proteins. The mechanical stress applied to the bonds of any polymer-bound drug or carrying vehicles upon the coil to globular transition, could act as an efficient release mechanism. Current thermoresponsive copolymers do not possess the ability to immobilise proteins and undergo the coil to globular transition at the desired temperature range of 40-43 °C, above human body temperature but below that of hyperthermic temperatures. The process of creating a thermoresponsive copolymer that possess these properties is described in this chapter.

3.1.1 Poly-N-isopropylacrylamide as a thermoresponsive polymer

The thermoresponsive polymer Poly N-isopropylacrylamide (PNIPAM) was first synthesised in 1950 from its monomer N-isopropylacrylamide, and has been extensively researched due to its inverse solubility upon heating.[229] The structure of PNIPAM is relatively simple and the presence of amine and carbonyl groups aid its ability to form hydrogen bonds in aqueous solution (Figure 3.4).

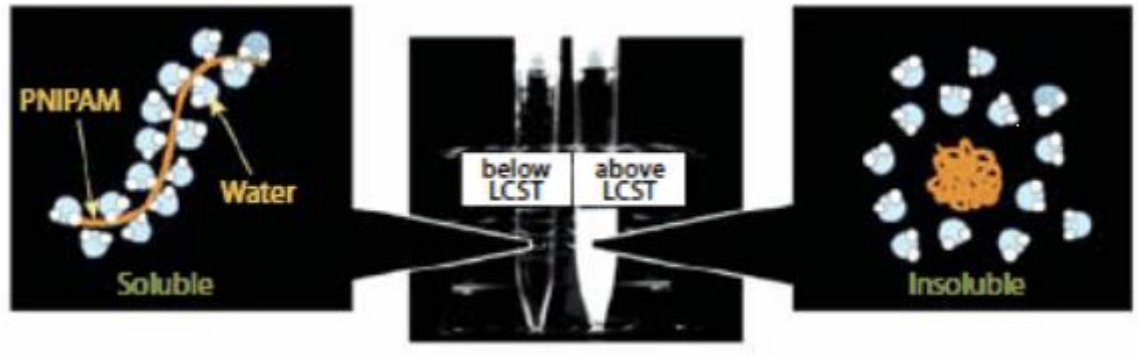


Figure 3. 1: Structure of poly N-isopropylacrylamide (PNIPAM) and the phase change that occurs at the LCST. The diagram demonstrates the rearrangement in structure and the change in solution appearance as a result of the thermodynamic changes when the LCST is reached. [230]

While in aqueous solution at a low temperature, PNIPAM adopts a coil like structure, to maximise enthalpy of hydration through hydrogen bonding between the amide group within the polymer and the surrounding water molecules. However, upon heating above 32°C, the polymer undergoes a reversible lower critical solution phase transition temperature (LCST) (Figure 3.1). This phase transition involves the coil structure of PNIPAM collapsing into a hydrophobic globular structure, releasing water molecules.[132] The thermodynamic driving force behind this change to hydrophobicity can be explained by the Gibbs equation:

$$\Delta G = \Delta H - T\Delta S \qquad \text{Equation 3.1}$$

For any reaction to occur the Gibbs free energy change (ΔG) must have a negative value. At temperatures below 32°C, ΔG is dominated by the enthalpy change of hydration (ΔH) which has a large negative value due to the exothermic hydrogen bonding between the polymer and water molecules. When the polymer is heated above 32°C, the entropy term ($T\Delta S$) has a much larger contribution, thus it becomes thermodynamically favourable to release water from the coil structure. Hence, with rising temperatures the

structure of the polymer changes from coil to globular and therefore the solubility in aqueous solution is reversed (Figure 3.1).[61]

Copolymerisation has been used to alter the composition of PNIPAM with the intention of changing its properties to satisfy a function. For example, copolymerisation can be exploited to adjust the lower critical solution temperature (LCST). In addition, depending on the co-monomer used in the synthesis, the pH sensitivity, thermoresponsivity and the amount of crosslinking present in the monomer can be controlled. Importantly, chain end functionalised PNIPAM can also be synthesised.[231] Depending on the reaction conditions, desired terminal groups can be added to PNIPAM, including those that allow biocompatibility and attachment of catalysis complexes.[231]

The unique properties of PNIPAM have led to some remarkable applications of the polymer. These include use as membranes, sensors, tissue engineering materials and use in drug delivery systems.[232]

3.1.2 RAFT as a polymerisation technique and chain transfer agents

Several polymerisation methods involve reversible deactivation radical polymerisation using thiocarbonylthio compounds as chain transfer agents.[119,120,229,233] RAFT polymerisation is perhaps one of the most studied and utilised of these chain growth methods. As is common with radical polymerisation methods, RAFT polymerisations can be performed with conditions to control molecular weight and polydispersity. These polymerisations can produce complex polymer matrices with good functional group tolerance and high polydispersity control. For this reason it is a widely used polymerisation technique in modern chemistry and the primary polymerisation technique used in this study.[217]

The mechanism for RAFT polymerisation has both kinetic and thermodynamic considerations. The kinetic mechanism is easily described by typical initiation, propagation, and termination steps, however, after the classical propagation step there are 3 additional steps; RAFT pre-equilibrium, re-initiation and the main RAFT equilibrium step (Figure 3.2).[234]

The initiation step is caused by a free radical source such as azobisisobutyronitrile (AIBN) which releases two tertiary carbon free radicals upon decomposition. The tertiary carbon radical then reacts with a single monomer to yield a polymeric radical. The standard propagation step follows convention, where the active radical chain reacts with further monomer units.[235] Typically, the rate of reaction is determined by the initiation step and therefore the breakdown of the free radical source.

During the RAFT pre-equilibrium step, the polymeric radical reacts with the RAFT reagent to form a raft adduct radical. This is an equilibrium step so will fragment to reform the starting radicals or a polymeric RAFT agent and a radical R group originating from the RAFT reagent. The subsequent re-initiation step results from the newly formed radical R group reacting with another monomer unit to form an additional active polymer chain.

The main RAFT equilibrium is the key step to control this type of polymerisation reaction. This involves a rapid interchange process in which the radicals present are "shared" among all species that have not undergone termination. Thus, chains have equal opportunity to react with monomers and consequently have similar weights. This is the step which controls the polydispersity index (PDI) and average molecular weight of the radical polymerisation.[217,218]

Lastly, termination acts as in any other classical radical controlled polymerisation, where bi-radical species combine to form a "dead" polymer chain. Ideally a RAFT chain transfer agent molecule is hindered as to not undergo termination reactions. This is achieved through the most stable product in the equilibrium steps being the radical sulphur adduct, hence at any given time the concentration of propagating chains is so low the rate of termination is negligible. A reaction scheme for a typical RAFT reaction mechanism is illustrated below in Figure 3.2.

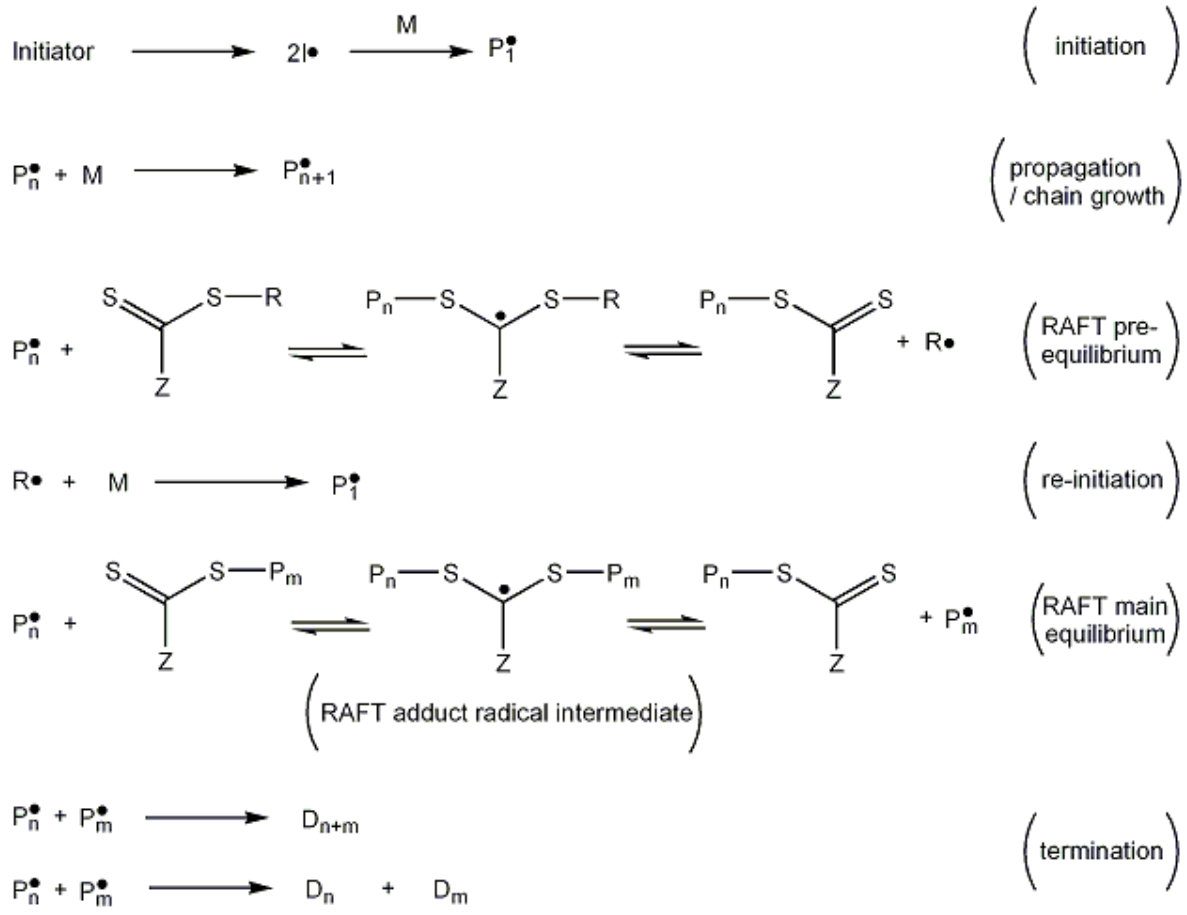


Figure 3. 2: The reaction scheme of a typical RAFT polymerisation reaction. The main equilibrium steps occur simultaneously and dictate the reaction rate. Taken from G Moad et al.[236]

The thermodynamics of RAFT polymerisation are relatively simple. The basic driving force is the exothermic formation of the polymer chain; however, the equilibrium present complicates the prediction of the product (Figure 3.2). The position of the main RAFT equilibrium step is reliant upon the relative

stabilities of the RAFT fragmentation molecule and its products. If the RAFT radical adduct is sufficiently stable, the concentration of active species is reduced, hence the reaction is referred to as a 'rate retarded RAFT polymerisation'. Higher temperatures and high concentrations of the RAFT adduct favour the formation of fragmentation products.[218] In reactions without rate retardation, the rate of reaction is determined by the rate of propagation. Since termination and initiation are much faster reactions, the rate is proportional to the concentration of active radical polymers.

In contrast to other controlled radical polymerisations, RAFT polymerisation does not control molecular weight by reducing bi-radical termination reactions. RAFT polymerisation controls the molecular weight by ensuring the majority of polymer chains initiate growth at same point in time and assumes their reaction conditions are identical.[236] A RAFT chain transfer agent typically has a thiocarbonylthio group (S=C-S) with substituents R and Z (Figure 3.2) that impact the polymerization reaction kinetics. Initiation of the polymerization reaction is accomplished utilizing conventional thermal, photochemical, or redox methods and it is the proper choice of the RAFT reagents appropriate for a particular monomer and reaction medium that will largely determine success of a RAFT polymerization experiment.

2-(Dodecylthiocarbonothioylthio)-2-methylpropionic acid (DDMAT) is an example of a reversible addition fragmentation (RAFT) chain transfer agent commonly used as an iron oxide nanoparticle steric stabilising molecule(Figure 3.3).[120] Typically, RAFT agent stabilised nanoparticles are prepared via ligand exchange synthesis in solution with already stabilised nanoparticles (Figure 3.3).[96] The structure of DDMAT is key to its use as a RAFT agent and a stabilising ligand (Figure 3.3). Usually, thiocarbonthioyl groups are used for this process as they produce fragmentation products that steer the reaction in the direction of desired yield (Figure 3.2).

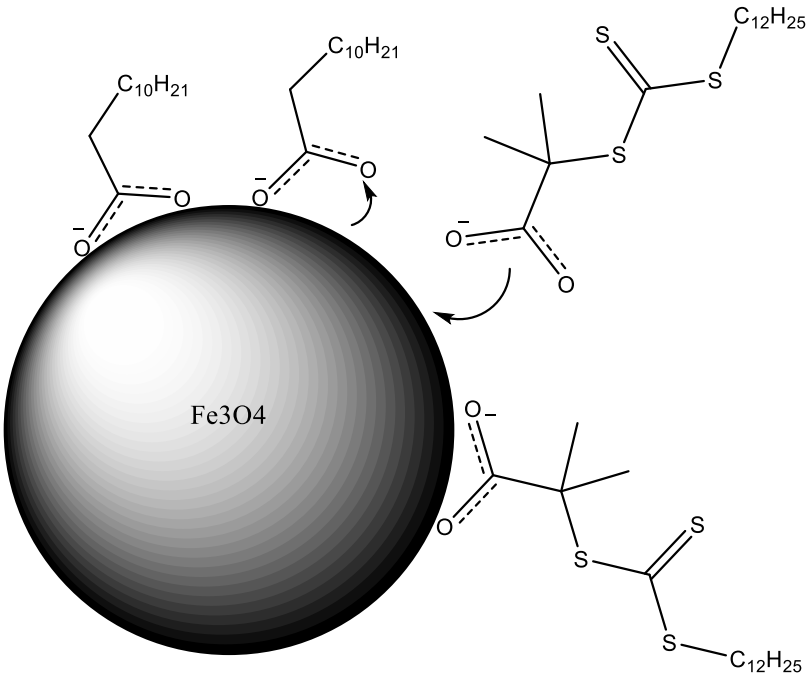


Figure 3. 3: Exchange reaction on the surface of Iron oxide nanoparticles. Lauric acid ligands on the surface are exchanged with excess DDMAT molecules present in solution.

3.1.3 Radical copolymerisation

Radical copolymers can be synthesised by a variety of different methods to form different sequences of monomer units within a polymer chain. The precise control of polymer composition allows macro properties of the polymer to be precisely adjusted.[237 – 239]

In radical polymerisation the sequence of monomers is dictated by the affinity of the terminal radical monomer to bind other monomers present in solution. In a reaction with two types of monomer present, we define reactivity ratio (r), as the ratio of the rate constants for the reaction of one monomer radical with itself over the other monomer present in the reaction (Equation 3.2).[240] If the two monomers present in a reaction were type A and B, the r values would be defined as:

$$r_A = \frac{k_{AA}}{k_{AB}} \qquad r_B = \frac{k_{BB}}{k_{BA}} \qquad \text{(Equation 3.2)}$$

The structure of the copolymer itself depends on the molar ratio of the monomers in synthesis, reaction conditions and the r values. If the r value is greater than 1 then the polymer has a greater tendency to bind with itself, but if the r value is close to zero then the monomer has a higher affinity to bind with the alterative monomer present.[239] Some r values of common monomers are listed below (Table 3.1).[237]

Table 3. 1: Examples of free Radical monomer reactivity ratios.[237]

Monomer A	*Monomer B*	*r1*	*r2*	*Temperature (° C)*
Styrene	Methyl Methacrylate	0.52	0.46	60
Styrene	Acrylonitrile	0.40	0.04	60
Styrene	Maleic anhydride	0.041	0.01	60
Methyl Methacrylate	Vinyl Chloride	10	0.1	68
Methyl Methacrylate	Vinyl acetate	20	0.015	60

The Mayo equation shown below describes the tendency of the monomers A and B in a reaction to form a polymer with a consistent -A-B-A-B- alternating sequence (Equ 3.3). [240]

$$\frac{d[M_A]}{d[M_B]} = \frac{[M_A](r_A[M_A]+[M_A])}{[M_B]([M_A]+r_B[M_B])} \qquad (Equation\ 3.3)$$

Monomers with low r values and similar molar ratios in reactions produce uniform alternating monomer sequences and allow for synthesis of polymers with enhanced functionality.[120] For example copolymerised styrene maleic anhydride is a copolymer commonly formed with a copolymerisation value very close to 1 when the molar ratios are equal (Equ 3.2).[238]

The reaction ratio and the resulting structure is unknown for a vast variety of monomers when copolymerised. When copolymerised with a co-monomer with a very high r value the resulting copolymer will exhibit a block structure with distinct monomer regions. This can be utilised to produce polymers with surfactant properties or with distinct functionalities. Three monomers copolymerised where two have low r values to react with each other will form an alternating block distinct from the third monomer with a high r value.

With the aims of the thesis considered, a thermoresponsive copolymer that could undergo a structure change at the desired temperature range and was capable of binding to proteins needed to be developed. The copolymer would also need to be capable of binding to and be heated by a SPION, be soluble in aqueous solution, exhibit biocompatibility and show stability over an extended period of time in physiological conditions.

3.2 Materials and methods

3.2.1 RAFT polymerisation of unbound polymers

For the synthesis of the free copolymer, 25 mg of DDMAT was dissolved in 10 mL DMF under a nitrogen atmosphere. Monomer(s) were added to final a concentration of 10 mM and 1.17 mg AIBN was added, still under a nitrogen atmosphere. The reaction flask was then degassed by three freeze-thaw pump cycles, heated to 65 $^{\circ}$ C and stirred for 48h. After 48h the solution was diluted with dimethyl fumarate (DMF) and precipitated in diethyl ether, centrifuged at 10,000 g for 5 minutes and washed, this was repeated three times. Synthesis of copolymers was done with the desired monomers being added in their desired ratios for a total monomer content of 10 nM. The synthesis was undertaken in an anaerobic chamber, after given time

intervals co-monomers were added and the reaction allowed to continue. Once the reaction was deemed completed the product was extracted in the same method as described above.

3.2.2 Poly – (methacrolein-b-(NIPAM-co-acylamide) synthesis

Copolymer synthesis was performed unbound to particles. DDMAT (25 mg) was dissolved in 5 mL Dimethyl fumarate under a nitrogen atmosphere. Methacrolein (79 μL, 1 mM) was added to the solution followed by 1.17 mg Azobisisobutyronitrile (AIBN), still under a nitrogen atmosphere. Following this, N-isopropyl acrylamide (4.5 mM, 508 mg) and acrylamide (4.5 mM, 380 mg) were added to the reaction mixture. The reaction flask was then degassed by three freeze-thaw pump cycles and heated to 65° C and stirred for 2 weeks. Following this the solution was diluted with 35 mL Tetra hydro furan, precipitated in 40 mL diethyl ether (All Sigma-Aldrich Merck Life Science UK Limited, Gillingham, UK) and removed by centrifugation at 15,000g for 10 minutes, this was repeated three times.

3.2.3 Analysis methods

Visual LCST measurement of polymers

Samples of PNIPAM and PN-ION were made up to 10 mg/mL in clear colourless glass vials, these were then placed in water above a hotplate and heated. Reading from a mercury thermometer placed in the water, the LCST for each sample was observed. Three measurements were taken for each sample and an average temperature taken.

UV-VIS LCST measurement of polymers

For more accurate measurements the 10 mg/mL polymer samples were heated to 90 °C and placed inside a UV-VIS spectrometer. The temperature was monitored via the use of thermo couples and the LCST determined by the temperature at which the solution hit an absolute minimum adsorption at 800nm.

FT-IR

PerkinElmer Frontier IR/FTIR (Seer Green, Beaconsfield, UK) was used for the determination of surface functional groups on a sample, with a scan range from 600-4000 cm^{-1}. Samples were run as a dry powder above a KBr crystal and scanned for 64 repeat measurements. The data was processed and presented as transmission signal.

Nuclear Magnetic Resonance

Multinuclear NMR was assessed for both C^{13} and H^{1} using a 500 MHz Bruker Avance (Bruker instruments UK, Banner La, Coventry CV4 9GH). The samples of copolymer were dispersed in deuterium oxide at a concentration range of 10-40 mg/mL depending on the mass of sample available. MestReNova version 11.0.01 software was used to analyse the spectra.

C^{13} and H^{1} NMR predictions were done by using ChemDraw professional NMR prediction software. The spectra were predicted from copolymer models created within ChemDraw, up to the molecular weight limit the software could accommodate. Three dimensional models of the copolymers were generated in Chem office Chem 3D modelling software again using copolymer models created within ChemDraw. The modelling method is molecular mechanics.

Gel permeation chromatography

For GPC analysis samples were prepared at concentrations of 2 mg/mL in DMF with 5 mM NH_4BF_4. Samples were run on an Agilent Infinity II MDS instrument equipped with differential refractive index (DRI), viscometry (VS), dual angle light scatter (LS) and variable wavelength UV detectors. The system was equipped with 2 x PLgel Mixed D columns (300 x 7.5 mm) and a PLgel 5 μm guard column. Samples were run at 1 mL/min at 50 °C. Poly(methyl methacrylate) standards (Agilent EasiVials) were used for calibration between 955,000 – 550 $gmol^{-1}$. Analyte samples were filtered through a nylon membrane with 0.22 μm pore size before injection. Respectively, experimental molar mass (Mn, SEC) and dispersity (Đ) values of synthesized polymers were determined by conventional calibration and universal calibration using Agilent GPC/SEC software.

Differential scanning calorimetry

DSC instruments (model: DSCQ10) manufactured by TA Instrument was used to study the thermal characteristics of polymers. Samples (7-13 mg) were loaded in aluminium cells, and sealed hermetically. The thermogram for each sample was obtained for a temperature range from −15 °C to 85 °C at the heating rate of 1 °C min^{-1}.

3.3 Results

3.3.1 Poly-N-isopropylacrylamide synthesis and analysis

Initially PNIPAM was synthesised by the described RAFT polymerisation, as a model upon which to base the synthesis and analysis of the copolymers (Figure 3.4). Subsequent copolymerisations were synthesised with different ratios of the three constituent monomers of the design. Each type of polymer was analysed in the same manner. Analysis methods included FT-IR, H^1 and C^{13} NMR, DSC, UV-VIS and SEM. The LCST

of the polymers was determined by UV-VIS spectroscopy combined with dynamic light scattering and visual methods.

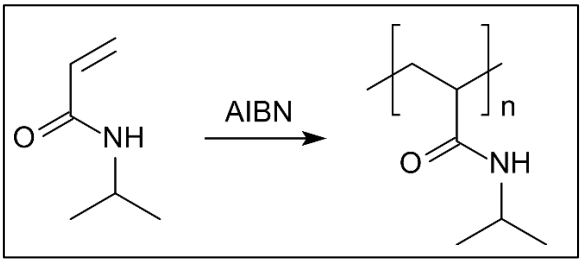
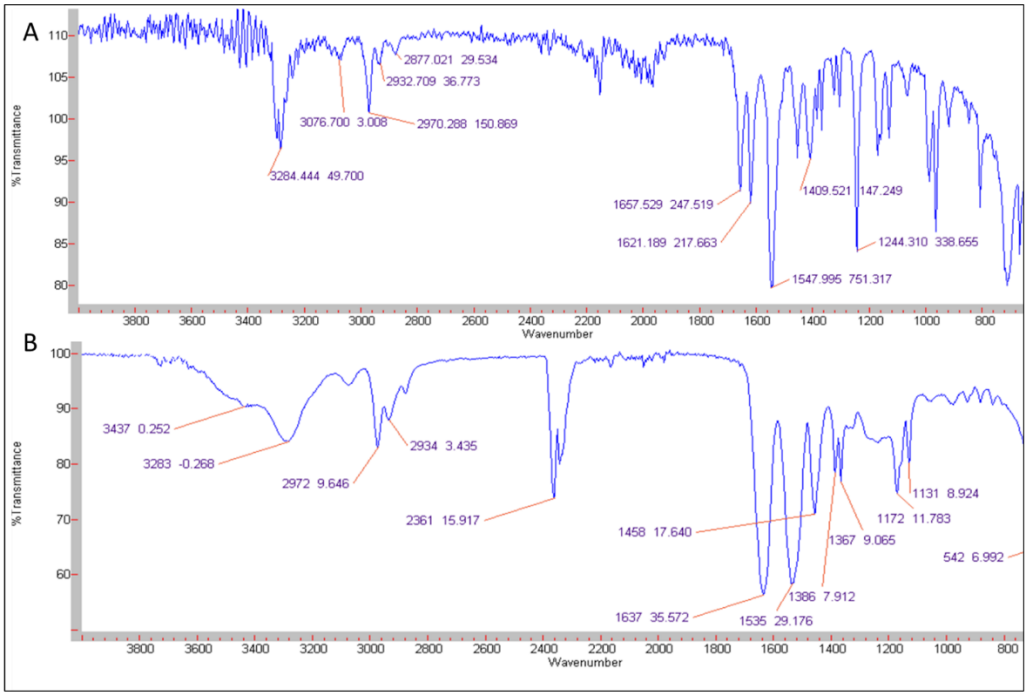
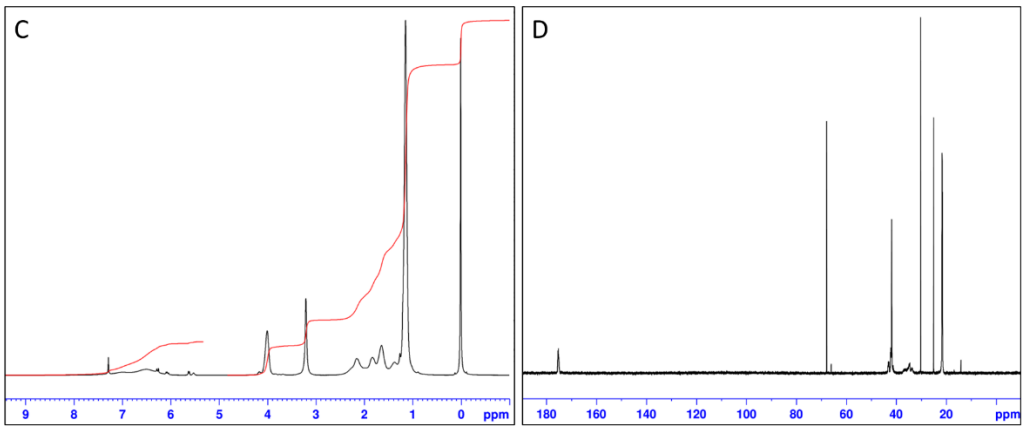


Figure 3. 4: Polymerisation of n molecules of NIPAM, initiated by AIBN to form PNIPAM.

The polymerisation was confirmed by the appearance of the polymer precipitate when the reaction mixture was poured into cold diethyl ether. The yield in this polymerisation was determined by the weight of monomer conversion, since in the RAFT process the molecular weight of the monomer is unchanged. In the free polymer synthesis, 0.985 g of polymer was produced from 1.14 g of NIPAM used in synthesis, giving a yield of 86.4 % (+/- 5.6 %).





E

Wavenumber (cm^{-1})	Functional group
3284	O-H (Narrow)
2990-2850	C-H
1700-1500	C=O (Amide)
1400-1200	C-H

F

Wavenumber (cm^{-1})	Functional group
3283 (Broad)	N-H (Amide)
2975-2850	C-H
1637, 1535	C=O (Amide)
2360-2250	C-H
1370-1350	C-H

Figure 3. 5: Identification of the structure of PNIPAM by spectroscopy methods. FT-IR of the monomer NIPAM, in its monomer state (A) and after RAFT polymerisation to form PNIPAM (B). The ^{1}H NMR spectrum of synthesised PNIPAM (C) and the Hydrogen decoupled ^{13}C NMR spectrum (D), both samples were run in deuterated chloroform solvent as described in the materials and methods. Full scale sizes and assignments of these spectrums can be found in the appendix (Figure A.8). Integral values along with multiplicity are visible on spectrum but are represented by the red integral peaks. Due to the nature of polymer NMR limited information can be obtained from integral peaks. The analysis The x axis represents chemical shift in comparison to the signal from tetra methyl silane (TMS). The assigned functional groups from the FT-IR spectrum of the monomer NIPAM (E) and the polymer PNIPAM (F).

The PNIPAM structure was first confirmed by a white precipitate appearing in the extraction procedure, this was then confirmed by comparing the FT-IR spectra of the monomer and polymer (Figure 3.5 A and B). The two C=C peaks in NIPAM at 1656 cm^{-1} disappear and are replaced by a single more intense peak owing to the altered environment of the C=O bond. Note the broadening of the N-H bond signal from NIPAM to PNIPAM, due to the new hydrogen bonds formed with neighbouring monomer units.

NMR spectrums were analysed manually, and visible peaks were assigned to the expected environments of the polymer structure. The H^1 NMR spectrum observed showed the following peaks (Figure 3.5 C); Alkane polymer proton environment showed a triplet at δ 1.46ppm with an integral peak of 2, polymer chain environment showed a quintet at δ 1.95ppm with an integral peak of 1. The amide proton was observed as a very broad peak from δ 6-6.77ppm, the N-C-H group proton showed a multiplet signal at δ 3.85ppm with an integral peak of 1, and the alkane proton(s) shown by a doublet at δ 1.04ppm with an integral peak of 6.

C^{13} NMR was also run on free PNIPAM (Figure 3.5 D), this resulted in five peaks shown that correspond to the five carbon environments in the polymer. The alkane carbon environment gives rise to the signal present at δ 22 ppm, the isopropyl environment corresponds to the signal at δ 42 ppm, the amide carbon shows a signal at δ 177 ppm, the carbon environment adjacent to the amide nitrogen gives rise to the signal at δ 68 ppm and finally the high intensity signal at 30 ppm is due to the alkane backbone environment. Full scale sizes and assignments of these spectrums can be found in the appendix (Figure A.8).

Both the carbon and hydrogen NMR spectra reinforced the conclusion PNIPAM had been formed and minimal impurities were present in the sample. This further supported the conclusion that PNIPAM had been successfully polymerised by the RAFT polymerisation technique.

Structure confirmation of the product as PNIPAM is demonstrated by the analysis of the FT-IR and NMR spectra. The method of polymerisation was shown to be successful, and the structure was able to be determined with the methods available. Subsequently, produced polymers were analysed in the same fashion and results presented in a similar format. Often, PNIPAM spectra were used as a reference for structure determination of other polymers as a method of comparison.

Following washing and isolation, the LCST of PNIPAM was initially determined by visual methods (Figure 3.6 A). A solution of 10 mg/mL in water was heated linearly in a temperature-controlled water bath until the initially clear solution became opaque with the appearance of a white precipitate. The temperature at which any precipitate could be observed with the naked eye was taken as the temperature of the LCST, the solution was observed with a black background to aid visual observation (Figure 3.6 A and B). The LCST for non-grafted PNIPAM was found to be 32.7 ˚C by the visual observation method.

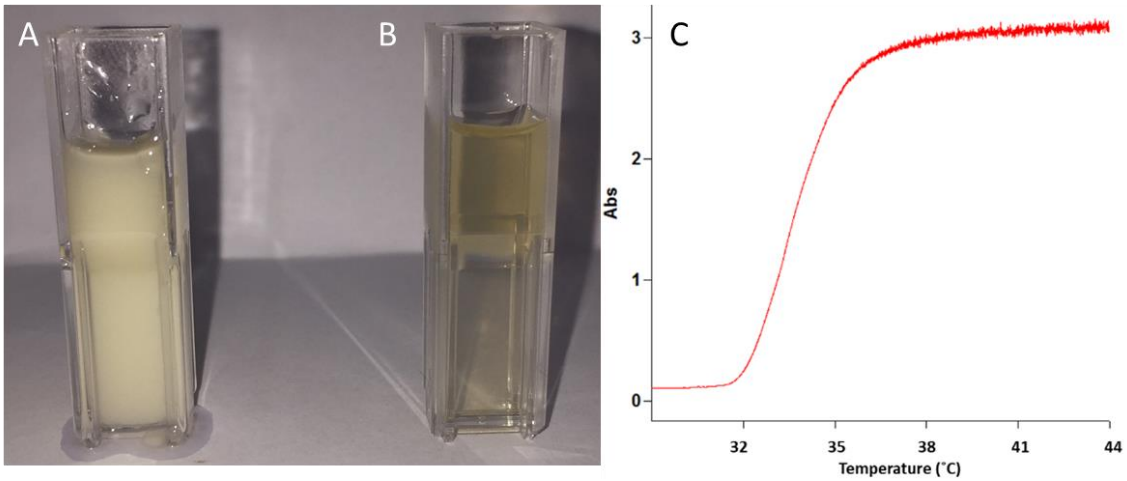
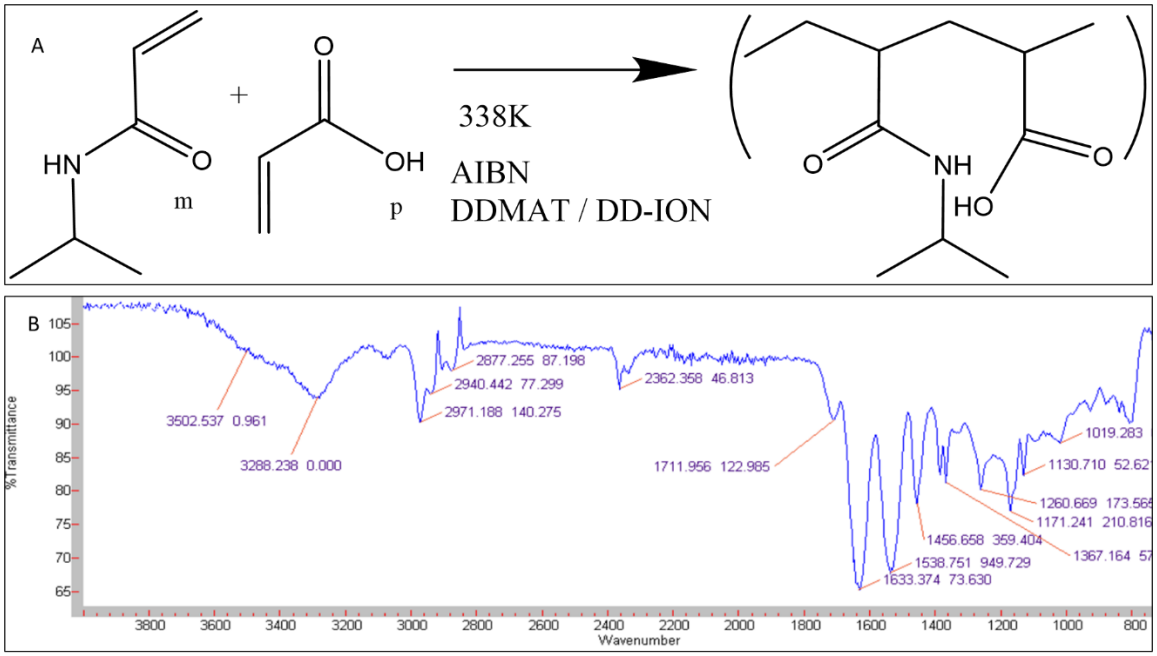


Figure 3. 6: Determination oof the LCST of PNIPAM. A 10 mg/mL solution of PNIPAM below the LCST (B) and above the LCST (A). Vial A shows the appearance of a white precipitate when a solution of PNIPAM in water is heated above the LCST. C shows a UV-VIS spectrum of the absorbance of PNIPAM at 800nm in relation to temperature of the sample. The LCST is denoted as the temperature at which the polymer starts to drop out of solution and shows absorbance.

As a more thorough and reliable method, UV-VIS spectroscopy was used to determine the LCST by a change in absorption at 800 nm upon the phase change (Figure 3.6 C). The UV-VIS absorption was run as a function of time and run concurrently with thermocouples. The absorption and temperature data alignment were made possible by the thermocoupling software and an absorption – temperature graph created (Figure 3.6 C). The LCST was found to have a value of 31.9 °C by this method, a fraction of a degree lower than that of literature sources (32.1 °C).[241 – 243]

3.3.2 Copolymerisation of NIPAM-Acrylic Acid

Acrylic acid was used as the initial hydrophilic co-monomer to increase the LCST of the designed copolymer. Firstly, the feasibility of copolymerisation with NIPAM was investigated to confirm literature reports.[244] Synthesis was performed with a monomer molar reaction ratio of 80:20 NIPAM to acrylamide respectively (8 mM NIPAM, 2 mM Acrylic acid) (Figure 3.7 A).



C

Wavenumber (cm^{-1})	Functional group
3283 (Broad)	N-H (Amide)
3000	O-H (Acid)
2975-2850	C-H
1711	C=O (Acid)
1637, 1535	C=O (Amide)
2360-2250	C-H
1370-1350	C-H

Figure 3. 7: Reaction scheme for the RAFT copolymerisation of NIPAM and Acrylic acid (A) and the FT-IR spectrum of the resultant product (B). The assigned functional groups from the FT-IR spectrum of the synthesised copolymer PNIPAM-co-acrylic acid (C).

The reaction resulted in a product with a percentage yield of 86 %(+/-14 %). After washing and drying the product had a more yellow /off white colour, in comparison to the white product of pure PNIPAM. FT-IR analysis also confirmed the prescence of acrylic acid in the resulting polymer (Figure 3.7 B).

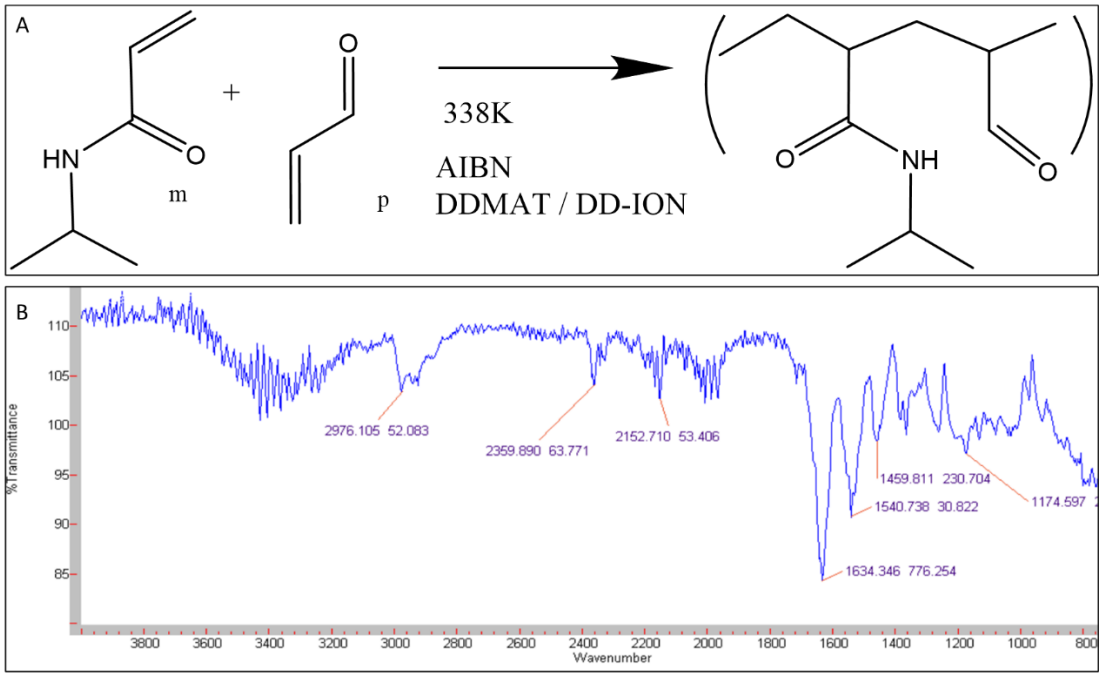
A C=O new acid peak present at 1711cm^{-1} and a broader signal between 3300-3600 cm^{-1} confirmed the prescence of the acid group of Acylic acid within the copolymer (Figure 3.7C). The remaining peaks on the spectrum indicated PNIPAM was present.

With the feasability of incoporating acrylic acid as a hydrophilic monomer into the copolymer confirmed, the next step was confirming the feasibilty of incoporating Acrolein as a comonomer for protein binding.

3.3.3 Copolymerisation of NIPAM and Acrolein

The copolymerisation was carried out in a nitrogen filled flask after three freeze thaw pump cycles, in a manner similar to that of a straight PNIPAM synthesis (Figure 3. 8 A). The ratio of Acrolein to NIPAM was 1:1 in order to maximise protein immobilisation and enable detection of both present monomers. Although

the molar ratio of the two monomers was 1:1 in the reaction, the lower reaction rate of acrolein results in a lower rate of inclusion in the synthesised copolymer.



C

Wavenumber (cm^{-1})	Functional group
3283 (Broad)	N-H (Amide)
2975-2850	C-H
1720	C=O (Aldehyde)
1635, 1535	C=O (Amide)
1390	C-H (Aldehyde)
2360-2250	C-H
1370-1350	C-H

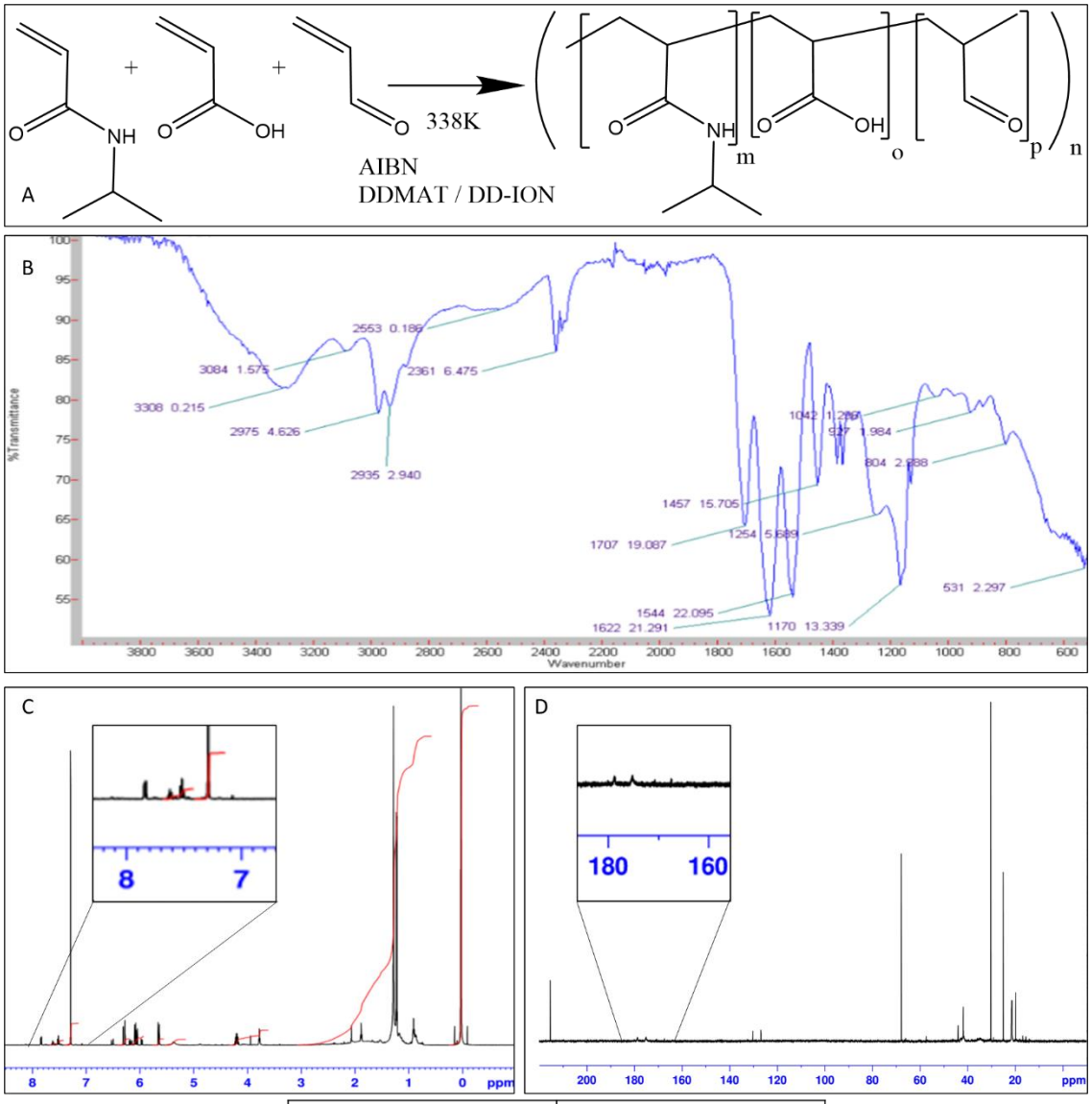
Figure 3. 8: Reaction scheme for the RAFT copolymerisation of NIPAM and acrolein (A) and the FT-IR spectrum of the poly-acrolein-NIPAM product (B). The assigned functional groups from the FT-IR spectrum of the synthesised copolymer PNIPAM-co-acrolein (C).

The reaction percentage yield was somewhat reduced from that of pure PNIPAM and copolymerisaed NIPAM-AA, with a yield of 64 %(+/- 7.7 %, n=3), likely due to the lower reactivity of acrolein. To confirm the identity of acrolein within the copolymer FT-IR was again used (Figure 3.8 B, C). In the FT-IR the N-H, C=O and other NIPAM peaks were observed with a slight shifting of the C=O enviroment within the spectrum (Figure 3.8 B). The aldehyde C=O enviroment was confirmed by the prescence of a new peak at

1714 cm^{-1}. The LCST of the product was measured at 14 $^{\circ}$ C by visual and UV-VIS methods. Although a drop in the LCST was expected, this was a very low temperature indicating the prescence of Acrolein within the product.

3.3.4 Copolymerisation of NIPAM, acrylic acid and Acrolein

Initially, NIPAM-co-acrolein and NIPAM-co-acrylic acid were synthesised to investigate whether these monomers could be copolymerised with existing methods, and to assist with structure determination of the resulting copolymer. NIPAM-co-acrolein was used further as the polymer with which to start protein immobilisation testing. Once the structure of the two types of copolymers had been confirmed, copolymerisation was performed, including all three constituent monomers (Figure 3.9 A). The structure of each type of copolymer was determined again by FT-IR and NMR. Since the differing types vary only in molar ratio, the fine structure of the polymer would be very similar for each polymer type, excluding those where a constituent monomer has a ratio of 0. The presence of the combined copolymer was first verified by the appearance of a white precipitate in the extraction procedure.



E

Wavenumber (cm^{-1})	Functional group
3308 (Broad)	N-H (Amide)
3084	O-H (Acid)
2975-2850	C-H
1707	C=O (Acid/aldehyde)
1622, 1544	C=O (Amide)
2360-2250	C-H
1370-1350	C-H

Figure 3. 9: Reaction scheme for the copolymerisation of NIPAM, acrylic acid and Acrolein and identification of the structure by spectroscopy methods. Example of a copolymerisation reaction between NIPAM, acrylic acid and acrolein to form a copolymer under RAFT polymerisation (A). The FT-IR spectrum of the synthesised PNIPAM-acrylic acid- acrolein copolymer (B). (C) shows the H^1 NMR spectra of the synthesised copolymer, the inset highlights the peaks between 7 and 8.3 ppm. (D) shows the C^{13} NMR spectra of copolymer, note the distinct peaks between 160-180 ppm that are highlighted in the inset. The solvent used was deuterated chloroform. The x axis represents chemical shift in comparison to the signal from tetra methyl silane (TMS). The assigned functional groups from the FT-IR spectrum of the synthesised copolymer PNIPAM-co-acrolein-co-acrylic acid (E).

FT-IR data was used to determine monomer inclusion in the synthesised copolymer (Figure 3.9 B and E). The amine N-H stretch was present at 1170 cm^{-1} along with an N-H stretch at 3291 cm^{-1}, confirming the presence of the NIPAM monomer. The acid C=O peak at 1707 cm^{-1} and C-O peak 1254 cm^{-1} confirmed the presence of acrylic acid in the monomer and could mask the acrolein signal(Figure 3.9 B and E).

The H^1 NMR spectrum of the copolymer contained the same peaks observed in PNIPAM as well as those assigned to the inclusion of acrylic acid and acrolein monomers (Figure 3.9 C). The large peak at 7.1 ppm is assigned to the solvent. Several environments present between 7.3 and 8 ppm indicate the presence of several acid and amide environments. This suggests a level of randomness in the repeating structure of the comonomer. New C-H environments at δ 1.2, 1.8, 2.8 and 3.7 ppm have been assigned to the C-H chain environments of acrolein and acrylic acid. Some unreacted monomer C=C peaks were observed between 5.9-6.5 ppm. Full sized and assigned NMR spectrums of this copolymer can be found in the appendix in Figure A9.

The C^{13} spectrum proved useful in structure determination (Figure 3.9 D). Also showing the same peaks observed in the spectrum for NIPAM, the C^{13} showed the definitive presence of acid and aldehyde functional groups belonging to acrolein and acrylic acid. A peak at δ 215 ppm corresponds to the presence of an aldehyde carbon, owing to the acrolein monomer. A peak at δ 179 ppm corresponds to the acid carbon in acrylic acid and the peak at 174 ppm the amide carbon. Further C-C chain carbon peaks were observed at δ 18,16, 43 and 58 ppm. Again, C=C peaks were observed from unreacted monomer between 120-140 ppm.

It was concluded that the polymerisation of the Poly-NIPAM-co-acrylic acid-co-acrolein was successful as confirmed by the FT-IR and NMR data. The exact fine structure of the polymer was harder to determine; since acrolein and acrylic acid have not been copolymerised alone the reactivity ratios are unknown.

LCST tests were carried out in the same fashion as that described for PNIPAM. As expected, with an increase in acrolein molar ratio the LCST of the copolymer decreased. However, it was noticed with increasing acrylic acid content, the LCST was also decreasing.

Table 3. 2 : Depiction of the LCST of each type of copolymer created, based on the molar ratios of the constitute monomers at the start of the polymerisation process. Not necessarily the resultant molar ratio in the synthesised product.

NIPAM %	*Acrolein %*	*Acrylic acid %*	*LCST/ ° C*
100	0	0	32
50	50	0	14
50	0	50	24
50	25	25	19
45	25	30	18
40	25	35	17
40	20	40	23
40	25	35	20
93.3	0	6.7	30
80	0	20	28

No literature discovered at the start of the project had described this effect before. A report was found detailing this effect and the mechanism behind this phenomenon upon reinvestigation of contemporary literature.[244]

The end goal of the polymer design part of this project was to achieve a LCST phase transition between 39-42˚C for polymer grafted onto the surface of SPION, while still retaining the protein immobilisation ability. Therefore, acrylic acid as a comonomer could not provide the necessary thermodynamic properties when incorporated into the copolymer.

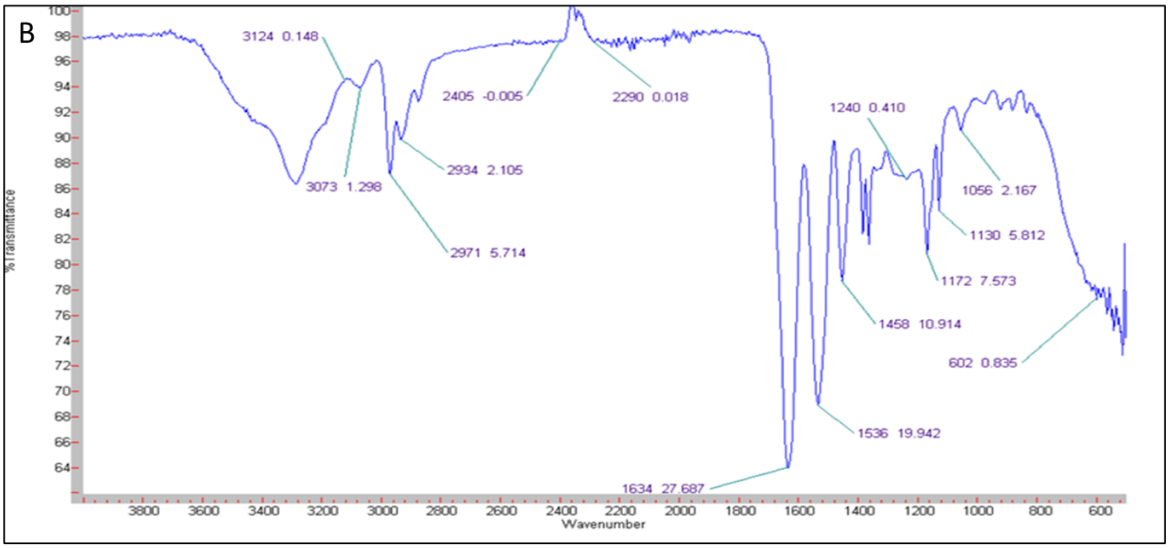
3.3.5 Copolymerisation of NIPAM and acrylamide

Acrylamide has a reaction ratio very close to 1 for its copolymerisation with NIPAM. This reaction ratio is due to the very similar structures of the monomers (Figure 3.10 A). While the structures of the monomers are similar, the lack of the isopropyl group on acrylamide makes acrylamide a much more hydrophilic monomer than NIPAM.

A



B



C

Wavenumber (cm^{-1})	Functional group
3300 (Broad)	N-H (Amide)
2975-2850	C-H
1634, 1536	C=O (Amide)
2360-2250	C-H
1450-1350	C-H

Figure 3. 10: Copolymerisation of NIAPM and acrylamide analysis and polymerisation. Reaction scheme for the RAFT copolymerisation of NIPAM and Acrylamide (A) and the FT-IR spectrum of the resultant product (B). The assigned functional groups from the FT-IR spectrum of the synthesised copolymer PNIPAM-co-acrylamide (C).

The reaction yielded a product with a percentage yield of 86 % (+/- 8.5 %). The copolymer synthesised was an off-white/cream colour and was readily soluble in water.

FT-IR analysis showed a very similar spectrum to that of pure PNIPAM (Figures 3.5 B and 3.10 B and C). Again, this can be explained by the fact all functional groups of acrylamide are also present in NIPAM. Only

the amide carbonyl groups showed a significant shift in wavenumber. Confirmation of the inclusion of acrylamide was reinforced by the dramatic increase of the LCST of the copolymer with an increasing molar ratio of acrylamide (Table 3.3).

Table 3. 3: Effect on the LCST of a synthesised copolymer with increasing content of acrylamide in the starting reagents.

NIPAM %	*Acrylamide %*	*LCST (°C)*
95	5	34
80	20	41
50	50	84

The increase of the LCST above the desired temperature was necessary to counteract the effect of the hydrophobic protein immobilising monomers.

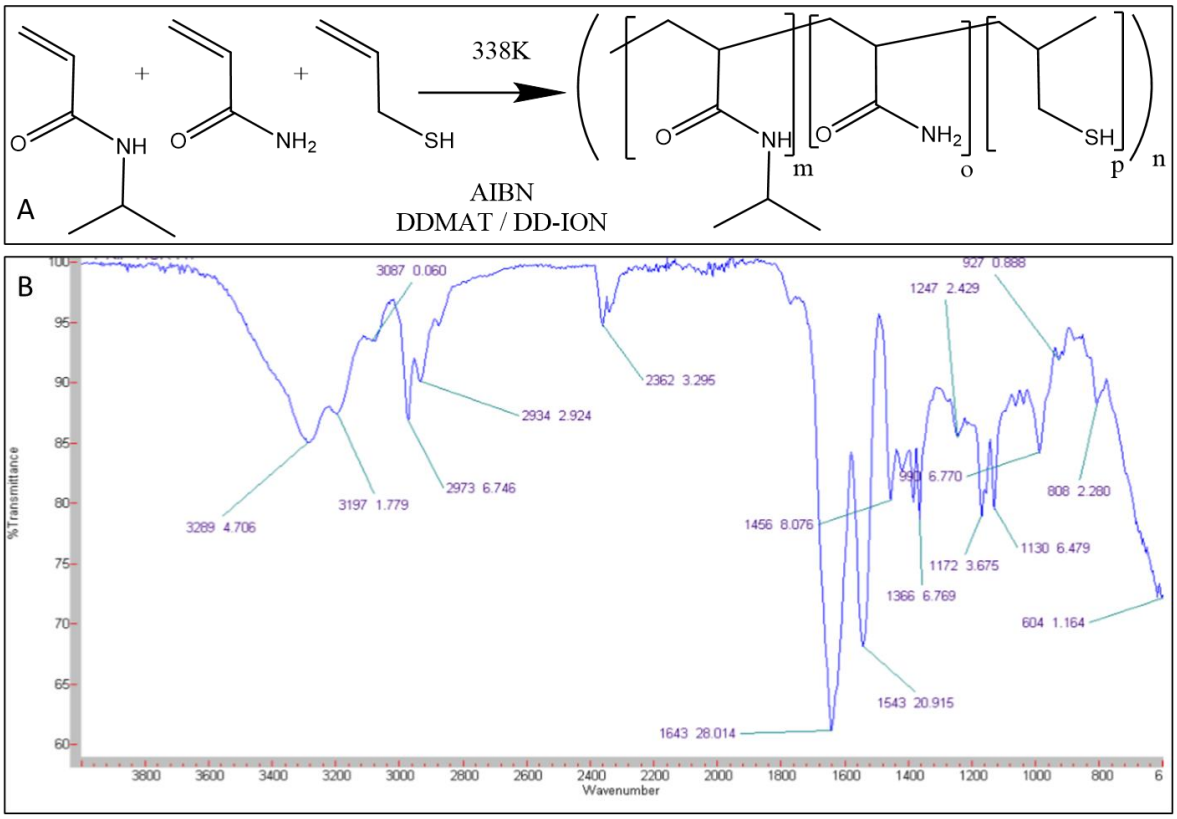
Copolymerisation of NIPAM-Acrylamide-Trans-2-pentenal

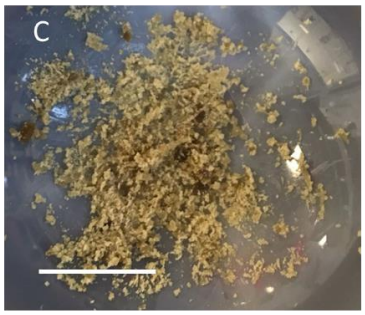
Acrolein was the monomer orignially intended as the protein immobilsing component of the copolymer. However, in december 2019 it became apparent there was no major manufacturer producing acrolein and it was not possible to obtain any more. Thus, an alternative aldehyde group containing monomer was needed.

Trans-2-pentenal was chosen for initial tests due to its structural similartiy to that of acroelin. However, after attempted copolymerisation with NIPAM, there was no evidence of inclusion of trans-2-pentenal from any NMR, FT-IR or LCST data. Again, an alternative monomer was investiagted.

3.3.6 Copolymerisation of NIPAM-Acrylamide-Allyl Thiol

Allyl Thiol, also known as allyl mercaptan, can bind to proteins through disulphide bridges between the monomer and that on the protein. The alkene component of the monomer allows it to react synonymously with other monomers present in raft reactions (Figure 3.11 A).





D

Wavenumber (cm^{-1})	Functional group
3299 (Broad)	N-H (Amide)
2975-2850	C-H
1643, 1543	C=O (Amide)
2360-2250	C-H
1450-1350	C-H

Figure 3. 11: Reaction scheme and analysis of copolymerised NIPAM, acrylamide and allyl thiol. The reaction scheme for the RAFT copolymerisation of NIPAM, acrylamide and Allyl Thiol (A). The FT-IR spectrum of copolymerised Poly-N-Isopropyl-co-Acrylamide-co-Allyl Thiol (B).The grey-brown product of the RAFT polymerisation of NIPAM, acrylamide and Allyl Thiol in crystalline form (C), the product absorbed water and formed a gel before it could be ground into a powder, the image was taken with an optical microscope the scale

bar is 2 cm. The assigned functional groups from the FT-IR spectrum of the synthesised copolymer PNIPAM-co-acrylamide -co-allyl thiol(D).

RAFT Polymerisation was attempted with NIPAM and Acrylamide as comonomers and the reaction was shown as a success by the appearance of a white-grey precipitate following precipitation in cold ether. The yield of the synthesis was greater than that of acrolein copolymers with a percentage yield of 92 % (+/-4.5 %, n=3), indicating a greater reaction rate for allyl thiol in comparison to acrolein. The polymer was dried and took on a light brown colour (Figure 3.11 C) opposed to PNIPAM which is predominantly white.

To further confirm successful polymerisation and inclusion of allyl thiol FT-IR was run on the brown powder (Figure 3.11 B). The most important distinction between this new copolymer and the former copolymer is the shape of the peaks 3300-3600 cm^{-1} indicating the influence of a new S-H group present, the expanded "shoulder" of the broad peak between 3000-3400 cm^{-1} is an indication of this (Figure 3.11 B).

To raise the temperature to that above body temperature with allyl thiol present the component ratios were varied as before and the LCST of the synthesised copolymer changed accordingly (Table 3.4).

Table 3. 4: Effect on the LCST of a synthesised copolymer with increasing content of allyl thiol in the starting reagents.

NIPAM %	*Allyl Thiol %*	*Acrylamide %*	*LCST (°C)*
60	20	20	36
50	20	30	49

The LCST was successfully increased above the target temperature of 40-43 °C. What was noticed after the first successful polymerisation was the change of the light brown powder changed to a dark brown gel like

substance. It is likely was a result of the oxidisation of the thiol groups in the copolymer to disulphide bridges by atmospheric oxygen and moisture.

Although this copolymer exhibited an LCST in the desired range, its oxidisation in atmospheric conditions makes it impractical for use as a drug transport platform technology, therefore further copolymers needed to be investigated.

Copolymerisation of NIPAM, Acrylamide and Crotonaldehyde

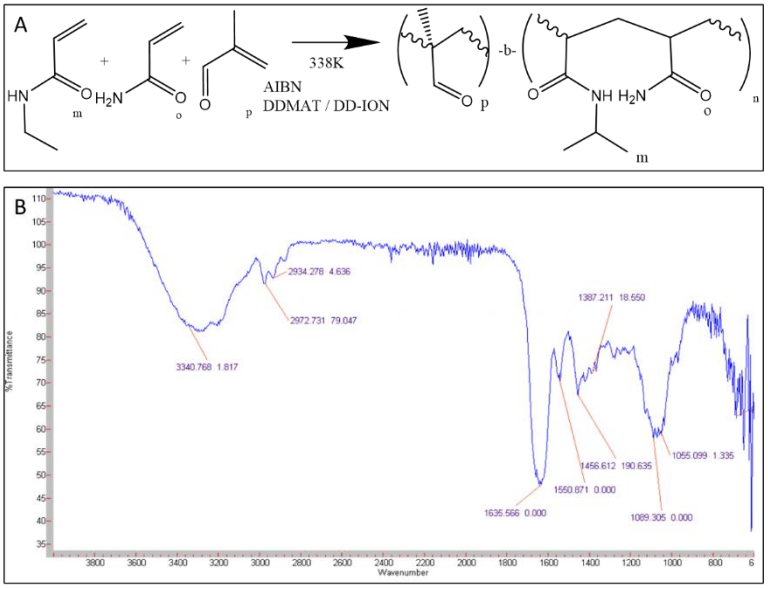
Crotonaldehyde copolymerisation was carried out at starting molar ratio of 45:45:10. A product was produced and separated for analysis. However, the precipitation and washing steps had to be done in strictly controlled conditions to ensure removal of crotonaldehyde in a safe manner. This was an essential step due to crotonaldehydes toxicity, flammability, corrosiveness, and carcinogenic nature.[245] Even small amounts left in a product could cause health issues. For this reason, it was not practical to continue experimentation.

3.3.7 Copolymerisation of NIPAM, Acrylamide and Methacrolein

Methacrolein, as its name suggests is a methylated version of acrolein at the α carbon position. Unlike acrolein it is commercially available. Previous studies have described its capacity for polymerisation in radical addition reactions.[246]

Due to the addition of the methyl group at the α carbon position, the double bond reacted with in radical polymerisation is more sterically hindered than within acrolein. This factor contributes to a much lower reactivity of methacrolein compared to acrolein. The methacrolein in this reaction was added initially without co-monomers and allowed to react for two weeks before NIPAM and acrylamide were subsequently

added and allowed to react for 48 hours. This was done with the intention of creating distinct block regions within the copolymer (Figure 3.12 A).



E

Wavenumber (cm^{-1})	Functional group
3340 (Very broad)	N-H (Amide)
2975-2850	C-H
1635 (Broad)	C=O (Amide, aldehyde)
1550	C=O (Amide)
2360-2250	C-H
1460-1350 (Broad)	C-H

Figure 3. 12: Reaction scheme and product analysis of the copolymerisation of NIPAM, Acrylamide and Methacrolein. The resulting copolymer has two distinct regions, a methacrolein block and an alternating NIPAM, acrylamide block (A). The FT-IR spectrum of synthesised PNIPAM, acrylamide and methacrolein copolymer (B). The PNIPAM-Acrylamide-methacrolein copolymer in a power form (C) and 10 mg copolymer after being dissolved in 1 mL water (D). The assigned functional groups from the FT-IR spectrum of the synthesised copolymer PNIPAM-co-acrylamide -co- methacrolein(E).

Due to the decreased reactivity of methacrolein compared to other protein immobilising monomers reaction yields were much reduced, with 49 % (+/-9.9 %) percentage yield achieved. The product appeared

as a brown- yellow precipitate and after grinding up in a pestle and mortar took on the form of a yellow-cream powder (Figure 3.12 C).

The FT-IR of the synthesised copolymer exhibited several main absorption features confirming the identity of the product (Figure 3.12 B). The 3298 cm^{-1} signal corresponds to the medium N-H stretching aliphatic primary amide of NIPAM, and hydrogen bonding broadens the peak. A signal at 3206 cm^{-1} corresponds to the medium N-H stretching aliphatic primary amine of acrylamide component, Hydrogen bonding again broadens the peak. The signal present at 2969-2931 cm^{-1} corresponds to the medium two C-H stretching alkane environments, polymer backbone and methyl groups. The 2830-2695 cm^{-1} signal corresponds to the medium C-H stretching aldehyde of methacrolein component. The 1680 cm^{-1} signal corresponds to the strong C=O stretching secondary amide both acrylamide and NIPAM masking C=O of methacrolein. Lastly the C-H bending 1390-1380 cm^{-1} signal corresponds to the methacrolein aldehyde. The FT-IR data shows clear differences between the PNIPAM and the PNIPAM-Acrylamide spectra (Figure 3.5 B and 3.12 A).

The H^1NMR spectrum confirmed the inclusion of the three monomers (Figure 3.13 C). The large peak at 4.6 ppm corresponds to the solvent peak from D_2O and the multiplet at 6.1 unreacted alkenes. The NMR data obtained from the new polymer supports the creation of a copolymer with the intended structure (Figure 3.13 and supplementary figure A10). The predicted data from Chem office NMR prediction software matches with the observed spectra (Figure 3.13 A and B), however, the software assumes the monomers are present in equal ratios and hence presents a much larger signal for methacrolein than observed in reality. The only discrepancy being the N-H peak which is variable in the observed

spectrum due to the repeating structure being variable. The signal of the aldehyde peak from the methacrolein copolymer is very small due to the low ratio of monomer in the copolymer; its appearance in the H^1 spectrum is no more than a small bump at 9.4ppm (Figure 3.13 C).

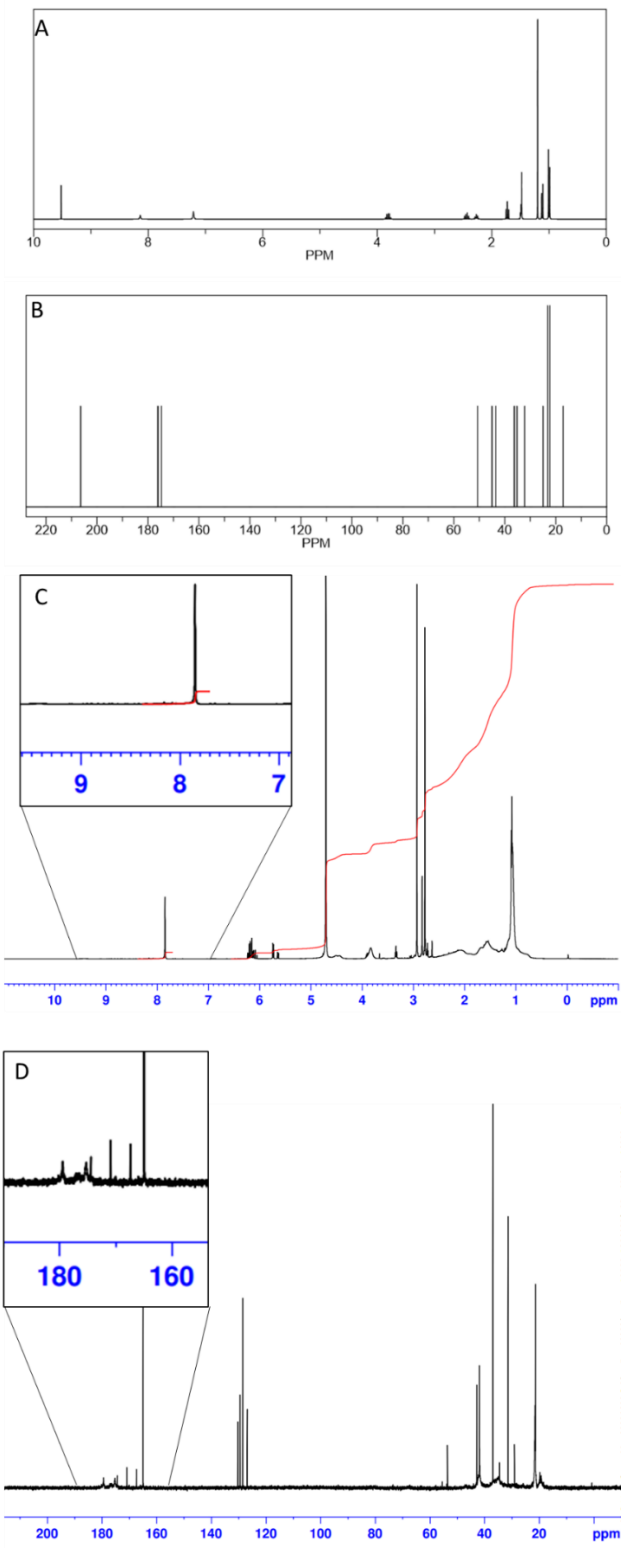


Figure 3. 13: NMR analysis of the product from the copolymerisation of NIPAM, Acrylamide, and Methacrolein. The predicted ^{1}H(A) and ^{13}C (B) NMR spectrums of the synthesised copolymer from Chem3D software. The software cannot simulate polymers and therefore assumes constituent monomers to be present in the same ratios, thereby deviating signals sizes from real spectrums. (A) shows the ^{1}H NMR spectra of copolymerised NIPAM-Acrylamide-Methacrolein. The inset highlights the several small peaks present between 7.5-9.6ppm indicating the presence of several amide proton environments and the acrolein environment. (B) shows the C^{13} NMR

spectra of copolymerised NIPAM-Acrylamide-Methacrolein. The inset highlights several peaks present between 160-180ppm indicating the presence of several amide carbon environments. The x axis represents chemical shift in relation to tetra methyl silane and the red lines indicate integral peaks of different proton environments. Both NMR's were run with the sample in deuterium oxide as the solvent. Full scale NMR's and detailed assignments are available in the appendix figure A10.

When compared to the spectrums of pure PNIPAM the presence of a broad peak at δ 9.5 ppm in the H^1 indicates the inclusion of methacrolein. The inclusion of several different environments between δ 6.5-8 ppm suggest the presence of more than one amide molecular environment within the copolymer, thus acrylamide and NIPAM are present in several different environments.

The C^{13} spectrum observed from the copolymer lined up with the predicted spectrum (figure 3.13 B and 3.13 D). The peaks observed around 130 ppm are unreacted alkenes. The signals from 160-180 ppm again predicted the presence of several amide environments, reinforcing what was observed in the H^1 spectrum. The signals from 50-55 ppm are due to the alkane backbone of the polymer and match with the prediction from the software. Due to the lower abundance of C^{13} as an isotope, and the low molar ratio of the monomer in the synthesis, the aldehyde environment from methacrolein is not visible in the spectrum. Full scale NMR's and detailed assignments are available in the appendix figure A10.

The two spectra indicate the inclusion of methacrolein and acrylamide within the copolymer. Methacrolein, due to its low reactivity and estimated reaction ratios with Acrylamide and NIPAM, has only one environment signal, indicating it forms a distinct block polymer region within the copolymer. NIPAM and Acrylamide show several signals for the amide environment indicating a random order, however, there is a dominant environment at 7.9 ppm and 165 ppm indicating some form of order. This implies the acrylamide, NPAM co-block of the copolymer is a majority alternating copolymer with some form of randomness.

To raise the temperature to that above body temperature with methacrolein present the component ratios were varied as before and the LCST of the synthesised copolymer changed accordingly (Table 3.5). A Methacrolein reactant ratio of 10% was used for further copolymerisation reactions. This was due to the increase in LCST upon reduced reactant ratio of methacrolein, and the fact that there was no difference in protein loading between copolymers with a 20 or 10% reactant ratio of methacrolein (Chapter 4). This lack of change of protein loading can be explained by the low reactivity of methacrolein. Indicating that in the two week reaction time methacrolein is not completely reacted.

Table 3. 5: Effect on the LCST of a synthesised copolymer with varying content of NIPAM, acrylamide and methacrolein in the starting reagents.

N-ISOPROPYLACYLAMIDE %	ACRYLAMIDE %	METHACROLEIN %	LCST/RELEASE TEMP (°C)
50	30	20	27
40	40	20	36
35	45	20	43
40	50	10	55
45	45	10	49

The ratio of 45:45:10 (NIPAM:Acrylamide:Methacrolein) showed an ideal LCST for loading onto SPIONs (Table 3.5). This was the copolymer starting reactant ratios taken forward in the project.

Differential scanning calorimetry (DSC) was run on selected polymers to gauge and quantify thermodynamic properties, most notably the phase transition temperature. This is not the same as the solution phase transition temperature, since DSC samples must be run dry. Other features include melting

and decomposition events. This data is useful to distinguish the copolymer from PNIPAM thermodynamically.

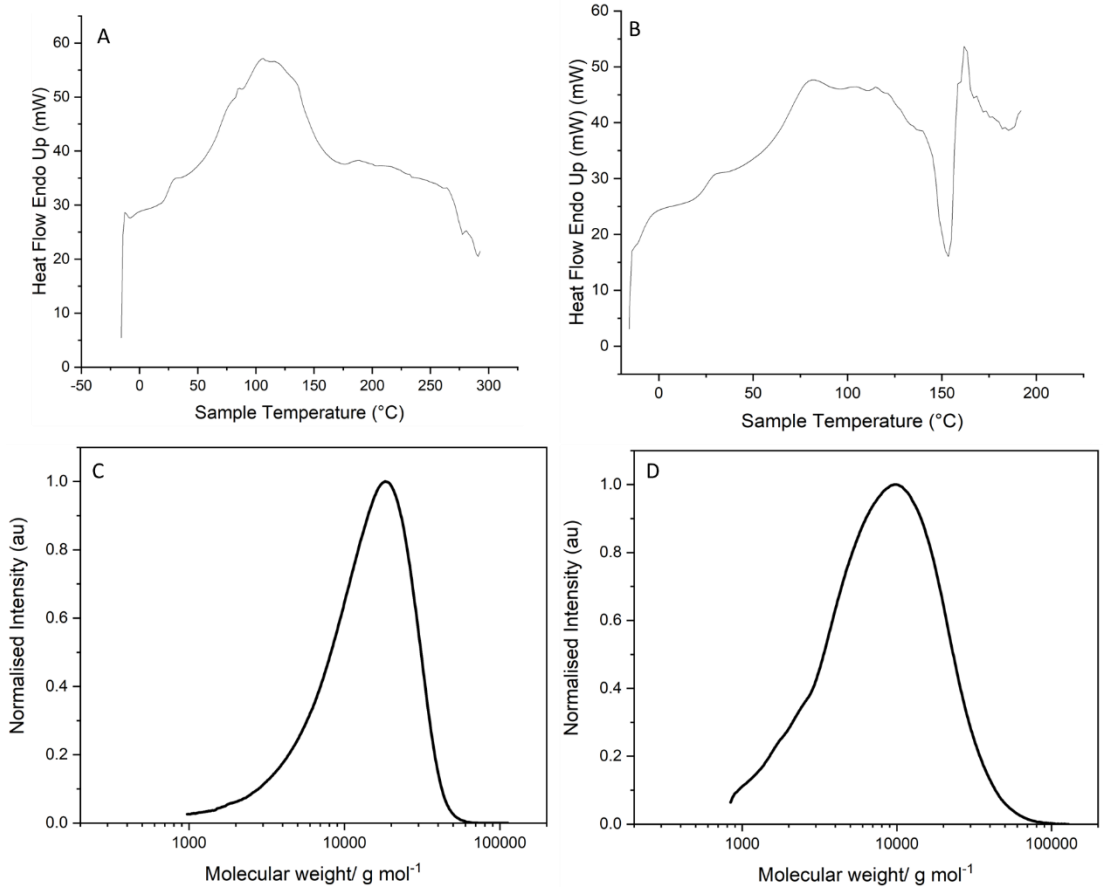


Figure 3. 14: Thermodynamic and physical data of PNIPAM and copolymerised NIPAM, Acrylamide, and Methacrolein. DSC curve of (A) PNIPAM, and (B) the copolymer of NIPAM, Acrolein and acrylamide at a reactant ratio of 45:45:10 respectively. Endothermic events are represented by peaks in the graph, therefore exothermic events a trough. For a constant temperature increase of the sample with no thermodynamic events, the DSC curve would be a flat line. C shows the molecular weight distribution of PNIPAM as synthesised by RAFT polymerisation. Molecular weight intensity is normalised to the logarithm of the peak maxima intensity. (D) represents the molecular weight distribution of NIPAM-Acrylamide-Methacrolein copolymer synthesised at a starting molar ratio of 45:45:10 respectively. Molecular weight intensity is normalised to the logarithm of the peak maxima intensity.

The DSC curves showed a number of thermodynamic events for pure PNIPAM and for the synthesised NIPAM-Acrylamide- Methacrolein copolymer (Figure 3.14 A and B). In PNIPAM, a glass transition occurs at 24.98 ˚C with a (change in heat capacity) (ΔCp) of 0.327 J/g˚C (Figure 3.14 A). This indicates an endothermic phase change, possibly the unravelling of polymer chains in the coil state. The melting point

peak was observed at 102 ˚C, four degrees apart from literature values.[241] This is likely a result of a greater polymer chain length in our sample, giving rise to larger intermolecular forces and therefore a higher melting point. A greater polydispersity in the PNIPAM synthesised broadens the width of the melting point endothermic event in the DSC curve (Figure 3.14 A).

In the NIPAM-Acrylamide- Methacrolein copolymer, a glass transition occurs with at 24.35 ˚C with a Δ Cp of 0.377 J/g˚C (Figure 3.14 B). Indicating an endothermic phase change, possibly the unravelling of polymer chains in the coil state. The melting point peak was observed at 81 ˚C; the deviation from the melting point of PNIPAM is due to different intermolecular forces between polymers, as a result of the inclusion of acrylamide and methacrolein. Also contributing to the melting point change is the difference in the molecular weight of the synthesised copolymer compared to PNIPAM (Figure 3.14 A and B). An interesting feature observed at 145 ˚C is a large exothermic event (Figure 3.14 B). This could be explained by a crystallisation event, due the copolymer forming solid crystals more thermodynamically stable than those before the melting point.

GPC Data:

Gel permeation chromatography (GPC) a form of size exclusion chromatography, was used to obtain values for the degree of polymerisation, poly-dispersity index, molecular weight and molecular number of the synthesised copolymer.

As a comparison, PNIPAM was also run in the GPC and compared to the synthesised copolymer (Figure 3.14 C and D). A poly dispersity index of 1.65 was calculated (Table 3.6). This value is less than that of conventional radical polymerisation but greater than that of other RAFT examples.[217,247] This indicates some

polymerisation control brought by the RAFT process. The MW was calculated to be 16,000 g mol^{-1}, a typical value for polymerisation under the conditions used with the reactant molar quantities. Using weight average molecular weight as chain mass, the number of NIPAM repeat monomers included in the synthesised polymer was 140 repeat NIPAM units.

Table 3. 6: Calculated dispersity and molecular values for synthesised PNIPAM (A), and NIPAM-Acrylamide-Methacrolein copolymer synthesised at a starting molar ratio of 45:45:10 respectively (B), where Mp is the molecular weight of the peak maxima, polydispersity (PD), number average molecular weight (Mn), the weight average molecular weight (Mw), size average molecular weight (Mz), and the viscosity molecular weight (Mv).

Polymer	*Mp (g/mol)*	*Mn (g/mol)*	*Mw (g/mol)*	*Mz (g/mol)*	*Mz+1 (g/mol)*	*Mv (g/mol)*	*PD*
PNIPAM	19001	9633	15936	21150	25448	20483	1.65
Copolymer	10207	5462	10948	18913	29158	17619	2.00

A poly dispersity index of 2 was calculated for the synthesised copolymer, this indicates a large degree in deviation of molecular weights from the mean. The M_W average calculated for the copolymer was 11, 000 $gmol^{-1}$. Using the value of weight average molecular weight as chain mass (Table 3.6), and assigning the molecular weight occupied by each monomer proportionally by the reactant molar ratio, the number of repeat units of each monomer was calculated. The number of NIPAM repeat monomers in this synthesised copolymer is 40 repeat units, acrylamide 56 repeat units, and methacrolein 14 repeat units. However, using the assumption that starting reaction molar ratio is equivalent to composition in the final product is not an accurate representation of the true nature of the copolymer and so must be observed with that in mind.

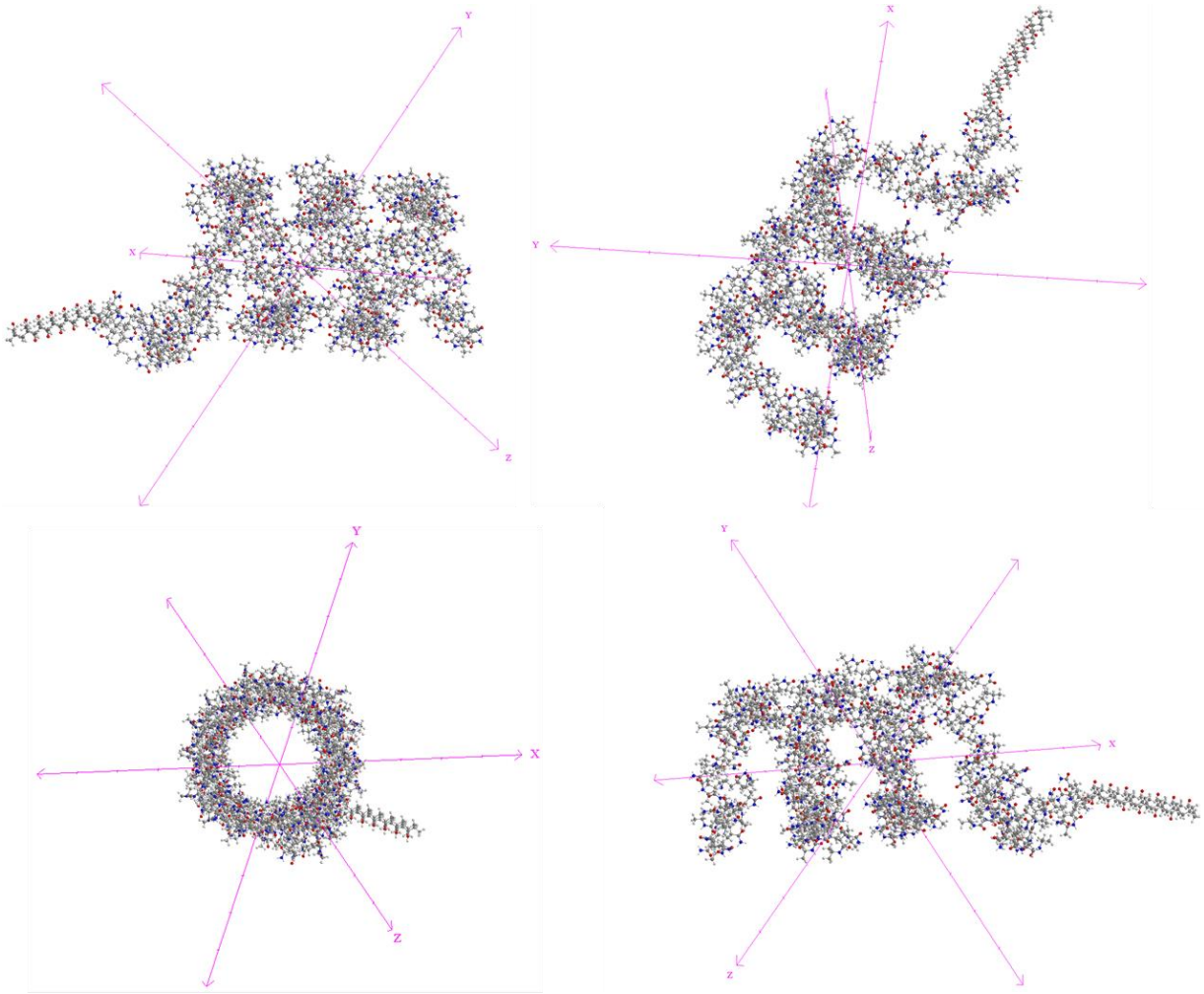


Figure 3. 15: The simulated three dimensional structure of the synthesised Poly-b-Methacrolein-b-NIPAM-co-acrylamide copolymer in its hydrophilic coil like state. The small linear chain substructure represents the approximated 14 methacrolein units. The coil structure represents the combined 56 acrylamide and 40 NIPAM monomers. Three dimensional models of the copolymers were generated in Chem office Chem 3D modelling software again using copolymer models created within ChemDraw. The modelling method is molecular mechanics.

The three-dimensional structure of the copolymer was modelled using ChemDraw 3D software, to aid visualisation of the overall structure of the copolymer (Figure 3.15). This was done using the approximate predicted numbers of repeat units calculated from GPC data (Table 3.6). The structures would contain randomly integrated monomers of the other substructure, but these would be at very low concentrations. The structure of the copolymer was modelled as a linear methacrolein chain and a coil structure contain PNIPAM-co-acrylamide.

3.4 Discussion

No copolymers capable of immobilising proteins and undergoing a phase change at the temperatures necessary for cargo release, between body and hyperthermic temperatures are known to exist in the literature at the present time. Thus, a novel copolymer capable of enabling a triggered release mechanism was created.

3.4.1 DDMAT as a chain transfer agent

DDMAT was used as the chain transfer agent in polymerisations for a number of reasons. The terminal carboxylic acid group allows DDMAT to easily donate as a Lewis base onto the surface of iron oxide nanoparticles, possessing a high binding constant and therefore gives good surface coverage. The dodecyl alkane chain helps provide steric support to particles, preventing aggregation in solution and the central thiocarbonothioylthio group is key to the pre-equilibrium step in the RAFT chain transfer polymerisation.[233] DDMAT as a chain transfer agent performs very well with acrylamide and acrylamide derivative monomers, including NIPAM.[248] It is also capable of mediating polymerisations of methacrolates well. Possessing a carboxylic group able to act as a lewis base and bind to metal oxide surfaces, DDMAT provides a method of surface anchored RAFT polymerisation. DDMAT was the best option for the chain transfer agent of the polymerisation reactions because of its high affinity for mediating acrylamide type molecules in RAFT reactions, its possession of a carboxylic acid group that allows binding onto the surface of SPIONS, and when compared to other RAFT mediators, its low cost.[211]

3.4.2 PNIPAM synthesis and characterisation

As a starting point for the synthesis and study of the copolymers, PNIPAM was first created using the specified RAFT polymerization. Analysis of the FT-IR and NMR spectra showed that the product is

confirmed to be PNIPAM in terms of its structure.[241,243,244] The successful polymerization technique was demonstrated, and the structure could be identified using the tools at hand. The spectra also provided a useful reference for future copolymerisation as a comparison. The LCST of the synthesised PNIPAM, at 31.9 °C was very close to literature sources (31.5-33 °C).[242,249]

3.4.3 Synthesis of PNIPAM-co-Acrolein

Acrolein has been shown in literature to immobilise proteins and is a relatively well studied compound.[250] It can immobilise proteins such as BSA by interaction of its aldehyde group with functional groups within the complex structure of the protein.[119] Most notable of these interactions is imine bond formation under mild conditions between its carbonyl group and a primary amine group in proteins, forming a Schiff base linkage.[251] Its simplicity makes polymerisation predictable and it behaves well in most polymerisation models. Follwing copolymerisation the structure of the desired copolymer was confirmed. However, copolymerstion with NIPAM resulted in a reduced yield, compared to pure PNIPAM, likely due to the lower reactivity of Acrolein.[119,250] The hydrophobic nature of the acrolein monomer however, results in a smaller negative enthalpy from the hydrogen bonding of the polymer with water. Since the desired phase change temperature is above body temperature, hydrophilic monomers must be added to counterbalance this effect.

3.4.4 Synthesis of PNIPAM-co-acrolein-co-acrylic acid

The imperative function of the polymers investigated in this project is immobilisation and selective release of the drug carrying vehicle. To create this selective release the polymer must undergo the release mechanism (the LCST phase change) when triggered by radio wave induced heating. This LCST must therefore occur

above the human body temperature of 37.5°C. At 43 °C hyperthermia will induce cell death, which is undesirable since it is often uncontrollable and therefore avoided in this project.[15,127,128,252] Therefore, the LCST must occur between 37.5 and 43°C, to avoid unwanted release in healthy tissue and to avoid uncontrollable cell death by hyperthermia. Acrylic acid was chosen as a hydrophilic co-monomer because it is readily available and previous studies had documented its copolymerisation with thermoresponsive polymers.

In the reverse effect to that described for copolymerisation with acrolein, the enthalpy change of hydrogen bonding for the copolymer is greater with a hydrophilic component like acrylic acid. Hence, literature reports indicate that the LCST of the phase change can be raised above body temperature with less than 2% acrylic acid (AA) present in the reaction.[241,253]

However, it was observed that the LCST was likewise declining as acrylic acid level increased (Table 3.2). The monomer that was added in order to increase LCST had the exact opposite effect.

In the conditions of low temperature, hydrogen bonds formed between H_2O and amide groups play an important role to make the PNIPAM soluble in water. However, when the temperature reaches the LCST, the hydrogen bond between H_2O and the amide groups is broken-down. The PNIPAM becomes insoluble in water due to the hydrophobic isopropyl groups and the entropy change of the release of water at higher temperatures becomes dominant in the Gibbs free energy equation (equ 3.1). The LCST becomes higher as NIPAM is copolymerized with hydrophilic acrylic acid monomer, but it decreases beyond a 10 % acrylic acid molar ratio. This is due to the

hydrogen bond between the carboxylate group in acrylic acid and the amide groups in NIPAM forming a stronger hydrogen bond than the one between H_2O and the amide groups. Therefore, there is less hydrogen bonding between H_2O and the amide groups to breakdown upon the phase change, a smaller value for the negative enthalpy term and hence the LCST decreases. On the contrary, when the molarity of acrylic acid is much more than NIPAM, the hydrogen bond between H_2O and acrylic acid becomes dominant. The copolymer tends to dissolve and therefore LCST increases. Therefore, acrylic acid as a comonomer could not provide the necessary thermodynamic properties when incorporated into the copolymer.[221]

3.4.5 Synthesis of PNIPAM-co-acrylamide

Acrylamide has been copolymerised with NIPAM in literature extensively, particularly in the synthesis of cross-linked hydrogels.[254] Acrylamide was chosen for use as a co-monomer due to its hydrophilicity, cheap cost, and similar reaction ratio to NIPAM. Although the monomer form of acrylamide is toxic, in copolymer form the toxicity is eliminated.[255] Increasing molar content of acrylamide in the copolymer synthesis resulted in an increase in the LCST (Table 3.3).

3.4.6 Synthesis of PNIPAM-co-acrylamide-co-Allyl thiol

Allyl Thiol, also known as allyl mercaptan, can bind to proteins through disulphide bridges between the monomer and that on the protein.[256,257] The alkene component of the monomer allows it to react with PINIPAM monomers present.[258] The yield of the synthesis was greater than that of acrolein copolymers indicating a greater reaction rate for Allyl thiol in comparison to acrolein. The structure of the copolymer

was confirmed and the LCST was raised to a sufficient level (Table 3.4). However, it became apparent the product was undergoing a reaction in atmospheric conditions. The formation of a gel like substance when the copolymer was left exposed to atmospheric conditions could be explained by a hydrogel forming by crosslinking of thiol groups. Atmospheric oxygen could be catalysing the formation of disulphide bridges between polymer chains, forming a crosslinking hydrogel. Since synthesis takes place in anaerobic conditions, oxidisation only takes place once the product is exposed to atmospheric conditions.

Although some protein immobilisation and release were observed it was shown to be less than 5% of that of the original polymer. Thiol oxidation to disulphide bonds, which prevents free thiol sites from forming bonds with proteins, may be to blame for this.

The search for an alternative protein immobilising co-monomer was prompted by the impracticality of storing a material in an anaerobic environment prior to usage.

3.4.7 Synthesis of PNIPAM-co-Acrylamide-co-Methacrolein

The only variation between the structures of acrolein and methacrolein is the presence of a methyl group at the carbon position. Its ability to copolymerize in radical addition reactions has been studied in the past. [246] However, NIPAM or acrylamide copolymerization hasn't been documented. Thus, the reaction time was adjusted to accommodate the expected lower reactivity of methacrolein. The block structure is desired for use in the nanoparticle-copolymer complex structure, where the hydrophobic methacrolein core is synthesised on the inner shell of the copolymer. This protects the immobilised drug bearing proteins and ensures the outer layer of the complex is hydrophilic and biocompatible. The structure of the resulting product from the copolymerisation was analysed and confirmed.

For subsequent copolymerisation **reactions**, the ratio of methacrolein reactant was decreased from 10 to 20%. This was caused by the rise in LCST following a reduction in the reactant ratio of methacrolein and the fact that the protein loading of copolymers with a 20 or 10% reactant ratio of methacrolein was the same (Chapter 4). The methacrolein's low reactivity can be used to account for this lack of change in protein loading. demonstrating that just a portion of the methacrolein is polymerised over the two-week reaction period.

The DSC data highlighted important thermodynamic differences between synthesised PNIPAM and the synthesised copolymer (Figures 3.14 A and B). Although not directly contributing to the end result of the drug delivery platform, the thermodynamic properties of the synthesised copolymer are important in any possible further research with the copolymers synthesised in this chapter.

The copolymer synthesised had smaller values of MW, MN and MP compared to PNIPAM. A greater value for polydispersity was also calculated, indicating a broader distribution of copolymer molecular weights. Both observations can be explained by the inclusion of methacrolein in the reaction mixture. The inclusion of low reactivity methacrolein contributed to the total number of moles of monomer available for synthesis, such that the reaction will not run to completion. This results in a lower average molecular for the reaction time given, in contrast to PNIPAM alone in the synthesis. In addition to this, acrylamide and methacrolein have lower molecular weights than NIPAM, and their inclusion in the polymer results in a lower molecular weight for the same number of repeat units. Initially in the synthesis, NIPAM and acrylamide will react with each other due to their high reactivity and their reaction ratios. This reaction would occur consistently and result in a lower polydispersity. However, methacrolein could react randomly with a propagating polymer strand, therefore reducing the following reaction rate of that strand massively in comparison to others. This

results in copolymer chains that have varied numbers of initial NIPAM-co-acrylamide groups, thus contributing to greater poly dispersity. The PDI index is large for a product of RAFT polymerisation, brought on by several factors, however, this did not have a significant impact on the observed LCST of the product.

Three-dimensional modelling of the synthesised copolymer provided useful visual data on the possible mechanism of drug release. The linear methacrolein chain is the site at which binding to proteins is expected to occur and NIPAM-acrylamide coil structure is where the structure change occurs. A possible mechanism for protein release upon the structure change, is that the immobilised proteins are squeezed by the coil collapse into the linear chain, applying mechanical pressure to the bond and promoting cleavage of the Schiff base linkage.

In comparison to other protein immobilisation methods the target formation of Schiff base linkages between protein and polymer has several advantages. Amine- thiol acetate bonding is one method. However, within BSA and HSA there are a greater number of available amine groups than thiol groups, allowing for greater rates of polymer-protein binding.[259] Unlike carboxylic acid groups that can also react with proteins, aldehydes do not affect the LCST of the copolymer in the same way, as seen with acrylic acid. Non-specific physical adsorption methods are too susceptible to non-stimulated release, covalent methods are less prone to this.[260] Charged metal nanoparticle methods are not as versatile since they are unstable in solution and cause problems in interaction with compounds in the body.[261] Crosslinked polymer networks lose the advantage of the EPR effect and also do not cross cell membranes at high rates.[262] Overall the formation of a Schiff base linkage between copolymer and protein was the most practical method of protein immobilisation for the design of the nanoparticle complex.

At the time of writing there are no literature reports of a copolymer (Poly-NIPAM-co-acrylamide-co-methacrolein) synthesised with the structure or properties described in this chapter.

3.5 Conclusion

In summary, PNIPAM was synthesised via RAFT polymerisation and analysed by a variety of methods, to serve as a basis for the intended copolymer, and to provide contrast in analysis of subsequent copolymerisation products.

Acrylic acid was copolymerised with NIPAM at varying molar ratios from 0.1-50 % but did not raise the LCST of the synthesised copolymer. Acrolein was copolymerised with NIPAM and showed good protein immobilisation ability, however, it is not commercially available. Trans-2-pentenal did not show reactivity with the RAFT copolymerisation protocols attempted. Although successfully copolymerised with NIPAM, crotonaldehyde proved to hazardous to be a viable option for continued synthesis.

A copolymer synthesised with the required properties was NIPAM-co-acrylamide-co-methacrolein. The identity of the copolymer was confirmed using a variety of techniques including NMR, FT-IR, and DSC. Due to the reactivity of the monomers present, the copolymer likely takes on a block structure with two distinct regions, a methacrolein block and an alternating NIPAM, acrylamide block. This property could be exploited to create a core/shell system of hydrophobic and hydrophilic layers both when grafted onto the surface of nanoparticles, or when forming micelle structures. The LCST of the copolymer could be adjusted by varying reaction molar ratios of the constituent monomers, a ratio exhibiting an LCST above target temperature was taken forward for synthesis on the surface of nanoparticles. GPC data gave valuable insights into polymer length, size and weight and allowed for three-dimensional modelling of the synthesised

copolymer. The novel synthesised copolymer has a huge number of potential applications in the field of drug delivery, medical science and beyond.

The immobilisation and release of drug bearing proteins by the phase change of this copolymer is detailed in chapter 4. The synthesis of the copolymer on the surface of superparamagnetic iron oxide nanoparticles to form a nanoparticle copolymer complex (NCC) is discussed in chapter 5.

Chapter 4: Model drugs for delivery

4.1 Introduction

The type of cancer therapy is determined by the location, size, and stage of the disease as well as the general health of the patient. Cancer genome sequencing aids in identifying the precise type of cancer a patient has in order to choose the most effective treatment.[17]

Chemotherapy, which involves using particular chemical substances to stop the growth of the tumour, has been practised for many years. By interfering with DNA synthesis or delaying mitosis, cytotoxic chemotherapy's basic tenet is to harm and kill rapidly dividing and growing cells. Because most cancer cells proliferate at a pace that is significantly higher than that of healthy cells, these medications may be effective in precisely destroying cancer cells. But some healthy cells, like the bone marrow's blood stem cells, can also multiply swiftly and be affected. As a result, significant side effects such as infertility, hair loss, and decreased generation of blood cells are frequent side effects among chemotherapy patients.[263] To reduce these side effects, targeted forms of chemotherapy are needed. A more specific form of treatment would allow for higher doses of drug to be used, and therefore the potential of higher survival rates.

4.1.1 Sarcoma, brain, breast, and liver cancer cell lines

Rhabdomyosarcoma (RMS) is a malignancy that arises from skeletal muscle tissue.[264] It is the most common type of soft tissue sarcoma in children and adolescents younger than 20 years old.[265] There are two major subtypes of RMS, embryonal and alveolar. Embryonal RMS usually presents in children less than 10 years old and has a 5-year survival of close to 75%. Alveolar RMS occurs at about the same incidence throughout childhood and adolescence and shows lower survival rates; the survival rate for 5 years is less than 50%.

Patients with refractory or relapsed RMS show even lower survival rates, with survival ranging from 10 to 30% after 5 years.[266] Both alveolar and embryonal RMS are treated primarily with surgery, if this is not possible, chemotherapy and or radiotherapy are used to shrink the tumour to an operable size. Recently, immunotherapy has been investigated as a viable treatment method in clinical trials.[267]

U87-MG cells are commonly used in cancer research as an example of a brain cancer cell line. Glioblastoma is treated primarily with surgery, followed by radiotherapy and chemotherapy.[268] In some circumstances, during surgery, thin, round wafers containing chemotherapeutic medication may be inserted into the brain. As the wafers slowly dissolve, the medication is released, eliminating cancer cells.[31] Survival rates are relatively low, with just 30.5% survival rate after 5 years.[4]

Again, surgery, chemotherapy and radiotherapy are the primary forms of treatment for breast cancer. Paclitaxel and doxorubicin are common chemotherapy drugs for the treatment of breast cancer.[269] It has one of the highest survival rates of any cancers, however, it is also one of the most common cancers, still leading to many deaths.[4]

Surgery, chemotherapy and radiotherapy are used to treat liver cancer, radiofrequency ablation and percutaneous ethanol injections are also used commonly. Unfortunately, liver cancer does not respond well to the majority of chemotherapy treatments. Recent developments have demonstrated that utilising a combination of chemotherapy medications may be more beneficial than using only one.[270] Although survival rates have improved, 5 year liver cancer survival rates are still very low, just 17.6% in 2013.[4]

Chemotherapy is used to treat these cancers following surgery or as a sole treatment when surgery is not possible. Improving the efficacy of chemotherapy is essential to reduce side effects and increase survival rates. Targeted delivery methods are a way of achieving this.

4.1.2 Bovine serum albumin as a drug carrying vehicle

Bovine serum albumin (blood plasma fraction V) (BSA) has many uses in scientific research, particularly in biochemical, biomedical and bioengineering research.[52] Because BSA is a cheap, readily available, stable, and a moderately non-reactive protein, it has many applications both *in vitro* and *in vivo*. Due to the size and complexity of BSA, it has a large number of non-specific binding sites, this, along with its biocompatibility, makes it an ideal candidate as a drug delivery vessel.[31,271,272] BSA has also been studied in nanoparticle form, particularly as a vehicle for drug delivery, for several chemotherapeutic compounds BSA assisted delivery is clinically available.[273 – 275] The similarity of BSA to Human serum albumin (HSA), makes it an ideal candidate for a drug delivery platform, since HSA is a major component of human blood proteins.[35] It is important to note that no BSA based nanoparticles have yet been approved for use in the clinic.

4.1.3 Paclitaxel, vinblastine and paracetamol as model drugs for delivery

Paclitaxel is one of several cytoskeletal drugs that target tubulin. Paclitaxel-treated cells have faults in mitotic spindle assembly, chromosome segregation, and therefore cell division.[33,276] In microtubule assembly paclitaxel stabilizes the microtubule polymer and protects it from disassembly. Chromosomes are thus unable to achieve a metaphase spindle configuration. This blocks the progression of mitosis and prolonged activation of the mitotic checkpoint triggers apoptosis or reversion to the G0-phase of the cell cycle without

cell division.[276,277] The ability of paclitaxel to disrupt spindle function can be ascribed to its suppression of microtubule dynamics, but other studies have demonstrated that suppression of dynamics occurs at concentrations lower than those needed to block mitosis.[278] Compared to many other chemotherapy drugs, Paclitaxel is cheap and readily available.[279] Paclitaxel in its most basic state is very potent and causes high cell death at concentrations as low as a few nanomolar.[280] However, with this potency comes with very severe side effects, although, some of these effects can be attributed to the solvent paclitaxel is carried by, Cremphor EL.[33] Paclitaxel can bind non-specifically to HSA nanoparticles to form Abraxane which is used commercially and has seen some success.[34,273,281] It prevents patients needing pre-treatment to prevent hypersensitivity that occours in conventional Paclitaxel treatment. It also utilises the EPR effect of the protein nanoparticles and has less severe side effects, although they are still significant.[273] The paclitaxel-HSA interaction causes conformational changes within the protein. The relative fluorescence intensity of the paclitaxel-bound HSA decreases, suggesting that perturbation around the Trp 214 residue takes place.[282] Since BSA and HSA are very similar structurally, it could be assumed a similar interaction takes place between BSA and Paclitaxel.[283] Paclitaxel’s extreme potency in causing cell death is reflected in its EC50 values which are very low, just 34 nM for RH-1 cells.[284]

Vinblastine is another type of tubulin binding chemotherapy medication. Microtubule-disruptive drugs like vinblastine have been reported to act by two distinct mechanisms.[285,286] At low concentrations they suppress microtubule dynamics and at higher concentrations they reduce microtubule polymer mass. It has also been theorized they produce microtubule fragments by stimulating microtubule minus-end detachment from their organizing centres.[285,286] Analogous to paclitaxel, Vinblastine is a potent anti-cancer agent but again possess harsh side effects.[285] Attachment of Vinblastine to BSA nanoparticles has been documented

previously, potentially enhancing the therapeutic effect, however this has only been demonstrated *in vitro*.[287] Quenching studies indicated that the drug-binding site for vinblastine within BSA is in close proximity to tryptophan residues.[288] Vinblastine shows a high potency for causing cell death in many different types of cancer, brain cancers typically show EC50 values from 10-100 nM with U87-MG cell lines showing less response, with an EC50 of 230 nM.[289] Breast cancer cell lines show EC50 values of 20-200 nM and MCF-7 specifically shows a response of 120 nM.[289] Particularly in brain cancers vinblastine causes a significant therapeutic response where Paclitaxel does not.[33,288]

Paracetamol has been a widely used painkiller and a fever medication since it was first introduced in 1886. The effect of paracetamol on liver cells has been the focus of a huge number of studies for a variety of reasons, namely the toxicity of its metabolites to hepatocyte cells.[290] Liver damage results not from paracetamol itself, but from its metabolite, N-acetyl-p-benzoquinone imine (NAPQI).[291] NAPQI decreases the liver's glutathione and directly damages cells in the liver. Acetylcysteine, otherwise known as N-acetylcysteine (NAC), works to greatly reduce paracetamol toxicity by replacing body stores of the antioxidant glutathione. Glutathione conjugates with the toxic NAPQI metabolite so that it does not react with cellular proteins, allowing it to be safely excreted.[292] Cysteamine and methionine have been shown to prevent hepatotoxicity, while studies show that both are associated with worse side effects than acetylcysteine.[293,294] Furthermore, acetylcysteine has been shown to be a more potent antidote, particularly in patients past 8 hours post-ingestion and for those who exhibit liver failure symptoms.[295] Paracetamol is toxic to liver cells when metabolised in the body. Liver cancer cells that have spread to other parts of the body are also susceptible to the effect of paracetamol.[290,293] There is ongoing research into the use of paracetamol to

potentially treat liver cancer that has spread to other parts of the body. Combining this with using acetylcysteine to protect healthy liver tissue could potentially be a powerful treatment method.

Herein, we test three chemotherapeutic agents, paclitaxel, vinblastine, and paracetamol on their ability to cause cell death in a variety of cell lines. With the potency of the drugs established, it was then necessary to investigate the potential to bind these drugs to BSA which could act a carrying moiety. With the BSA-drug complex synthesised, the immobilisation and release of the protein onto the novel copolymer was investigated.

4.2 Materials and methods

4.2.1 Drug binding to BSA

Paclitaxel (Sigma-Aldrich Merck Life Science UK Limited, Gillingham, UK; 1.2mg) was dissolved in 100 μL pure ethanol. This was combined with 9.9 mL pure H_2O containing 6 mg BSA and the solution was stirred at 21 °C for 3 hours. Vinblastine and paracetamol attachment was achieved using a similar process, with the equivalent molar ratio of each drug (1.27 mg and 33.2 mg respectively) in place of Paclitaxel. Paracetamol was dissolved in 10 mL of pure H_2O due to its solubility.

4.2.2 Protein immobilisation on copolymers

To measure protein released from the synthesised copolymer, an equilibrium solution was formed with 8 mg of copolymer and 6 mg of BSA dissolved in 5 mL PBS. The solution was cooled to 4 °C and stirred for 24 hours. After this, solutions were raised above the LCST of the polymer and precipitants were removed by centrifugation at 10,000 g and washed three times with PBS. To measure the immobilised BSA the

polymer was stirred for 5 minutes below the LCST in 1 mL PBS, then stirred for 5 minutes above the LCST and finally precipitated out. The supernatant was tested for protein content by a standard Bradford protein assay. This process was repeated three times to ensure maximum detection of immobilised protein.

Bradford protein assay

To measure the content of protein immobilised on copolymers a protein assay was run. Samples were run against eight control concentrations of BSA from 0.01-10 μg/mL in PBS, that were used to form a calibration curve. To a 96 well plate, 2 5 μL of Bradford reagent was added to 100 μL sample and the solutions mixed by agitation from a pipette tip. The plate was incubated at room temperature for 15 minutes before being read for absorbance at 595 nm in a plate reader. The gradient of the linear section of the calibration curve was used to calculate the protein content of samples.

4.2.3 Cell lines

The biological effect of drugs was tested *in vitro* on RMS immortalized cancer cell lines obtained from the American Type Culture Collection (ATCC; Manassas, VA, USA). The five cell lines tested were RD (ATCC code CCL-136), RH30 (CRL-7763), U87-MG(HTB-14), MCF-7(HTB-22) and HEP-G2 (HB-8065) cells. The RD cell line was obtained from the stock centre as immortalised cells originally from the pelvic mass of a 7-year-old female. It is categorised as an embryonal type Rhabdomyosarcoma based on histologic appearance of the tumour biopsies and the cultured cells.[296] The RH30 (same patient as the RMS13 cell line) was obtained from bone marrow metastasis of a 16-year-old male with untreated metastatic alveolar RMS.[297] U87-MG is a glioblastoma cell line that shows epithelial morphology that was isolated from malignant gliomas from a male patient.[298] MCF7 are epithelial cells isolated from the breast tissue of a 69-

year-old, white, female patient with metastatic adenocarcinoma.[299] HEP-G2 is a cell line exhibiting epithelial-like morphology that was isolated from a hepatocellular carcinoma of a 15-year-old, white, male youth with liver cancer.[300]

Cell culture

Cells were grown in growth medium (Dulbecco's modified Eagle's medium [Sigma-Aldrich]) supplemented with 10 % (v/v) fetal calf serum (Sigma-Aldrich), 2 mM L-glutamine (Sigma-Aldrich), 100 U/mL penicillin (Sigma-Aldrich), and 0.1 mg/mL streptomycin (Sigma-Aldrich) and then incubated at 37 $^{\circ}$C in a 5 % CO_2 atmosphere. Cells were passaged every 3 – 4 days.

Cell viability experiments

Cells were seeded in 96-well plates at 1×10^4 cells/well in growth media and left overnight in the incubator for the cells to adhere. The following day cells were treated for 24 h with varying concentrations of each drug. After treatment, the media on the cells was removed and the cells were washed in PBS twice. Cells were fixed in 100 μl of 1% (v/v) glutaraldehyde (aq; Sigma-Aldrich, Gillingham, UK) for 30 min and stained with 100 μl of 0.5 % (w/v) crystal violet solution (aq; Sigma-Aldrich) for at least 1 h. The plate was washed with water and dried overnight and cells were solubilized using 150 μl of solubilizing solution (1 % [w/v] sodium dodecyl sulphate (Fisher Scientific, Loughborough, UK) and 10 % (v/v) acetic acid (Sigma-Aldrich)). The absorbance of the solution was measured at 590 nm using a Tecan Infinite f200 microplate reader. Samples were blank corrected and expressed as a percentage of the control cell viability. Experiments were performed in triplicates. Cell viability was normalised as a percentage compared to untreated cells serving as a control.

The EC50 estimation for the response of cell lines to drugs administered was calculated via the Hill equation, which is a function of the agonist concentration, [A]:

$$E = \frac{E_{max}}{1 + (\frac{EC_{50}}{[A]})^{n_H}} \qquad Equ\ 4.1$$

where E is the observed response or effect above baseline, and nH, the Hill coefficient reflects the slope of the curve.[301]

The EC50 denotes the point of inflection of the Hill equation, beyond which increases of [A] have less impact on E. In dose response curves, the logarithm of [A] is often taken, turning the Hill equation into a sigmoidal logistic function. In this case, the EC50 represents the rising section of the sigmoid curve. EC50 is calculated as the response measure being cell death. Due to the limited number of repeats of data points of cell viability used in the EC50 calculation, the value calculated must be regarded as an estimate.

4.2.4 Analysis methods

HPLC

For drug detection of chemotherapy agents, drug containing protein samples were prepared at a concentration of 0.2 – 0.3 mg mL^{-1} in PBS, 200 µL of the samples were then mixed with 50 µL Trypsin EDTA and incubated for 45 mins to ensure protein degradation. The samples were then put through an 8000 Da filter and placed in HPLC vials. Samples of Paclitaxel were analysed on an Agilent 1120 compact LC. The column used for stationary phase was a ZORBAX Eclipse C18 column (4.6 x 150 mm, 5 micron), detection was run at 228 nm with a deuterium lamp. The mobile phase for the separation of paclitaxel consisted of 58 % (v/v) acetonitrile and 42 % (v/v) HPLC grade water. A Paclitaxel peak was detected at

2.67 minutes and each run had a finishing time of 6 minutes. Vinblastine was measured using the same method, but with the detection wavelength set to 245 nm. A vinblastine peak was detected at 4.14 minutes and the run length time was 8 minutes. Paracetamol HPLC detection was run similarly with 25% (v/v) acetonitrile and 75 % (v/v) HPLC grade water being used as the mobile phase, with a detection wavelength of 210 nm. A paracetamol peak was observed at 3.83 minutes and the run length time was 5 minutes. For all drugs a concentration gradient of pure drugs at varying concentrations was run alongside the sample. This concentration gradient was used a as a reference for calculation of drug content in the sample. The peak integration area was plotted for the concentration gradient and a linear equation formed. The peak integration area for the sample was then substituted into the equation and a concentration for the sample calculated.

Statistical analysis

Significance was assessed using a one-way ANOVA test on Graphpad Prism 9, comparing each concentration of added drug to the untreated cell control. P *values are represented by; ****=p<0.001,***=p<0.005 **= 0.01, *=p<0.05, ns=p>0.05.* The data is presented as the means ± standard deviation as error bars, where n= 3.

4.3 Results

4.3.1 Effect of chemotherapy agents on cell lines

To ensure validity of the drug carrying platform, the model drugs chosen were first tested on cell lines unbound to any carrying vehicle. Concentrations of added drug were varied over the range of literature EC50 values for the corresponding cell lines.[284,289]

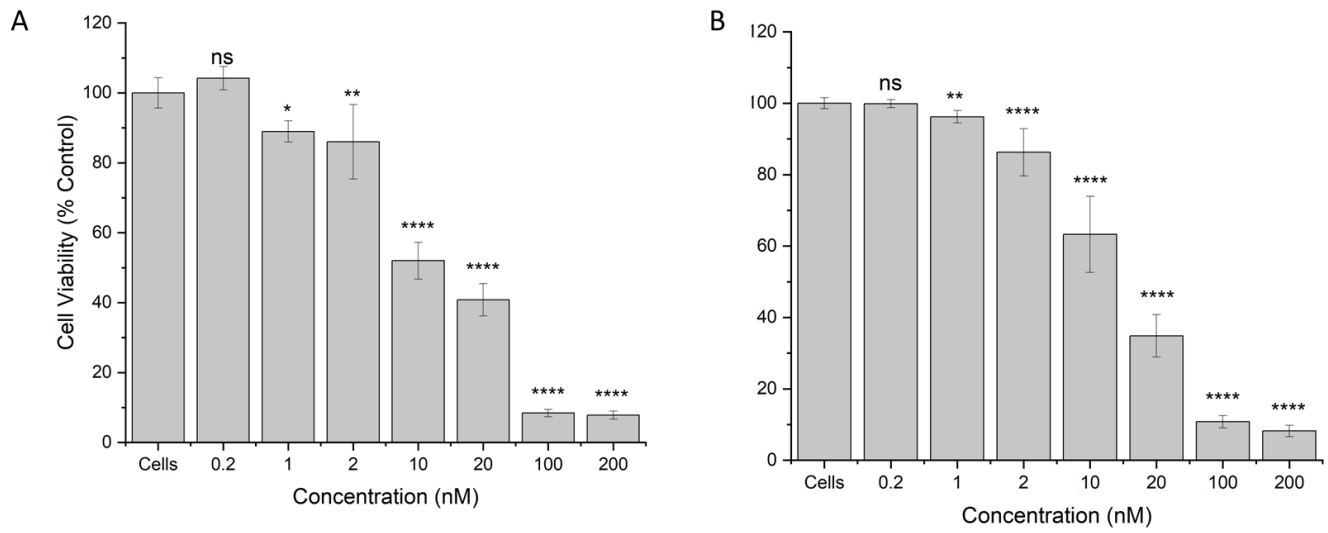


*Figure 4. 1: The effect of varying paclitaxel concentrations on the cell viability of RD cells (A) and RH30 cells (B). Error bars are representative of standard deviation of cell viability, significance was assessed as a one-way ANOVA test in comparison to the untreated cell control, labelled cells. P values are represented by; ****=p<0.001,***=p<0.005 **= 0.01, *=p<0.05, ns=p>0.05. Data shows mean +/- SD, n=3.*

The effect of Paclitaxel concentrations on RD cells showed significant cell death at concentrations greater than 1 nM, Concentrations lower than 1 nM did not cause a detrimental effect to cell viability (Figure 4.1 A). Cell death plateaued at 10 % cell viability between concentrations of 100-200 nM. The estimated EC 50 values for the effect of paclitaxel on RD cells were calculated to be 11.6 nM. [19]

RH30 cells showed a similar response to paclitaxel as RD cells showed (Figure 4.1 B). Cell viability dropped significantly at concentrations greater than 2 nM. Cell viability was further reduced, by a considerable margin between 10-20 nM, dropping below the EC50 which was estimated to be 15.6 nM.[19]

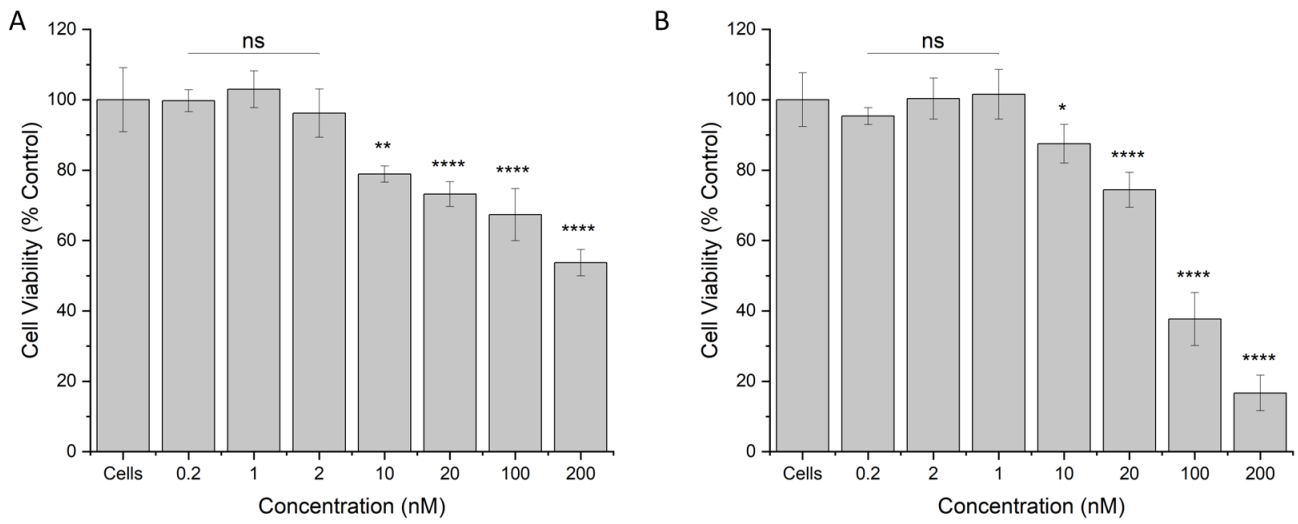


*Figure 4. 2: The effect of Vinblastine on the cell viability of U87-MG (A) and MCF-7 (B) Cells. Error bars are representative of standard deviation of cell viability, significance was assessed as a one-way ANOVA test in comparison to the untreated cell control, labelled cells. P values are represented by; ****=p<0.001,***=p<0.005 **= 0.01, *=p<0.05, ns=p>0.05. Data shows mean +/- SD, n=3.*

The effect of Vinblastine on U87-MG showed a slightly lower response rate to that seen in literature. With an EC50 value estimated at 252 nM the response still lies within expected bounds.[289] Significant cell viability reduction is observed for concentrations of 10 nM and above (Figure 4.2 A). Cell viability decreased in a linear fashion for increasing concentrations of vinblastine, with 200 nM causing an observed 46 % (+/-4.2 %) reduction in cell viability, compared to the untreated control.

Vinblastine induced a greater response in MCF-7 cell lines compared to the response in U87-MG cells for the same concentrations. Again, significant reduction in cell viability was observed at concentrations of 10 nM and greater, however a massive reduction in cell viability was observed for concentrations greater than 20 nM (Figure 4.2). Thus, the estimated EC50 value was 84.3 nM, far lower than that observed in U87-MG cells, indicating a higher sensitivity of MCF-7 cells towards vinblastine.

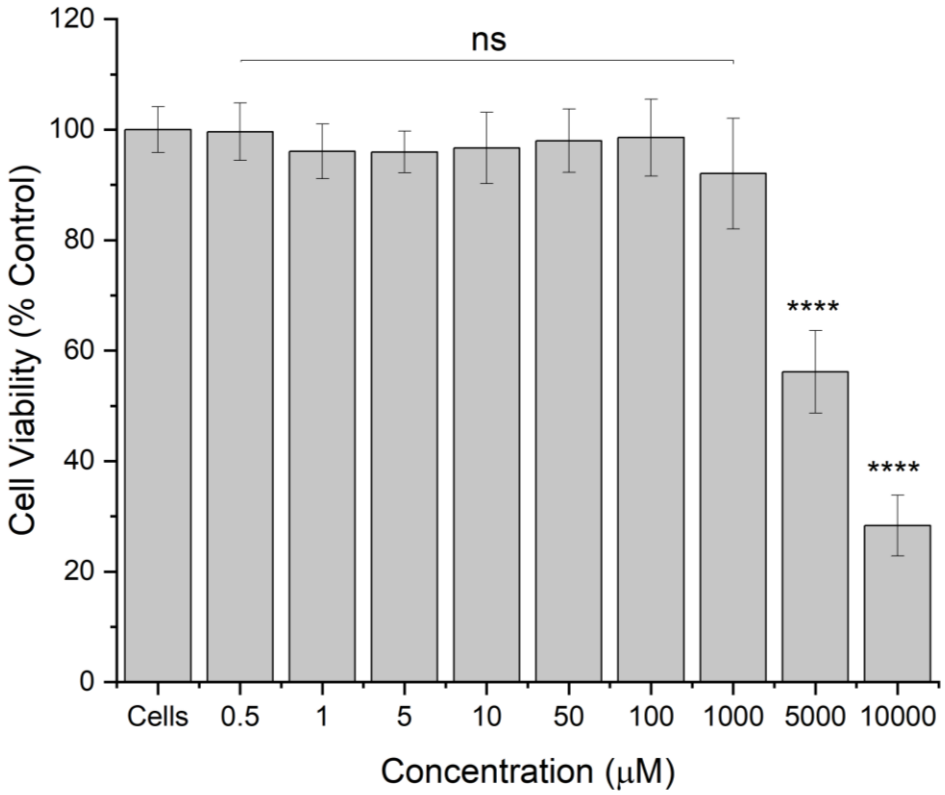


*Figure 4. 3: The effect of paracetamol on the cell viability of HEP-G2 cells. Error bars are representative of standard deviation of cell viability, significance was assessed as a one-way ANOVA test in comparison to the untreated cell control, labelled cells. P values are represented by; ****=p<0.001,***=p<0.005 **= 0.01, *=p<0.05, ns=p>0.05. Data Data shows mean +/- SD, n=3.*

HEP-G2 cells showed significant cell death at concentrations of 5000 μM (Figure 4.3). The EC50 value was estimated at 5.58 mM, which is very high in comparison to both Paclitaxel and vinblastine, but not outside of reasonable bounds. High rates of loading for paracetamol onto the nanoparticle complex are essential to achieve the high therapeutic concentrations of paracetamol.

4.3.2 Binding chemotherapy agents to bovine serum albumin

Bovine serum albumin was intended to be the carrying vehicle for chemotherapy agents. This was intended as a means of binding the drugs for delivery, to act as a carrying moiety that could be bound to the thermosensitive copolymers of the nanoparticle complex.

Paclitaxel

Due to its poor aqueous solubility paclitaxel had to be dissolved in an organic solvent before its addition to albumin. Some of the drug precipitated after mixing the two solutions of paclitaxel and ethanol. After the equilibrium solution had been stirred for the desired time the BSA was precipitated in ethanol and washed thrice with centrifugation. Precipitated BSA was then broken down in trypsin EDTA before being passed through an 8000 Da filter. The total paclitaxel was determined in solution from HPLC measurements of the degraded BSA solution, compared against a concentration gradient.

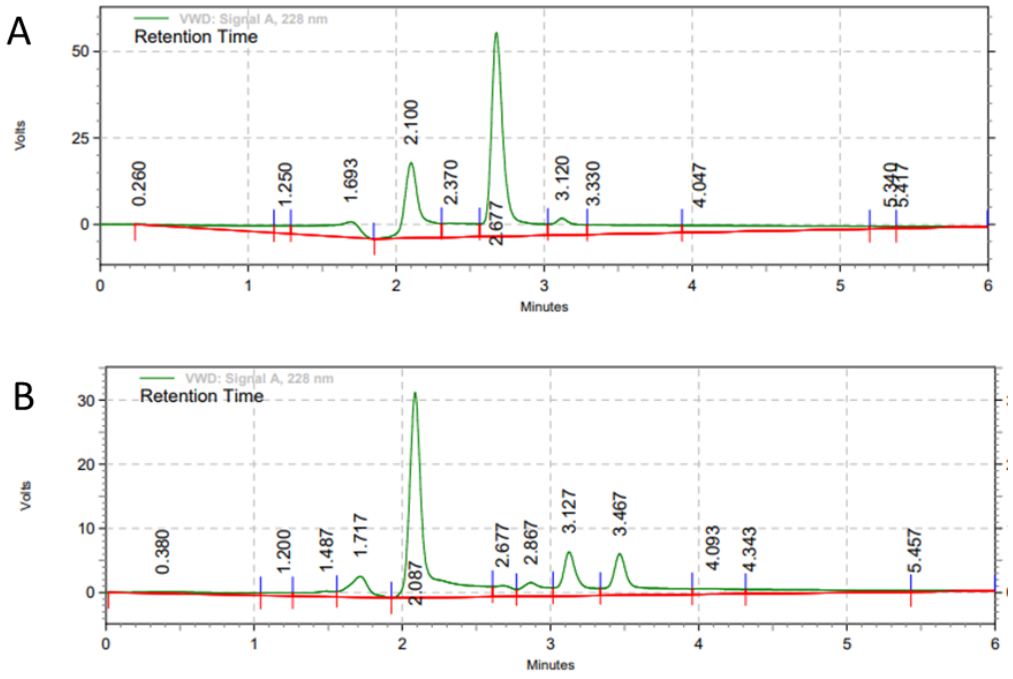


Figure 4. 4: HPLC chromatogram demonstrating the Paclitaxel detection. A is the spectrum from a 500 μ M solution of paclitaxel from the concentration gradient. B is a signal from a 0.1 mg/mL BSA-PAC sample. BSA degradation products are present from 3.12-3.6 minutes and the paclitaxel peak can be observed at 2.67 minutes. The green line represents the signal intensity received and the red line is the baseline.

The paclitaxel peaks were observed at a retention time of 2.67 minutes and were not masked by any of the breakdown products of BSA, nor the water or ethanol peaks present (Figure 4.4). Paclitaxel peaks observed in the calibration gradient, internal standard, and samples were all observed with the same shape and

retention time. By comparing the concentration of paclitaxel detected within the particles with the content of BSA in the sample, loading was calculated. It was found paclitaxel loaded to BSA at a ratio of 1.1:1 (Paclitaxel: BSA).

Vinblastine

Vinblastine was bound to BSA in the same manner as Paclitaxel. Since vinblastine is a less established and studied drug, detection needed to be optimised. First, a protocol was designed in the HPLC to ensure detection was possible. The parameters were initially based on the detection of paclitaxel, however, it was apparent trypsin used to breakdown BSA was masking the signal produced by vinblastine. The protocol adjusted and tuned until the Vinblastine signal was unmasked.

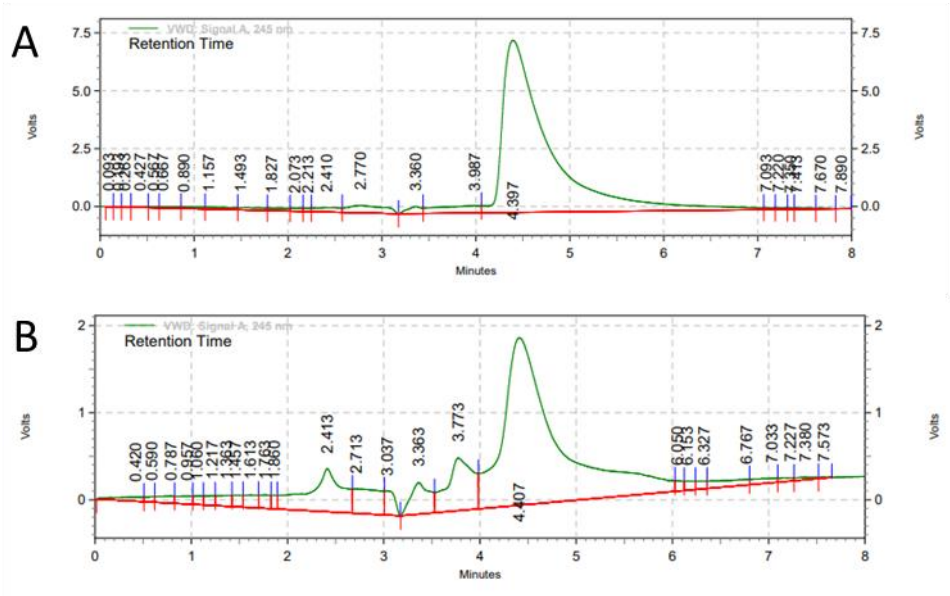


Figure 4. 5: HPLC chromatogram demonstrating vinblastine detection. A known concentration of 500 μ M (A) and a signal from a 0.1 mg/mL BSA-VIN sample (B). BSA degradation products and PBS signals are present from 2.12- 4 minutes and the vinblastine peak can be observed at 4.407 minutes. The green line represents the signal intensity received and the red line is the baseline.

Following successful detection, a concentration gradient for vinblastine was created using a 0.5 mg/mL standard as the constant between sample measurements. The detection wavelength was also adjusted to detection for the maximum absorption wavelength of vinblastine at 245 nm.

The calibration curve allowed accurate determination of the concentration obtained from attachment to BSA (Figure 4.5). 0.062 mg of Vinblastine was calculated to have come from the 1 mg BSA degraded by trypsin. This gives a loading efficiency of around 30% by mass. The molar ratio of Vinblastine to BSA was calculated as 5.1:1.

Paracetamol-BSA binding

To cause cell death in HEP-G2 cancer cell lines it was necessary to deliver paracetamol using the nanoparticle complex. To do this, it needed to be bound in some capacity to BSA. Similarly, to paracetamol and vinblastine, an equilibrium solution was formed with an excess of Paracetamol. Content immobilised was again detected by degradation with trypsin and HPLC against a concentration gradient of paracetamol (Figure 4.6).

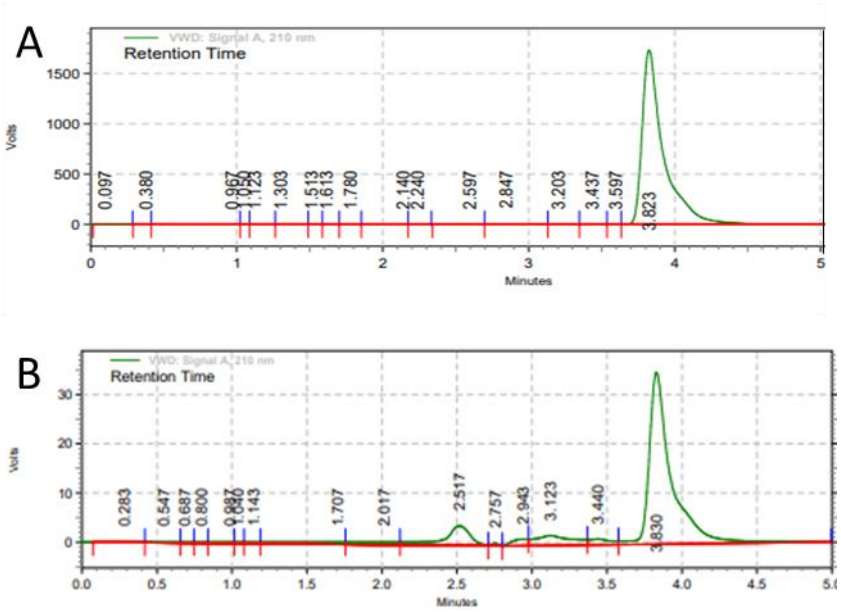


Figure 4. 6: HPLC chromatogram demonstrating paracetamol detection. A known concentration of 500 μ M (A) and a signal from a 0.1 mg/mL BSA-PARA sample (B). BSA degradation products are present from 2.4 - 3.5 minutes and the paracetamol peak can be observed at 3.8 minutes. The green line represents the signal intensity received and the red line is the baseline.

The Paracetamol content of the sample was compared to a concentration gradient of Paracetamol run alongside the sample as an internal standard.

Using the HPLC data it was calculated that in 1 mg of BSA-paracetamol complex (BSA-PARA) there is 0.08 mg of Paracetamol. The loading molar ratio of paracetamol to BSA was calculated at 35:1, much higher than paclitaxel and vinblastine in molar ratio but comparable in mass ratio.

Table 4. 1: The loading ratios of chemotherapeutic agents to BSA. Ratios are given as molecules loaded onto each BSA protein.

Compound	*Molar loading ratio to BSA*	*Loading percentage by weight*
Paclitaxel	1.1:1	5.8
Vinblastine	5.1:1	7.2

Paracetamol	35:1	7.5

Three chemotherapy agents selected for delivery to cancer cells were successfully bound to and released from (by means of degradation) bovine serum albumin as a drug carrying vehicle. Paclitaxel, vinblastine, and paracetamol show loading rates that can allow for nanoparticle assisted delivery of therapeutic concentrations (Table 2.1).

4.3.3 Immobilising BSA-Pac on synthesised copolymers

BSA protein was immobilised on the synthesised copolymer as a means of attaching the BSA to the larger nanoparticle complex. The copolymer (poly-b-(NIPAM-co-acrylamide)-b-methacrolein, synthesised with a starting ratio of 45:45:10 respectively) and protein were incubated at 4 °C for 24 h with rocking. After which the polymer BSA matrix was spun out (10000 g for 5 minutes at room temperature) and samples collected for analysis by Bradford protein assay. A "cycle" consisted of raising the polymer – BSA matrix above the LCST of the polymer and rocking for 5 mins, followed by rocking below the LCST for 5 mins and finally being precipitated out again for separation by centrifuge. The supernatant was then tested for BSA released from the polymer on each cycle. The BSA content was measured by the Bradford protein assay test and compared to a calibration curve of know protein concentration.

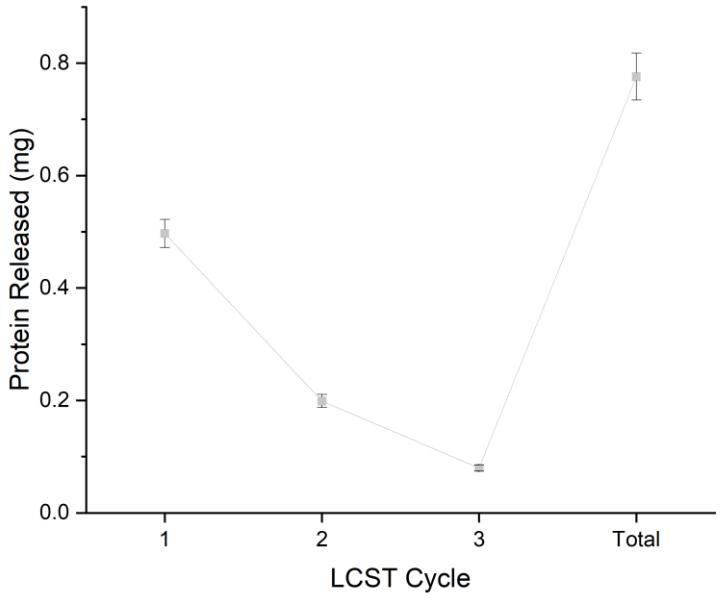


Figure 4. 7: The cycled release of BSA from the copolymer. Release is given over successive cycles of raising the solution temperature above and below the LCST of the copolymer, thus inducing a structure change and protein release. The mean +/- standard deviation is represented by the error bars, n=3.

Subsequent variation of temperature above and below the LCST showed a large degree of protein release after agitation and the induced phase change (Figure 4.7). Subsequent cycles showed the ability of the polymer to retain a fraction of the immobilised protein through several LCST phase transition cycles. No detectable protein release was detected after the third LCST cycle.

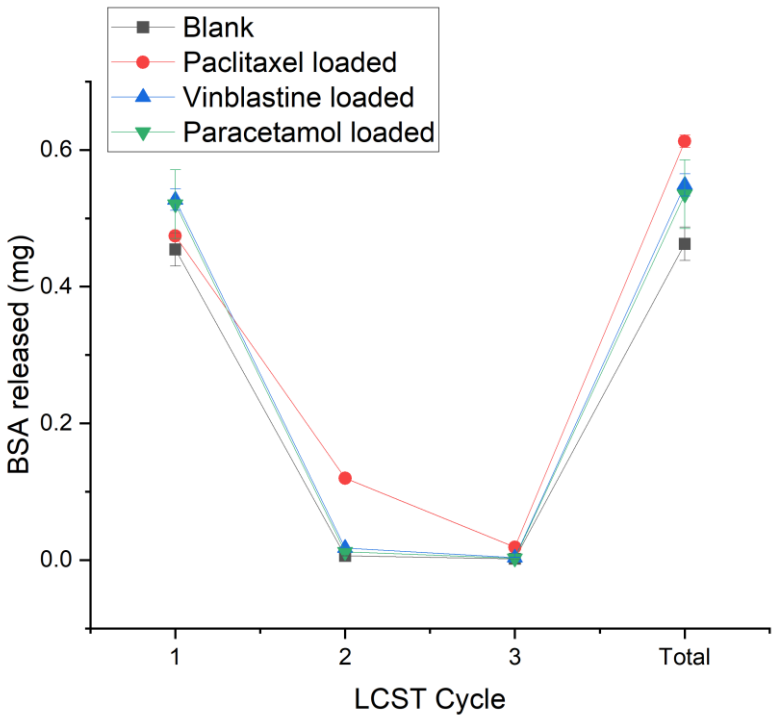


Figure 4. 8: The cycled release of BSA- drug proteins from the synthesised copolymer. Drug bearing protein release from copolymer over successive cycles of varying the temperature above and below the LCST of the synthesised copolymer. The mean +/- standard deviation is represented by the error bars, n=3.

Given the ambiguity of binding sites for the chemotherapeutic molecules, it was considered possible drug loading could affect protein immobilisation on the copolymer. Thus, protein immobilization and release were tested for types of drug loading protein, alongside unladed BSA. The experiment was run parallel to the original immobilisation test, the samples were all compared to the same concentration gradient.

No significant difference was observed in protein immobilisation and release from the copolymer depending on the specific drug bound to the immobilised protein (Figure 4.8). No change in retention, or staggered release, was observed between differing drug loaded versions of BSA.

4.4 Discussion

4.4.1 Effect of chemotherapy agents on cell lines

Cell viability changes were measured bare chemotherapy agents paclitaxel, vinblastine and Paracetamol. This was done to ensure these drugs were effective in causing cell death in the cell types present in the lab and for comparison to determine any synergistic or antagonistic effect of drug delivery by the nanoparticle complex. Five different cell lines were chosen, from a variety of different types of cancer, in order to show the versatility of the drug delivery platform created in this project.

When Paclitaxel was delivered to paediatric RD cells, the EC50 value calculated (11.6 nM) was within the range reported on other cell lines (1-50 nM) and was considered in reasonable bounds, there is no literature for direct comparison.[280] For paclitaxel delivered to RH30 cells the EC50 value is comparable to that of RD but shows a slight reduction in response to Paclitaxel. Again, when compared to literature values (1-50 nM, depending on cell type) this value is well within the reported response range.[284]

When U87-MG cells were subject to vinblastine the EC50 value calculated was very similar to that of literature (252 nM in this study, 230 nM in literature).[289] Vinblastine induced a greater response in MCF-7 cell lines compared to the response in U87-MG cells for the same concentrations, showing a slightly lower EC50 value than that observed in literature (84.3 nM in this study 130 nM in literature).[289] Although lower than literature sources, the EC50 value is within the expected range for a microtubule stabilising drug. Differences observed could be a result of the number of passages of the cell line from those tested on, to that of literature.

As a common painkiller and anti-inflammatory drug, the effect of paracetamol on the majority of mammalian cells at therapeutic dosage is negligible.[302] In liver cells however its metabolite causes significant toxicity. No response from paracetamol was observed at concentrations below 1 mM, at 1 mM a response was observed but it was not considered significant ($p>0.05$, figure 4.3). A clearly significant response was observed at 5 mM with a reduction in cell viability of 47 % (SD +/- 4 %). A further reduction in cell viability was observed from 5-10 mM, indicating a critical response dose between 1 and 5 mM paracetamol. The EC50 value was calculated at 5.58 mM, which is very high in comparison to both Paclitaxel and vinblastine, but not outside of reasonable bounds. The calculated EC50 is comparable to that seen in literature 6-7.4 mM.[303,304]

Due to the high concentration of paracetamol needed to induce a response in HEP-G2 cells, high rates of loading for paracetamol onto the nanoparticle complex are essential to achieve a therapeutic effect.

Poor lymphatic drainage of cancerous tissue and poorly formed endothelial cells in tumour blood vessels results in a greater uptake and retention of chemotherapy molecules when bound to nanoparticles.[26,305] This effect combined with nanoparticles being the ideal size range to enter mammalian cells could result in a smaller EC50 value for each of these chemotherapy agents when delivered by the nanoparticle copolymer matrix.

4.4.2 Binding chemotherapy agents to bovine serum albumin

By binding a variety of drugs to BSA as a carrying vehicle it can be shown the nanoparticle complex has the potential as a drug delivery platform to treat many different types of cancer. The efficacy of drug uptake has been improved for several compounds by delivery by a protein delivery vehicle. Docetaxel, paclitaxel, citral

and rhodamine B uptake has been increased by delivery by BSA nanoparticles.[31,306,307] The benefits of delivering potent drugs but reducing systemic side effects are not limited to a reduction in off-target effects but results in a cost reduction for the overall treatment of patients. Since efficacy is increased, drug dosages can be reduced and therefore so can cost. The similarity of BSA to HSA, as well as favourable biocompatibility and large number of non-specific binding sites make it ideal molecule for this role.

Paclitaxel has been shown to bind to sites in BSA in a variety of different studies. There are however, very few examples of binding for vinblastine and paracetamol.[34,308,309]

Paclitaxel

The loading ratio observed in the experiments was within the same range as that of earlier research, but with a 75 % reduction in contrast to high loading ratios observed, according to results from the same experiment with HSA reported in the literature.[34,282] The lower loading capacity seen in this study can be attributed to the fact BSA molecules are not formed into nanoparticles. Therefore, removing the possibility of drug entrapment within particles when they are crosslinked and reducing the total trapped drug. Protein nanoparticles were not desired in this study, due to the potential complications in loading to the larger nanoparticle copolymer complex. In addition, due to constrictions on the budget for paclitaxel purchase in this study, it was not possible to add an excess of Paclitaxel to the loading solutions, hence binding rates are not as high as reported literature. Further discussions on the nanoparticulate delivery of paclitaxel are found in the discussion in chapter 6.

Vinblastine

Although the same molar ratio of drug to BSA was used in both equilibrium solutions, vinblastine showed a higher loading efficiency than paclitaxel. Possibly due to better access to binding sites within the protein. A loading ratio of 5:1 vinblastine to BSA molecules was observed (Table 4.1). By weight the vinblastine was found to bind to BSA at a ratio of 1:13 respectively, this is around 50 % of the loading capacity seen in literature for the loading of vinblastine to BSA nanoparticles (1:6). [308] Again, the lower loading capacity of vinblastine observed in comparison to literature sources can be attributed to the fact BSA molecules are not formed into nanoparticles, and therefore molecules are not bound by crosslinking, trapping drug.

Paracetamol

Unlike vinblastine and paclitaxel, paracetamol has a small molecular weight and a small molecular volume, thus there is a much larger potential for binding sites within BSA. The size of paracetamol makes the molar ratio of loading much higher. The number of access sites paracetamol can bind with on BSA compared to larger vinblastine and paclitaxel molecules gives rise to the difference in the loading molar ratios. The OH group present on paracetamol can bond with acids or amines covalently or form association bonds via hydrogen bonding. Studies previously have indicated a higher binding constant for BSA-paracetamol at a pH higher than 7.2, hence our protocol was performed in PBS (pH 7.4). At the time of writing there have been no publications documenting the total extent of binding paracetamol to BSA molecules.[310,311] However, there has been studies that have indicated some level of interaction between HSA and paracetamol *in vivo*.[310]

A positive consequence of the toxicity of paracetamol to the liver has been the potential of using paracetamol as a chemotherapeutic agent for metastases from primary liver cancer. The mechanism of paracetamol on

liver cell metastasis is virtually identical to that of normal liver cell toxicity. The capability for a combined treatment, delivering paracetamol to metastatic tumours with the added layer of protecting healthy liver tissue with NAC has the potential to be a powerful clinical treatment.

4.4.3 Uptake and release of BSA onto the (poly-b-(NIPAM-co-acrylamide)-b-methacrolein copolymer

Owing to its large size (66,000 Da) and variety of amino acids present in its structure, BSA possess the ability to form strong association and covalent bonds with a variety of functional groups. It has been shown that BSA can bind with epoxy, acid anhydride, thiol and carbonyl groups.[52] It is important to note that this binding is often reversible in aqueous solution, thus BSA has proven to be an exceptional vehicle for the delivery of a variety of drugs.[31,119,312] BSA has been shown to become immobilised on a variety of differing polymers for various applications as discussed in section 3.4 [119]

Protein immobilisation on copolymers is expected to take place via a Schiff base linkage between amine groups present on BSA and aldehyde groups within the copolymer. Release of the protein is intended to occur during the coil to globular phase transition of the copolymer, upon reaching the LCST. The coil to globular transition squeezes the relatively large 7 nm BSA molecule, causing mechanical constriction and therefore weakening the imine bond with the copolymer, resulting in protein release.[313]

Subsequent variation of temperature above and below the LCST showed release after agitation and the induced phase change (Figure 4.7). Successive cycles showed the ability of the polymer to retain a fraction of the immobilised protein through several LCST phase transition cycles. This effect could be useful in tiered drug release in a clinical setting, as it would allow the drug to be released over a set number of pulses. If the

desired effect had been reached in a target site, then the rest of the drug can remain immobilised within the polymer, ready for release at a different cell cycle stage in order to combat the "fractional kill" effect. The term "fractional kill" refers to the poorly understood phenomena in oncology wherein one round of chemotherapy does not completely eradicate all cells within a tumour. The cell cycle specificity of chemotherapy medications is thought to be responsible for the partial death of malignancies in response to therapy.[314,315] Repeated dosages must be given because only a portion of the cells are killed with each treatment. The frequency and duration of treatments are limited by the toxicity to the patient of the drugs being administered.[316] A nanoparticle delivery method capable of releasing drug in bursts using an external stimulus could provide a means of delivering drugs in cycles, with only one admission of the treatment to the body.

There was no difference in the immobilisation and subsequent release of BSA from the copolymer when loaded with any chemotherapeutic agent (Figure 4.8). This data indicates a consistent release of protein is observed from the complex and can allow for direct calculations of total drug released, *via* protein drug loading rates.

4.5 Conclusions

In conclusion, the model chemotherapeutic agents intended for delivery by remote activation, all induce cell death in selected cell lines. The response of the cell lines to drug exposure follows literature trends.

It has been demonstrated that three different chemotherapy agents can be bound to Bovine serum albumin as a vehicle for drug delivery. Paclitaxel has been bound for delivery to RD and RH30 cells, and to act as a model drug to demonstrate the principles of the project. Vinblastine has been bound to act as a second

model drug for delivery to cell lines resistant to Paclitaxel, such as MCF-7 and U87-MG cells. Paracetamol has been bound to BSA with the specific intentions of delivery to liver cancer cell metastasis and as a demonstration of small molecule delivery by this platform technology.

BSA can be released from the polymer by a change in temperature, in principle this can be utilised in many applications as an activation to release drugs with a stimulus. Moreover, the copolymer showed retention and then release of BSA over successive cycles, allowing for the potential of controlled cycles of release. Protein release was not affected by loading of drugs onto said protein, neither was the total uptake of protein. Indicating drug loading and binding with aldehyde groups on the copolymer occur at different sites within the protein.

Chapter 5: Nanoparticle-polymer complex assembly

5.1 Introduction

To improve the therapeutic index of chemotherapy treatments greater control over the site of action is needed. This can be partially achieved through the use of nanoparticle delivery systems, however, further refinement can be attained by controlled release. Nanoparticle delivery systems are an ideal size for extravasation from the vascular system into tissues, and movement across cell membranes into the cytoplasm. Active targeting directs a carrier to a particular organ, cell, or organelle by changing its natural distribution patterns. The effectiveness of this procedure is reliant on the blood flow and location of the first medication delivery. Drug circulation times may also be greatly increased by attachment to nanoparticles or encapsulation, improving the drug half-life.[32] The size, shape, and charge of nanoparticles will also affect circulation times and uptake rates by cells.[317,318]

Magnetite particles are easily functionalised with a variety of fluorophores, polymers, targeting ligands, peptides, and even smaller nanoparticles *via* chemical modification, surface coating or grafting.[15,319] Dispersants adsorbed on NP surfaces allow for functionalization of NPs, an option that becomes increasingly important for many applications especially in the biomedical field. Potential targeting moieties are antibodies, peptides, aptamers, DNA and RNA sequences. [15,212,319]

Magnetic nanoparticles are able to convert electromagnetic energy into heat. This is typically accomplished by the hysteresis loop mechanism in AMFs (carried by radio waves) due to Neel relaxation in high frequency fields. Magnetic nanoparticles show potential in oncology for their use in induced magnetic hyperthermia,

localized drug delivery by external magnetic fields, and also as contrast agents in magnetic resonance imaging (MRI).[15] The most frequently used materials are magnetite (Fe_3O_4) and maghemite (g-Fe_2O_3). The main advantage in using an alternating magnetic field (radio waves) as a stimulus lies in its non-ionizing and specific nature.

Controlled release may be achieved *via* intrinsic or extrinsic mechanisms. Intrinsic release mechanisms rely on changes in the cell chemistry as a consequence of altered cancer cell metabolism.[158] Extrinsic activation permits controlled release from a source outside of the cell. Herein, we exploit radio waves (alternating magnetic field; AMF) for extrinsic activation due to their inert nature and high penetration depth. Since the majority of tissues in the body have no absorption in the radio wave spectrum, there is no possibility of off-target effects as seen with shorter wavelengths in treatment such as radiotherapy and PDT.[15]

5.2 Materials and methods

5.2.1 Superparamagnetic iron oxide nanoparticle poly – (methacrolein-b-(NIPAM-co-acrylamide) synthesis

DDMAT stabilised SPIONs (DD-ION) were synthesised as described in section 2.2.

Copolymer synthesis was performed on the surface of the DD-ION particles. DD-ION (125 mg) was dissolved in 5 mL dimethyl fumarate under a nitrogen atmosphere. Methacrolein (79 μL, 1 mM, final concentration) was added to the solution followed by 1.17 mg Azobisisobutyronitrile (AIBN), still under a nitrogen atmosphere. The reaction flask was then degassed by three freeze-thaw pump cycles and heated to 65° C and stirred for 2 weeks. Following this, N-isopropyl acrylamide (4.5 mM, 508 mg, final concentration) and acrylamide (4.5 mM, 380 mg, final concentration) were added to the reaction mixture.

After a further two days the solution was diluted with 35 mL Tetrahydrofuran, precipitated in 40 mL diethyl ether (All Sigma-Aldrich Merck Life Science UK Limited, Gillingham, UK) and removed by magnetic decantation, this was repeated three times. Magnetic decantation involved the application of a permanent magnet to the bottom of a glass beaker to retain particles while the solvent is removed.

Drug bearing protein immobilisation on the NCC

Drug binding to BSA was performed before immobilisation on the nanoparticle-polymer complex to ensure efficient uptake. The BSA drug complexes were synthesised and isolated as described in section 4.2.

NCC-drug synthesis was as follows: An equilibrium solution was formed with 16 mg of the nanoparticle-copolymer complex, and 6 mg of BSA-Drug complex in 5 mL PBS. The solution was cooled to 4°C and stirred for 24 hours.

Finally, 50 mg of fluorescein isothiocyanate (FITC; Sigma-Aldrich, Gillingham, UK) was added, and the solution stirred at 4°C for another 24 hours. FITC was added to act as a fluorescent marker on the nanoparticle complex. Following this the particles were precipitated in ethanol and extracted by magnetic decantation before redispersion in water. This wash step was repeated three times before the particles were lyophilised.

Exchange of bound ligands/polymer from iron oxide nanoparticles for analysis

In order to analyse grafted polymers, 50 mg of polymer grafted iron oxide nanoparticles were dissolved in 10 mL of glacial acetic acid and 10 mL of chloroform. The solution was stirred at room temperature for 24 h. The precipitants were removed by centrifugation (5 minutes at 10000 g) and magnetic decantation and

discarded, the clear solution remaining was removed and evaporated to dryness. This was then washed with THF and dried once more before being ground into a powder for analysis.

Protein immobilisation and release from the NCC

To measure protein released from the synthesised NCC, an equilibrium solution was formed with 16 mg of NCC and 6 mg of BSA dissolved in 5 mL PBS. The solution was cooled to 4 °C and stirred for 24 hours. After this, solutions were raised above the LCST of the copolymer and precipitants were removed by centrifugation at 10,000 g for 5 minutes and washed three times with PBS. To measure the immobilised BSA the NCC was stirred for 5 minutes below the LCST in 1 mL PBS, then stirred for 5 minutes above the LCST, and finally precipitated out and removed by magnetic decantation. The supernatant was tested for protein content by a standard Bradford protein assay (Chapter 4.2). This process was repeated seven times to ensure maximum detection of immobilised protein.

Sonication of NCC solutions

For sonication of samples a 35 W, 44 kHz, Grant Ultrasonic 1L Bath sonicator (B8R05650) was used. The samples were placed in a holder within the bath to prevent direct contact with the walls of the sonicator. Sonication is performed at room temperature. The water temperature is maintained during sonication and the initial water level is kept consistent for all samples.

Dynamic light scattering LCST measurement of the NCC

The hydrodynamic diameter of the NCC was measured using a Malvern instruments, Zetasizer Nano. Samples were run in a Disposable Folding Capillary Cuvette (DTS1070). To determine the hydrodynamic diameter particles were solubilised in PBS buffer at a concentration of 0.1 mg / mL (pH 7.4) prior to the

measurement. Particle solutions were put through a 0.6-micron filter and bath sonicated at room temperature for 90 seconds before testing. Samples were not sonicated or run through a filter between time points on the stability experiment. 12 runs were read before each calculation of hydrodynamic diameter and each sample was run three times. Intensity analysis was used for hydrodynamic diameter calculations. To measure the LCST of the nanoparticle complex, the temperature of the sample was increased from 25-65 °C in order to observe any changes in diameter dependent on temperature. Samples were bath sonicated for 5 minutes at room temperature between measurements.

5.2.2 Induction heating of the NCC

To activate the complex and stimulate protein release, the same protocol for induction heating was used as described in section 2.2. SAR calculations were also carried out in the same method as described in chapter 2.

5.2.3 Analysis techniques

Zetapotential and TEM were carried as described in Chapter 2.2.

GPC, FT-IR, DSC and NMR spectroscopy was carried out as described in Chapter 3.2.

Scanning electron microscopy

Secondary scatter electron images of the specimens were taken using a Carl Zeiss Evo LS15 VP-Scanning Electron Microscope (Zeiss, Jena, Germany). The particles were suspended in ethanol and sonicated for 2 min. Sample (50 μL) was dropped onto separated carbon adhesive discs (Agar Scientific, Standsted, UK) on short pin specimen stubs. After evaporation of the solvent the sample was dry-cast on the sticker. All

specimens were then sputter-coated with 3 nm Pd – Au (under high vacuum in Argon, coat for 60 s at 20 mA) on a Quorum® SC7620 sputter coater before the testing. Images were taken using SmartSEM interface (Zeiss®, Jena, Germany)

Fluorescence spectroscopy

Fluorescence spectroscopy was performed on a Cary Eclipse fluorescence spectrometer, Ex. 495 nm, Em. 500-700 nm (2.5 nm slits) at 25˚C(Agilent technologies, 5301 Stevens Creek Blvd. Santa Clara, CA 95051 United States).

Visible and fluorescent cell imaging

Visible images of cells were taken using a 100x magnification on a Motic 101M microscope with a Moticam 2500 camera and MHG 100B laser [Motic, Xiamen, China]. Fluorescent images were taken in the dark on the same device under a 495 nm light from a mercury lamp.

5.3 Results

5.3.1 Poly-N-isopropylacrylamide stabilised iron oxide nanoparticles

As an initial proof of concept for the formation of a nanoparticle copolymer complex and as means of contrast and comparison, PNIPAM stabilised SPIONs were synthesised. DDMAT stabilised nanoparticles were used as the chain transfer agents in RAFT polymerisation. This polymerisation was done in tandem with a reaction using free DDMAT in place of DDMAT ION.

The polymerisation was confirmed by the appearance of the polymer precipitate when the reaction mixture was poured into cold diethyl ether. The powders isolated from the reaction were white due to the free

polymer, and light brown due to the ION grafted polymer. Interestingly the ION-PNIPAM achieved a similar yield (84.2 % (+/- 6.6 %)) to that of free PNIPAM and therefore a similar monomer conversion. This suggests that the amount of DDMAT bound to the surface of SPIONs was similar to that which was freely added. However, after magnetic decantation and subsequent washing cycles, the weight of the product decreased by just under a quarter of initial weight. This indicates that a proportion of the product was unbound polymer chains.

The FT-IR spectrum of the PNIPAM synthesised on the surface of SPIONS (ION-PN) confirmed the identity of the product (Appendix). The key feature is the identical spectra between bound and unbound PNIPAM, owing to the fact Fe_3O_4 that shows no IR absorption in this range. This, coupled with the very similar monomer conversion rate of the two reactions, indicated that the synthesis of both free and SPION bound PNIPAM have occurred synonymously.

The LCST for bound polymer was measured at 30 °C using a thermometer and optical means, which is a little lower than that of free PNIPAM. This observation was confirmed by dynamic light scattering measurements. This is likely due to the hydrophobic surface of the ION and the close proximity of polymer chains to one another. Reducing the entropy change upon the phase change and subsequent release of water and hence lowering the LCST (Equation 3.1).

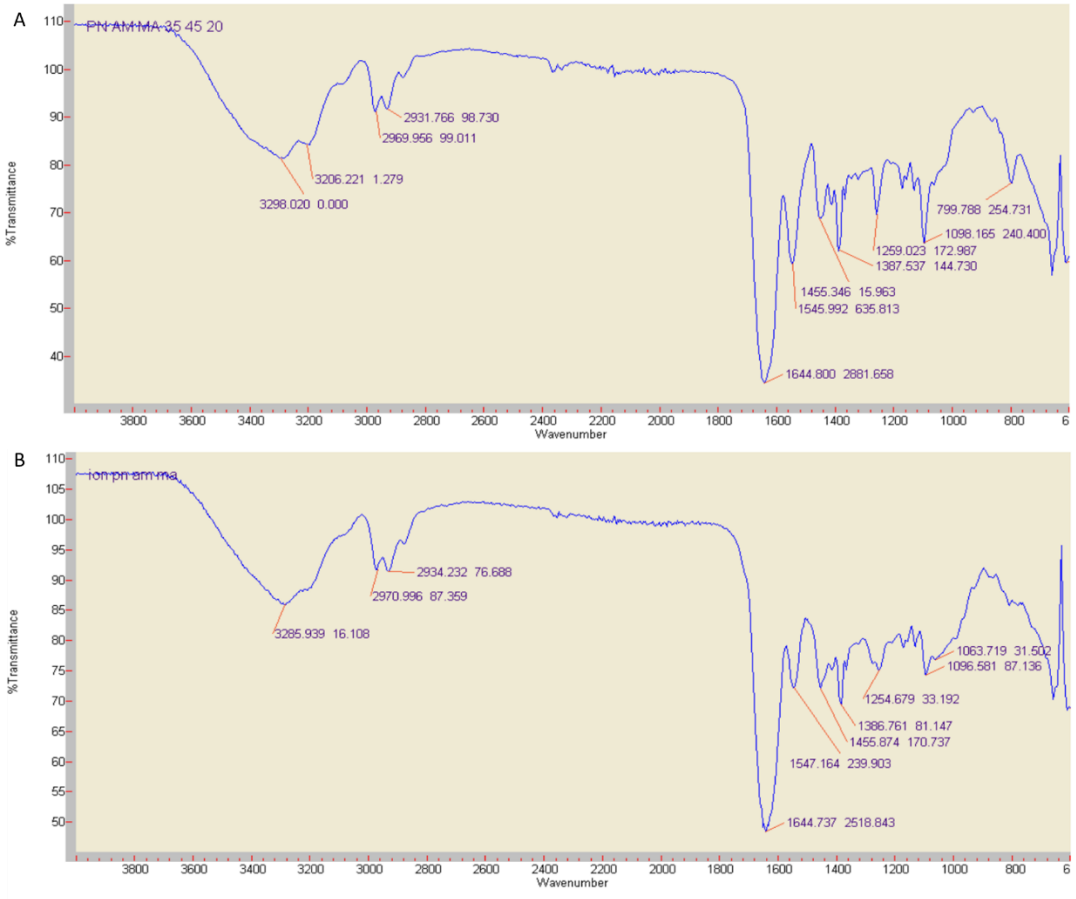
5.3.2 Nanoparticle copolymer complex synthesis and analysis

With the proof of principle of SPION bound polymers confirmed, an initial particle bound copolymer was synthesised. The SPION bound synthesis of Poly－(methacrolein-b-(NIPAM-co-acrylamide) was

undertaken in the same manner as unbound copolymers (Chapter 3) with SPION bound DDMAT acting as the chain transfer agent in place of free DDMAT.

The methacrolein in this reaction was added initially without co-monomers and allowed to react for two weeks before NIPAM and acrylamide were subsequently added. This was done with the intention of creating distinct block regions within the copolymer. The block structure is a key component of the larger nanoparticle-copolymer complex structure, where the hydrophobic methacrolein core is synthesised on the inner shell of the copolymer. This protects the immobilised drug bearing proteins and ensures the outer layer of the complex is hydrophilic and biocompatible.

Successful polymerisation was confirmed by the appearance of a dark brown precipitate upon mixing the reaction solution with diethyl ether. After washing and magnetic decantation, the yield of the reaction was found to be 37.4 % (+/-7.9 %). The NCC was readily soluble in water and PBS at room temperature and highly magnetic, even when in solution. As with unbound polymers, FT-IR was initially used to identify the copolymer (Figure 5.1 B).



C

Wavenumber (cm^{-1})	Functional group
3298 (Very broad)	N-H (Amide)
2975-2850	C-H
1644 (Broad)	C=O (Amide, aldehyde)
1545	C=O (Amide)
2360-2250	C-H
1460-1350 (Broad)	C-H

D

Wavenumber (cm^{-1})	Functional group
3285 (Very broad)	N-H (Amide)
2975-2850	C-H
1644 (Broad)	C=O (Amide, aldehyde)
1547	C=O (Amide)
2360-2250	C-H
1460-1350 (Broad)	C-H

Figure 5. 1: Spectroscopy of SPION synthesised polymers. FT -IR of copolymerised NIPAM, acrylamide and methacrolein in a molar ratio of 45:45:10 synthesised in free solution (A), and the equivalent polymer synthesised on the surface of SPIONs (B). The assigned functional groups from the FT-IR spectrum of the freely synthesised copolymer PNIPAM-co-acrylamide -co- methacrolein (C), and the equivalent copolymer synthesised on the surface of SPIONs (D).

The FT-IR spectra of the SPION synthesised copolymer exhibits several main absorption features confirming the identity of the product (Figure 5.1 B, D).[320] The 3298 cm^{-1} signal corresponds to the medium N-H stretching aliphatic primary amide of NIPAM, and hydrogen bonding broadens the peak. A signal at 3206 cm^{-1} signal corresponds to the medium N-H stretching aliphatic primary amine of the acrylamide component, and again hydrogen bonding broadens the peak. The signal present at 2969-2931 cm^{-1}

corresponds to the medium two C-H stretching alkane environments, polymer backbone and methyl groups. The 2830-2695 cm^{-1} signal corresponds to the medium C-H stretching aldehyde of methacrolein component. The 1644 cm^{-1} signal corresponds to the strong C=O stretching secondary amide both acrylamide and NIPAM masking C=O of methacrolein. Lastly the C-H bending 1390-1380 cm^{-1} signal corresponds to the methacrolein aldehyde. The FT-IR spectra of the assembled complex showed data consistent with the free polymer, indicating no difference in the copolymer formed in free solution or on the surface of SPIONs.

The zeta potential of the NCC was determined to indicate the charge, if any of the stabilising copolymer and provide information of the environment of the particles in aqueous solution. Zeta potential data showed the complex had a charge of -4.12 mV (SD $\pm$ 4.7 mV) (Figure 5.2 C). This is expected as a result of the outer shell of the copolymer comprising amide bearing monomers.

In order to study the NMR spectra of the copolymer synthesised on the surface of SPION cores, the copolymers must first have been removed by a ligand exchange reaction, to prevent SPIONs from affecting the spectrometer reading.[61] This undoubtably reduces the purity of the sample and makes the NMR spectra less clear and brings more noise.

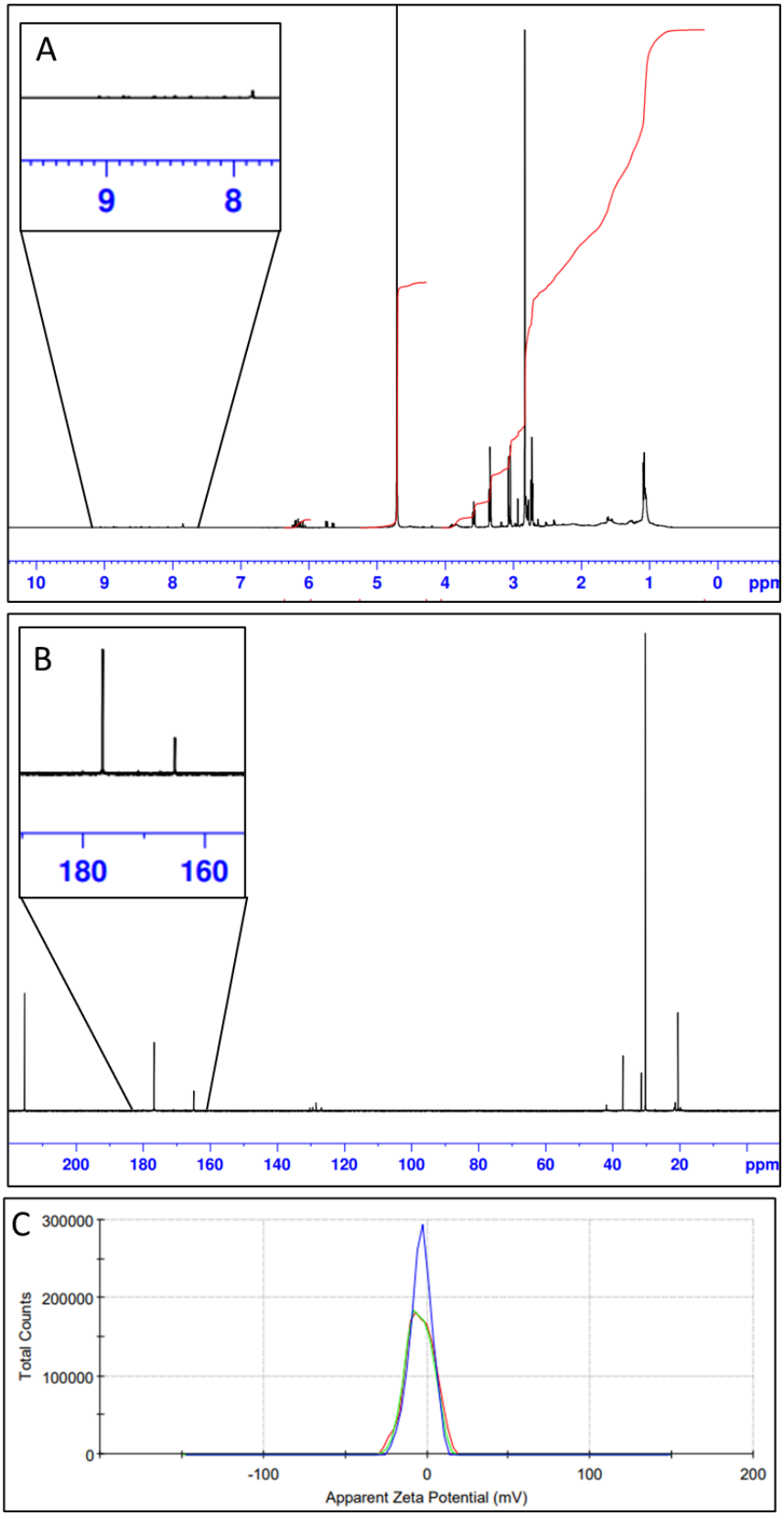


Figure 5. 2: The spectroscopic analysis of the NCC. (A) shows the ^{1}H NMR spectrum of copolymerised NIPAM-Acrylamide-Methacrolein. The inset highlights several small peaks present between 7.5-8.5 ppm indicating the presence of several amide proton environments. (B) shows the ^{13}C NMR spectrum of copolymerised NIPAM-Acrylamide-Methacrolein, the inset highlights the peaks between 160-180 ppm, indicating the presence of several

amide carbon environments. The samples were run in deuterium oxide as a solvent. Full scale spectrums and assignments can be found in the appendix in figure A11. (C) shows the zeta potential of NCC over three repeat measurements, each measurement was conducted by 100 scans of the sample.

The NMR data obtained from the new polymer supports the creation of a copolymer with the intended structure grown on the surface of SPIONs (Figures 5.2 A and B, appendix A11). The predicted data from chemistry software matches with the observed ^{1}H and ^{13}C spectrums. The only discrepancy being the N-H peak which is variable in the observed spectrum due to the repeating structure being variable and the lack of the aldehyde proton (Figure 5.3 A, appendix A11 A). The lack of the observation of an aldehyde proton can be explained by the low content of monomer in the product and the low signal the functional group provides. The H^{1} NMR spectrum was run on a low concentration sample, with a greater concentration the aldehyde proton would appear. Again, the inclusion of several different environments between δ 6.5-8 ppm suggest the presence of more than one amide molecular environment within the copolymer. Thus, acrylamide and NIPAM are present in several different environments.

The ^{13}C spectrum observed from the copolymer lined up with the predicted spectrum and the spectrum observed for the free copolymer (Figure 5.2 B, appendix A11 B). The peaks observed around 130 ppm are unreacted alkenes. The signals from 160-180 ppm again predicted the presence of several amide environments, reinforcing what was observed in the H^{1} spectrum. The signal present at 216 ppm represents the aldehyde carbon present in the copolymer, confirming the presence of methacrolein. The signals from 50-55 ppm are a signal from the alkane backbone of the polymer (Figure 5.2 B appendix A11 B). The higher concentration of copolymer used to observe the ^{13}C NMR gave rise to a cleaner spectrum with clear indications of constituent monomers within the synthesised product.

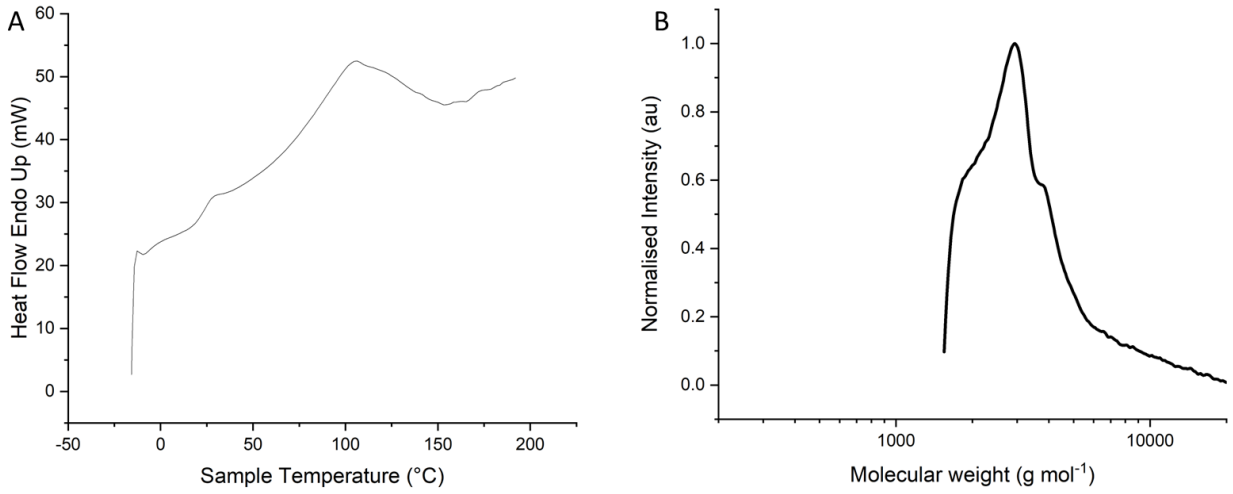


Figure 5. 3: Thermodynamic analysis of the NCC. (A) shows the DSC curve of 45:45:10 copolymer of NIPAM, Acrolein and acrylamide respectively synthesised on the surface of SPIONs. The nanoparticle copolymer complex was run without any copolymer removal. Endothermic events are represented by peaks in the graph, therefore exothermic events a trough. For a constant temperature increase of the sample with no thermodynamic events, the DSC curve would be a flat line. (B) is GPC analysis showing the molecular weight distribution of NIPAM-Acrylamide-Methacrolein copolymer synthesised on the surface of SPIONs at a starting molar ratio of 45:45:10 respectively. Molecular weight intensity is normalised to the logarithm of the peak maxima intensity. The x-axis scale is logarithmic.

Gel permeation chromatography was again used to determine the extent of polymerisation for the designed copolymer synthesised on the surface of SPIONs (Figure 5.3 B). After removal from the nanoparticle copolymer complex by ligand exchange, the samples were analysed akin to freely synthesised copolymer.

Table 5. 1: Calculated dispersity and molecular values for synthesised NIPAM-Acrylamide-Methacrolein copolymer synthesised at a starting molar ratio of 45:45:10 respectively on the surface of SPION, where Mp is the molecular weight of the peak maxima, polydispersity (PD), molecular weight (Mn), the weight average molecular weight (Mw), size average molecular weight (Mz), and the viscosity molecular weight (Mv).

Mp (g/mol)	Mn (g/mol)	Mw (g/mol)	Mz (g/mol)	Mz+1 (g/mol)	Mv (g/mol)	PD
2944	3120	4502	7646	11958	7058	1.442949

An average molecular weight of 4502 g mol^{-1} was determined and the PDI was found to be 1.41. Using weight average molecular weight as chain mass, and assigning the molecular weight occupied by each monomer proportionally by the reactant molar ratio, the number of repeat units of each monomer was calculated. The

number of calculate repeat units within the SPION synthesised copolymer was 17 NIPAM units, 24 acrylamide repeat units and 6 methacrolein repeat units.

Using the mass obtained from synthesis of the NCC, the starting mass of DD-ION, and the molecular weight of the copolymer from GPC measurements, the number of copolymer chains per nanoparticle was calculated. It was found the number of chains was estimated to be 88 copolymer chains per magnetite core. However, this calculation assumes all SPION cores are extracted following synthesis, all copolymer chains show equal distribution across nanoparticles, and all copolymer chains are bound to SPION cores.

Differential scanning calorimetry (DSC) was run on the entirety of the NCC to gauge and quantify thermodynamic properties, most notably the phase transition temperature (Figure 5.3 A). This is not the same as the solution phase transition temperature since DSC samples must be run dry. Features include melting and decomposition events. This data is useful to distinguish the SPION synthesised copolymer from PNIPAM and from that of the free copolymer thermodynamically.

In the NCC, a glass transition occurs at 25.86 ˚ C with a ΔCp of 0.173 J/g˚C (Figure 5.6). This could indicate an endothermic phase change, possibly the unravelling of polymer chains in the coil state. The melting point peak was observed at 104.65 ˚C, the deviation from the melting point of PNIPAM is due to different intermolecular forces between polymers, a result of the inclusion of acrylamide and methacrolein. The difference in the molecular weight of the NCC also contributes to the melting point difference (Figure 5.3B). The DSC data highlights important thermodynamic differences between NCC and the freely synthesised copolymer.

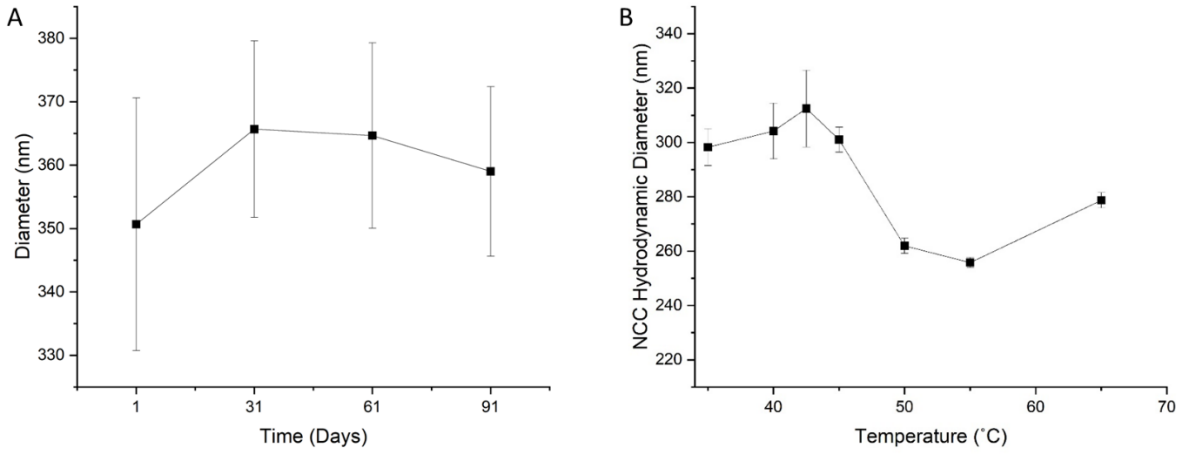


Figure 5. 4: Hydrodynamic diameter measurements of the NCC. (A) shows the stability of the NCC in buffer conditions. The hydrodynamic diameter of the NCC measured in PBS at 25 °C over a time period of 90 days. (B) shows the temperature dependent hydrodynamic diameter of NCC, as measured by dynamic light scattering. Swelling of the complex is observed until the LCST of 42.5°C is reached, at which the hydrodynamic diameter decreases. The error bars represent mean standard deviation, n=3.

The hydrodynamic diameter of the NCC was determined by dynamic light scattering. The hydrodynamic diameter of the nanoparticle-copolymer complex was measured at 297 nm (± 42 nm) (PDI = 0.161) at 37.5 °C (Figure 5.4 B). The intensity peak of this measurement indicated there was very little aggregation in samples in aqueous solution at 0.1 mg/mL.

The stability of the nanoparticle copolymer complex was tested over 90 days while stirring at 37.5 °C in PBS (Figure 5.4 A). There was no deviation in hydrodynamic diameter over this time, indicating the stability of complex in buffer conditions over a sustained period of time.

Electron microscopy was used to further study the morphology of the magnetic core and the larger NCC structure. Both SEM and TEM were employed to this end. TEM to study the effect, if any, copolymer synthesis had on the SPION core and SEM to study the state of the larger complex in dry conditions (Figure 5.5).

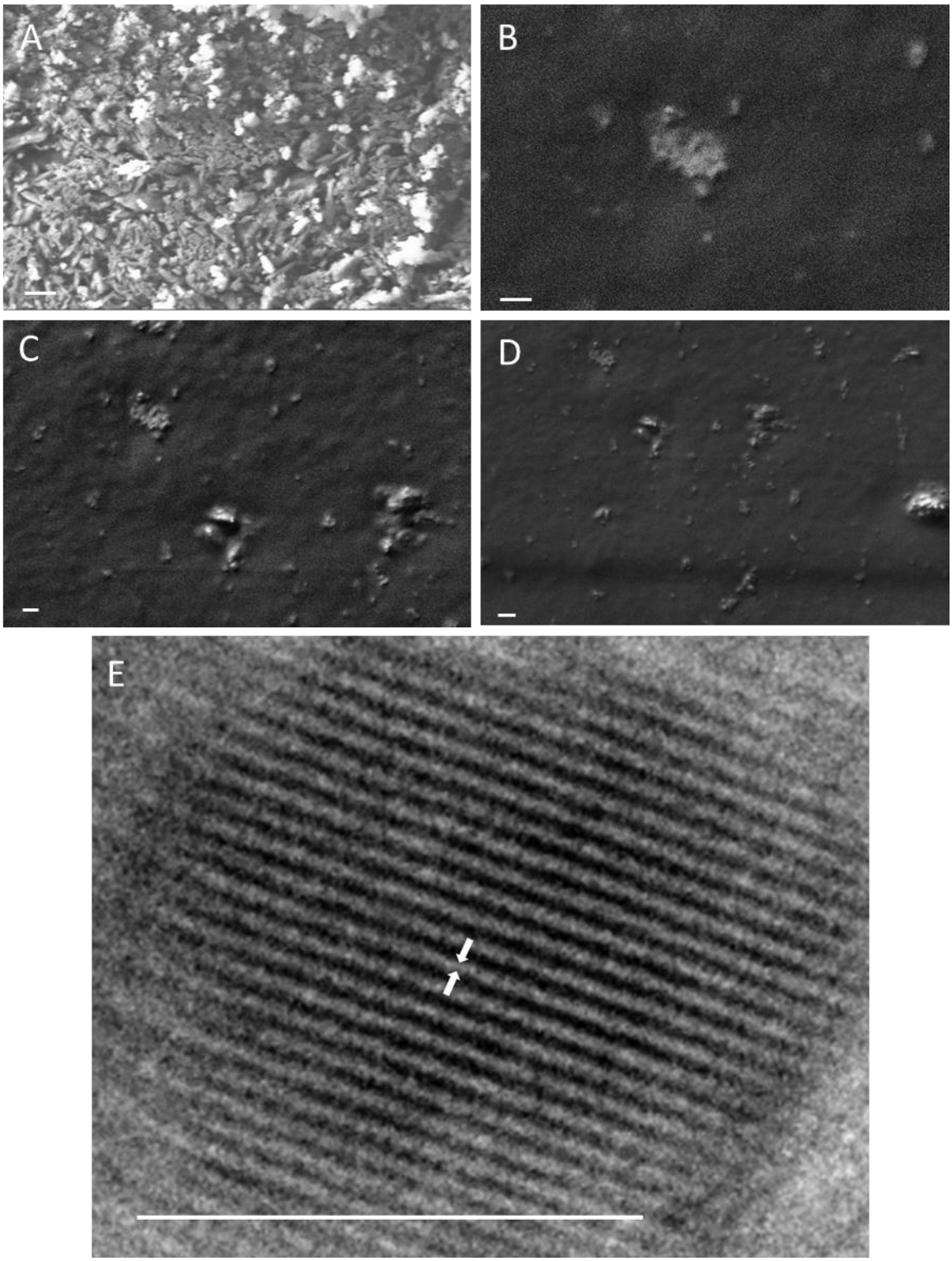


Figure 5. 5: Electron microscopy images of the NCC particles splutter coated in a gold-palladium alloy. Image A shows an SEM image after the powder deposition of particles at 6000x magnification, image B shows another SEM image of particles following solution deposition at 10,000 x magnification, and images C and D show further images at 5000x magnification. The scale bar is 2 μ m. E shows a TEM image of spherical SPION core indicating the unit cell spacing. The scale bar is 5 nm and the arrows indicate a spacing of 4.1 Angstroms measuring half the unit cell length.

Figure 5.8 E shows a TEM image of the SPION core within the polymer complex. The single crystalline nature of the SPION core is visible, showing an average overall diameter of 7.4 nm (SD+/-1.8 nm, n=30). The unit cell spacing of the inverse spinel structure of magnetite is visible. The white arrows indicate the equivalent of half a unit cell length.[101] The single crystal nature of the SPION core is clearly visible indicating a single magnetic domain is present, thus induction heating efficiency should be maximised.

During SEM imaging particulates were observed and a mean diameter of 257 nm (SD +/- 74 nm, n=30) was observed, consistent with hydrodynamic diameter analysis in the collapsed NCC state (Figure 5.4 B). The morphology of the particulates was spherical in nature although often distorted. These observations support the idea of the synthesised polymer forming a shell around the nanoparticle core while in a solid dry state. It is worth noting in the analysis of these SEM images that these are particles dispersed by powder/solution evaporation and then splutter coated, therefore the morphology is distorted by this process. The discrepancies in size and shape are expected as a result of the changes in the molecular weight of polymer chains formed and the number of anchored polymer chains to each particle.

The LCST of the NCC was determined by monitoring the hydrodynamic diameter of the complex in real time while the temperature was increased. The structure change was examined using variable temperature dynamic light scattering (Figure 5.4 B). The demonstration of a physical size change was a good indication of the potential to use the phase change to act as a forced release mechanism for bound carrier proteins.

As with the freely synthesised copolymer, the LCST of the NCC was adjusted by varying the constituent molar ratios of the monomers present during synthesis (Table 5.2).

Table 5. 2: Effect on the LCST of the synthesised NCC with varying content of NIPAM, acrylamide and methacrolein in the starting reagents.

N-isopropylacylamide (%)	*Acrylamide (%)*	*Methacrolein(%)*	*LCST/Release temp (˚C)*
50	30	20	27
40	40	20	36
35	45	20	48
45	45	10	40-42.5

An LCST of 42.5˚C was achieved when the NCC was synthesised with a starting reactant ration of 45:45:10 NIPAM, acrylamide, methacrolein, respectively (Table 5.2). This puts the structure change in the ideal temperature range between normal human body temperature and hyperthermic temperatures.

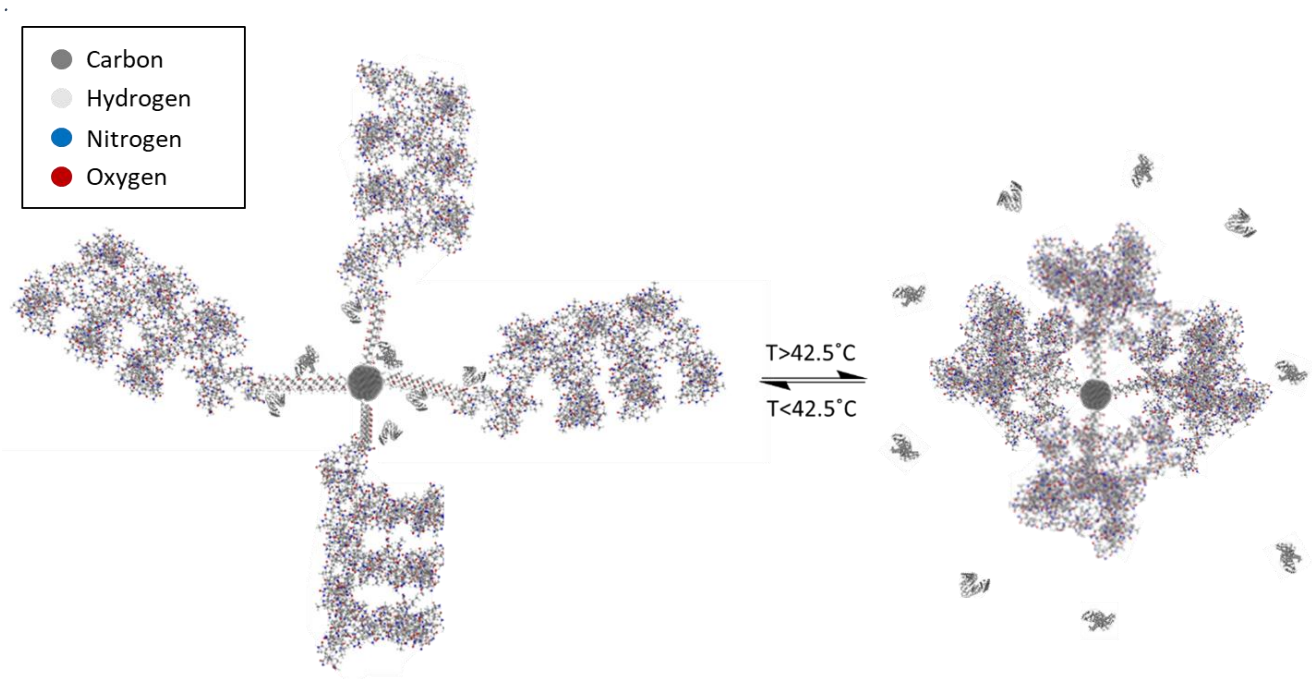


Figure 5. 6: Schematic diagram illustrating the physiological mechanism of protein-bearing drug release from the NCC upon reaching the LCST. A visualisation of the activation of the complex upon heating causing the collapse of grafted polymer chains and the subsequent release of bound proteins.

The nanoparticle copolymer complex (NCC; Figure 5.6) was designed to perform as an activatable carrying moiety for a variety of chemotherapeutic agents. Varying the ratio of monomers in the designed copolymer

yields a SPION bound polymer capable of undergoing a phase transition at the desired temperature (Table 5.2). It was observed that accompanying the phase change of the complex is a massive increase in magnetic flocculation in solution (Figure 5.7 A and B).

When dispersed in water at room temperature the NCC is stable for greater than 24 h, even after settling on the bottom the particles can be solubilized with the slightest of agitation. When placed next to a magnet, particles remain in solution while below the LCST (Figure 5.7 A). However, when heated above the LCST the particles are drawn to a magnet immediately, within 30 seconds of an applied magnetic field the particles accumulate in the direction of the field, leaving only negligible particles in solution because of Brownian motion (Figure 5.7 B). This property is a side effect of the functionality of the copolymer designed in the project, which although not strictly relevant to this project, this property could have many applications in industrial systems.

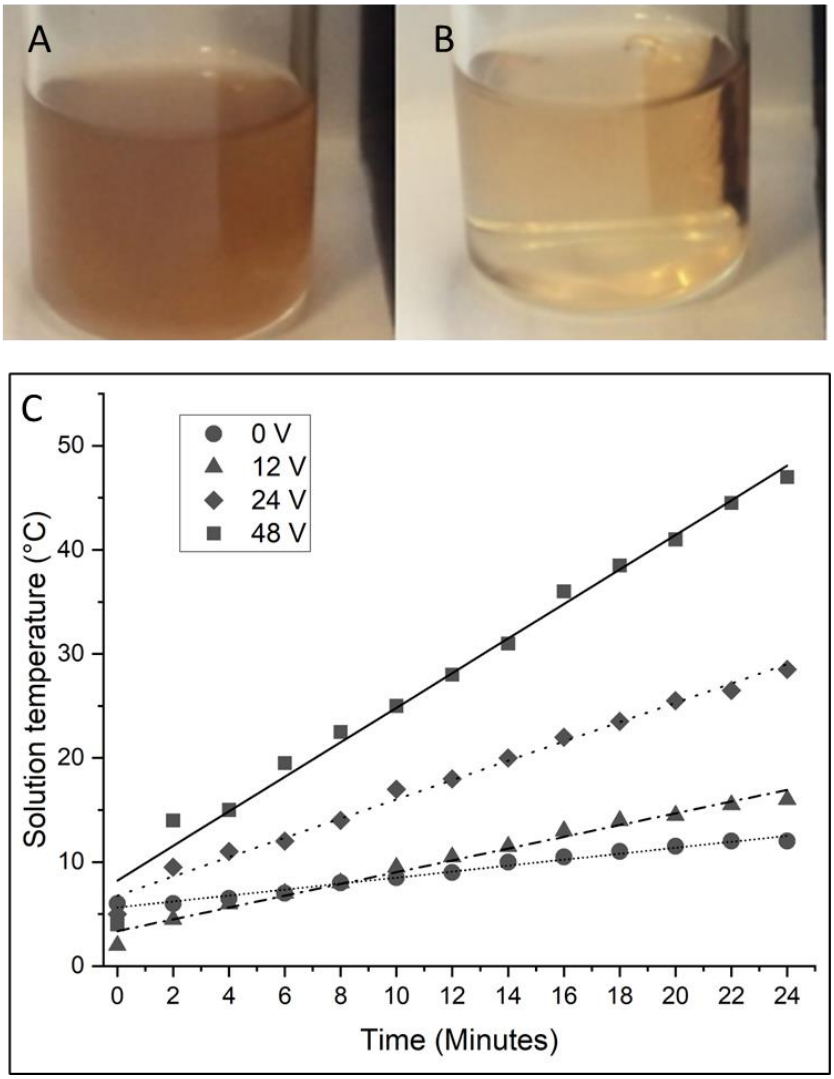


Figure 5. 7: NCC (Copolymer ratio PNIPAM-Acrylamide-Methacrolein 45:45:10) below (A) and above (B) the lower critical phase transition temperature of the complex. A neodymium magnet is placed to the right of each vial and exerts a permanent magnetic field attracting particles to the right hand side of the vial. Induction heating rates of NCC concentrations. (C) shows the induction heating rates of NCC at a concentration of 100 mg/mL solution in water, observed at differing AC circuit voltages from 0-48v.

The efficiency of induction heating of the constructed NCC was assessed at varying input voltages from 0-48 volts. The observed temperature increases showed linear trajectories (Figure 5.7 C) in line with the linear regime model.[208] As expected, higher input voltages resulted in a higher rate of heating for particles, proportional to the increase in voltage. The fastest heating rates were observed as +1.79 $^{\circ}C\ min^{-1}$ with an input power of 48 volts. The specific absorption rate of the NCC of a 100 mg/mL solution was calculated at 1.25 Wg^{-1}.

5.3.3 Radio wave stimulated release of BSA from the Nanoparticle copolymer complex and FITC attachment

BSA was chosen as the carrier for chemotherapy agents because of its biocompatibility, availability, and the possibility of immobilisation on polymers containing aldehyde functional groups.[321] This is a reversible condensation reaction between the aldehyde groups on the methacrolein component of the polymer, and amine groups present on BSA.[34] Protein immobilisation was performed analogous to the free copolymer. A total of 0.291 mg (± 0.027 mg) of BSA was immobilised by 6 mg of the NCC. Approximately 4.85% (± 0.45%) by weight of NCC was assessed to be drug carrying protein after immobilisation. This protein carrying capacity is similar to that of the free polymer when adjusted for the weight inclusion of SPIONS within the complex.

It was noticed that upon protein immobilisation the hydrodynamic diameter of the nanoparticle complex increased by 36% (+/- 8.9%, n=3) of the original NCC diameter. This could be a result of the physical size of BSA molecules swelling the complex by drawing more aqueous solution, into the hydrophobic inner shell. The hydrodynamic diameter once again reduces upon total protein release.

Figure 5.8 shows the release profile of BSA from the NCC upon active release cycles. Active release consisted of inductively heating the NCC solution above and then cooling below the LCST of the complex. The first three cycles showed significant protein release with activation, and negligible release with no activation. After three cycles, the amount of released protein reduces considerably, and after seven cycles no protein can be detected. 'Pre-activation' particles showed little release throughout the time points.

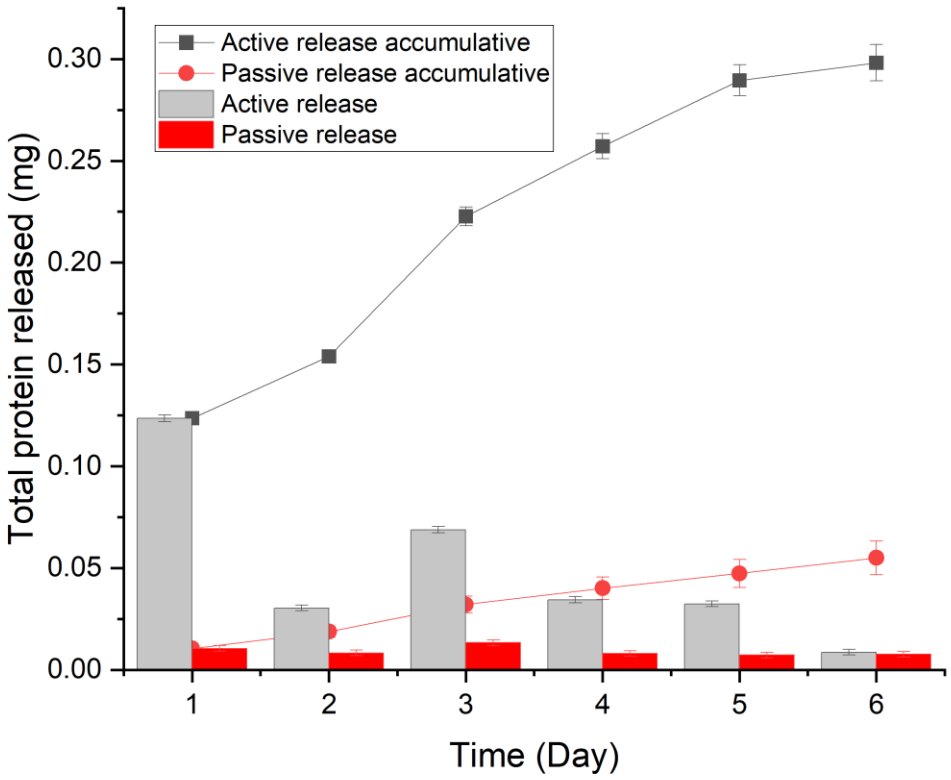


Figure 5. 8: Release profile of BSA from protein loaded NCC as measured by Bradford protein assay. Stimulated and passive release are shown, as well as cycled and accumulative release. Active release refers to a sample of the NCC being inductively heated above the LCST for 5 minutes, then being cooled to 37.5°C and the supernatant tested for protein content. Passive release refers to a sample of the NCC left at 37.5°C throughout the experiment and the supernatant being tested for protein content. Error bars represent the mean +/- standard deviation, n=3.

The release profile of BSA from NCC was monitored over 7 days under buffer conditions (Figure 5.8). The first five cycles (over five days) show significant protein release with activation, and negligible release with no activation. After five cycles, the amount of released protein reduces considerably, and after six cycles no protein release can be detected. Passive release of proteins represented only a small fraction of the amount released by stimulation (Figure 5.8).

Attachment of a fluorophore to the nanoparticle complex provides the potential for *in vitro* and *in vivo* imaging and tracking of the NCC. With the number of available functional groups present on BSA the overall strategy was to bind the fluorophore to the protein prior to immobilisation on the NCC. This was

initially attempted with Dansyl Chloride. The product of the reaction following lyophilisation was clear white crystals, which were ground into a fine white powder. The binding of Dansyl chloride to BSA was confirmed a success by the fluorescence of the product under a UV light (λ = 495 nm).

However, once bonding of the fluorophore to BSA was complete, it was observed the protein would no longer bind to the nanoparticle copolymer complex at significant rates. It is likely that BSA-Dansyl chloride was not bonding to the NCC due to the fact dansyl chloride binds to proteins via a reaction with amine groups. This could block protein binding by occupying the amine sites on the protein that react with the aldehyde groups within the grafted copolymer. Following this, fluorescein isothiocyanate was investigated as a potential fluorophore for binding.

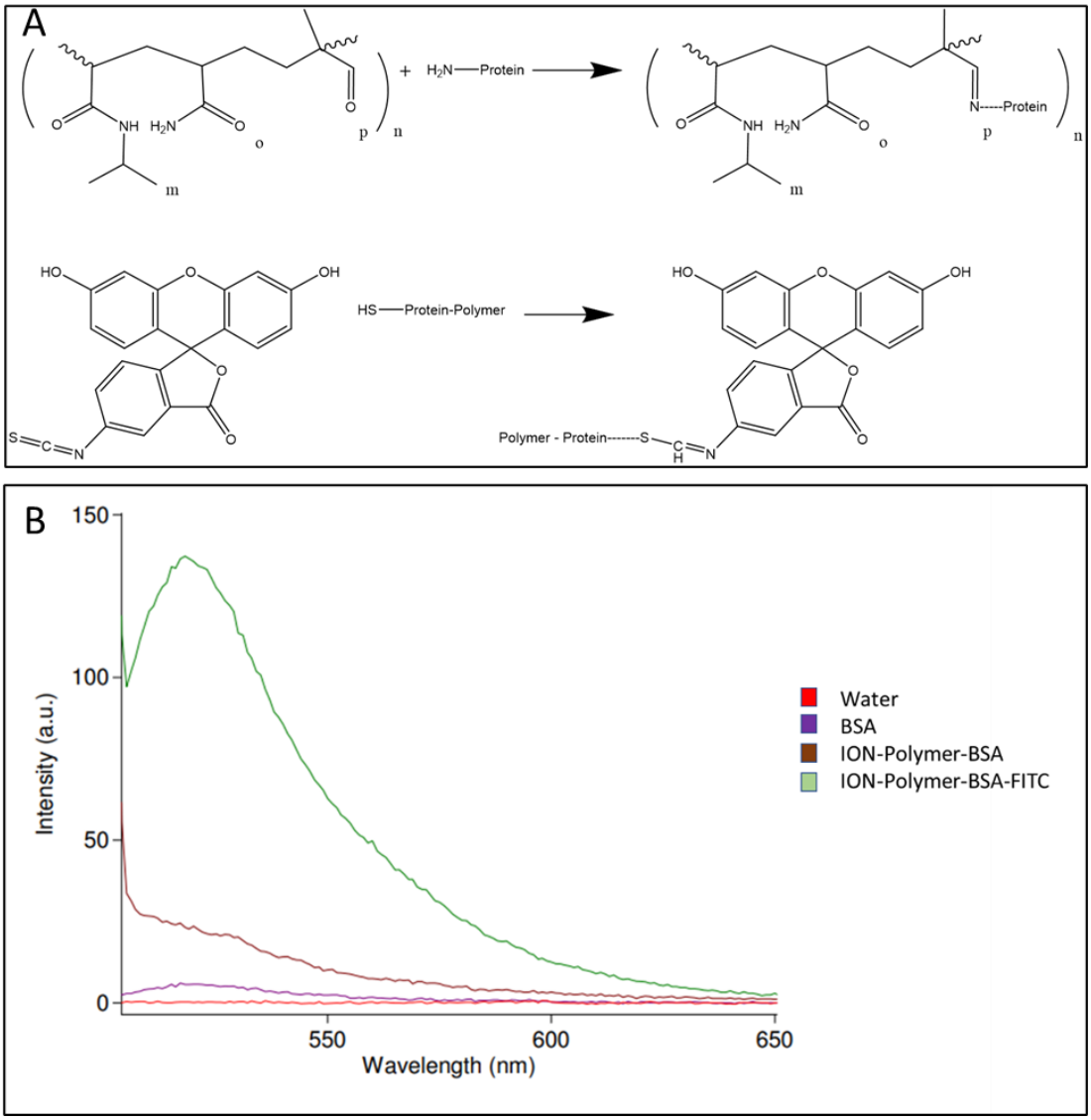


Figure 5. 9: Fluorescence tagging reaction and fluorescence of the resulting product. (A) the reaction scheme of the immobilisation of BSA on the NCC and subsequent binding of FITC to immobilised proteins via sulphur bridge formation. (B) The fluorescence spectrum from 500-650 nm of Water, BSA, NCC , and NCC-FITC. The solutions concentrations were made up to 0.1 mg/mL.

Fluorophore attachment was achieved through FITC binding to sulphide groups and available amine groups (Figure 5.9 A) following protein immobilisation on the nanoparticle-polymer complex. The presence of FITC in the nanoparticle complex (FITC- NCC) was confirmed by visualisation under UV light and fluorescence spectroscopy (Figure 5.9 B and 5.10 (λ = 495 nm)).

The samples and controls were excited with a 495 nm wavelength from a Xenon flash lamp and the emission spectrum was measured between 500 nm and 700 nm. Water (red line), BSA alone (blue line), and the

untagged nanoparticle-polymer complex (brown line) showed negligible fluorescence (Figure 5.9 B). The NCC control (brown line) showed some scattering related signal while the fluorescent tagged complex (green line) showed a clear and definite emission peak at 520 nm, akin to FITC emission. It is worth noting, the total content of FITC in the NCC has not been quantified.

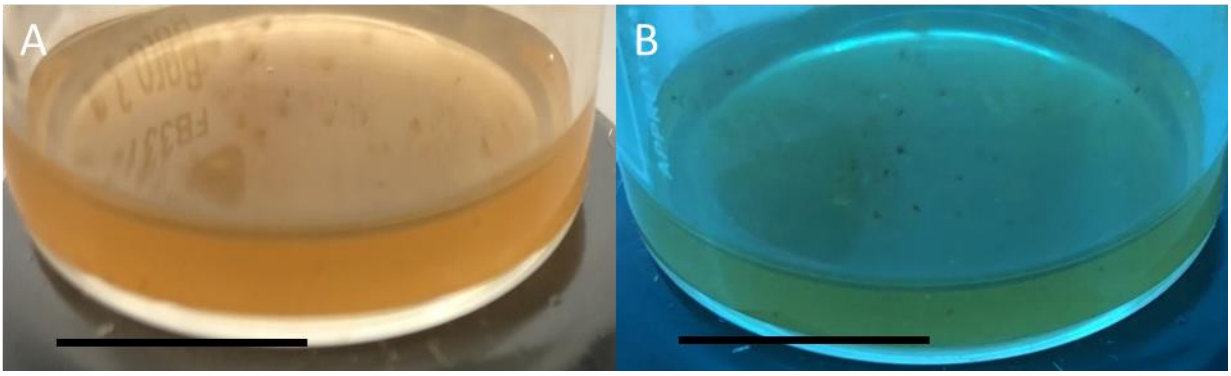


Figure 5. 10: Fluorescence effects of binding a fluorophore to the nanoparticle complex. FITC bound BSA-NCC complex in a 1 mg/mL solution under and visible light (A) and a UV light (B). The image was taken with optical microscope and fluorescent light of 495 nm is present in image (B). The scale bar is equivalent to 4 cm.

5.4 Discussion

5.4.1 SPION surface synthesised poly-N-isopropylacrylamide

Synthesis of nanoparticle bound PNIPAM was successful as confirmed by analysis techniques. Total yields of the reaction were similar to unbound polymer synthesis, however, upon magnetic extraction of all surface bound polymer chains, yield decreased by a quarter. This indicates a proportion of the product was unbound polymer chains. It is likely this is a result of the RAFT polymerisation mechanism (Figure 3.2), where the propagating chains in solution are not bound to the chain transfer agent.[322] Therefore, when the reaction stops, these propagating chains are left unbound to SPIONs and are not extracted during magnetic decantation. This affect has been observed in literature examples of surface initiated RAFT polymerisations of NIPAM.[323] It is possible however, that some polymer chains remain entangled in with NCC particles

during the magnetic decantation process, this could be reduced by repeated cycles of bath sonication in water and magnetic decantation.

5.4.2 Nanoparticle copolymer complex synthesis and analysis

Synthesis of surface bound copolymer was confirmed by FT-IR, NMR, and zeta potential analysis. After washing and magnetic decantation, following synthesis, the yield of the reaction was found to be lower than of the freely synthesised copolymer. This can be explained by the deliberate block synthesis method which forces the synthesis of a methacrolein chain off DDMAT, followed by a NIPAM-co-Acrylamide core. The lower reactivity of methacrolein reduces the overall yield due to its lower reactivity and its occupation of all propagating chains. Due to the surface binding of DDMAT, there is a reduced angle of approach for any activate chains to bind and form the equilibrium adduct (Figure 3.2).Therefore steric hinderance reduced the rate at which propagating chains can combine and disassociate with the surface bound CTA.[323]

The hydrophobic methacrolein core was synthesised on the inner shell of the copolymer, and the block structure was a crucial feature of the larger nanoparticle-copolymer complex structure. This keeps the drug-bearing proteins immobilised and makes sure the complex's outer layer is hydrophilic and biocompatible. This shell structure was confirmed with zeta potential measurements giving a slightly negative zeta potential (Figure 5.2 C) This is expected as a result of the outer shell of the copolymer comprising amide bearing monomers. Confirming the hypothesised inner – outer shell-like structure of methacrolein – acrylamide/NIPAM respectively. The negative methacrolein aldehyde groups would result in a much greater negative zeta potential.

Copolymer chain properties

The deliberate block synthesis method resulted in a reduced chain length in comparison to the freely synthesised copolymer due to the lower reactivity rate of the methacrolein monomer. A smaller PDI was observed for the copolymer synthesised on the surface of SPIONs than that observed in free synthesis of the copolymer, or free PNIPAM. This could again be attributed to the forced block structure of copolymer synthesis. The very low reaction rate of the initially synthesised methacrolein chain allows the RAFT equilibrium steps to dominate the synthesis (Section 3.1), ensuring similar reaction times for copolymer chains and a therefore a low PDI. The inclusion of NIPAM and acrylamide following this only allows a limited reaction time to start an acrylamide-NIPAM coil. Since the introduced monomers must react with a propagating methacrolein chain, the RAFT adducts dominate the equilibrium steps in synthesis.[217]

Size by microscopy and dynamic light scattering

The size of the NCC (297 nm), while considerably larger than the ideal size to enter cell membranes, was measured within the size range to take advantage of the EPR effect *in vivo* (Figure 5.4).[324] However, the size difference differed from batch to batch of NCC synthesis, ranging from 260-370nm. This could be caused by slight differences in reaction times allowed for the NIPAM/acrylamide coil, caused by a slightly different number of propagating chains available, a result of small discrepancies in the mass of initiator added. Additionally, it could be a result of very small changes in the mass of monomers added to the reaction flask. It did not appear to affect the LCST of the NCC. It could be assumed that synthesising the copolymer off the surface of the SPIONS with a smaller total number of moles of monomer present, would result in a reduced hydrodynamic diameter. It is also worth noting, between size measurements to determine the LCST samples were bath sonicated for 90 seconds at room temperature, to assure previous measurements would not affect the DLS result.

The stability of the NCC was measured in buffer conditions over 90 days (Figure 5.4 A). There was no deviation in hydrodynamic diameter over this time, indicating the potential stability of complex in physiological conditions over a sustained period of time. Prior to the stability measurement on day 0 samples were filtered through a 0.6-micron filter and bath sonicated for 5 minutes, however, samples were not sonicated or run through a filter between time points. To ensure there are no aggregates or large particles in a sample that could potentially cause harm *in vivo*, it would be necessary to filter and sonicate samples prior to further experiments in animal models or any clinical work done. Although, these experiments do not take into account many physiological factors that may contribute to degradation of the complex, it is an indication of the potential for stability *in vivo*.[325]

LCST of synthesised NCC

The temperature at which the surface anchored copolymer undergoes a coil to globular transition has been engineered to undergo a phase change at 42.5 ˚C. As hypothesised, the phase change is accompanied by a reduction in hydrodynamic diameter. At temperatures just below the phase change (40 ˚C), there is larger deviations in the diameter of the NCC (Figure 5.4 B). This indicates some copolymer chains undergo the phase transition at this temperature. After the massive reduction in diameter at 42.5 ˚C the deviation is reduced massively, indicating all copolymers have undergone a phase change. The premature size change for some copolymer chains could be a result of slightly different compositions, resulting in a different LCST. It is possible this premature phase change results in passive protein release (Figure 5.8). Further refinement of the polymerisation process could potentially increase control over reaction conditions, reducing any deviations in the structure of the synthesised copolymer.

Upon reaching the LCST the NCC undergoes a solubility change, becoming insoluble in aqueous solution.[133] When the particles are exposed to a permanent magnetic field, and the LCST is triggered, particles are instantly extracted by the field (Figure 5.7 B). This property is a side effect of the functionality of the copolymer designed in the project, which although not strictly relevant to this project, this property could have many applications in industrial systems.

Induction heating of NCC by radio waves

The NCC particles were heated efficiently in aqueous solution by the designed induction heating device (Figure 5.7 C). The heating rates were lower than that of SPIONs for the same concentration by mass per volume, this is a result of the copolymer chains occupying a higher proportion of the mass per volume of the particles than DDMAT occupies on SPIONs. Regardless, the NCC was heated sufficiently by induction heating to over the activation temperature. As hypothesised the SAR was lower than that of Lauric acid stabilised SPIONs, 1.25 Wg^{-1} for the NCC and 1.76 Wg^{-1} for LA-ION. This 30 % reduction in SAR can be attributed to the bound copolymer in the NCC, which occupies half of the total weight of the complex.

5.4.3 Protein immobilisation and release from the nanoparticle copolymer complex

Protein release from the complex was observed when stimulated by radio waves. Protein release can be staggered over a number of days, and without stimulation protein release is a minimised (Figures 5.8). This evidence of protein retention without heating serves as the basis for the potential of selective drug release from copolymers bound to SPIONS, thus allows for “activation” of drug release. Protein release from the NCC was staggered over more cycles of the LCST than the free copolymer. This could be an effect of the close proximity of copolymer chains to each other, trapping protein molecules that would otherwise be

released. It is also possible the inner shell of the copolymer that immobilises the proteins is sterically hindering release. The demonstration of staggered release over the course of a week provides good evidence for the potential to allow a staggered course of treatment over seven days or possibly longer, with only a single administration of the drug loaded NCC. The rational for the advantages of staggered release are discussed in section 4.4.

It was discovered that the hydrodynamic diameter of the nanoparticle complex increased with protein immobilisation. This might be due to the complex swell due to the physical size of BSA molecules attracting additional aqueous solution into the hydrophobic inner shell. At the time of entire protein release, the hydrodynamic diameter again decreases.

Fluorophore attachment to the NCC

Dansyl chloride was initially chosen as a tracking fluorophore to bind to the NCC. However, it became apparent binding of the fluorophore was inhibiting protein immobilisation on the NCC. It is likely that BSA-dansyl chloride was not bonding to the NCC due to the fact dansyl chloride binds to proteins *via* a reaction with amine groups. This could block protein binding by occupying the amine sites on the protein that react with the aldehyde groups within the grafted copolymer.

FITC was chosen as a fluorophore for attachment due to its cheap cost, ready availability and ability to form sulphur bridges with other molecules, namely BSA (Figure 5.9 A).[326] Isothiocyanates are also reactive toward nucleophilic sites such as amines (i.e. lysines), sulfhydryls (i.e. cysteines) and the phenolate ion of tyrosine side chains, all of which are present at high rates within BSA.[272] It was also determined that preventing FITC from blocking protein immobilisation could be achieved by tagging the fluorophore to BSA after protein immobilisation (Figure 5.9 A). FITC was successfully bound to the NCC *via* immobilised BSA, this was

detected in spectrometry and fluorescence imaging (Figures 5.9 B and figure 5.10). The fluorophore attachment enables tracking *in vitro* but will also be important for clinical use in order to assess magnetic localization *in vivo* or to monitor tumour physiology during treatment. The ability to bind a fluorophore to the carrier protein is a property that allows for potential tracking of drug locations within the human body, within tumours and within cells. This could massively aid further work on monitoring protein and drug pathways during treatment. It is also possible to bind a fluorophore directly to the NCC. Again, this could be exploited to monitor nanoparticle movement, in contrast to protein and drug tracking.

5.4.4 Comparison to other protein release methods reported in literature

Other protein immobilisation and release strategies exist in several different forms. The proteins used vary depending on the study and so direct quantitative comparisons are not always possible.

There are several examples in the literature of hydrogel networks capable of protein retention and release. In these gels proteins are trapped within the crosslinked hydrogel network and are retained/released based on electrostatic interactions.[327] Poly ethylene glycol (PEG) based hydrogel mesh networks have been shown to release protein over 35 days.[328] However this method of protein delivery has drawbacks in comparison to the delivery system described in this chapter. Release is not stimulated, therefore occurs passively, not only this but there is no method of localising release, leading to the possibility of off target effects. There is also the potential for complications of a large hydrogel network moving through blood vessels. This is an inherent problem with the use of hydrogels as delivery systems, therefore they must be directly injected into the target site.

PEG base delivery systems have seen extensive research, there are several clinically available PEG based systems. Several properties of PEG based systems are advantageous features for *in vivo* drug delivery, such as their protein repellent properties.[329] However, studies have shown that patients often exhibit antibody formation against PEG. [330] Also non-degradability of PEG may lead to polymer accumulation *in vivo*.[331] Again, all clinically approved PEG based delivery systems have no means of stimulated release or a method of spatial targeting, therefore off target effects could narrow the therapeutic effect of these delivery systems.

There are seven clinically available liposome delivery systems.[331] Liposomes can improve drug circulation times, and can be easily functionalised with targeting moieties and PEG to aid in delivery. However, a limiting factor in liposomal delivery systems is limited ability to achieve large molecule encapsulation.[331]

In comparison to literature examples of delivery systems, the technology platform described in this chapter has a high loading capacity of protein, retention of said protein over seven days unless stimulated, and a highly effective stimulation method to trigger delivery. In addition, the magnetic properties of the technology allow for localisation, and the ability to tag fluorophores to the complex allows for visualisation of the delivered cargo and/or the nanoparticle complex. The devised complex overcomes many of the issues faced by current delivery systems.

5.5 Conclusions

To conclude, the Poly – (methacrolein-b-(NIPAM-co-acrylamide)) copolymer was successfully synthesised on the surface of superparamagnetic iron oxide nanoparticle cores, forming a core-shell structure. The copolymer was synthesised in such a way that there are two distinct regions to the copolymer, an inner hydrophobic drug immobilising region and an outer hydrophilic coil region that undergoes a

structure change upon the LCST. The LCST of the synthesised copolymer was meticulously engineered to occur at the desired temperature range of 41-43°C. This target temperature was chosen since it is above that of human body temperature but below that of mammalian cell hyperthermic temperatures. The NCC exhibited a temperature trigger capable of releasing drugs by nonharmful, biocompatible means.

The nanoparticle copolymer complex showed efficient induction heating at varying input powers and concentrations with the constructed device. Moreover, the LCST of the nanoparticle copolymer complex could be triggered by means of induction heating from an external radio wave source without contact with the sample.

Bovine serum albumin was successfully immobilised and subsequently released from the nanoparticle complex upon radio wave activation. Furthermore, it was shown that this could be staggered over seven days, allowing for the potential of staggered drug dose without the need for multiple administrations to the patient. In addition to this, without activation, there was minimal protein release from the complex, showing the potential for a highly effective triggered release drug delivery system by an external stimulus.

The fluorophore fluorescein isothiocyanate was adhered to the nanoparticle complex for potential *in vivo* and *in vitro* imaging. The fluorophore can be bound to both the drug carrying proteins and the nanoparticle complex itself, potentially allowing for tracking and imaging of drug and or the nanoparticle complex.

Chapter 6: Selective cell death in cell lines

6.1 Introduction

Several methods of combining thermoresponsive polymers and stimulation by an AMF have been shown to improve specificity of drug delivery. None have been tested in clinical trials to date.

Therapeutic medications have been encapsulated and delivered to cancer locations using ION-carrying liposomes and micelles. Typically, the shells are made of a thermosensitive polymer like poly-N (isopropylacrylamide) or poly (vinylcaprolactame). One technique involves the use of a very low frequency alternating magnetic field (< 1 kHz), which causes the IONs to drag and squeeze the liposomes until they rupture and release the payload.[63,125,332,333,334] These emulsion-based nanocapsules have made it possible to trigger the delivery of therapeutic molecules that are both hydrophobic and hydrophilic at the same time. Compounds including FITC-DNA, fluorophores, and pyrene are kept confined inside their phases until activated.[334] When initiated in this manner drug delivery can have a high selectivity and payload efficiency. It is not a perfect approach, though, as the size and makeup of the micelles or liposomes can vary greatly during synthesis and frequently have undesirable impacts on how well the medication penetrates tumour tissue, impeding the effectiveness of delivery *in vivo*.

Research into trapping medicines and IONs inside a polymer matrix for delivery to tumour locations has increased as a result of improvements in thermosensitive polymers and the optimization of inductive heating techniques. An extremely tuneable drug release upon stimulation has been demonstrated for a combination particle made of a poly(ethylene oxide)-poly(propylene oxide)-poly(ethylene oxide) triblock copolymer matrix incorporating polyvinyl alcohol shell, ION, and medicines like ethosuximide. An excellent

mechanism of drug release is provided by the reversible collapse of the copolymer and the enlargement of the PVA core with increasing temperature, opening and closing pores in the polymer matrix for drug release.[335] In the reverse effect, drug release from a polymer matrix can be suppressed by heating with an AMF. Pores in the crosslinked polymer matrix lined with nanocomposites of poly-N(isopropylacrylamide) and ION are closed during inductive heating. This offers a way to stop drug delivery after the desired therapeutic impact has been attained, lowering the risk of off-target toxicity because the polymer will collapse and the holes in the matrix will close.[336] A self-assembling peptide-functionalized iron oxide core – mesoporous silica shell nanoparticle showed selective drug release and cell death under stimulation from an AMF. The surface grafted peptides block pores in the silica until heated by AMF, when a temperature of 50 ˚C is reached the peptides straighten and allow drug release from pores in the silica. However, the need to reach 50 ˚C will result in cell death by hyperthermia, a fundamental problem of the study.[337]

The main benefit of using radio waves as an activation technique for cancer treatment is that it is non-ionizing and highly penetrating. It also has the capacity to reach parts of the body where other stimuli frequently fail. Radio waves can be directed at specific areas of the body with no harm to the surrounding tissue. The possibility of using persistent magnetic fields as a directing agent to further accumulate magnetic particles and medications in tumour tissue may prove to be an effective way to lessen the build-up of toxic therapeutics in essential organs.[338] In this study the intention was to create a magnetically localised drug delivery system that minimizes toxicity in tissue until stimulation by a alternating magnetic field, carried by radio waves. The construct of the nanoparticle copolymer complex (detailed in chapter 5) was tested on its ability to cause selective cell death.

6.2 Materials and methods

6.2.1 Cell culture and viability experiments

The same cell lines and cell culture protocols were followed as detailed in section 4.2.

Cells were seeded in 96 well plates at 1×10^4 cells/well in growth media and left overnight in the incubator for the cells to adhere. Cells were then treated with differing concentrations of the nanoparticle – copolymer complex and controls in 250 μL growth medium. After treatment, the media on the cells was removed and the cells were washed in PBS (Sigma-Aldrich Merck Life Science UK Limited, Gillingham, UK) twice. Experiments were performed in triplicate and repeated on three separate occasions.

Hoechst stain was added to wells following washing in PBS. The stain was added in PBS to a final concentration of 10 μM and allowed to incubate at room temperature for 30 minutes. Subsequently, cells were washed once again with PBS and imaged under fluorescence microscopy with an excitation wavelength of 495 nm.

HEP-G2 protection with N-acetylcysteine

To prevent delivered paracetamol from causing toxicity in HEP-G2 cells when concentrations of drug were added to the cell media, acetylcysteine was also added to a final concentration of 0.5 mM. This concentration was chosen as it is within the range of concentrations used to prevent paracetamol overdoses within the clinic.[339]

Flow cytometry experimental procedure

Cells were seeded in 24 well plates at 8 × 10^4 cells/well in growth media and left overnight in the incubator for the cells to adhere. Cells were then treated with differing concentrations of NCC and controls in 50 μL growth medium. After treatment, the media on the cells was removed and the cells were washed in PBS twice. Harvested cells were aliquoted up to 1 x 10^6 cells/100 μL into FACS tubes (Merck KGaA, Darmstadt, Germany). The cells were centrifuged in 2 mL PBS at 300 x g for 5 minutes and then the buffer decanted from pelleted cells. This process was repeated a total of 3 times. To adjust flow cytometer settings for Propidium Iodide (PI; Sigma-Aldrich, Gillingham, UK) PI staining solution (5 - 10 μL) was added to a control tube of otherwise unstained cells and a control tube of ethanol treated cells. The cells were mixed gently and incubated for 15 minutes in the dark. PI fluorescence was determined (using the FL-3 channel) with a BD Sciences FACSCalibur™ Flow Cytometer (1 Becton Drive Franklin Lakes, NJ 07417, US). Collected PI fluorescence was gathered in the FL-3 channel. To each sample 5 - 10 μL of PI staining solution was added 15 minutes prior to analysis. The stop count for events was set at 10,000.

6.2.1 Spheroid experimentation

Spheroids were created in 96-well plates. Agarose (1% (w/v); (Cambridge bioscience, Munro House, Trafalgar Way, Bar Hill, Cambridge, United Kingdom) was dissolved in PBS and heated in the microwave for 6 mins, before addition of 100 μl to each well in a 96 well plate. The gel was allowed to cool for 1 hour undisturbed so that a non-adherent, concave surface was formed. While cooling, UV light was used for decontamination of the agarose surface. Cells were then seeded (1 x 10^4 per well) in 100 μl cell growth medium (Dulbecco's modified Eagle's medium [Sigma-Aldrich]) supplemented with 10 % (v/v) fetal calf serum, 2 mM L-glutamine, 100 U/mL penicillin, and 0.1 mg/mL streptomycin (all Sigma-Aldrich

Gillingham, UK). Plates were then incubated at 37 ° C in a 5 % CO_2 atmosphere for 4 days to allow the formation of spheroids. Diameters were measured using three dimensions of radius and were performed in triplicate on three separate occasions. Activation of the NCC was carried out for two cycles 4 hours after incubation with the NCC, a further two cycles at 24 hours, and another two cycles at 48 hours.

Haemolytic Activity of ION-Polymer complex:

Fresh horse blood stabilized with heparin (Generon Clinical Sciences, Slough, United Kingdom) was used to assess the haemolytic activity of the nanoparticle-polymer. Healthy red blood cells (HRBCs) were isolated from 1 mL of fresh horse blood by centrifugation at 1000 rpm for 10 min at 4°C and washed with PBS at least three times. HRBCs were then diluted ten times with PBS buffer. The diluted HRBC suspension (0.1 mL) was added to 1 mL of water (positive control), pure PBS (negative control), or PBS buffer containing nanoparticle-polymer complex ranging from 0.1 to 1 mg/ mL. After gentle shaking, the mixtures were kept still for 24 h, at room temperature in different batches with triplicates. Then, after centrifugation of the mixture (5000 rpm, 1 min), the absorbance of the supernatant (haemoglobin) was recorded using a Perkin Elmer Lambda 25 UV – VIS spectrometer (PerkinElmer, MA,USA). The extent of haemolysis was calculated by dividing the difference in absorbance between the sample and the negative control by the difference in absorbance at 541 nm between the positive and negative controls.

6.2.2 Magnetic directing capacity of ION-Polymer complex

Two separate plates of cells were prepared, one for magnetic direction and fluorescence treatment of cells, and another for control cells. Cells were seeded in 6 well plates at 20 × 10^4 cells/well in 2.5 mL growth media and left overnight in the incubator at 37.5°C (5% CO_2) for the cells to adhere. Cells were then treated with

0.2 mg/mL of FITC-NCC for 24 hours. After treatment, the media from both plates of cells was removed and the cells were washed in PBS three times before harvesting with 200 µL trypsin (Sigma-Aldrich Merck Life Science UK Limited, Gillingham, UK). Cells incubated with concentration of the NCC and control cells were merged in equal numbers within a third six well plate in 2.5 mL growth medium, in the presence of a permanent magnetic field (carried by a neodymium magnet of diameter 2 cm) and allowed to settle for 24 hours. Subsequently, the plates were imaged under fluorescence.

Fluorescence imaging

Fluorescence imaging was performed on a Versa doc molecular imager (Molecular Imager 4000 system, VersaDoc ™ MP Imaging Systems, Watford, UK) using Ex. 495 nm, Em. 520 nm wavelengths. Images were taken directly of cell culture plates after washing by PBS.

Inductive heating

Inductive heating was carried out using a 2000W ZVS Low Voltage induction Heating Board with a Module Tesla Coil and a Flyback Driver Heater. The working coil consisted of a copper tube wound with 10 coils and a 6-inch coil diameter. The coil was water cooled to prevent external heat input to the sample. The coil had a sufficient diameter to allow cell culture plates to fit inside the coil. A variable laboratory power supply system was used to supply the circuit board with current and voltage. Input voltages and heating times were dependent upon the concentration of particles used as measured in non-sterile conditions. It was assumed there was no deviation in heating times for concentration of NCC when in solution with cells. Activation of the NCC was achieved by inductively heating the particles within the plate for the pre-determined time raising the solution temperature to 43˚C and holding that temperature for 5 minutes, then allowing the plate

to cool to 37.5˚C and then heating again. This process was repeated a total of six times for maximum drug bearing protein release. Samples left in a pre-activation state were incubated at 37.5˚C and were not stimulated by radio waves.

Statistics and reproducibility

All statistical analysis of experimental data was performed using Microsoft™ Excel [Microsoft, NM, US]. Origin plot pro V12 was used for graph plotting. Error bars in the experiments indicate standard deviation (SD). The difference was considered significant and shown when the p values were less than 0.05.

Significance was assessed using a two-way ANOVA test, where the two independent variables were concentration of added drug and activated or inactivated particles, values were compared to that of the untreated cell control. P values are represented by; ****=$p<0.001$,***=$p<0.005$ **= 0.01, *=$p<0.05$, ns=$p>0.05$. The data is presented as the means ± standard deviation as error bars, where n= 3.

Bath sonication

Bath sonication and filtration of the particles before use was carried out as detailed in chapter 5.2.

Microscope imaging

The cells were imaged with a Motic AE31 microscope equipped with a mercury lamp and filters for DAPI and FITC.

Other software

FlowJo VX [FlowJo, LLC, OR, US] was used to analyse and compare flow cytometry data. For all image analysis and measurement, the Leica Application Suite X (LAS X) was employed.

6.3 Results

6.3.1 Haemolysis effects of the nanoparticle copolymer complex

The main intention of the development of this drug delivery platform was the ability to "activate" drug release, thereby enhancing any therapeutic effect. Initially, haemolysis rates of blood with varying concentrations of the complex were studied in order to demonstrate biocompatibility of the NCC *in vivo*. The NCC was incubated with horse blood for 24 hours at room temperature and the degree of haemolysis determined (Figure 6.1).

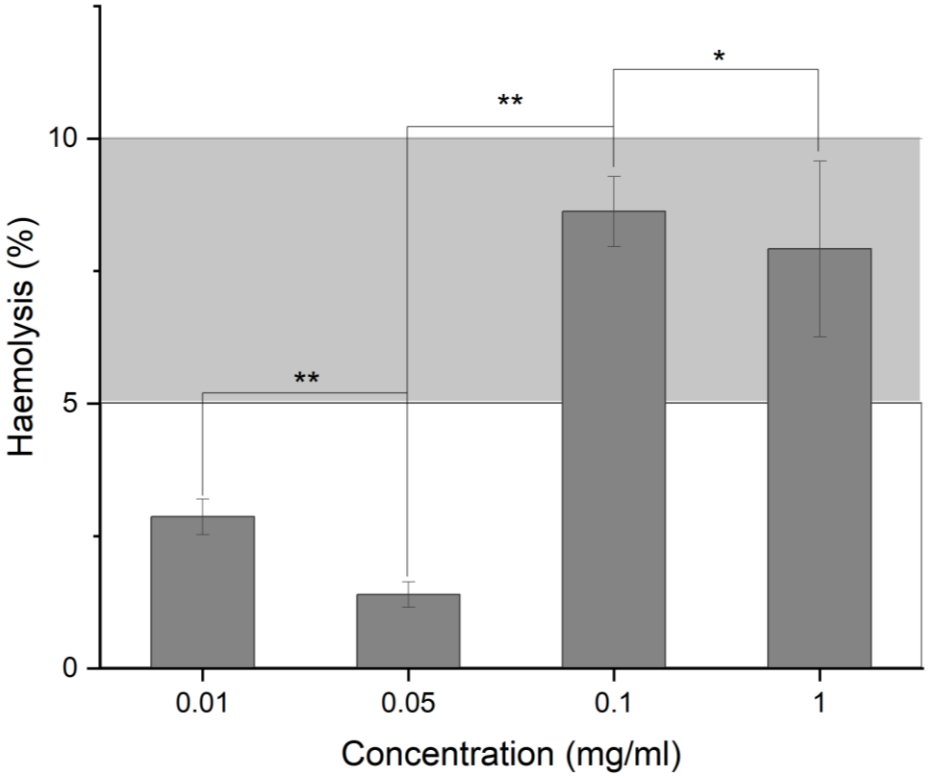


*Figure 6. 1: Haemolysis percentages highlighting the biocompatibility of the unloaded NCC. PBS was used as a negative control and water as a positive control to indicate haemolysis. Mean standard deviation is given as error bars P value significance indicators, ***=p<0.01, **= 0.05<p>0.01, *=0.5<p>0.05.*

At the highest concentration of 1 mg/mL NCC haemolysis was seen to be 7.9 ± 1.6 %. Concentrations of 0.01 and 0.05 mg/mL showed significantly less haemolysis compared to 0.1 and 1 mg/mL concentrations.

There was no significant change in haemolysis rates from 0.1-1 mg/mL. Compounds are assumed to be generally biocompatible if haemolysis is below 10 %, although, to properly make this assessment further tests such as opsonisation, complement activation, and leukocytes activation would need to be run.[340]

6.3.2 Initial cell viability assessment

Protein staining methods such as crystal violet could not be used as a measure of cell viability due to the inclusion of BSA within the NCC. Therefore, the effect of the NCC to cause cell death in immortalised cancer lines was initially investigated qualitatively by Hoechst staining of active nuclei. This method of staining could not be used quantitatively due to the presence of NCC in surviving cells potentially blocking fluorescence signals from detection by equipment. As an initial investigation however, it proved a useful tool in investigating the principle of activated delivery. Paclitaxel and vinblastine were delivered to RD and U-87 MG cells, respectively, and the added NCC was either "activated" by an externally applied radio waves to stimulate drug release or left in a "pre-activated state" without stimulation (Figure 6.2). Activation was achieved by placing the cell culture plate within an induction coil for a predetermined time, dependent on nanoparticle concentration, to raise the temperature to 42.5 °C, holding this temperature for five minutes and then allowing the plate to cool back to 37.5°C. This was repeated six times over one hour to ensure maximum drug bearing protein release. A control with the NCC not containing drugs was not included in this experiment, however, as with data shown in figures 6.3, 6.4, and 6.5, there was no observed negative affect of heating the particles without drug delivery.

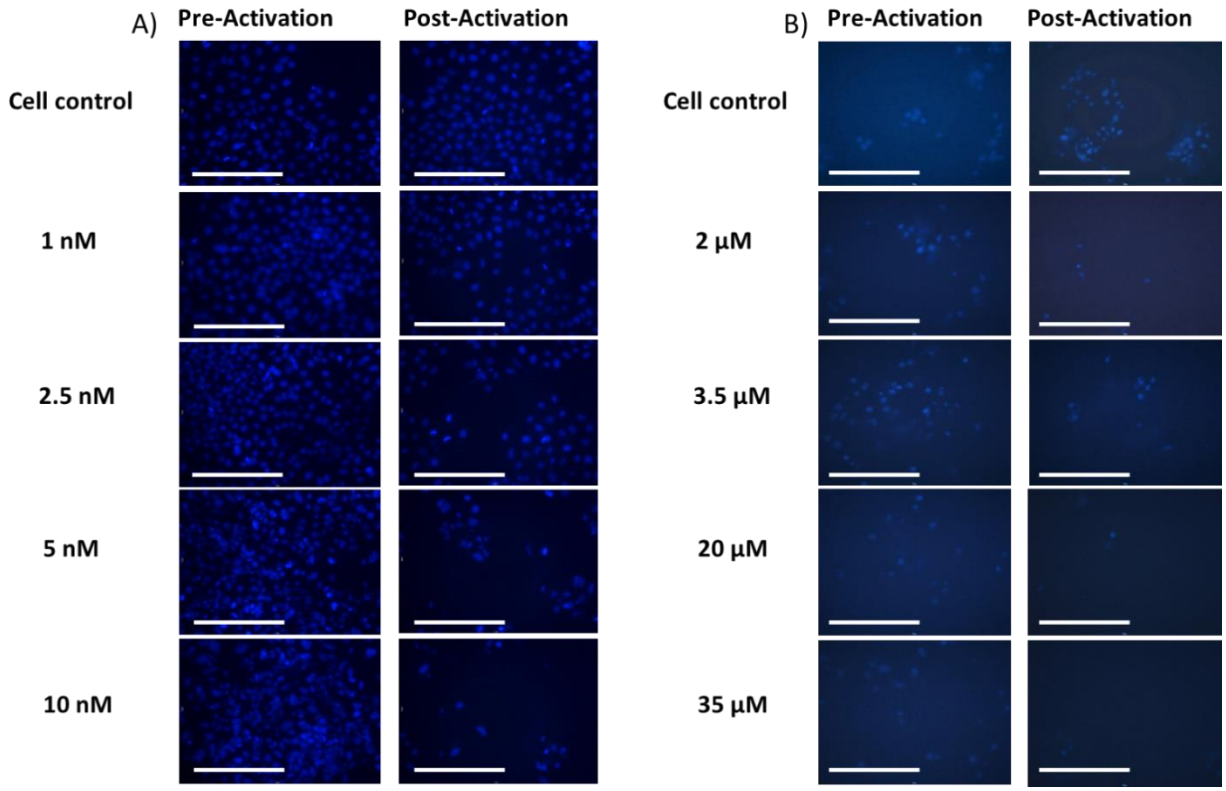


Figure 6. 2: Qualitative images demonstrating stimulated cell death by radio wave activation. Hoechst staining comparison between cells treated with activated NCC or NCC left in a pre-activated state. (A) RD Cells and (B) U-87MG cells imaged under 495 nm light when stained with Hoechst, after treatment with pre-activation NCC (left) and post-activation NCC (right) at the following concentrations listed vertically downwards; Cell control, 1 nM, 2.5 nM, 5 nM and 10 nM and B) Cell control, 2 µ M, 3.5 µ M, 20 µ M and 35 µ M. The scale bar is equal to 100 µ m. The images were taken with a Motic AE31 microscope equipped with a mercury lamp and filters for DAPI and FITC.

Imaging the plates after staining confirmed the hypothesis that enhanced cell death is caused by stimulated release of the drugs from the NCC. In RD cells there are consistently fewer viable cells present when the complex is activated in comparison to the "pre-activation" state, this effect becomes more pronounced with increasing concentrations of Paclitaxel (Figure 6.2 a). A similar trend was observed with vinblastine delivered to U87-MG cells; cell viability was reduced massively upon activation of the complex. However, it appeared in U87-MG cells, with high concentrations of delivered drug, cell viability was reduced for "pre-activation" NCC. Although cell viability reduction was not near the levels seen for the activated complex (Figure 6.2 b).

6.3.3 Effect of NCC activation on cell viability

The initial qualitative results provided a good indication of the hypothesis and therefore further quantitative data was obtained. Flow cytometry combined with propidium iodide stain, was used to determine cell viability differences between treated populations of cells, particularly in comparing pre-activation and post-activation effects. Since propidium iodide is not permeant to live cells, it is commonly used to detect dead cells in a population.[341] Gating was performed for cell population determination, with the untreated cell controls used as viable populations and ethanol treated cells used as a dead cell reference.

The NCC was loaded with paclitaxel (NCC-PAC), vinblastine (NCC-VIN) or paracetamol (NCC-PARA) and tested for activity against rhabdomyosarcoma (RD figure 6.3 A, RH30 figure 6.3 B), and glioblastoma (U-87 MG figure 6.4 A), breast (MCF-7 figure 6.4 B) and Liver (HEP-G2 figure 6.5) cell lines. Paclitaxel was delivered to RD and RH30 cells as an initial proof of concept drug delivery system, vinblastine was delivered to U-87 MG and MCF-7 cells as a second model drug due to the cell lines resistance to paclitaxel, and Paracetamol to HEP-G2 cells. FACS analysis was used to determine the degree of cell death after incubation with the complex, comparing viability of cells when the complex was activated to those left in a pre-activation state.

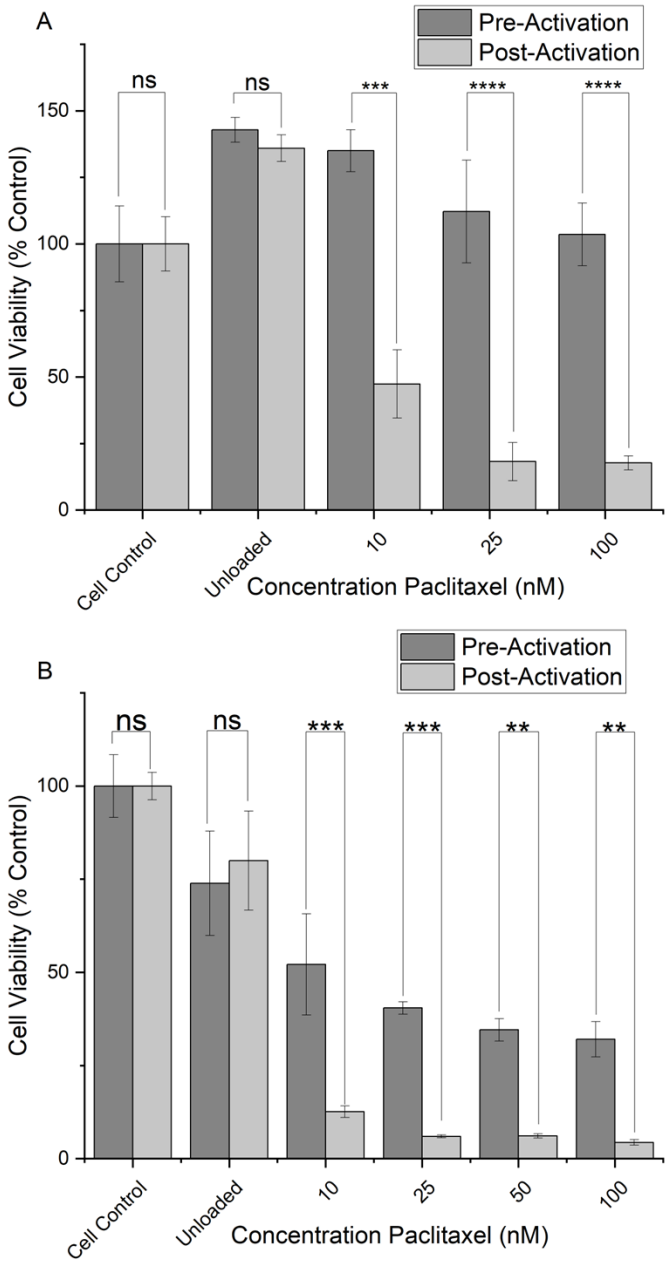


*Figure 6. 3: Effects of NCC assisted delivery of Paclitaxel to cancer cells. Cell viability was assessed by delivering chemotherapy agents to cells in vitro to RD cells (A) and RH30 cells (B), the x axis represents concentrations of drug carried and released by the NCC. Cells refer to the cell only control and is set to 100%. Unloaded refers to cells incubated with a 2 mg/mL solution of the NCC without bound drugs. All data labelled as pre-activation refers to populations of cells that have not been exposed to a radio wave stimulus, and have remained at a temperature of 37.5˚C throughout the experiment. All data labelled as post-activation refers to populations of cells that are exposed to 6 cycles of the radio wave stimulus, including the cell only and unloaded particle controls. All data is scaled as a percentage of cell survival normalised to the cell only control. Significance was assessed using a two-way ANOVA test, where the two independent variables were concentration of added drug and activated or inactivated particles, values were compared to that of the untreated cell control. P values are represented by; ****=p<0.001,***=p<0.005 **= 0.01, *=p<0.05, ns=p>0.05. The data is presented as the means ± standard deviation as error bars, where n= 3.*

After activation with radio waves a high degree of cell death was seen. In RD cells 10 nM concentrations showed a 52% (+/- 7.2 %) cell viability reduction, and 25 nM NCC-PAC resulted in 83 ± 6% cell death when compared to cell control after activation (Figure 6.3A). At concentrations greater than this, cell viability plateaued. At all concentrations, there was no significant pre-activation cell death seen (Figure 6.3, $p>0.05$). Between all activated and pre activation concentrations there was a significant reduction in cell viability when the complex was activated by radio wave activation (Figure 6.3 A, p values <0.05).

The estimated value for the EC50 of PAC-NCC when activated was 8.92 nM. This value is slightly lower than that observed for the bare drug in chapter 4.

Like to RD cells, paclitaxel was delivered by the NCC to RH30 Rhabdomyosarcoma cells (Figure 6.3 B). Cell viability was affected slightly by the presence of 2 mg/mL unloaded particles (Figure 6.3 B, unloaded), although this is a high concentration of particles, it indicates a small degree of toxicity of the NCC in this cell line.

All concentrations of activated NCC caused large amounts of cell death, a concentration of 10 nM reducing cell viability by 78%. At concentrations of 25 nM and above, changes in cell viability plateaued, as seen when delivered to RD cells and for the drug in free form (Figures 4.2 and 6.3 A and B). However, a minimum cell viability of 5 % (+/-2.1%) was observed at 100 nM delivered drug. Pre-activation particles also showed a reduction in cell viability at all concentrations observed, although not significant in comparison to the reduction in viability of activated NCC. For a delivered concentration of 10 nM paclitaxel, pre-activation state NCC caused a 48 % (+/- 8.2 %) reduction in cell viability, whereas activated NCC caused an 86 % (+/- 3 %) reduction. For higher concentrations pre-activation particles also showed a plateau effect on cell

viability (Figure 6.3 B). The estimated EC50 value (5.14 nM) for paclitaxel when delivered to RH30 cells by activated NCC was reduced considerably in comparison to the admission of the free drug alone.

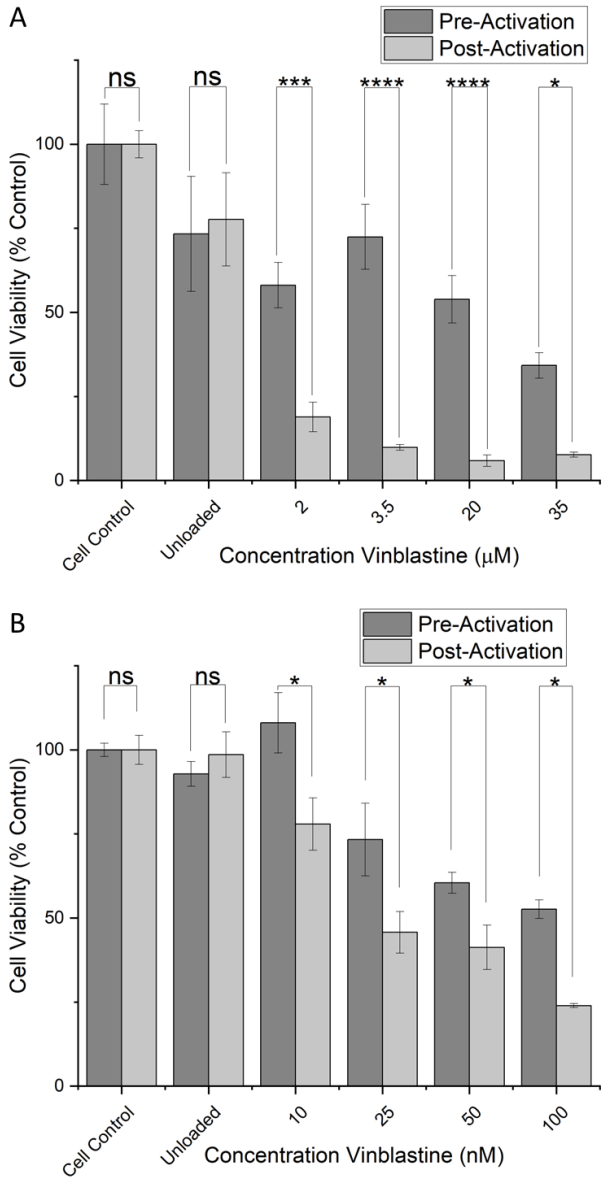


*Figure 6. 4: Cell viability was assessed by delivering vinblastine via the NCC to cells in vitro to U87-MG cells (A) and MCF-7 cells (B). The x axis represents concentrations of drug carried and released by the NCC. Cells refer to the cell only control and is set to 100%. Unloaded refers to cells incubated with a 2 mg/mL solution of the NCC without bound drugs. All data labelled as pre-activation refers to populations of cells that have not been exposed to a radio wave stimulus, and have remained at a temperature of 37.5˚C throughout the experiment. All data labelled as post-activation refers to populations of cells that are exposed to 6 cycles of the radio wave stimulus, including the cell only and unloaded particle controls. All data is scaled as a percentage of cell survival normalised to the cell only control. Significance was assessed using a two-way ANOVA test, where the two independent variables were concentration of added drug and activated or inactivated particles, values were compared to that of the untreated cell control. P values are represented by; ****=p<0.001,***=p<0.005 **= 0.01, *=p<0.05, ns=p>0.05. The data is presented as the means ± standard deviation as error bars, where n= 3.*

As a second model drug, Vinblastine was delivered to U-87 MG cells using the NCC ((Figure 6.4 A). Incubation of the unloaded NCC with U-87 MG cells did show limited cell death, pre- and post- activation. This is likely due to U-87 MG cell susceptibility to high concentrations of iron present in the solution, showing a much lower tolerance than RD cells and exhibiting a similar response to that of RH30 cells.[209] A high degree of cell death is seen for activated particles. Delivery of 2 μM vinblastine resulted in 83% (+/- 6%) reduction in cell viability (Figure 6.4 A). Near total cell death (95% ± 1.8%) was seen in U-87 MG cells after incubation with NCC-VIN equivalent to 20 μM vinblastine (Figure 6.4 A).

The estimated EC50 value for vinblastine when delivered to U87-MG cells was reduced slightly in comparison to the administration of the free drug alone. The estimated EC50 for activated NCC was 216 nM and 252 nM for the bare drug.

Parallel to the delivery to U87-MG cells, Vinblastine was delivered to MCF-7 breast cancer cells at concentrations around the calculated bare drug EC50 (chapter 4). No significant cell death was observed with a 2 mg/mL concentration of unloaded particles, activated or left in a pre-activation state ($p>0.5$, Figure 6.4 B). At low concentrations only activated particles caused cell death, a 24 % (+/-4.6 %) reduction in cell viability was observed for a concentration of 10 nM activated NCC, compared to no significant cell death for pre-activation particles ($p>0.5$ Figure 6.4 B). The greatest observed reduction in cell viability occurred at 100 nM delivered drug in an activated NCC state, with a 77 % (+/-1 %) reduction in cell viability. In comparison to the NCC left in a pre-activation state which caused a 48 % (+/-3.5 %) reduction in cell viability, there was a significant difference ($p<0.05$, Figure 6.4 B). Generally, activated concentrations of NCC caused large reductions in cell viability at all concentrations tested. Pre-activation particles caused some cell death at higher concentrations but significantly less than that of activated NCC (Figure 6.6).

Indicating a successful stimulated chemotherapy effect, with the estimated EC50 calculated at 23.55 nM for vinblastine delivered by activated NCC, it is clear the efficiency of delivery has been drastically improved by use of this technology platform.

Paracetamol could potentially be used for metastasis from liver cancer. Delivery was investigated using NCC as a delivery vehicle. N-acetylcysteine (NAC) can reduce the toxicity of paracetamol towards liver cells. To investigate whether NAC could protect non-targeted tissue, NAC was added to cells simultaneously to delivery of paracetamol via the NCC (Figure 6.5).

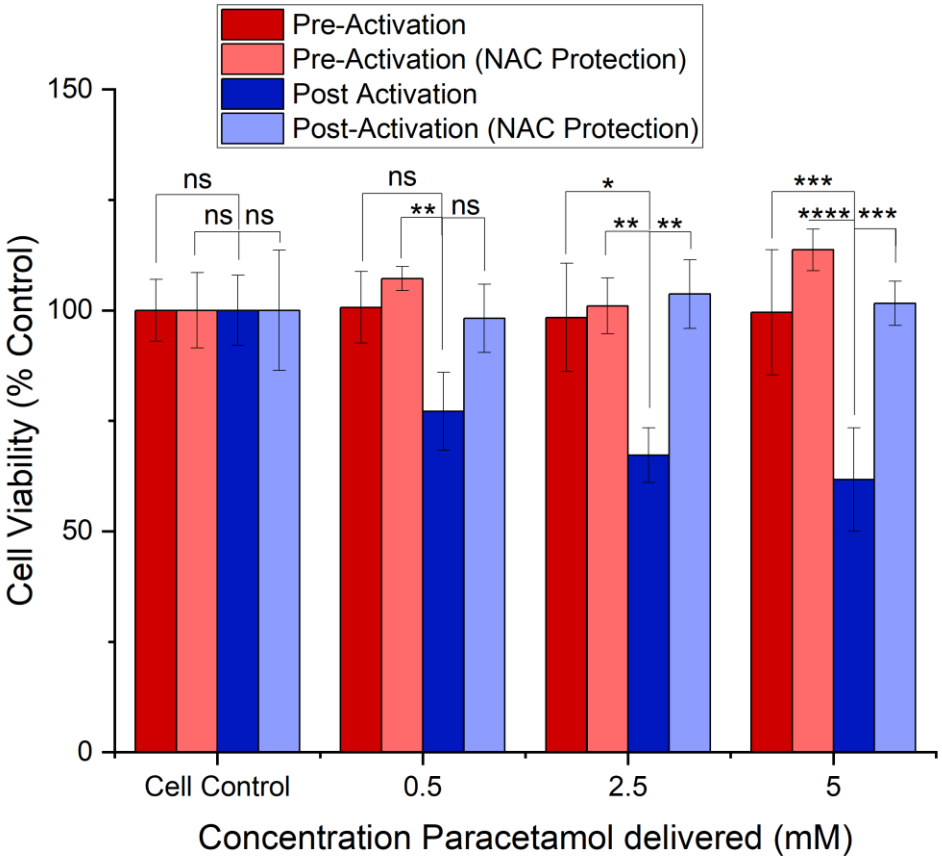


Figure 6. 5: Cell viability was assessed by delivering paracetamol via the NCC to HEP-G2 cells in vitro. The x axis represents concentrations of drug carried and released by the NCC. Cell viability was assessed by delivering chemotherapy agents to cells in vitro. Cells refer to the cell only control and is set to 100%. All data labelled as pre-activation refers to populations of cells that have not been exposed to a radio wave stimulus, and have remained at a temperature of 37.5°C throughout the experiment. All data labelled as post-activation refers to populations of cells that are exposed to 6 cycles of the radio wave stimulus, including the cell only and unloaded

*particle controls. NAC protection refers to cell populations that have been incubated with 0.5mM acetylcysteine throughout the experiment. All data is scaled as a percentage of cell survival normalised to the cell only control. Significance was assessed using a two-way ANOVA test, where the two independent variables were concentration of added drug and activated or inactivated particles, values were compared to that of the activated particles without NAC protection. P values are represented by; ****=p<0.001,***=p<0.005 **= 0.01, *=p<0.05, ns=p>0.05. The data is presented as the means ± standard deviation as error bars, where n= 3.*

Significance is compared to activated NCC without NAC protection, since all other controls have an aspect of inhibition to a therapeutic effect.

Cell death was seen for all activated but not NAC protected samples. The reduction in cell viability was more pronounced with increasing concentrations of delivered paracetamol, reaching a maximum effect of a 44 % (+/-4.2 %) reduction in cell viability at 5 mM paracetamol. The estimated EC50 was calculated at 10.13 mM for paracetamol delivered by activated NCC. There was a significant difference from all activated and unprotected particles to any other samples. Indicating a highly selective release, and the effective protection of liver cells from this therapeutic effect by admission of a 0.05 mM concentration of NAC.

6.3.4 Effect of NCC drug delivery on spheroids

In addition to 2D cell culture models, 3D spheroid models were used as a representation of avascular tumours. This experiment was done to investigate the penetration capabilities of the NCC into pseudo tumour environments. After being allowed to grow for four days, spheroids were subject to varying concentrations of NCC and activated by six LCST cycles. The diameter was measured over 72 hours and plotted as a diameter change from the diameter measured at t=0. Significance was assessed as a comparison to the size change of untreated control spheroids (Figure 6.6).

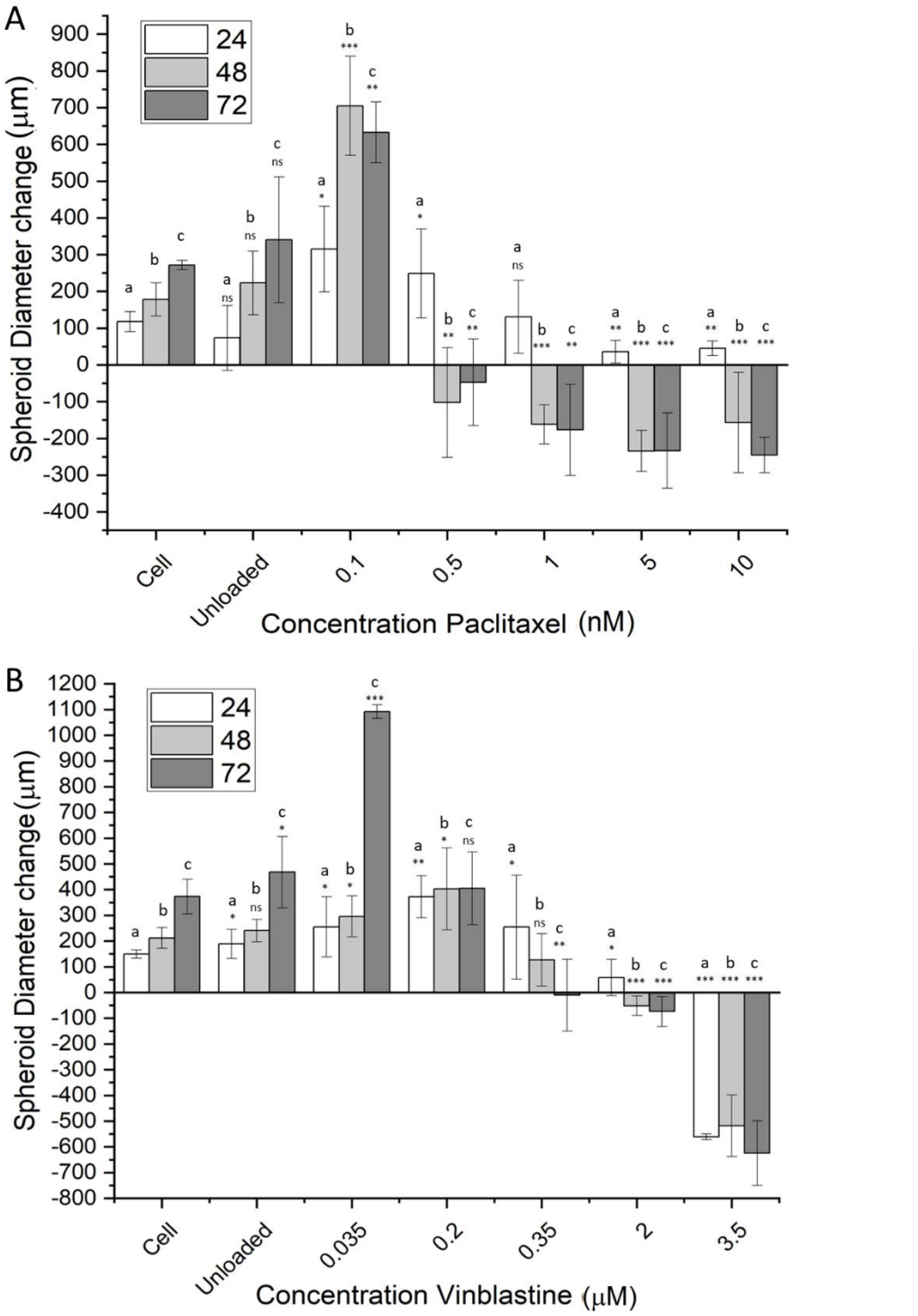


Figure 6. 6: The effect of drug delivery by the NCC on spheroid models. Spheroid diameter changes from t=0 in the presence/ absence of varying concentrations of activated NCC-Drug. (A) shows RD spheroid diameter change when paclitaxel is delivered by the NCC, and (B) shows the diameter change for U87-MG cells with the delivery of vinblastine. Change in diameter is shown over a period of 72 h. Diameters were measured using three dimensions of the radius and were performed in triplicate. Cells refer to the cell only control and is set to 100%. All data is listed as a spheroid diameter change in comparison to diameter at t=0, a represents comparison to 24 hours, b 48 hours, and c 72 hours. Significance was assessed as a one-way ANOVA test in comparison to the

*untreated cell control, labelled cells. P values are represented by; ****=p<0.001,***=p<0.005 **= 0.01, *=p<0.05, ns=p>0.05. Data shows mean +/- SD, n=3.*

Figure 6.6 A shows the diameter change in RD spheroids from the addition of activated NCC-PAC. Change in diameter is shown over a period of up to 72 hours. It is clear from Figure 6.8 that a greater reduction in spheroid diameter is seen with increasing concentrations of NCC-PAC. After 24 hours there was no significant deviation is spheroid diameter from the control up to 5 nM concentration. Concentrations greater than this showed a much smaller diameter increase than that of the cell control ($p<0.05$, Figure 6.6 A). After 48 hours a large increase in spheroid diameter was observed for 0.1 nM drug concentration. Drug concentrations of 0.5 nM and greater showed a significant decrease in spheroid diameter after 48h (Figure 6.6 A). After 72 hours spheroid diameter had reduced after incubation with 0.01 nM drug, but the diameter increase was still significantly greater than that of the control. After 72 hours concentrations of 0.5 nM and above showed a diameter reduction in comparison to the cell. Additionally, for higher concentrations, after 72 hours incubation some of the spheroids started to disintegrate entirely, contributing to larger deviation in measured diameter.

Using the same method, the capacity of the NCC to deliver vinblastine to U-87 MG cells was investigated (Figure 6.6 B). There was no difference in spheroid diameter change observed for unloaded particles in comparison to the cell control, over the entirety of the time observed (Figure 6.6 B). After 24 hours no significant difference was observed for diameter change in comparison to the control up to 2 μM added drug. At 3.5 μ M added drug, there was a dramatic reduction in spheroid diameter (Figure 6.6 B), indicating a critical concentration of vinblastine delivered. 48 hours after incubation, a concentration of 2 μM drug showed significant diameter reduction ($p<0.05$) and spheroids subject to a concentration of 3.5 μM drug

started to lose integrity. After 72 hours incubation concentrations of 350 nM and greater showed significant reductions in cell viability.

HEP-G2 spheroids were used as a further model to demonstrate the penetration capacity of the NCC for the deliverance of drugs in a tumour environment.

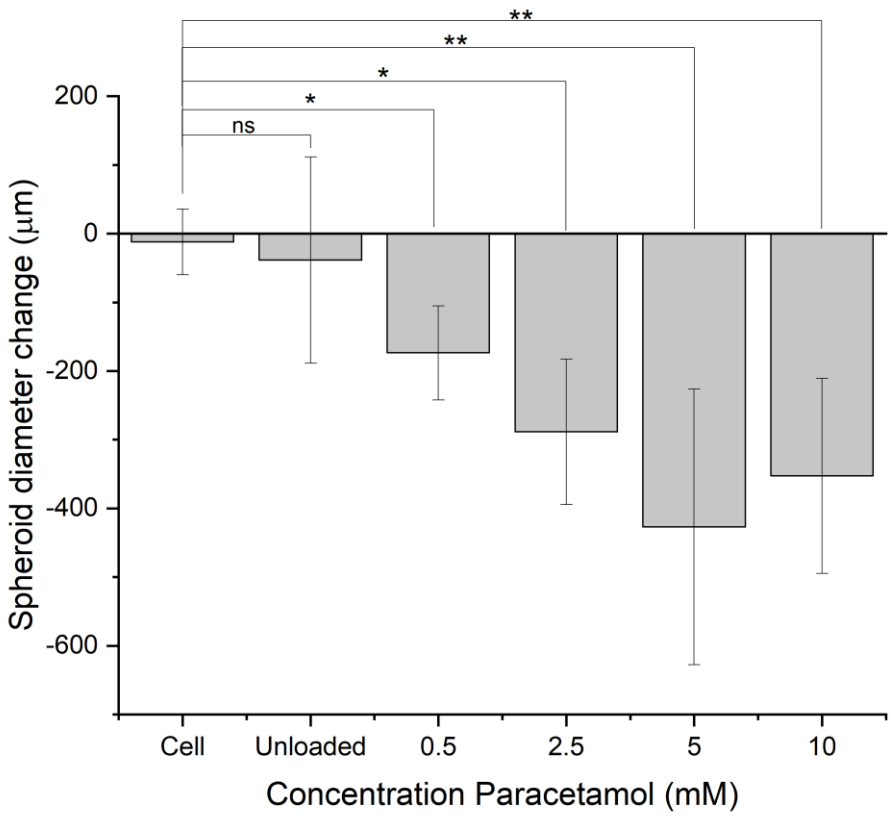


*Figure 6. 7: The effect of paracetamol delivery by the NCC on HEP-G2 spheroid models. The change in diameter of HEP-G2 spheroids after 24 hours incubation with Paracetamol loaded NCC. Diameters were measured using three dimensions of the radius and were performed in triplicate. Significance was assessed as a one-way ANOVA test in comparison to the untreated cell control, labelled cells. P values are represented by; ****=p<0.001,***=p<0.005 **= 0.01, *=p<0.05, ns=p>0.05. Data shows mean +/- SD, n=3.*

Similar to other cell lines tested there was no significant deviation in spheroid diameter compared to the control, for the treatment with unloaded NCC (p>0.5, Figure 6.7). After 24 hours there was a marked reduction in spheroid diameter for concentrations of 0.5 mM and above. Concentrations of 0.05 and 0.25

mM did show a reduction in spheroid diameter compared to the untreated control, however it was not considered significant, with p values of 0.16 and 0.06 respectively (Figure 6.7).

After 48 hours incubation it appeared that all treated Hep-G2 spheroids fell apart and there was no measurable sample for any concentrations of added drug. Both the untreated cell control and the unloaded NCC control remained intact but showed no growth in diameter over 72 hours.

6.3.5 Magnetic dictation of cells as a demonstration of magnetic direction capabilities

The magnetic direction capability of SPIONs has been demonstrated *in vivo* previously.[221,342] However, it has not been demonstrated for a nanoparticle construct such as the one described in this thesis. Therefore, it was necessary to demonstrate the capability of magnetic direction for spatial control of drug release with this drug delivery platform. Since the use of mouse models was not feasible, an *in vitro* experiment was devised.

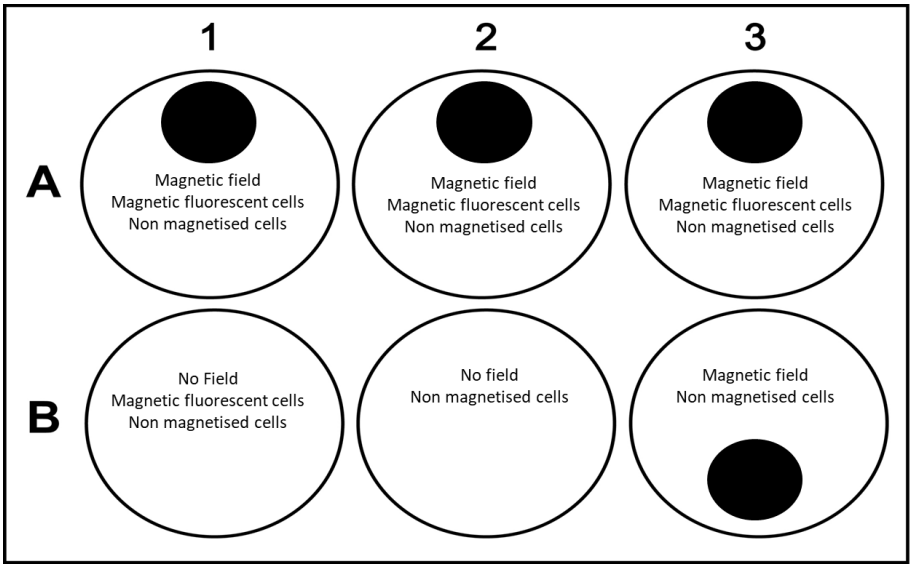


Figure 6. 8: The 6 well plate setup for the demonstration of magnetic dictation of cells by NCC-FITC. The black circles represent the position of the neodymium magnets below the plate.

A population of cells was treated with FITC-NCC for 24 hours at a concentration of 0.1 mg/mL. Following this, the magnetic particle containing fluorescent cells (MG-FLU cells) were washed, counted and mixed with an equal number of untreated control cells (CNTR cells). The mixture of magnetic particle containing and unmagnetized cells were placed in a multi-well plate with permanent magnetic fields present (Figure 6.8). The hypothesis being that MG-FLU cells will be dictated to settle around the magnet present, while CNTR cells will be distributed randomly across the well. Three controls were applied in the experiment to ensure validity: a well without an applied field with a combination of MG-FLU cells and CNTR cells, a well with only CNTR cells with an applied field and a well with only CNTR cells and no applied field. A completely random distribution of cells was expected in all control wells. The experiment was performed on two different cell lines, RD and U-87 MG cells.

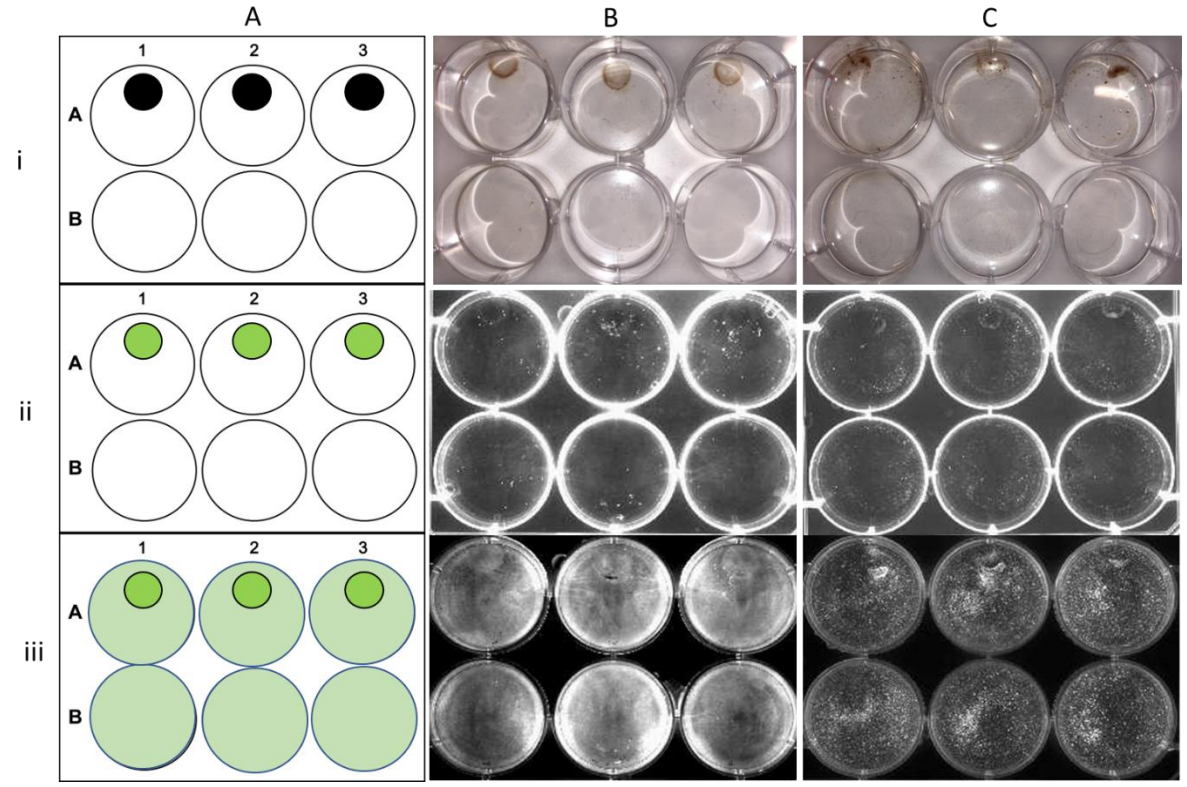


Figure 6. 9: Magnetic localisation of cells in vitro. Demonstration of the magnetic direction ability of NCC in localizing RD cells (column B) and U-87 MG cells (column C) around a permanent magnetic field. Column A shows the position of permanent magnets in the plate in row i, the expected regions of fluorescence from the

magnetised cells in row ii, and the expected fluorescence exhibited from all viable cells in row iii. Permanent magnets were placed in wells A1, A2, A3 and B2. NCC-FITC bearing cells were mixed with control cells in wells A1, A2, A3 and B1, well B3 contained no NCC-bearing cells and no magnetic field as a control. Row (i) depicts the visible light image of the plate. Row (ii) displays the same plate fluorescently imaged at an excitation wavelength of 495nm. Row (iii) shows the plate imaged fluorescently as in (ii) before but with viable cell membrane dye present fluorescently tagging all viable cells.

Cells (RD; Figure 6.9 B, and U-87 MG; Figure 6.9 C) containing the NCC-FITC were regionally fixed as a demonstration of the magnetic directability. Cells with internalised NCC particles are directed to settle under the permanent magnetic field when applied; this is exhibited by the presence of FITC fluorescence in these cells. Under FITC excitation a distinctive ring of fluorescence around the position of the magnet can be observed, indicating that the MG-FLU cells have been dictated to settle around the permanent magnetic field (Figure 6.9 B and C). The lack of fluorescence in other areas of the well demonstrate that MG-FLU cells have been gathered at very high rates. To demonstrate that CNTR cells are present and distributed randomly on the plate, a fluorescent membrane dye was added after FITC imaging. A random distribution of cells was seen across all three controls. Furthermore, the magnetic field did not affect the distribution of non-NCC containing cells (membrane stained) within the plate, nor the cell viability of either population. Without the presence of a magnetic field, the MG-FLU cells were distributed randomly across the well.

6.4 Discussion

6.4.1 Haemolysis effects of the nanoparticle copolymer complex

If the amount of haemolysis is less than 10%, a substance is said to be typically biocompatible.[340] This data indicated the NCC could be generally biocompatible, a useful property for moving forward with this technology to the clinic. Although, this data does not indicate how the NCC would affect healthy tissue in

physiological conditions, thus further *in vivo* experimentation would need to be done to confirm biocompatibility.

6.4.2 Enhanced cell death with radio wave stimulation of the NCC

The aim of this study was to create a drug delivery platform that could improve the specificity of drug delivery to cancer cells. The principal manner in which this was attempted was the retention of drug bearing proteins to the nanoparticle complex until release by means of stimulation by radio waves. To demonstrate the versatility of the complex, three examples of chemotherapeutic agents were delivered selectively to cancer cell lines.

Paclitaxel

An increase in cell viability was seen when RD cells were subjected to a 2 mg/mL concentration of unloaded NCC, this was likely due to the availability of iron as a micronutrient allowing RD cells to proliferate.[343] In RD cells neither pre-activation unloaded NCC, nor pre-activation NCC-PAC caused cell death at any concentrations tested (up to 100 nM; Figure 6.3 A), indicating no off target effects of the activation method or toxicity from the complex itself. The calculated value for the EC50 of paclitaxel when delivered by the activated nanoparticle copolymer complex was 8.92 nM. This value is slightly lower than that observed for the bare drug in chapter 4 (11.9 nM). This could be a consequence of the efficiency of nanoparticles crossing cell membranes in comparison to the drug alone, thus increasing the observed therapeutic effect of the drug. The unloaded and the pre-activation particles caused no significant cell death whereas the activated complex caused huge reductions in cell viability even at low concentrations (Figure 6.3 A).

Delivery of paclitaxel to the RH30 cell line showed similar cell viability reductions to that of paclitaxel delivered to RD cells when the complex was activated. Some reduction in cell viability was observed for the 2 mg/mL unloaded concentration of the NCC (24 %), this indicates some level of sensitivity of RH30 cells to the complex. Unlike in the RD cell line, pre-activation particles also showed a reduction in cell viability at all concentrations observed, although not significant in comparison to the reduction in viability of activated NCC. For higher concentrations pre-activation particles also showed a plateau effect on cell viability (Figure 6.3 B). This is likely due to some passive release of drug bearing protein from the NCC being broken down at higher rates in RH30 than in RD cells, leading to a greater effect overall of the NCC, both when activated and left in a pre-activation state. In addition to this, the presence of the NCC acting as a micronutrient allowing RD to proliferate may have compensated for any viability reduction due to passive release of drug. The EC50 value (5.14 nM) for paclitaxel when delivered to RH30 cells by activated NCC was reduced considerably in comparison to the admission of the free drug alone (16 nM, chapter 4).

Comparison to current paclitaxel delivery methods

Being one of the most used chemotherapy drugs, paclitaxel delivery has been enhanced by the use of nanoparticles in a huge number of ways. A vast number of polymeric nanoparticles have been developed, these help increase drug circulation times and uptake.[344] Abraxane is a clinically used HSA-paclitaxel nanoparticle.[273] Abraxane has shown significant tumour responses and prolonged disease control in small cell lung cancer and metastatic breast cancer. Although it has improved the efficacy of paclitaxel in comparison to conventional delivery (by chremphor el) it lacks any form of active targeting. Polymeric nanoparticles consisting of paclitaxel and poly-L-glutamic acid made it to phase three clinical trials, but failed due to lack of efficacy and unacceptable levels of toxicity.[345 – 347] Paclitaxel loaded cationic liposomes

developed by MediGene showed considerable survival benefits for patients.[348] Similar to abraxane, liposomes and polymeric particles typically lack targeting or smart release systems, therefore will pose a high level of systemic toxicity to patients.

Magnetic particles and stimulated release systems are a new field of development for the delivery of paclitaxel, inherently smart release systems aim to reduce systemic toxicity. Paclitaxel bound to magnetic particles increased the stability and water solubility of the drug. The inhibition of cellular growth was even more pronounced when magnetic targeting was applied to the bound-paclitaxel.[349] Paclitaxel-loaded magnetic particles modified with methoxy polyethylene glycol (PEG)-lysine-oleic acid have been shown to accumulate in kidneys around a buried ultrasmall magnet, demonstrating an example of *in vivo* magnetic localisation in combination with paclitaxel delivery.[350] Although, showing beneficial properties these loaded particles show not form of controlled release. Paclitaxel-loaded magnetic nanoparticles encased in a biotinylated N-palmitoyl chitosan sphere have been developed and showed a 37 % reduction in cell viability with a 0.1mg/mL concentration of particles. This is a lesser affect than observed by the system developed in this study, which caused a 54 % reduction in cell viability at the same concentration of added particles (Figure 6.5 A and B) (NCC post activation, 25 nM drug = 0.1 mg/mL NCC). Magnetoelectric nanoparticles coated in glycerol monooleate, Tween-20, or ethyl-3-(3-dimethylaminopropyl)carbodiimide showed controlled release of paclitaxel in a low frequency AMF field (<1 kHz). The AMF induces electromagnetic changes in the coating layer that entraps paclitaxel. After stimulation a reduction in cell viability of 19% in SKOW cells was seen for a concentration of 0.05 mg/mL particles.[351] Again, this reduction in cell viability is less than in any cell lines tested in this study with the equivalent concentration of particles.

Vinblastine

A high degree of cell death is seen for activated particles with delivery of vinblastine with activated NCC. Incubation of the NCC-VIN with U-87 MG cells did show some degree of cell death from pre-activation particles, however, there is still a high degree of discrimination between pre- and post-activation for the NCC construct ($p<0.01$, Figure 6.4 A). The fact that unloaded NCC does not cause significant cell death after AMF activation indicates that there is minimal direct hyperthermic damage to the cells, and that the temperature increase of the particles serves only to modify the polymer to cause drug release.

Vinblastine delivered to MCF-7 cells showed large reductions in cell viability. Generally, activated concentrations of NCC caused large reductions in cell viability at all concentrations tested. Pre-activation particles caused some cell death at higher concentrations but significantly less than that of activated NCC (Figure 6.4 B). Indicating a successful stimulated chemotherapy effect, with the EC50 calculated at 23.55 nM for vinblastine delivered by activated NCC and 33 nM for the bare drug, it is clear the efficiency of delivery has been drastically improved by use of this technology platform.

Comparison to current vinblastine delivery methods

At the time of writing, there are no clinically available nanoparticle delivery methods for vinblastine.

Vinblastine loaded polymeric nanoparticle have been shown to encapsulate vinblastine and release it over 48 hours. The particles were engineered to serve a as drug carriers for targeted delivery of vinblastine to FA-receptor-positive tumour cells, slowing the growth of xenografted tumours. The study showed high vinblastine accumulation in tumour tissue but low release in blood or healthy tissue.[352] However, like other non-stimulant responsive systems, there is still the possibility of off target release. Chitosin microparticles encasing vinblastine and SPIONs, showed stimulated release of vinblastine when permanent magnetic fields

were applied to tear open particles. However, concentrations of 1 mg/mL particles showed only a 8 % reduction in cell viability with MCF-7 cells, a fraction of the effect for the equivalent concentration used in this study (0.1 mg/mL NCC = 116 nM vinblastine caused 77 % cell death in MCF-7 cells).[353]

Paracetamol

Paracetamol is biocompatible with most body tissues, thereby reducing any potential off target effects. However, the treatment of metastasis from the liver, with paracetamol, has one major drawback, the toxicity of paracetamol to healthy liver tissue. Localized drug release could greatly reduce this off-target effect, but at the clinical concentrations used for chemotherapy, a further level of protection may be needed. N-acetylcysteine (NAC), can be used to eliminate the effect of paracetamol toxicity in liver tissue.[339] Administering NAC to healthy liver tissue while destroying any metastases could therefore eliminate side effects.

Some nanoparticle formulations for the delivery of paracetamol have been devised. However, these designs are tailored towards general systemic admission to the body, not for a chemotherapeutic effect. Core – shell biodegradable microspheres loading human serum albumin and paracetamol were fabricated with a hydrophilic alginic acid shell and a hydrophobic poly(lactic-co-glycolic acid) core. These microspheres showed paracetamol release over two weeks.[354] Glycerol Monostearate lipid nanoparticles of 270 nm size showed paracetamol encapsulation and release.[355] No paracetamol delivery methods in literature showed forms of active targeting or specific release mechanisms.

It can be concluded, with the assessment of *in vitro* data, that in principle the delivery of paracetamol to metastases from the liver, can be carried out selectively by delivery using the NCC, while protecting healthy

liver tissue by intravenous injection of NAC. This could be developed into an extremely discriminant way to treat a deadly metastatic cancer with one of the lowest rates of survival.

General effects of delivery by the NCC

Throughout the cell lines tested, there was no significant difference in cell death observed for activation vs pre-activation unloaded concentrations of NCC. This indicates there is no cell death caused by the activation through application of radio waves, reinforcing the hypothesis that the stimulus method is biocompatible. When drugs were delivered with activated NCC, cell death was significantly higher than the same concentration with the NCC left in in a “pre-activation state”. Particularly, in low concentrations of delivered drug, significant cell death was caused by the activated NCC, but little or no significant cell death was observed for the pre-activation sample. This indicates a degree of selective therapeutic effect upon radio wave activation of the complex. At higher concentrations of drugs delivered, some cell death was observed for the NCC in a pre-activation state, this could be a result of passive release of drug bearing proteins of the complex. This passive release could potentially be remedied with further enhancement of the copolymer synthesis method (Chapter 5).

When compared to the AMF stimulated methods in section 6.1, our system shows several advantages: one being the self-contained nanoparticle copolymer complex not forming a larger hydrogel/polymer matrix. This allows it to utilise the EPR effect and allows more efficient crossing of cell membranes, unlike a larger structure. In addition, the NCC is stable for an extended period, unlike liposomes and micelle structures which degrade and release any payload in a simplistic burst release fashion. The potential for staggered drug

release from the NCC could allow for staged treatment to counter the fractional kill effect, with only one administration of treatment.

The estimated EC50 values for the delivery of paclitaxel and vinblastine were reduced by delivery with activated NCC, this could be an effect of the higher rates of nanoparticle transfer across cell membranes than drugs alone. [356]

The data presented is evidence to support the conclusion that the platform presented in this project can provide a drug delivery method that has the capacity to have a limited cytotoxic effect until release is triggered by a harmless external stimulus in the form of radio waves. In comparison to other paclitaxel, vinblastine and paracetamol carriers, the system described in this study showed greater reductions in cell viability, and greater spatial control. Although stimulation of the NCC consistently showed significant increases in cell death, in some cases significant cell death was observed for samples that weren't stimulated. The two-way ANOVA test validated this conclusion, with all activated concentrations showing significance differences when compared to the untreated control and the equivalent pre-activation concentration.

6.4.4 Effect of drug delivery to cell spheroids

The spheroid models showed good biocompatibility for the unloaded NCC, as no significant cell death is seen with any cell line. Concentrations of delivered drug showed reduction in spheroid diameter compared to the untreated control, exhibiting a level of penetration into the greater structure. Generally, spheroid diameter continued to reduce as incubation time increased. Higher concentrations of delivered drug generally caused a quicker reduction in spheroid diameter.

In RD cells incubation with a concentration of 0.1 nM delivered drug caused an increase in spheroid diameter up to 72 hours (Figure 6.8). After 72 hours spheroid diameter had reduced after incubation with 0.1 nM drug, but the diameter increase was still significantly greater than that of the control. This is likely a result of the different cell death mechanism paclitaxel shows at low concentrations causing cells and therefore the spheroid to swell.[280]

The disintegration of treated HEP-G2 spheroids after 48 hours is likely a result of the weak structural integrity of HEP-G2 cells in comparison to RD and U87-MG spheroids.

6.4.5 Magnetic localisation of cells and nanoparticles

Cells were successfully directed to settle around applied fields after internalisation of the NCC (Figure 6.9). Without a field present, the cells and therefore particles are randomly distributed. Cells with no internalisation of the NCC were not affected in terms of distribution or cell viability. The data shows that in principle the NCC could be localised *in vivo* by the implementation of magnetic fields. However, mouse modelling work would need to be done to assess what capacity the particles could be directed by gradient fields that are used for current localisation methods.[357]

6.5 Conclusion

We have reported here the development of a highly discriminant, directable, and controllable method of chemotherapy drug delivery. We have shown that the complex is capable of immobilising and releasing, upon radio wave activation, drug carrying bovine serum albumin. The complex was shown to be generally biocompatible by low rates of haemolysis in blood, and no significant toxicity observed in pseudo tumour models. It was demonstrated that the complex, once drug loaded and activated, can induce cell death by

controlled release of paclitaxel, vinblastine, and paracetamol. Selective cell death can be achieved using the activation method, giving the possibility of chemotherapy with reduced side effects. The platform shows the potential to efficiently and selectively deliver a huge variety of drugs, not limited to chemotherapy. In comparison to clinically available delivery methods, the technology described in this project shows potential to provide a much more effective delivery method.

Pseudo tumour models showed that the complex could penetrate tissue and cause significant shrinking of spheroids over a three-day period. Through dictation of cell location by magnetisation with the nanoparticle complex, in principle it is proven that the complex can be easily manipulated by magnetic fields to gather in specific locations for treatment. This allows the possibility for spatial as well as temporal drug release within the body.

Consequently, this complex provides a method for chemotherapy agent delivery that has the potential to provide effective treatment while reducing or eliminating side effects. Discontinued drugs with severe side effects could be effectively utilised with this treatment since the therapeutic effect would be systematically increased.

Chapter 7: Computational modelling of induction heating parameters

7.1 Introduction

For inductive heating of superparamagnetic particles at high frequencies and low concentrations, joule heating is not possible, the single crystal particles are too small for significant current resistance. Furthermore, there is only one magnetic domain present in each particle (assuming single crystal) so there is no contribution from hysteresis losses.[49,106,108,115,205] The heat is instead driven by two distinct processes, the first being Brown relaxation and the second Neel relaxtion.[106,358] Brown relaxation occurs when a nanoparticle physically rotates to align with the applied field, resulting in heat dissipation through frictional interaction between the particle and its surrounding medium. For field frequencies greater than 100 kHz, the contribution from brown relaxation is negligible.[224] Neel relaxation occurs when the nanoparticle remains stationary and the magnetic moment rotates within the crystal. Both relaxation events place the particle in an energy well releasing thermal energy in accordance with the first law of thermodynamics.[359]

The heating rates of particles can be predicted mathematically following the linear response theory (LRT) of heating.[206] Herein we use the linear response theory to develop a model capable of predicting heating required for activation of the particles described in this project *in vivo*. In a larger scheme, the developed model would consider many aspects of treatment, such as the drug dosage required to be delivered, location of tumour, type of tumour and the vascular environment, to provide ideal parameters of treatment, such as NCC dosage and induction heating parameters. As a part of the intended larger scheme, the model detailed in this chapter takes into account factors such as the frequency and strength of the field used, the SPION

core diameter of particles used, and the total mass of the nanoparticle copolymer complex. The model described in this chapter can predict the heating efficiencies and activation times of the NCC based on the LRT.

7. 2 Materials and methods

7.21 Script language used

Python is a high-level, interpreted, general-purpose programming language. Its design philosophy emphasizes code readability with the use of significant indentation.[360] Python is dynamically-typed and garbage-collected. It supports multiple programming paradigms, including structured (particularly procedural), object-oriented and functional programming. [361,362]

Script interface

Scripts were created and run in JupyterLab user interface provided by the Anaconda platform with an open-source licence. Results were formatted into excel spreadsheets and heat maps of the results were produced and analysed.

7.2.2 Constant values

The values used for the constants in the calculations were as follows; Boltzmann constant (kB) $1.38e^{-23}$ m^2 kg s^{-2} K^{-1}, human body temperature (starting temperature, T)=310.5 K. Magnetic permeability of water (Uw) $1.256e^{-6}$ H m^{-1}, pi 3.141, Temperature dependent saturation magnetisation (Ms) $2.97x10^5$ Am^{-1}, Temperature dependent anisotropy (Keff) $4e^4$ Jm^{-3}, lifetime constant (Tau_O) $1e^{-9}$ s, permeability of free

space, (Uo) π *4e-7 T m A^{-1}, density of magnetite nanoparticle 5170000 g m^{-3}, temperature change of particles ΔT 5.5 K, heat capacity magnetite (Cp_m) 0.636 Jg^{-1} K^{-1}, Heat capacity copolymer 0.307 Jg^{-1} K^{-1}.

Assumptions of the model in relation to the constants use include; value of temperature dependent saturation magnetism and the temperature dependant anisotropy for iron oxide particles doesn't change from 310.5-315 K. In addition to this, it is assumed that the specific heat capacity of the copolymer does not vary from the value measured in chapter 3.

7.2.3 Variables

The input variables used in the pilot model included a frequency range from 80-800 kHz, particle diameters from 5-15 nm, and a field strength from 2000-15,000 Am^{-1}.

7.3 Results

7.3.1 Model design and calculations

The overall goal of the simulations in this study was to predict the perfect treatment parameters (Figure 7.1). This included dosage of nanoparticle copolymer complex, number of release cycles of drug, and the ideal induction heating parameters for the stimulated release. The inputs to the model would be the location and physiology of the tumour; giving information on the field strength the particles would be subject to at the target location. After calculating the field strength the particles would be subject to, and the relaxation rates of the SPION cores, the model would predict the ideal frequency for heating and also the necessary exposure time for active release (Figure 7.1). Also giving information on the likely accumulation rates of the

nanoparticle copolymer complex within the tumour, combining that with the efficacy of the delivered drug to that cancer type, would allow for an effective dose to be calculated by the model.

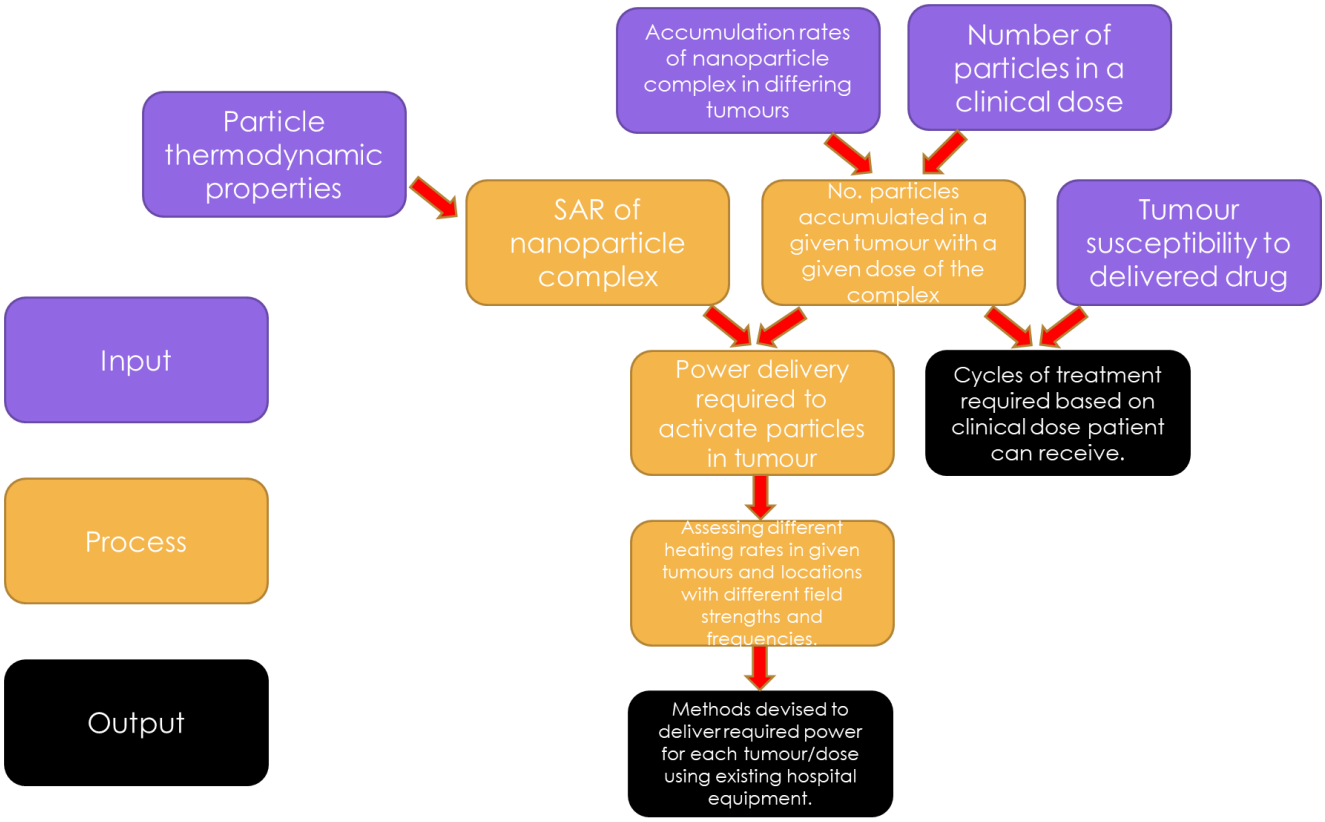


Figure 7. 1: Overall model flow chart design for use in the clinic. With the patients treatment parameters acting as an input, the model can process the information and output ideal parameters for dosage and activation of the complex in the tumour location.

Before the larger model could be constructed and tested, a smaller pilot model for prediction of heating times was designed and created (Figure 7.2). The inputs of this pilot model being the thermodynamic properties of the particles, namely magnetic relaxation times and specific heat capacities, dependent on particle diameter. The result is heating efficiencies of the particles dependent on the induction heating parameters, including time of irradiation to heat particles from 37.5 °C to 42.5 °C.

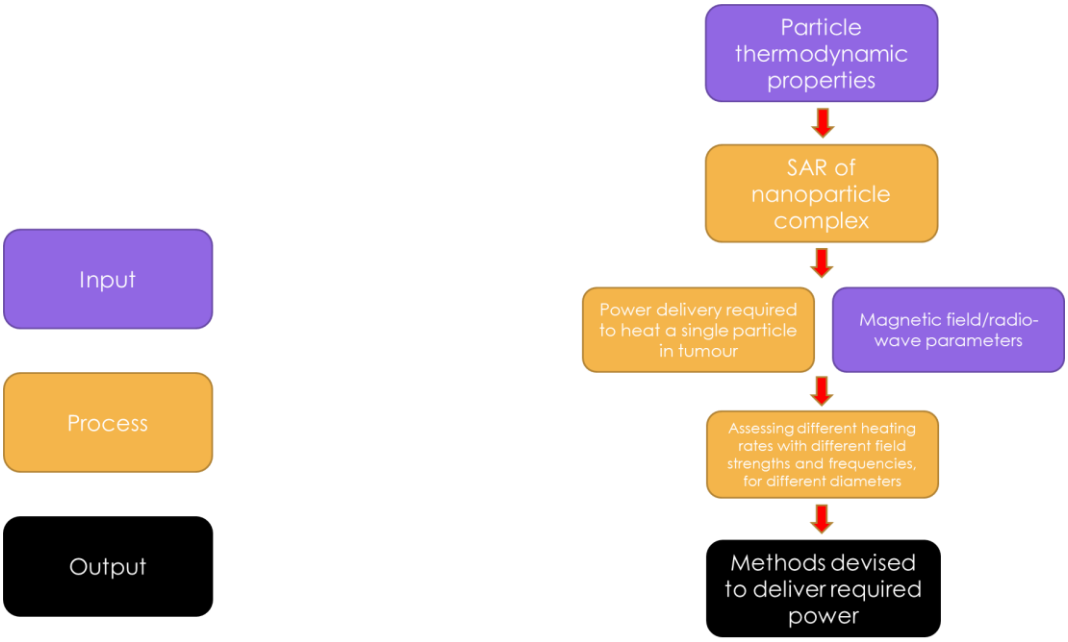


Figure 7. 2: Pilot model design. Flow chart design for the initial pilot model for prediction of heating times of differing particles, with the particle properties and induction heating parameters acting as an input, the model processing the information and outputting ideal parameters for activation of particles and stimulated release.

Simulated nanoparticle heating rates were calculated by adaption of the linear response theory (Equation 7.8).[107] Initially, physiological and thermodynamic parameters of the nanoparticle in question require to be calculated. Calculating the volume of a particle core with a given diameter (D, meters), which is necessary for calculating the mass of particles:

$$V = \frac{4\pi}{3}\left(\frac{D}{2}\right)^3 \quad Equation\ 7.1$$

Calculation of the mass (m, grams) of a particle with Diameter D is given by the equation:

$$m = V \times p \quad Equation\ 7.2$$

Where ρ represents the density of magnetite (grams m^{-3}). The energy required to heat a single particle core and the mass of grafted copolymer (Q_C and Q_P) can be calculated separately:

$$Q = m \times c \times \Delta T \quad Equation\ 7.3$$

Where m is the mass of each component, c the heat capacity of each component and ΔT the change in temperature. For the total energy required to heat the complex to activation, the sum of the energy for each component is simply added together.

The relaxation time of particles is needed to calculate how much heat is generated in relation to the frequency of the changing field. K_{eff} is the temperature dependent value for K, the magnetic anisotropy of the particles; for a five-degree temperature change, it is assumed the change in the value for this property is negligible. Due to the high frequencies used in this study and in the clinic, combined with the constrictive effects of human tissue, it is assumed that there is no heat contribution from Brownian relaxation. Therefore, Neel relaxation is the only contributing heating effect, and lifetime of the particles (τ) can be calculated by:

$$\tau = \frac{e^{\frac{K_{eff} \times V}{k_B \times T}}}{\frac{K_{eff} \times V}{k_B \times T}} \tau_0 \quad Equation\ 7.4$$

Where τ_O is the lifetime constant, V is the volume of the nanoparticle core, k_B is the boltzman constant, and T is the temperature in Kelvin.[363] Therefore, the power input of particles per unit volume, given in watts per meter cubed per second, following the linear response model is given by:

$$Power\ input(SAR/PLIN) = \pi \mu_O^2 \frac{M_s^2 V}{3 k_B T} H^2 f \frac{2\pi f \tau}{1 + (2\pi f \tau)^2} \quad Equation\ 7.5$$

Where H is field strength (A m^{-1}) , f is frequency of the field (Hz), saturation magnetisation (Ms) is 2.97x10^5 Am^{-1} (57.5 emu g^{-1}=297.3 emu cm^{-3}) and permeability of free space (Uo) is π *4e-7 T m A^{-1}. Therefore, to transform this value into the power input per particle, in watts per second:

$$Power\ generated\ per\ particle = Power\ input \times V \quad Equ\ 7.6$$

Since energy is equal to power multiplied by time, assuming no heat dissipation from the sample to the surroundings and following the first law of thermodynamics. The time taken to heat a single particle from body temperature to activation temperature with the given input values:

$$Heating\ time = \frac{Q_{Particle}}{Power\ per\ particle} \quad Equ\ 7.7$$

The values for power input/SAR (PLIN), Power per particle (PPP) and Time taken for activation were calculated by the script dependant on the variables of field frequency, field strength and particle diameter. The results were formatted in heat maps where one variable was fixed and the patterns in the results studied by change in the other variables.

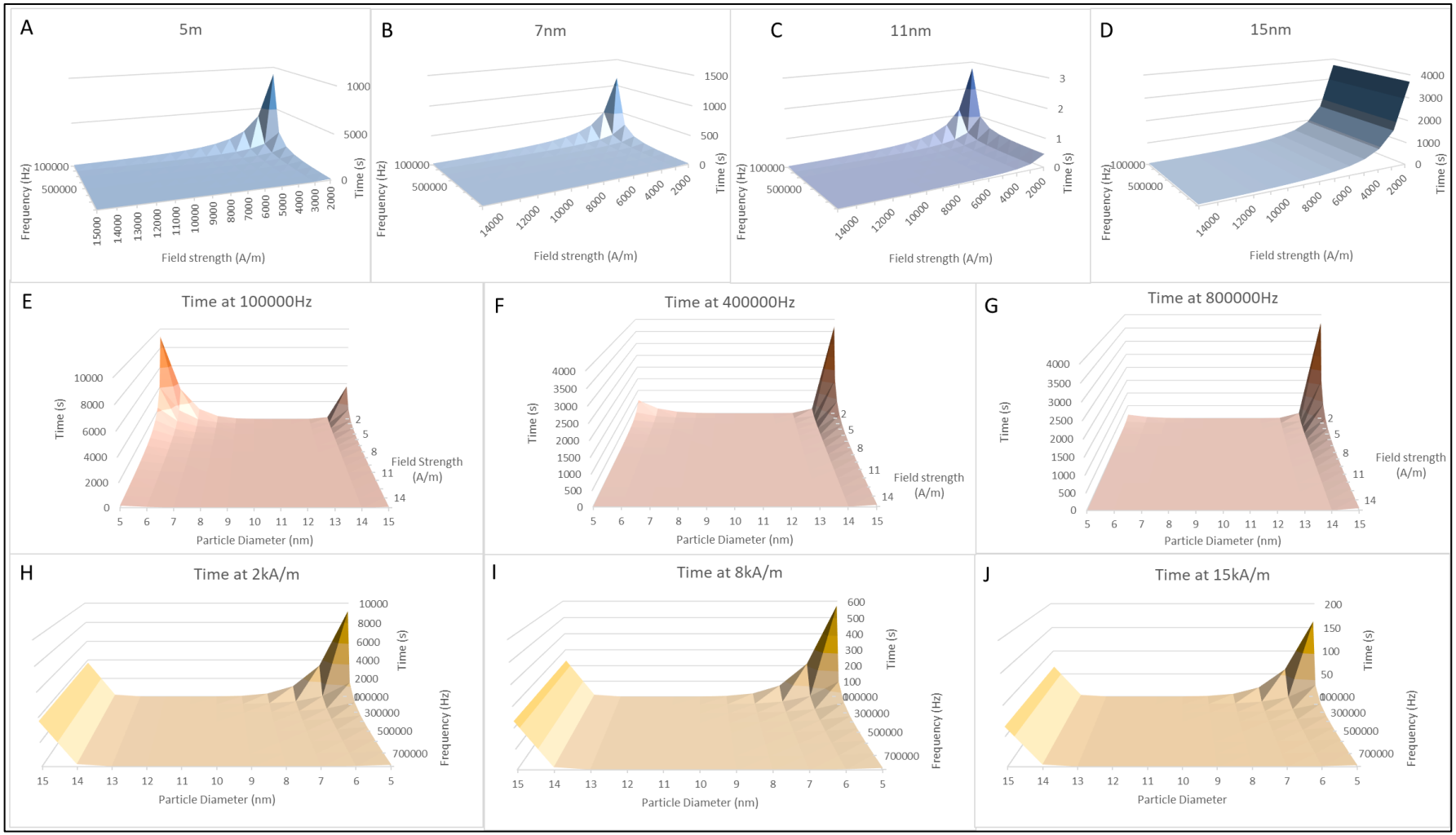


Figure 7. 3: Predicted heating times required for activation of the NCC dependent on induction heating and particle parameters. The heating times required to heat particles from human body temperature to activation temperature based on the linear response theory (Equation 7.7). The results are presented by fixing one of the variables; a-d diameter is fixed, e-g frequency of the field is fixed and h-j where the field strength is fixed.

7.3.2 Study of parameters affecting activation heating times

When the inputs are run through the programme the results are produced and formatted rapidly, subsequently the heat maps are produced fixing either particle diameter (Figure 7.3 a-d), field frequency (Figure 7.3 e-g) or field strength (Figure 7.3 h-j).

In relation to diameter, heating times are at their lowest overall for 10-12 nm particle diameters. As particle diameter decreases from 10 nm heating times increase, the same is true for particle diameters greater than 12 nm, as the diameter diverges further from 12 nm the heating times increase. Heating times were minimal at low frequencies and low field strengths for all diameters except 15 nm particles (Figure 8.3 a-d). For 15 nm particles frequency had no effect on particle heating times. An increase in frequency generally caused a decrease in heating times from in nanoparticles of 5-13 nm in diameter (Figure 8.3 e-g).

Shortest heating times were observed at 11/12 nm with 15 kA/m fields and 800 kHz frequency. The longest heating times were observed for 5/15 nm particles at low field strengths and low frequencies.

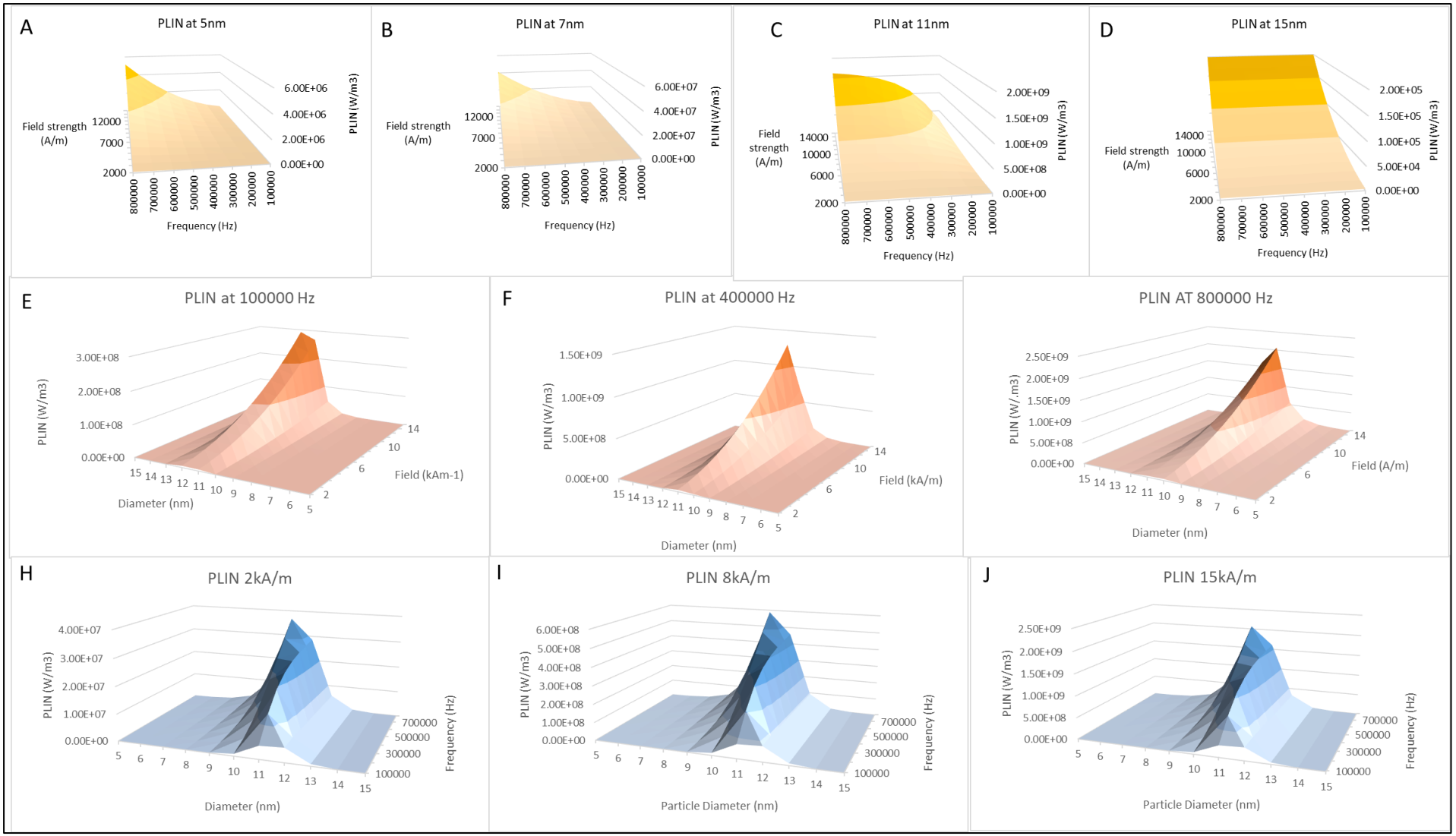


Figure 7. 4: SAR or Power generated by NCC particles from the linear response model (PLIN) In Wm^{-3}. The results are presented by fixing one of the variables; a-d diameter is fixed, e-g frequency of the field is fixed and h-j where the field strength is fixed.

7.3.3 Study of parameters affecting linear heating rates (SAR)

The measurement of PLIN (SAR) of the particles was processed akin to time taken for activation (Figure 7.3) with the rates of heating/absorbance rate represented as a power input value (Figure 7.4).

Again, SAR reaches its maximum for all diameter particles at the highest frequencies and the strongest field strengths. Stronger fields always increase PLIN, proportional to field strength squared, this is represented by the exponential curve of the heat map with increasing field strength (Figure 7.4 E,F, and G). With a fixed frequency field the highest PLIN values were observed at 12 nm at 100 kHz, 11 nm at 400 kHz and 10 nm at 800 kHz with 15 kA/m fields. The lowest PLIN values were observed for 15 nm particles at low field strength. As frequency increases from 100-800 kHz the diameter of the most efficiently heated particles diameter decreases.

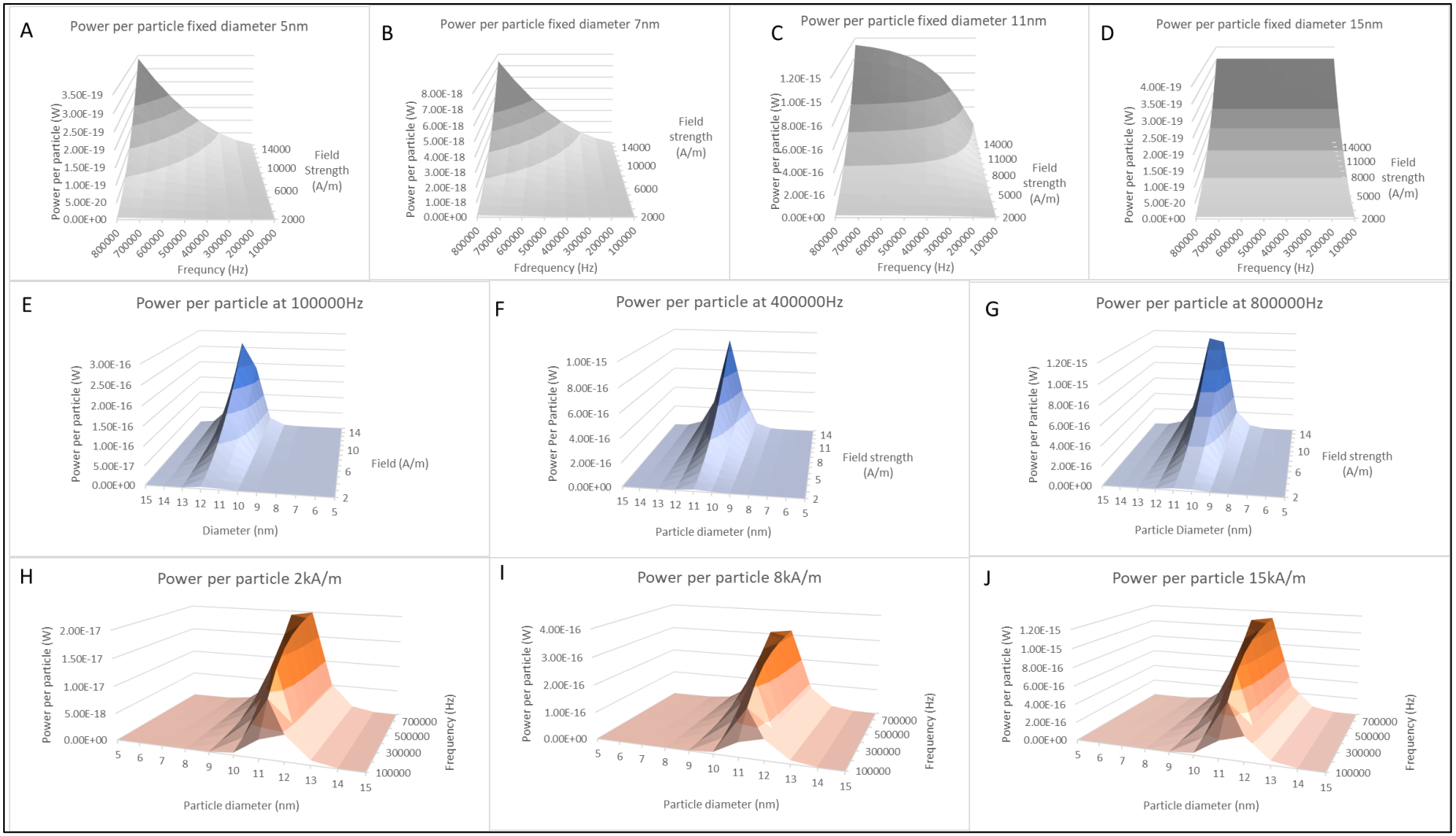


Figure 7. 5: Power generated per particle from the linear response model (PPP). The results are presented by fixing one of the variables; a-d diameter is fixed, e-g frequency of the field is fixed and h-j where the field strength is fixed

7.3.4 Study of parameters affecting power produced per particle

The results of the power supplied per particle (PPP) (Figure 7.5) showed very similar trends to that of SAR. The results for fixed diameter and fixed frequency graphs showed identical trends (Figure 8.4 a-g and Figure 8.5 a-g) with the exception of the power per particle exhibiting a maximum at 400 and 800 kHz with 11 nm diameter particles. This contrasts with SAR where 10 nm particles showed the maximum at 800 kHz. This change could be a result of the slightly larger diameter of the 11nm particles allowing for a greater total output of power than 10 nm particles, which have a smaller volume (Figure 8.5 e,f, and g). PPP is greatest at 11-12 nm depending on frequency where lower frequency favours 12 nm and higher frequency favours 11 nm (Figure 8.5 g & j). With small diameters PPP is scarcely changed by field strength and frequency is the greatest factor in the power supplied by the particle. This trend is observed in the SAR of smaller particles, shows the reverse in terms of heating times. In contrast, larger particles (>13 nm) frequency has very little or no effect on SAR and PPP and field strength is the dominating parameter.

7.4 Discussion

7.4.1 Linear response theory calculations

The heating rates of SPIONs are classically derived using a linear response theory (LRT).[49] The high frequency alternating field forces these relaxation processes to happen at the frequency of the AC current, hence heat generation is massive. Heat generated by a single domain particle (A) is given by (Equ 7.8):

$$A = \mu_0 \pi H^2 X'' \quad Equation\ 7.8$$

Where (μ_0) is the magnetic permeability of medium, (H) is Field strength and (χ'') is the out-of-phase susceptibility of particles. χ'' is essentially dependant on other variables that can be controlled by the applied field or the particle makeup.

$$X'' = X_0 \frac{2\pi f\tau}{1 + (2\pi f\tau)^2} \quad Equation\ 7.9$$

Relaxation time (τ), frequency of the applied field (f) and equilibrium susceptibility of particles (χ_0) all dictate the value of X''. The overall relaxation time (τ) is given by both relaxation process times of Brown and Neel relaxation mechanisms.

$$\frac{1}{\tau} = \frac{1}{\tau_N} + \frac{1}{\tau_B} \quad Equation\ 7.10$$

Where τ_N is Neel relaxation time and τ_B is Brown relaxation time. Both relaxation processes may occur and contribute to heat generation.

$$\tau_N = \frac{\frac{\sqrt{\pi}}{2\tau_0} e^{\frac{KV_M}{k_B T}}}{\sqrt{\frac{KV_M}{k_B T}}} \quad Equation\ 7.11 \qquad \tau_B = \frac{3\eta V_H}{k_B T} \quad Equation\ 7.12$$

These lifetimes are for solutions of particles in a given solution in which they are subject to Brownian motion. Given that K is the anisotropy constant for the particles, η is the viscosity of the medium, V_H is hydrodynamic volume of particle, V_M Magnetic volume of particle and τ_0 is $1x10^{-9}$ seconds (to balance units for lifetime with anisotropy constant).[15,49]

Essentially these deviations highlight the fact the heating efficiencies of superparamagnetic nanoparticles are dependent on the relaxation process of the particles, which are in turn dependant on a single magnetic domain present in each SPION. This highlights the importance of the single crystal nature of the SPION for efficient inductive heating. In the model developed here Neel relaxation is considered the only the relaxation process, hence the lifetime value is only that of Neel relaxation (equation 7.4), otherwise the calculations used in this study follow the LRT.

7.4.2 Field effects

As dictated by the linear regime model (Equation 7.8) heating rates show a linear increase with the square of the field strength.[107] It was observed in the model that stronger fields always decreased activation time, proportional to energy/ field strength squared as in equation 7.5 and dictated by the linear regime model. The PLIN values and PPP values all increased proportional to field strength squared, for all frequencies and particle diameters. This agrees with literature simulations for particles.[116,227]

7.4.3 Frequency effects

The impact of magnetic field frequency on heating rates PLIN, also dubbed specific absorption rates (SAR) has also been researched widely with most data confirming similar trends. At a fixed field strength, greater frequencies generally caused increased heating rates for superparamagnetic particles.[364,365] Again for a fixed field strength linear enhancements of heating rates were found with a linear increase in the square of frequency.[214] Although most studies indicate frequency increases heating rates, but the extent of the effect depends upon other factors, such as field amplitude and the magnetic properties of the samples. An

important prediction of the LRT model is that particles reach the upper limit of heating efficiency when the relaxation time of the particles matches the period of AMF (equation 7.9).[363]

As frequency increases from 100-800 kHz the diameter of the most efficiently heated particles diameter decreases, this is likely due to the matching of the relaxation rate of the smaller particles with the higher frequency field. It is indicated that particles with a diameter less than 10 nm have a relaxation rate that is faster than the field strengths tested in this study, however, it has been suggested that frequencies above this point may cause adverse side effects.[366]

An increase in frequency generally caused a decrease in heating times from in nanoparticles of 5-13 nm in diameter (Figure 8.3 e-g). At greater diameters it is clear that the particle relaxation times have become greater than that of all the frequencies tested, and lifetime has become greater than the inverse of 1/100 kHz. Higher frequencies had a greater effect at reducing the heating times of smaller particles compared to larger ones, indicating that relaxation times of smaller particles are closer to the relaxation times of the field frequencies tested.

Heating times were minimal at low frequencies and low field strengths for all diameters except 15 nm particles (Figure 8.3 a-d). For 15 nm particles frequency had no effect on particle heating times. This can be explained by the fact that the relaxation time of the particles has become longer than the lifetime of the changing field, such that the frequency of the field becomes irrelevant. In this situation the limiting factor in relaxation is now particle relaxation time, rather than field lifetime. This effect is predicted by the LRT and agrees with other modelling predictions.[363] This can be explained by the fact that at larger diameters lifetime becomes big enough that frequency in this range becomes 0th order in the PLIN equation. The second

fractional term in equation 7.5 leads to a global maximum SAR when $2\pi f\tau = 1$ and so this equality defines the maximum heating rate of the system. When $2\pi f\tau < 1$ the bottom term of the fraction reduces to 1 and heating rate scales as the square of both the frequency and the magnitude of the applied field. When $2\pi f\tau > 1$ the frequency in the second fractional can essentially be cancelled out and SAR becomes independent of frequency. This theory from the LRT is reflected by the results of the model.

7.4.4 Diameter effects

Numerous experimental studies on particles of the superparamagnetic size rang reported that the maximum SAR was achieved with particles of ~15 nm in diameter.[227,367] Our model showed highest SAR rates for particles with 10/11 nm diameters. Although the frequencies used in these studies are less than the frequency range used in this model.

With small diameters frequency is the greatest factor in the power supplied by the particle. This trend is observed in the SAR of smaller particles, shows the reverse in terms of heating times. In contrast, larger particles (>13 nm) frequency has very little or no effect on SAR and PPP and field strength is the dominating parameter. This trend agrees with the predictions of the LRT as a consequence of the fractional term in equation 7.9.

With a fixed frequency and field, the highest PLIN values were observed at 12 nm at 100 kHz, 11 nm at 400 kHz and 10 nm at 800 kHz with 15 kA/m fields. This can be explained by the lifetime of the particles matching up with the lifetime of the field at each frequency respectively.

7.4.5 Comparison to specific absorption rates observed

The observed SAR for the NCC was calculated at 1.25 Wg^{-1} (chapter 5), the model calculated the SAR at 4.38 Wg^{-1} for the same induction heating parameters. The difference between the calculated value from the model and the observed value can be attributed to the assumptions made in the calculations of the model (section 7.4.6). The fact these values are in the same order of magnitude is encouraging, given how variable the SAR is with small changes in induction heating parameters (Figure 7.4). This data is a promising start for future development of the model.

7.4.6 Assumptions and limitations of the model

A thermodynamic assumption of the model is that 100 % conversion of input power transfers completely into heating of the entire nanoparticle complex, and no heat loss into surrounding solvent/ environment. In a tissue environment, there is a plethora of conditions that would affect heat transfer from the particle into the surrounding environment. *In vivo* experiments would need to be undertaken to properly gauge heating dissipation.

Within this model it is assumed that values of saturation magnetism and the temperature dependent anisotropy of iron oxide particles doesn't change from 310.5-315.5 K. In addition to this, it is assumed that the specific heat capacity of the copolymer does not vary with temperature. In reality there would be changes in these thermodynamic values and, even if minimal, would be important in calculations for clinical accuracy.

It is assumed there are no interparticle interactions. Therefore, aggregation and concentration effects are not considered within the model. In tumour environments and blood vessels it is likely there would be aggregation effects on heating efficiency. At typically used clinical concentrations, the high concentration of

nanoparticles within a tissue would result in interparticle influence in relaxation and therefore heating. The copolymers grafted onto the surface may provide a steric barrier against such magnetic particle interactions, but experimental data would be needed to confirm this.

It is also assumed in this model, that the mass of the grafted copolymer, and therefore its contribution to overall mass and energy required for heating does not vary for core diameter size change. The number and therefore mass of grafted polymer chains would vary with the change in surface area of the particle core, changing the required energy of heating from body to activation temperature.

Given the high frequencies studied in the model, it is assumed there is negligible heating contribution from Brown relaxation. This is due to the longer relaxation lifetimes for brown relaxation, only becoming effective at lower frequencies, and due to the experimentally determined hydrodynamic diameter of the particles, restricting physical rotation in solution.

7.5.7 Other factors that would affect heating rates *in vivo*

Naturally, with increasing solvent viscosity Brownian motion of particles is suppressed. However, as the hydrodynamic volume of particles increases ,the heating rates will again steadily decrease, once more due to greater restriction on translational and rotational movement.[116,224] As viscosity increases, the Brownian contribution to heating will decrease as well. This leaves Neel relaxation as the sole heating mechanism, thereby resulting in an overall lowered heating response at low frequencies, but little change in response for frequencies greater than 100 kHz.[224]

Nanoparticle concentration has been a key parameter of interest in developing particles for hyperthermia and active release, many studies have tried to examine the trend between concentration and heating

rates.[364,367,368] Conflicting experimental data has shown both enhancements and reductions in heating for increasing particle concentrations. Deatsch and Evans conclude that higher particle concentration decreases relaxation time, which would necessarily lead to an increase in heating rates; however, the authors note that this not hold true when particles agglomerate at high concentrations.[227] The effect of aggregation and compactness of aggregates on heating efficiency is heavily debated, however, in most cases, a decrease of efficiency with increasing degree of aggregation is either measured or predicted.[215,363] In the modelling presented in this chapter, the influence aggregation and concentration of particles on heating rates are not studied, however it is likely they would have an impact in physiological conditions.

In comparison to other literature sources the PLIN values (SAR) are comparable for the range of particle diameters, field strengths, and frequencies used.[129,227,358,369] Heating times for activation of the particles in this study are not comparable to literature, since the particles are novel, and therefore the thermodynamic properties are not considered published. Another model published, takes into account heat dispersion from particles into the surrounding medium, using rate equations.[370] Although, the results also show maximum heating efficiencies for the same particle diameters determined here.

7.5.8 Further work and adaptations

Further work to the model would focus on developing the pilot model further for use during *in vivo* experimentation, for example; adjusting the heat generation equations to a more accurate heating model by using rate equations for the changes in temperature dependent properties.[370] Adding a function within the model to predict the accumulation rates of the nanoparticle in a given tumour would be necessary. Calculating the parameters of heating a tumour to a temperature needed for efficient drug release given the

accumulation rates of the particles within the tumour would be vital for use in a clinical setting. Adjusting heating times based on the strength of the field at the target location given the distance of the tumour from the coil would need to be incorporated. Taking tumour types, locations, sizes and proliferation into account in the model to help predict the concentration of drug and therefore nanoparticle complex required for effective treatment. With this information the programme could predict cycles of treatment required based on clinical doses patient can receive and what is ideal for effective treatment. For eventual use in the clinic, *in vivo* experimentation results could be fed into a machine learning algorithm to train the programme to predict treatment parameters to a very high degree of effectiveness.

7.5 Conclusions

A program predicting the necessary heating times to trigger drug release from the complex has been developed for eventual use in animal model experiments and clinical trials. Frequency, field strength, location of tumour and particle size inputs can be varied depending on the treatment a patient is undergoing. The program can output the heating times required for drug release dependant on tumour location, the strength and frequency of the field, and what particles are being used. The results followed the conclusions of many literature studies but importantly modelled the response of the nanoparticle copolymer complex developed in this study. The model follows the linear response theory of heating well. It conforms to the general trends that have been reported in induction heating of magnetite particles. The model provides a starting point to develop a programme capable of predicting ideal parameters for treatment with accurate results. With further work and the implementation of machine learning, the model could become a powerful tool for use in the clinic.

Chapter 8: Conclusion and future directions

8.1 Summary of findings and limitations

The main aim of the work described in this thesis was to create a radio-wave responsive drug delivery platform. This comprised a superparamagnetic iron oxide nanoparticle core, with novel thermosensitive copolymers grafted onto the surface. Bound to the copolymers are drug bearing proteins that are selectively released when the complex is activated. Activation of the complex can be achieved by stimulation with an alternating magnetic field carried in the form of radio waves. Radio waves cause induction heating in the iron oxide core of the particles, heating the copolymers to the activation temperature, inducing a structure change and releasing the drug bearing proteins. Overall, the drug delivery technology developed has a high degree of control over spatial and temporal release, with a harmless stimulant able to penetrate all body tissues.

An induction heating device was development to operate at a high frequency and with adjustable input power and a water-cooling system to prevent external heat input. The device was able to heat particles effectively even at low concentrations and the adjustable input meant that the temperature of a solution could be maintained without turning the device on and off. The ability to change the diameter of the working coil allowed for a variety of different samples to be irradiated, including cell culture plates. The cooling system allowed the device to continue operating for extended periods of time without the need to reduce power. Overall, the device was cheap to build and incredibly cheap to run. The ability to change the working coil diameter means that the device could be used to stimulate drug release in any part of the body. The ease of operation and low cost gives the potential of allowing patients undergoing therapy to use the device for

treatment in the comfort of their own home, while still giving a tiered release over several days. Thus, reducing the trauma and cost of repeat hospital trips.

A novel thermosensitive copolymer capable of undergoing a phase change and immobilising proteins, was crucial to the system. The copolymer was comprised of three components: N-isopropylacrylamide, acrylamide, and methacrolein. Through a variety of analytical techniques, the structure of the copolymer was confirmed. Due to the respective reactivity towards other co-monomers, the copolymer contained two distinct block polymer regions. A coil structure containing random acrylamide-NIPAM repeating units that collapses into a globular structure, and a linear methacrolein chain that binds to proteins via Schiff base linkages. Varying the molar ratio of the comonomers during synthesis changed the LCST and allowed for the phase change to take place above normal human body temperature. The copolymer showed the ability to immobilise up to 9.6 % by weight of protein. Upon undergoing an induced phase change, the copolymer exhibited effective protein release over three LCST cycles but retained the protein when not induced. The novel copolymers described in this project have many potential applications within biomedicine and elsewhere in industry. The size change upon a temperature trigger could be applied to many drug delivery systems and other medical devices.

The copolymers were successfully synthesised on the surface of superparamagnetic iron oxide nanoparticles and the structure confirmed by a variety of different analytical methods. The outer shell of the nanoparticle complex was a hydrophilic acrylamide-co-NIPAM region of the copolymer, to ensure biocompatibility and to shield the inner hydrophobic, protein carrying methacrolein chain. The nanoparticle copolymer complex gave a mean diameter of 290nm, when measured by DLS after passing through a 600 nm filter and waterbath sonication. No degradation was observed when incubated in PBS at 37°C for over 90 days. The

LCST of grafted copolymers was designed to occur between 40-43 ˚C and was accompanied by a diameter reduction of the complex. The superparamagnetic core of the complex could be efficiently inductively heated to the activation temperature. Drug bearing proteins could be released from the nanoparticle complex remotely by radio-wave activation at the desired temperature range 40-42 ˚C, and this release could be staggered over six release cycles. When left in physiological solution for 7 days without activation, the release of drug bearing proteins was minimal. The fluorophore FITC was bound to the complex by sulphur bridges onto carried proteins. This created a method of tracking and visualising the effects of the nanoparticle copolymer complex during both *in vivo* and *in vitro* experiments.

When acting as a drug delivery platform for paclitaxel, the nanoparticle copolymer complex reduced the EC50 concentrations for both RH30 and RD rhabdomyosarcoma cell lines when drugs were released upon activation. Over 90 % cell viability reduction was observed in RD cells after 24 hours treatment and radio wave induced drug release. Moreover, RD cells showed a negligible reduction in cell viability when drug release was not stimulated. RH30 cells showed large reductions (86-95%) in cell viability after 24 hours treatment with activated particles. Some reduction in cell viability was seen without activating the particles at high concentrations, however, it was only half of the effect as when particles were activated. When acting as a drug delivery platform for Vinblastine, EC50 concentrations were again reduced in comparison to the bare drug for U-87 MG and MCF-7 cell lines, when the complex was activated. Both cell lines saw a massive reduction (83-95% and 40-70% for U87-MG and MCF-7 cells respectively) in cell viability after 24 hours incubation and stimulated drug release. Again, some reduction in cell viability was seen without activating the particles at high concentrations, however, it was only two thirds of the effect as when particles were activated.

Paracetamol was delivered to HEP-G2 cells by the activated nanoparticle copolymer complex. When activated, large reductions (15-44%) were seen in cell viability, while no reduction in cell viability was observed without activation of the complex. Furthermore, when the cells were incubated with acetylcysteine before the treatment, no cell death was observed. This indicates the potential to use the nanoparticle copolymer complex as drug delivery method for paracetamol for liver cancer that has metastasised to other areas of the body. The treatment would be performed while protecting healthy liver tissue with acetylcysteine. This could be a very powerful treatment method for liver cancer patients without side effects.

Biocompatibility was tested using horse blood treated with varying particle concentrations for 24 hours. No concentrations showed greater than 10 % haemolysis. This data, combined with no reduction in cell viabilities after 24 hours when cells are treated with unloaded nanoparticle complex, indicate the biocompatibility of the complex, although tests of complement activation and immune cell interaction are required further probe this.

Over 72 hours the nanoparticle copolymer complex showed effective penetration into RD and U-87 MG spheroids. Spheroid diameters reduced over three days, indicating good treatment potential in a pseudo tumour environment.

Cells magnetised by internalisation of the nanoparticle copolymer complex could be directed to specific locations using permanent magnetic fields. The location of the directed cells was confirmed by fluorescence from FITC bound to the nanoparticle complex. Furthermore, cell viability of magnetised cells was not affected by magnetic direction, nor were non magnetized cells. In principle it is proven the particles can be magnetically directed throughout the body.

A programme predicting the necessary heating times to trigger drug release from the complex has been developed for eventual use in animal model experiments and clinical trials. Frequency, field strength, location of tumour, and particle size inputs, can be varied depending on the treatment a patient is undergoing. The programme can output the heating times required for drug release dependent on tumour location, the strength and frequency of the field, and what particles are being used.

In the current state of research of the drug delivery platform described in this thesis, there are several limitations that would need to be addressed with further research. For example, there is a need to filter and sonicate samples before use to ensure a good dispersity in aqueous solution and aggregates are not present. Not including this step could be potentially harmful to the patient or animal test subject. Drug loading on the proteins and the loading of the proteins on the nanoparticle complex is a procedure that could potentially be hard to scale up to clinical production levels. The level of passive release could also cause some unwanted side effects, if the complex is given in high doses. In addition to this, the size of the complex in its current state means it is likely to be removed by the liver or RES, possibly reducing the impact at the target site. Treatment could not be carried out at locations near certain implanted medical devices, for example near a pacemaker. This is due to the potential of the radio waves disrupting the function of the device. Further research would need to be done to ensure the complex would not adversely affect MRI scans patients may have during or after treatment.

8.2 Future work

Further studies on copolymer synthesis and analysis could further investigate the fine structure of the polymer produced to determine the exact sequence and synchronisation of monomers and further reduce passive payload release. Additional aldehyde containing monomers would be investigated to increase

reaction yields and decrease polymerisation time. Further work would look into a tiered release system, where part of the copolymer could undergo a phase change and release a drug at one activation temperature, and extended heating to a higher temperature would cause a different part of the copolymer strand to collapse and release its payload. Different release "sections" of the copolymer could release different drugs at different activation temperatures, different release copolymers could even be bound to separate types of particles. This segregated release method could provide an entire drug sequence treatment within one nanoparticle formulation allowing for an enhanced effect of synergistic or independent drugs.

Further specificity of the complex could be achieved by antibody or nanobody attachment as an endcap to polymers. This could be achieved with minimal adaption of current copolymer synthesis methods by simply adding the endcap with a radical termination group into the reaction mixture when the desired reaction time has been reached. The motivation behind this would be the increased uptake in tumour cells rather than healthy tissue. When used in combination with magnetic direction to tumour locations, and localised activation, the specificity of the combined treatment could provide highly discriminant destruction of cancer cells.

Incorporation of the nanoparticle copolymer complex into or on to the surface of microbubbles could give rise to a potential combined activation method. Initial activation could see the bursting of microbubbles using ultrasound stimulation, propelling the nanoparticles deeper into tumour tissue, and improving uptake via inertial and stable cavitation. Magnetic direction for particles within microbubbles would remain an effective method of spatial control, although the differing movement within tissue would need to be studied. Radio wave activation of the complex would take place as described in this thesis, but any off-target effects would be further reduced by the added layer of ultrasound triggered release.

Thermal imaging on a cellular level could be used as a method of investigating the bystander effect of the drug delivery method in tumour tissue. To study both the effect of heating of particles on bystander cells, and the effect fluid movement may have on activation efficiency. If done both *in vivo* and *in vitro* the results could allow for a greater understanding of heat effects on bystander cells and whether they could prove useful in enhancing the effect of drug delivery by this method.

Moving forward to the eventual use of this platform technology in the clinic, the next major step is *in vivo* experimentation. The primary focus would be on the discriminant destruction of tumour tissue using the described localisation and activation techniques. Other important investigations such as the effect of the nanoparticle copolymer complex on vital organs, their degradation in physiological conditions, and the ultimate fate of the nanoparticles would be investigated. Circulation times *in vivo* would need to be determined as well as any effect magnetic direction may have on body tissues.

Improvement of the heating rate model for use in the clinic could be achieved by the use of heat camera measurements of particles in vivo, dependent on input parameters of the heating device. A machine learning algorithm could be developed with the input data of real examples to learn and predict the best heating parameters for any tumour within any patient.

The induction heating device developed in this project could be refined further, with a higher frequency field produced, a greater field strength and a greater range of working coil diameters. Adapting the device for use at home by non-specialised persons would also be necessary for a “take home” treatment method.

8.3 Impact in oncology

The method of chemotherapy drug delivery described in this project has a created a platform for selective, discriminant chemotherapy drug delivery, for a huge range of chemotherapy molecules to almost any type of cancer. Synthesis of the complex is cheap, and some aspects of the synthesis such as SPION core formation and RAFT polymerisation are easy to scale up, other aspects such as the drug loading on BSA would need further development to enable clinical grade production. The components of the complex are all readily available and compared to current chemotherapy methods, there is a reduction in the amount of drug needed. No specialist equipment is needed in synthesis, and before drug loading the nanoparticle polymer complex is stable for months at ambient conditions. Magnetic direction *in vivo* has been demonstrated previously, and can easily be achieved with simple and cheap permanent magnetics in the clinic.[15,121,128] Using radio waves as an activation method in the form of a low frequency alternating magnetic field has many benefits. Radio waves can penetrate all tissues in the body and at these frequencies does not cause off target effects, leading to a safe but reliable activation method of drug release. Accurate drug delivery to specific organs can be achieved through this delivery method. The complex can be magnetically directed throughout the body to the target tissue, not necessarily limited to the delivery of chemotherapy drugs.

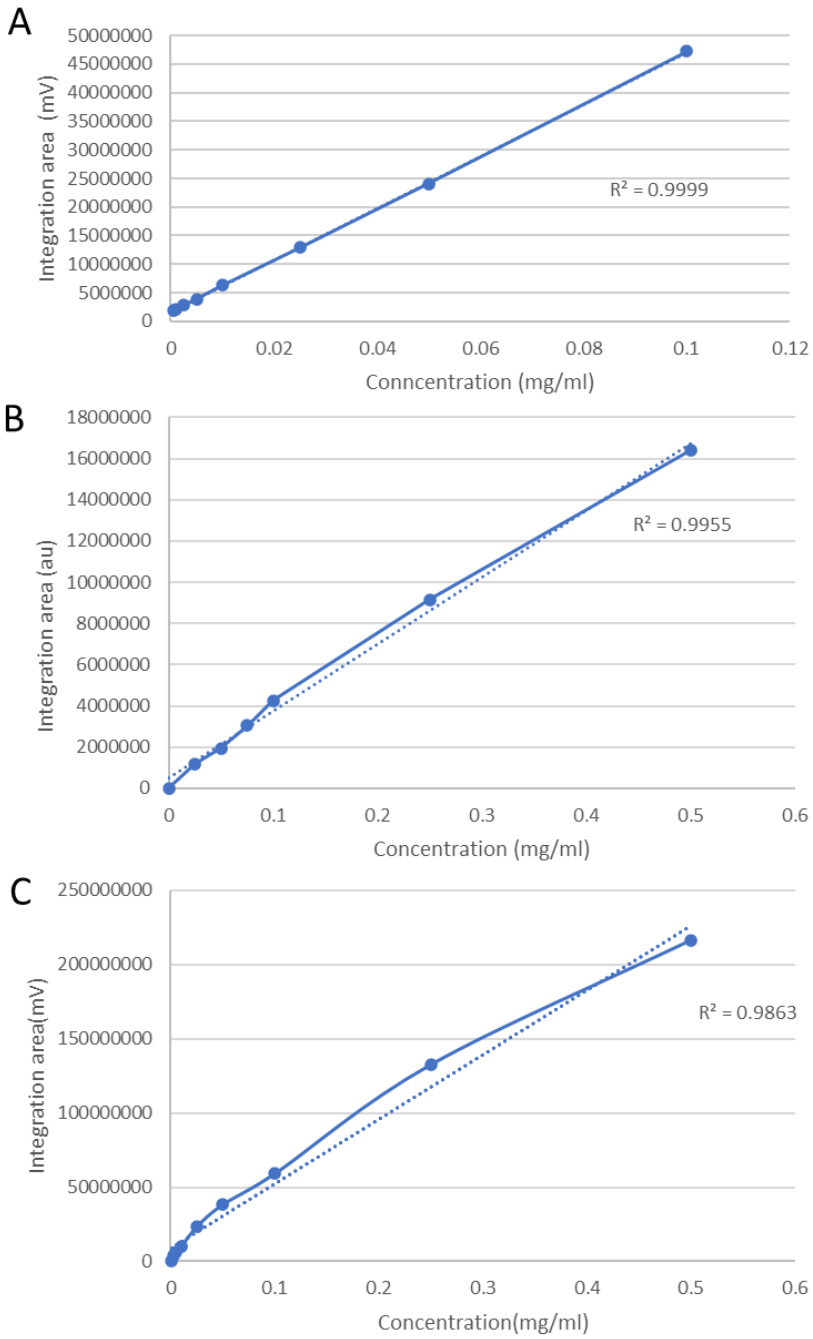
8.4 Closing remarks

The properties of the novel copolymer, including its protein immobilisation, structure change and solubility change at a tuneable temperature mean that there is a plethora of different potential application across science and engineering research. Particularly, there is huge potential for heat activated biological devices, such as thermosensitive polymer activated stents for cardiac purposes.

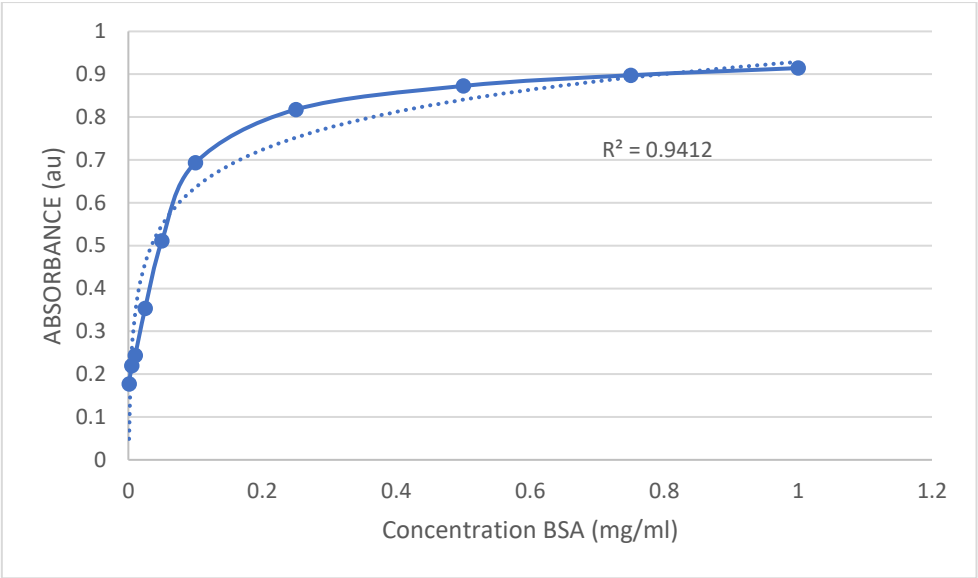
Combining the induction heating effect of the SPION core and the adjustable functionality of the copolymers has potential for use in many biological systems. Such as increasing gene transfection in biological samples or acting as nucleation points for bacterial cell structures. The change in solubility upon a temperature change could be used in industrial systems to remove unwanted microbes. This can be achieved by collection of the microbes by the polymers on the complex, destruction of these microbes by induction heating and removal of what remains by the change in solubility of the complex and easy magnetic removal.

The innovations and technology presented in this thesis have the potential to have an impact in clinical chemotherapy and indeed in worldwide cancer treatment. Not only could this technology be a vast improvement on current treatment methods but its basis can be adapted to tackle a huge variety of medical and commercial problems the world faces.

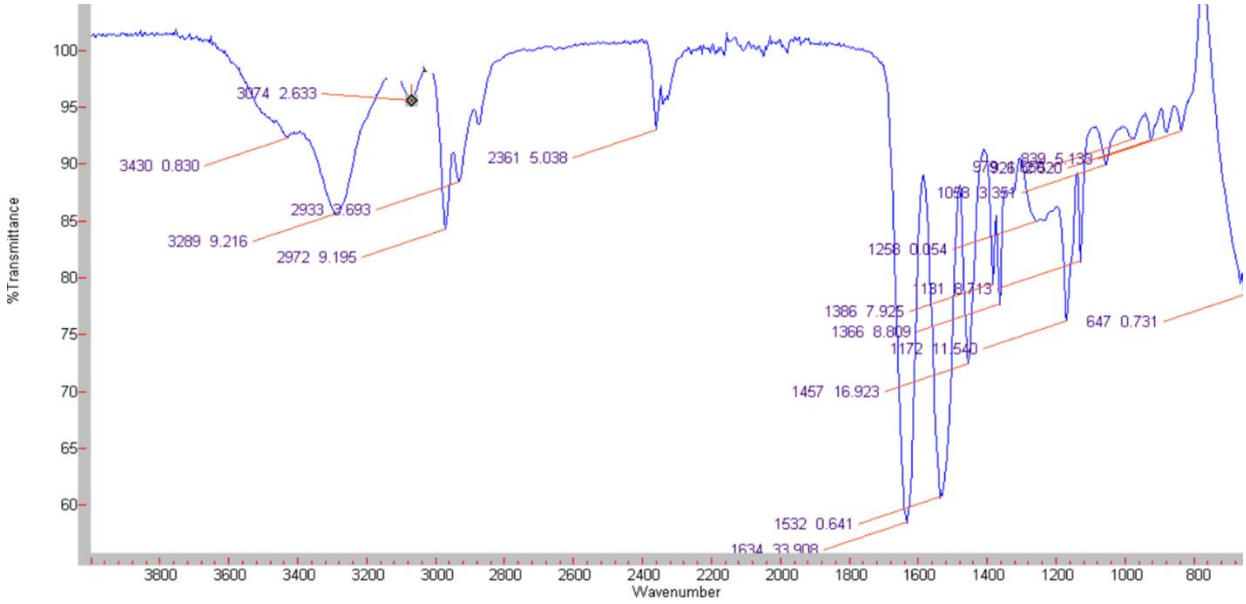
Appendix



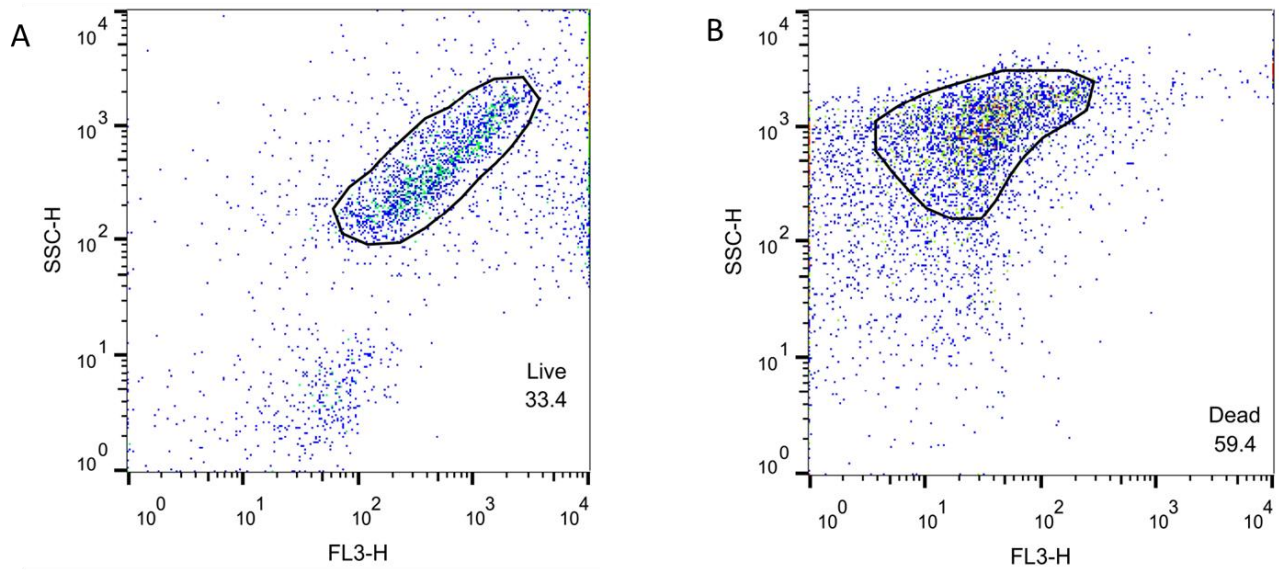
A. 1: Drug concentration calibration curves. HPLC concentration gradients of paclitaxel (A), vinblastine (B) and paracetamol (C) used to calculate drug loading rates onto BSA. The y axis represents the integration area of the drug peak retrieved from the HPLC chromatogram.



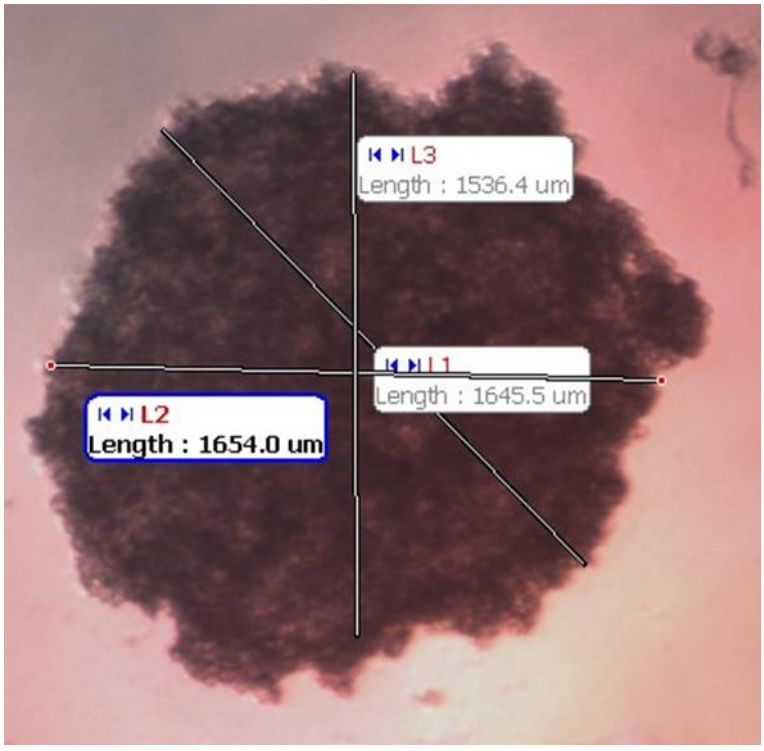
A. 2: An example of a BSA calibration curve used to determine protein release from the copolymer of the NCC during a Bradford protein assay. The y axis represents absorbance of concentrations as read by a plate reader at a 495nm wavelength..



A. 3: FT-IR spectrum of SPION bound PNIPAM.



A. 4:The flow cytometry data from untreated cells used as a live control A, and ethanol treated cells used as a dead control (B). The enclosed areas represent the gating used to determine and compare the alive and dead populations of cells. FL3-H represents the detection of fluorescence and SSC-H is side scatter and is related to cell integrity.

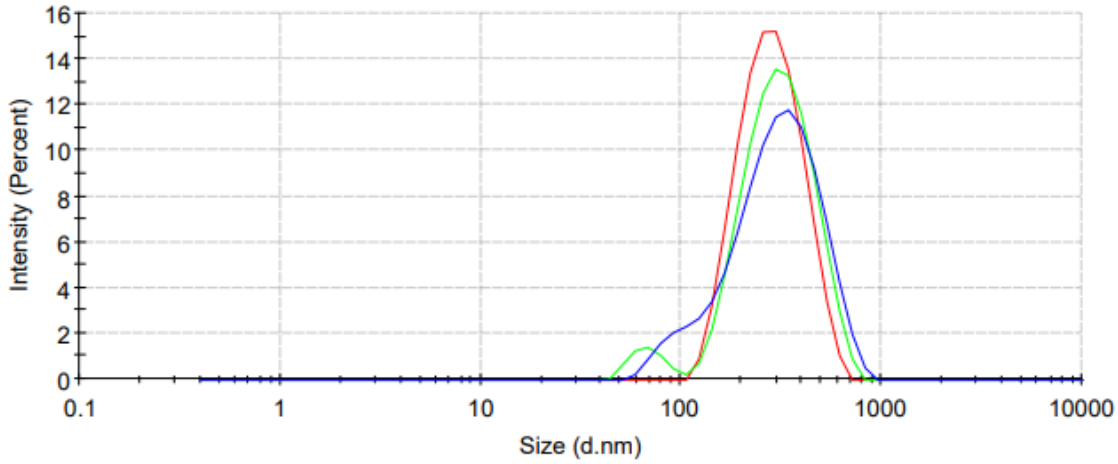


A. 5: An example of the measurement of spheroid diameter. Measurements were made along the horizontal, vertical and diagonal axis. Throughout the timepoints the axes of measurement were kept the same.

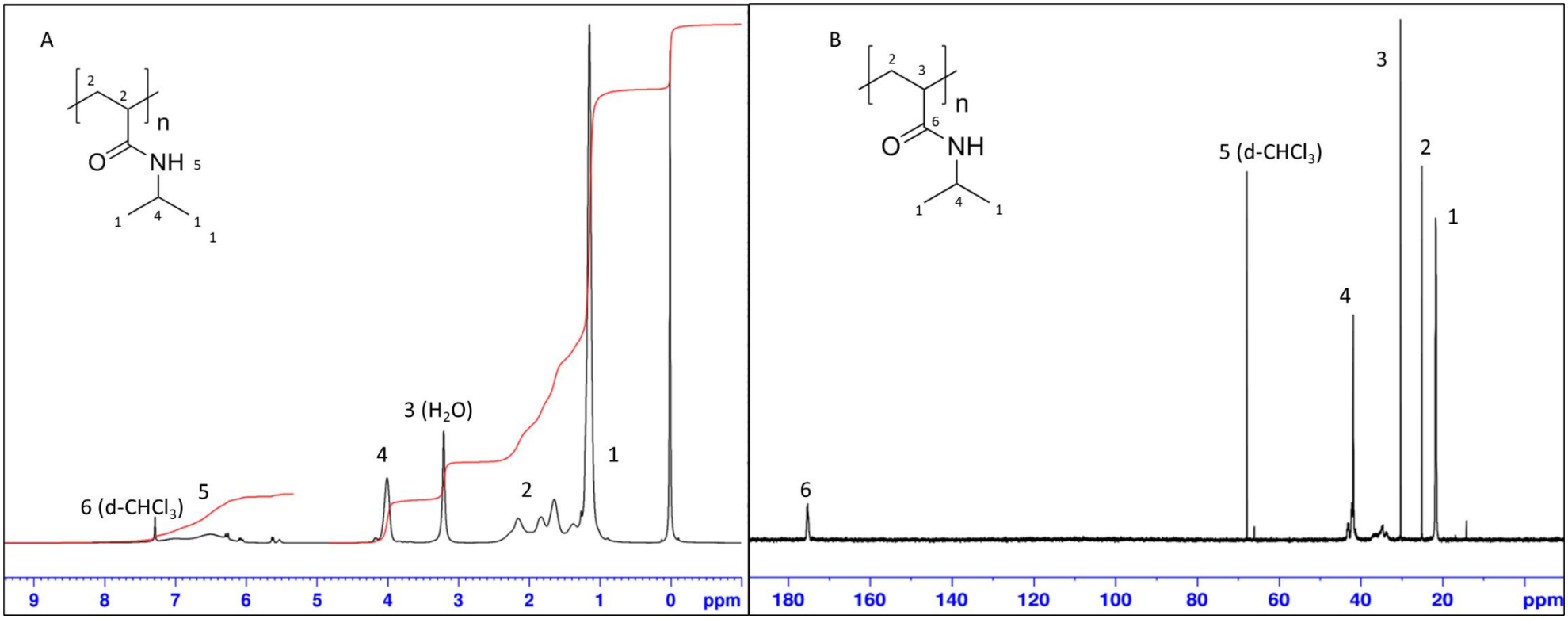
	RH30	
Paclitaxel (nM)	Post-activation	Pre-activation
Unloaded	ns	ns
10	****	**
25	****	****
50	****	****
100	****	****
	RD	
Paclitaxel (nM)	Post-activation	Pre-activation
Unloaded	**	**
10	****	*
25	****	ns
100	****	ns
	U87-MG	
Vinblastine (uM)	Post-activation	Pre-activation
Unloaded	ns	ns
2	****	*
2.5	****	*
20	****	*
35	****	**
	MCF-7	
Vinblastine (nM)	Post-activation	Pre-activation
Unloaded	ns	*
10	***	ns
25	****	*
50	****	***
100	****	***

Concentration Paracetamol delivered	Post-activation	Post-activation NAC	Pre-activation	Pre-activation NAC
0.5	0.053037542	0.880393118	0.933433692	0.355831277
2.5	0.0152178	0.841330266	0.881282573	0.899975402
10	0.023417025	0.889030664	0.96912309	0.137213736

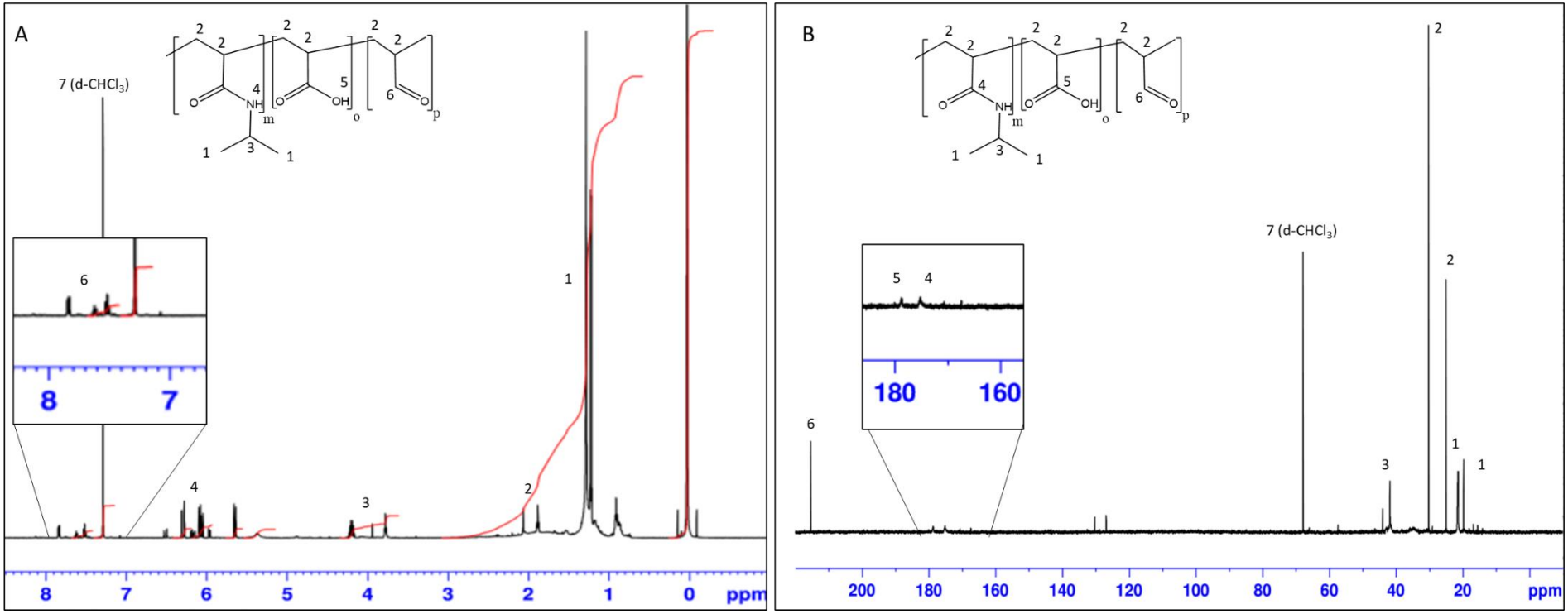
*A. 6: Significance values of drug delivery to cells via the NCC. Significance is tested against the untreated cell control by a one way Anova test . P values are classed by ***=p<0.01, **= 0.05<p>0.01, *=0.5<p>0.05.*



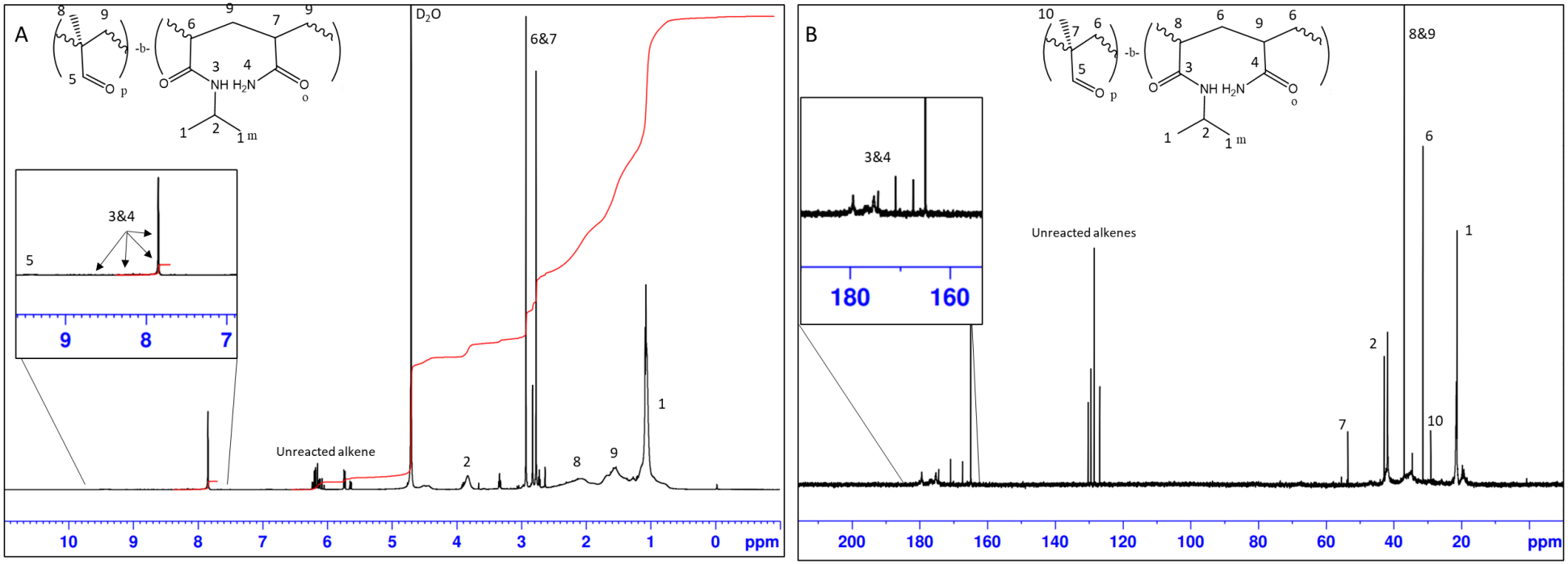
A. 7: DLS intensity profile for the NCC for hydrodynamic diameter measurement at 25˚C in PBS at a concentration of 0.1 mg/mL. Twelve repeat readings were made for each measurement and three repeat measurements were made, the PDI was calculated at 0.161.



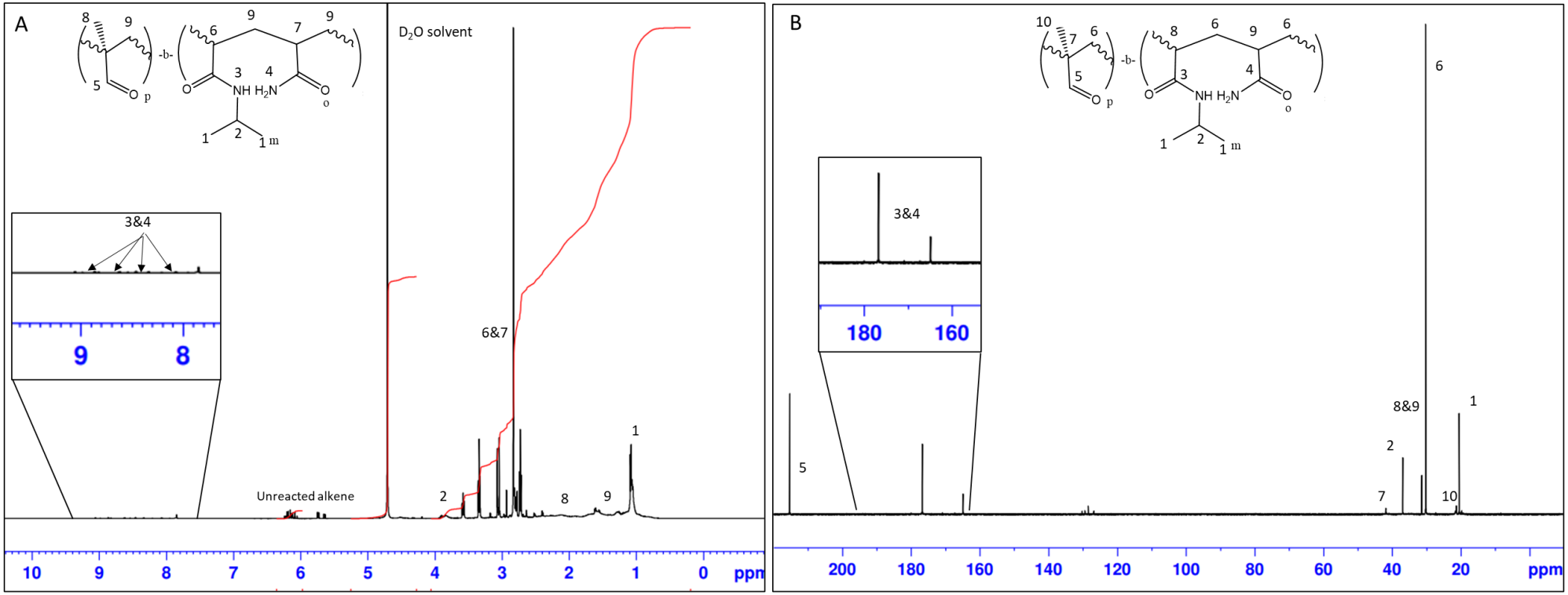
A. 8 The fully assigned ^{1}H NMR (A) and ^{13}CNMR (B) spectrums of PNIPAM in deuterated chloroform solvent. Integral values along with multiplicity are visible on spectrum but are represented by the red integral peaks. Due to the nature of polymer NMR limited information can be obtained from integral peaks. Some water contamination is visible in the hydrogen spectrum. For the carbon spectrum hydrogen was decoupled.



A. 9: The fully assigned ^{1}H NMR (A) and $^{13}CNMR$ (B) spectrums of PNIPAM-co-acrylic acid-co-acrolein in deuterated chloroform solvent. Integral values along with multiplicity are visible on spectrum but are represented by the red integral peaks. Due to the nature of polymer NMR limited information can be obtained from integral peaks. For the carbon spectrum hydrogen was decoupled. Due to the random nature of the polymer structure, certain functional groups in the structure are assigned to groups of signals in the spectrum, due to their differing environment along the polymer chain.



A. 10: The fully assigned ^{1}H NMR (A) and $^{13}CNMR$ (B) spectrums of PNIPAM-co-acrylamide-co-methacrolein in deuterium oxide solvent. Integral values along with multiplicity are visible on spectrum but are represented by the red integral peaks. Due to the nature of polymer NMR limited information can be obtained from integral peaks. For the carbon spectrum hydrogen was decoupled. Due to the random nature of the polymer structure, certain functional groups in the structure are assigned to groups of signals in the spectrum, due to their differing environment along the polymer chain.



A. 11: The fully assigned [1]H NMR (A) and [13]CNMR (B) spectrums of PNIPAM-co-acrylamide-co-methacrolein synthesised on the surface of SPIONs, in deuterium oxide solvent. Copolymer samples were removed from SPION cores and purified before analysis. Integral values along with multiplicity are visible on spectrum but are represented by the red integral peaks. Due to the nature of polymer NMR limited information can be obtained from integral peaks. For the carbon spectrum hydrogen was decoupled. Due to the random nature of the polymer structure, certain functional groups in the structure are assigned to groups of signals in the spectrum, due to their differing environment along the polymer chain.

Bibliography

1. The top 10 leading causes of death in the United States. Available at: https://www.medicalnewstoday.com/articles/282929.php. (Accessed: 28th August 2019)

2. Plummer, M. *et al.* Global burden of cancers attributable to infections in 2012: a synthetic analysis. *Lancet Glob. Heal.* **4**, e609–e616 (2016).

3. Chow, R. D., Bradley, E. H. & Gross, C. P. Comparison of Cancer-Related Spending and Mortality Rates in the US vs 21 High-Income Countries. *JAMA Heal. Forum* **3**, e221229–e221229 (2022).

4. Jemal, A. *et al.* Annual Report to the Nation on the Status of Cancer, 1975-2014, Featuring Survival. *J. Natl. Cancer Inst.* **109**, (2017).

5. Adams, J. M. & Cory, S. The Bcl-2 apoptotic switch in cancer development and therapy. *Oncogene* **26**, 1324–1337 (2007).

6. Lowe, S. W., Cepero, E. & Evan, G. Intrinsic tumour suppression. *Nat. 2004 4327015* **432**, 307–315 (2004).

7. Goldberg, S. B. *et al.* Chemotherapy with Erlotinib or chemotherapy alone in advanced non-small cell lung cancer with acquired resistance to EGFR tyrosine kinase inhibitors. *Oncologist* **18**, 1214–1220 (2013).

8. Weidner, N., Semple, J. P., Welch, W. R. & Folkman, J. Tumor angiogenesis and metastasis--correlation in invasive breast carcinoma. *N. Engl. J. Med.* **324**, 1–8 (1991).

9. Folkman, J. Angiogenesis in cancer, vascular, rheumatoid and other disease. *Nat. Med.* **1**, 27–30 (1995).

10. Secondary cancer | Cancer Research UK. Available at: https://www.cancerresearchuk.org/about-cancer/secondary-cancer. (Accessed: 12th September 2022)

11. Berx, G. & van Roy, F. Involvement of Members of the Cadherin Superfamily in Cancer. *Cold Spring Harb. Perspect. Biol.* **1**, (2009).

12. Olin, M. R. *et al.* Oxygen is a Master Regulator of the Immunogenicity of Primary Human Glioma Cells. *Cancer Res.* **71**, 6583 (2011).

13. Barley, V. L. Oncology . Ed by R A J Spence and P G Johnston, pp. xiv+536, 2001 (Oxford University Press, Oxford), £22.95 ISBN 0 19 262982 4 . *Br. J. Radiol.* **75**, 856–856 (2002).

14. Bhutta, B. S., Alghoula, F. & Berim, I. Hypoxia. *StatPearls* (2022).

15. Silva, A. K. A., Espinosa, A., Kolosnjaj-Tabi, J., Wilhelm, C. & Gazeau, F. Medical Applications of Iron Oxide Nanoparticles. in *Iron Oxides* 425–472 (Wiley-VCH Verlag GmbH & Co. KGaA, 2016). doi:10.1002/9783527691395.ch18

16. Alderman, D. J. Fisheries Chemotherapy: A Review. in *Recent Advances in Aquaculture* 1–61 (Springer Netherlands, 1988). doi:10.1007/978-94-011-9743-4_1

17. Chemotherapy - Side effects - NHS. Available at: https://www.nhs.uk/conditions/chemotherapy/side-effects/. (Accessed: 29th August 2019)

18. Doxorubicin Hydrochloride.

19. Liebmann, J. E. *et al.* Cytotoxic studies of paclitaxel (Taxol) in human tumour cell lines. *Br. J. Cancer* **68**, 1104 (1993).

20. Hsiangl, Y.-H., Hertzbergj, R., Hechtj, S. & Lius, L. F. THE JOURNAL OF BIOLOGICAL CHEMISTRY Camptothecin Induces Protein-linked DNA Breaks via Mammalian DNA Topoisomerase I*. **260**, 14873–14878 (1985).

21. Epilation Definition & Meaning - Merriam-Webster. Available at: https://www.merriam-webster.com/dictionary/epilation. (Accessed: 9th January 2023)

22. Campos, S. M. & Ghosh, S. A Current Review of Targeted Therapeutics for Ovarian Cancer. *J. Oncol.* **2010**, 1–11 (2010).

23. Arcaro, A. Targeting PI3K/mTOR Signaling in Cancer. *Front. Oncol.* **4**, (2014).

24. Boothby, L. A., Doering, P. L. & Kipersztok, S. Bioidentical hormone therapy: A review. *Menopause* **11**, 356–367 (2004).

25. Vert, M. *et al.* Terminology for biorelated polymers and applications (IUPAC recommendations 2012). *Pure Appl. Chem.* **84**, 377–410 (2012).

26. Wong, A. D., Ye, M., Ulmschneider, M. B. & Searson, P. C. Quantitative Analysis of the Enhanced Permeation and Retention (EPR) Effect. *PLoS One* **10**, e0123461 (2015).

27. Du, J.-Z., Mao, C.-Q., Yuan, Y.-Y., Yang, X.-Z. & Wang, J. Tumor extracellular acidity-activated nanoparticles as drug delivery systems for enhanced cancer therapy. *Biotechnol. Adv.* **32**, 789–803 (2014).

28. Jain, S., Hirst, D. G. & O'Sullivan, J. M. Gold nanoparticles as novel agents for cancer therapy. *Br. J. Radiol.* **85**, 101–13 (2012).

29. Kobayashi, H., Watanabe, R. & Choyke, P. L. Improving conventional enhanced permeability and retention (EPR) effects; what is the appropriate target? *Theranostics* **4**, 81–9 (2013).

30. Tran, S., DeGiovanni, P.-J., Piel, B. & Rai, P. Cancer nanomedicine: a review of recent success in drug delivery. *Clin. Transl. Med.* **6**, 44 (2017).

31. White, B., Evison, A., Dombi, E. & Townley, H. E. Improved delivery of the anticancer agent citral using BSA nanoparticles and polymeric wafers. *Nanotechnol. Sci. Appl.* **10**, 163 (2017).

32. Davis, M. E., Chen, Z. (Georgia) & Shin, D. M. Nanoparticle therapeutics: an emerging treatment modality for cancer. in *Nanoscience and Technology* 239–250 (Co-Published with Macmillan Publishers Ltd, UK, 2009). doi:10.1142/9789814287005_0025

33. Gelderblom, H., Verweij, J., Nooter, K. & Sparreboom, A. Cremophor EL: the drawbacks and advantages of vehicle selection for drug formulation. *Eur. J. Cancer* **37**, 1590–1598 (2001).

34. Purcell, M., Neault, J. F. & Tajmir-Riahi, H. A. Interaction of taxol with human serum albumin. *Biochim. Biophys. Acta* **1478**, 61–8 (2000).

35. Paál, K., Müller, J. & Hegedûs, L. High affinity binding of paclitaxel to human serum albumin. *Eur. J. Biochem.* **268**, 2187–2191 (2001).

36. Alasvand, N. *et al.* Therapeutic Nanoparticles for Targeted Delivery of Anticancer Drugs. *Multifunct. Syst. Comb. Deliv. Biosensing Diagnostics* 245–259 (2017). doi:10.1016/B978-0-323-52725-5.00013-7

37. Duncan, R. Polymer conjugates for tumour targeting and intracytoplasmic delivery. The EPR effect as a common gateway? *Pharm. Sci. Technol. Today* **2**, 441–449 (1999).

38. Torchilin, V. Tumor delivery of macromolecular drugs based on the EPR effect. *Adv. Drug Deliv. Rev.* **63**, 131–135 (2011).

39. Nichols, J. W. & Bae, Y. H. EPR: Evidence and fallacy. *J. Control. Release* **190**, 451–464 (2014).

40. Danhier, F. To exploit the tumor microenvironment: Since the EPR effect fails in the clinic, what is the future of nanomedicine? *J. Control. Release* **244**, 108–121 (2016).

41. Shi, Y., van der Meel, R., Chen, X. & Lammers, T. The EPR effect and beyond: Strategies to improve tumor targeting and cancer nanomedicine treatment efficacy. *Theranostics* **10**, 7921–7924 (2020).

42. Wilhelm, S. *et al.* Analysis of nanoparticle delivery to tumours. *Nat. Rev. Mater. 2016 15* **1**, 1–12 (2016).

43. Sindhwani, S. *et al.* The entry of nanoparticles into solid tumours. *Nat. Mater. 2020 195* **19**, 566–575 (2020).

44. Bose, T., Latawiec, D., Mondal, P. P. & Mandal, S. Overview of nano-drugs characteristics for clinical application: The journey from the entry to the exit point. *J. Nanoparticle Res.* **16**, (2014).

45. Nel, A. E. *et al.* Understanding biophysicochemical interactions at the nano-bio interface. *Nat. Mater.* **8**, 543–557 (2009).

46. Zhu, M. *et al.* Physicochemical properties determine nanomaterial cellular uptake, transport, and fate. *Acc. Chem. Res.* **46**, 622–631 (2013).

47. Foroozandeh, P. & Aziz, A. A. Insight into Cellular Uptake and Intracellular Trafficking of Nanoparticles. *Nanoscale Res. Lett.* **13**, (2018).

48. Chithrani, B. D. & Chan, W. C. W. Elucidating the mechanism of cellular uptake and removal of protein-coated gold nanoparticles of different sizes and shapes. *Nano Lett.* **7**, 1542–1550 (2007).

49. Tong, S., Quinto, C. A., Zhang, L., Mohindra, P. & Bao, G. Size-Dependent Heating of Magnetic Iron Oxide Nanoparticles. (2017). doi:10.1021/acsnano.7b01762

50. Lu, F., Wu, S. H., Hung, Y. & Mou, C. Y. Size effect on cell uptake in well-suspended, uniform mesoporous silica nanoparticles. *Small* **5**, 1408–1413 (2009).

51. Moghimi, S. M. & Patel, H. M. Serum-mediated recognition of liposomes by phagocytic cells of the reticuloendothelial system - The concept of tissue specificity. *Adv. Drug Deliv. Rev.* **32**, 45–60 (1998).

52. Hirayama, K., Akashi, S., Furuya, M. & Fukuhara, K. Rapid confirmation and revision of the primary structure of bovine serum albumin by ESIMS and Frit-FAB LC/MS. *Biochem. Biophys. Res. Commun.* **173**, 639–46 (1990).

53. Milton Harris, J. & Chess, R. B. Effect of pegylation on pharmaceuticals. *Nat. Rev. Drug Discov.* **2**, 214–221 (2003).

54. Longmire, M., Choyke, P. L. & Kobayashi, H. Clearance Properties of Nano-sized Particles and Molecules as Imaging Agents: Considerations and Caveats. *Nanomedicine (Lond).* **3**, 703 (2008).

55. Zhu, G. H., Gray, A. B. C. & Patra, H. K. Nanomedicine: controlling nanoparticle clearance for translational success. *Trends Pharmacol. Sci.* **43**, 709–711 (2022).

56. Zhu, G. H. *et al.* Innate Immune Invisible Ultrasmall Gold Nanoparticles - Framework for Synthesis and Evaluation. *ACS Appl. Mater. Interfaces* **13**, 23410–23422 (2021).

57. Soo Choi, H. *et al.* Renal Clearance of Nanoparticles. *Nat. Biotechnol.* **25**, 1165 (2007).

58. Herrnberger, L. *et al.* Formation of Fenestrae in Murine Liver Sinusoids Depends on Plasmalemma Vesicle-Associated Protein and Is Required for Lipoprotein Passage. *PLoS One* **9**, e115005 (2014).

59. Wisse, E., Jacobs, F., Topal, B., Frederik, P. & De Geest, B. The size of endothelial fenestrae in human liver sinusoids: implications for hepatocyte-directed gene transfer. *Gene Ther.* **15**, 1193–1199 (2008).

60. Detampel, P. *et al.* In vivo clearance of nanoparticles by transcytosis across alveolar epithelial cells. *PLoS One* **14**, e0223339 (2019).

61. Estelrich, J., Sánchez-Martín, M. J. & Busquets, M. A. Nanoparticles in magnetic resonance imaging: From simple to dual contrast agents. *Int. J. Nanomedicine* **10**, 1727–1741 (2015).

62. McRobbie, D. W., Moore, E. A. & Graves, M. J. *MRI from Picture to Proton.* (Cambridge University Press, 2017).

63. Plassat, V. *et al.* Anti-Estrogen-Loaded Superparamagnetic Liposomes for Intracellular Magnetic Targeting and Treatment of Breast Cancer Tumors. *Adv. Funct. Mater.* **21**, 83–92 (2011).

64. Endo-Takahashi, Y. & Negishi, Y. Microbubbles and Nanobubbles with Ultrasound for Systemic Gene Delivery. *Pharmaceutics* **12**, 1–14 (2020).

65. Helfield, B., Zou, Y. & Matsuura, N. Acoustically-Stimulated Nanobubbles: Opportunities in Medical Ultrasound Imaging and Therapy. *Front. Phys.* **9**, 209 (2021).

66. Cormode, D. P., Naha, P. C. & Fayad, Z. A. Nanoparticle Contrast Agents for Computed Tomography: A Focus on Micelles. *Contrast Media Mol. Imaging* **9**, 37 (2014).

67. Mahan, M. M. & Doiron, A. L. Gold Nanoparticles as X-Ray, CT, and Multimodal Imaging Contrast Agents: Formulation, Targeting, and Methodology. *J. Nanomater.* **2018**, (2018).

68. Hsu, J. C. *et al.* Nanoparticle contrast agents for X-ray imaging applications. *Wiley Interdiscip. Rev. Nanomedicine Nanobiotechnology* **12**, e1642 (2020).

69. Bruns, O. T. *et al.* Next-generation in vivo optical imaging with short-wave infrared quantum dots. *Nat. Biomed. Eng. 2017 14* **1**, 1–11 (2017).

70. Kirti, K. Quantum dots as biological optical imaging tools. *J. Appl. Biotechnol. Bioeng.* **Volume 4**, (2017).

71. Xiao, L. & Yeung, E. S. Optical Imaging of Individual Plasmonic Nanoparticles in Biological Samples. *http://dx.doi.org/10.1146/annurev-anchem-071213-020125* **7**, 89–111 (2014).

72. Wardman, P. Chemical radiosensitizers for use in radiotherapy. *Clin. Oncol. (R. Coll. Radiol).* **19**, 397–417 (2007).

73. Boateng, F. & Ngwa, W. Delivery of Nanoparticle-Based Radiosensitizers for Radiotherapy Applications. *Int. J. Mol. Sci.* **21**, (2020).

74. Townley, H. E., Kim, J. & Dobson, P. J. In vivo demonstration of enhanced radiotherapy using rare earth doped titania nanoparticles. *Nanoscale* **4**, 5043–5050 (2012).

75. Duan, X., He, C., Kron, S. J. & Lin, W. Nanoparticle formulations of cisplatin for cancer therapy. *Wiley Interdiscip. Rev. Nanomed. Nanobiotechnol.* **8**, 776 (2016).

76. Zhang, Y. *et al.* Multifunctional co-loaded magnetic nanocapsules for enhancing targeted MR imaging and in vivo photodynamic therapy. *Nanomedicine Nanotechnology, Biol. Med.* **21**, 102047 (2019).

77. Shang, L., Zhou, X., Zhang, J., Shi, Y. & Zhong, L. Metal Nanoparticles for Photodynamic Therapy: A Potential Treatment for Breast Cancer. *Molecules* **26**, (2021).

78. Lucky, S. S., Soo, K. C. & Zhang, Y. Nanoparticles in photodynamic therapy. *Chem. Rev.* **115**, 1990–2042 (2015).

79. Hu, G. *et al.* Nanoparticles targeting macrophages as potential clinical therapeutic agents against cancer and inflammation. *Front. Immunol.* **10**, 1998 (2019).

80. Patra, J. K. *et al.* Nano based drug delivery systems: recent developments and future prospects. *J. Nanobiotechnology 2018 161* **16**, 1–33 (2018).

81. Kim, C. K. *et al.* Entrapment of hydrophobic drugs in nanoparticle monolayers with efficient release into cancer cells. *J. Am. Chem. Soc.* **131**, 1360–1361 (2009).

82. Salatin, S., Maleki Dizaj, S. & Yari Khosroushahi, A. Effect of the surface modification, size, and shape on cellular uptake of nanoparticles. *Cell Biol. Int.* **39**, 881–890 (2015).

83. Jo, D. H., Kim, J. H., Lee, T. G. & Kim, J. H. Size, surface charge, and shape determine therapeutic effects of nanoparticles on brain and retinal diseases. *Nanomedicine* **11**, 1603–1611 (2015).

84. Banerjee, A., Qi, J., Gogoi, R., Wong, J. & Mitragotri, S. Role of Nanoparticle Size, Shape and Surface Chemistry in Oral Drug Delivery. *J. Control. Release* **238**, 176 (2016).

85. Danafar, H. Applications of copolymeric nanoparticles in drug delivery systems. *Drug Res. (Stuttg).* **66**, 506–519 (2016).

86. Peer, D. *et al.* Nanocarriers as an emerging platform for cancer therapy. *Nat. Nanotechnol.* **2**, 751–760 (2007).

87. Ni, S. NANOPARTICLES CARRYING NATURAL PRODUCT FOR DRUG DELIVERY. *J. Drug Deliv. Ther.* **7**, 73–75 (2017).

88. Yoo, J., Park, C., Yi, G., Lee, D. & Koo, H. Active Targeting Strategies Using Biological Ligands for Nanoparticle Drug Delivery Systems. *Cancers 2019, Vol. 11, Page 640* **11**, 640 (2019).

89. Castillo, R. R. *et al.* Advances in mesoporous silica nanoparticles for targeted stimuli-responsive drug delivery: an update. *Expert Opin. Drug Deliv.* **16**, 415 (2019).

90. Steinhauser, I., Spänkuch, B., Strebhardt, K. & Langer, K. Trastuzumab-modified nanoparticles: optimisation of preparation and uptake in cancer cells. *Biomaterials* **27**, 4975–4983 (2006).

91. Yu, M. K., Park, J. & Jon, S. Targeting Strategies for Multifunctional Nanoparticles in Cancer Imaging and Therapy. *Theranostics* **2**, 3 (2012).

92. Yu, B., Tai, H. C., Xue, W., Lee, L. J. & Lee, R. J. Receptor-targeted nanocarriers for therapeutic delivery to cancer. *Mol. Membr. Biol.* **27**, 286 (2010).

93. Fu, Z. & Xiang, J. Aptamers, the Nucleic Acid Antibodies, in Cancer Therapy. *Int. J. Mol. Sci.* **21**, (2020).

94. Fu, Z. & Xiang, J. Aptamer-Functionalized Nanoparticles in Targeted Delivery and Cancer Therapy. *Int. J. Mol. Sci.* **21**, 1–39 (2020).

95. Steichen, S. D., Caldorera-Moore, M. & Peppas, N. A. A review of current nanoparticle and targeting moieties for the delivery of cancer therapeutics. *Eur. J. Pharm. Sci.* **48**, 416 (2013).

96. Laurent, S. *et al.* Magnetic iron oxide nanoparticles: Synthesis, stabilization, vectorization, physicochemical characterizations and biological applications. *Chem. Rev.* **108**, 2064–2110 (2008).

97. Stanley, S. A. *et al.* Radio-wave heating of iron oxide nanoparticles can regulate plasma glucose in mice. *Science (80-.).* **336**, 604–608 (2012).

98. Aslam, M., Schultz, E. A., Sun, T., Meade, T. & Dravid, V. P. Synthesis of Amine-Stabilized Aqueous Colloidal Iron Oxide Nanoparticles. *Cryst. Growth Des.* **7**, 471–475 (2007).

99. Classes of Magnetic Materials. Available at: http://www.irm.umn.edu/hg2m/hg2m_b/hg2m_b.html. (Accessed: 7th April 2018)

100. Superparamagnetism. Available at: https://bme240.eng.uci.edu/students/08s/ykim30/02_1.htm. (Accessed: 1st October 2022)

101. Spaldin, N. A. (Nicola A. *Magnetic materials : fundamentals and applications*. (Cambridge University Press, 2011).

102. Wasilewski, P. & Kletetschka, G. Lodestone: Natures only permanent magnet-What it is and how it gets charged. *Geophys. Res. Lett.* **26**, 2275–2278 (1999).

103. Hurlbut, C. S. (Cornelius S., Sharp, W. E. & Dana, E. S. *Dana's minerals and how to study them.* (Wiley, 1998).

104. Spaldin, N. A. *MAGNETIC MATERIALS Fundamentals and Applications Second edition*.

105. Sessoli, R. *et al.* High-spin molecules: [Mn12O12(O2CR)16(H2O)4]. *J. Am. Chem. Soc.* **115**, 1804–1816 (1993).

106. Gittleman, J. I., Abeles, B. & Bozowski, S. Superparamagnetism and relaxation effects in granular Ni-Si O 2 and Ni- Al 2 O 3 films. *Phys. Rev. B* **9**, 3891–3897 (1974).

107. Tong, S., Quinto, C. A., Zhang, L., Mohindra, P. & Bao, G. Size-Dependent Heating of Magnetic Iron Oxide Nanoparticles. *ACS Nano* **11**, 6808–6816 (2017).

108. Sun, X. *et al.* Aptamer-assisted superparamagnetic iron oxide nanoparticles as multifunctional drug delivery platform for chemo-photodynamic combination therapy. *J. Mater. Sci. Mater. Med.* **30**, 76 (2019).

109. Sugimoto, T. & Matijević, E. Formation of uniform spherical magnetite particles by crystallization from ferrous hydroxide gels. *J. Colloid Interface Sci.* **74**, 227–243 (1980).

110. Laurent, S. *et al.* Magnetic Iron Oxide Nanoparticles: Synthesis, Stabilization, Vectorization, Physicochemical Characterizations, and Biological Applications. doi:10.1021/cr068445e

111. Néel, L. & LOUIS NÉEL Professeur à la, P. M. Théorie du traînage magnétique des substances massives dans le domaine de Rayleigh THÉORIE DU TRAÎNAGE MAGNÉTIQUE DES SUBSTANCES MASSIVES DANS LE DOMAINE DE RAYLEIGH. *J. Phys. Radium* **11**, (1950).

112. Teja, A. S. & Koh, P.-Y. Synthesis, properties, and applications of magnetic iron oxide nanoparticles. *Prog. Cryst. Growth Charact. Mater.* **55**, 22–45 (2009).

113. Blaney, L. Lehigh Preserve Magnetite (Fe3O4): Properties, Synthesis, and Applications. **15**, (2007).

114. Gual, A., Godard, C., Castillón, S. & Claver, C. Soluble transition-metal nanoparticles-catalysed hydrogenation of arenes. *Dalt. Trans.* **39**, 11499 (2010).

115. ZHAO, D., ZENG, X., XIA, Q. & TANG, J. Inductive heat property of Fe3O4 nanoparticles in AC magnetic field for local hyperthermia. *Rare Met.* **25**, 621–625 (2006).

116. Nordebo, S., Sjöberg, D. & Bayford, R. *Inductive heating of conductive nanoparticles*. (2016).

117. Lauffer, R. B. Paramagnetic metal complexes as water proton relaxation agents for NMR imaging: theory and design. *Chem. Rev.* **87**, 901–927 (1987).

118. Plaza, J. L. *et al.* Electrostatically stabilised nanoparticles: self-organization and electron-beam patterning. *J. Nanosci. Nanotechnol.* **5**, 1826–31 (2005).

119. Xiao, Z. P., Yang, K. M., Liang, H. & Lu, J. Synthesis of magnetic, reactive, and thermoresponsive Fe3O4 nanoparticles via surface-initiated RAFT copolymerization of N-isopropylacrylamide and acrolein. *J. Polym. Sci. Part A Polym. Chem.* **48**, 542–550 (2010).

120. Ponnusamy, K., Babu, R. P. & Dhamodharan, R. Synthesis of block and graft copolymers of styrene by raft polymerization, using dodecyl-based trithiocarbonates as initiators and chain transfer agents. *J. Polym. Sci. Part A Polym. Chem.* **51**, 1066–1078 (2013).

121. Xiang, Z. *et al.* Induction heating-based low-frequency alternating magnetic field: High potential of ferromagnetic composites for medical applications. *Mater. Des.* **174**, 107804 (2019).

122. Zinn, S. (Stanley), Semiatin, S. L., Electric Power Research Institute. & Battelle Memorial Institute. Columbus

Laboratories. *Elements of induction heating : design, control, and applications*. (ASM International, 1988).

123. Prescott, L. F. Paracetamol, alcohol and the liver. *British Journal of Clinical Pharmacology* **49**, 291–301 (2000).

124. Induction Heating Applications. Available at: https://www.eldec.net/applications.html. (Accessed: 30th July 2019)

125. Pradhan, P. *et al.* Targeted temperature sensitive magnetic liposomes for thermo-chemotherapy. *J. Control. Release* **142**, 108–121 (2010).

126. *Physics of Ferromagnetism SECOND EDITION SOSHIN CHIKAZUMI*.

127. Ondeck, C. L. *et al.* Theory of magnetic fluid heating with an alternating magnetic field with temperature dependent materials properties for self-regulated heating. *J. Appl. Phys.* **105**, 07B324 (2009).

128. Hergt, R., Dutz, S., Müller, R. & Zeisberger, M. Magnetic particle hyperthermia: nanoparticle magnetism and materials development for cancer therapy. *J. Phys. Condens. Matter* **18**, S2919–S2934 (2006).

129. Rosensweig, R. E. E. Heating magnetic fluid with alternating magnetic field. *J. Magn. Magn. Mater.* **252**, 370–374 (2002).

130. Gavilán, H. *et al.* Magnetic nanoparticles and clusters for magnetic hyperthermia: optimizing their heat performance and developing combinatorial therapies to tackle cancer. *Chem. Soc. Rev.* **50**, 11614–11667 (2021).

131. Hoffman, A. S. “Intelligent” Polymers in Medicine and Biotechnology. *Artif. Organs* **19**, 458–467 (1995).

132. Wu, C. & Wang, X. Globule-to-Coil Transition of a Single Homopolymer Chain in Solution. *Phys. Rev. Lett.* **80**, 4092–4094 (1998).

133. Aseyev, V., Tenhu, H. & Winnik, F. M. Non-ionic thermoresponsive polymers in water. *Adv. Polym. Sci.* **242**, 29–89 (2011).

134. Roy, D., Brooks, W. L. A. & Sumerlin, B. S. New directions in thermoresponsive polymers. *Chem. Soc. Rev.* **42**, 7214–7243 (2013).

135. Osi, A. R. *et al.* Three-Dimensional-Printable Thermo/Photo-Cross-Linked Methacrylated Chitosan-Gelatin Hydrogel Composites for Tissue Engineering. *ACS Appl. Mater. Interfaces* **13**, 22902–22913 (2021).

136. Kretlow, J. D., Klouda, L. & Mikos, A. G. Injectable matrices and scaffolds for drug delivery in tissue engineering. *Adv. Drug Deliv. Rev.* **59**, 263–273 (2007).

137. Klouda, L. & Mikos, A. G. Thermoresponsive hydrogels in biomedical applications - a review. *Eur. J. Pharm. Biopharm.* **68**, 34 (2008).

138. Tan, I., Roohi, F. & Titirici, M. M. Thermoresponsive polymers in liquid chromatography. *Anal. Methods* **4**, 34–43 (2012).

139. Ward, M. A. & Georgiou, T. K. Thermoresponsive Polymers for Biomedical Applications. *Polymers (Basel).* **3**, 1215–1242 (2011).

140. Smart Polymers for Bioseparation and Bioprocessing. *Smart Polym. Biosep. Bioprocess.* (2001). doi:10.1201/9780367803698/SMART-POLYMERS-BIOSEPARATION-BIOPROCESSING-IGOR-GALAEV-BO-MATTIASSON

141. Robinson, R. K. (Richard K., Batt, C. A. & Patel, P. D. (Pradip D. . *Encyclopedia of food microbiology*. (Academic Press, 2000).

142. Mullin, L. B., Phillips, L. C. & Dayton, P. A. Nanoparticle delivery enhancement with acoustically activated microbubbles. *IEEE Trans. Ultrason. Ferroelectr. Freq. Control* **60**, 65–77 (2013).

143. Deng, C. X., Sieling, F., Pan, H. & Cui, J. Ultrasound-induced cell membrane porosity. *Ultrasound Med. Biol.* **30**, 519–526 (2004).

144. Chappell, J. C., Song, J., Burke, C. W., Klibanov, A. L. & Price, R. J. Targeted Delivery of Nanoparticles Bearing Fibroblast Growth Factor-2 by Ultrasonic Microbubble Destruction for Therapeutic Arteriogenesis. *Small* **4**, 1769 (2008).

145. De Temmerman, M.-L. *et al.* mRNA-Lipoplex loaded microbubble contrast agents for ultrasound-assisted transfection of dendritic cells. *Biomaterials* **32**, 9128–9135 (2011).

146. Chappell, J. C., Song, J., Burke, C. W., Klibanov, A. L. & Price, R. J. Targeted delivery of nanoparticles bearing

fibroblast growth factor-2 by ultrasonic microbubble destruction for therapeutic arteriogenesis. *Small* **4**, 1769–77 (2008).

147. Price, R. J., Skyba, D. M., Kaul, S. & Skalak, T. C. Delivery of colloidal particles and red blood cells to tissue through microvessel ruptures created by targeted microbubble destruction with ultrasound. *Circulation* **98**, 1264–7 (1998).

148. Burke, C. W. *et al.* Covalently linking poly(lactic-co-glycolic acid) nanoparticles to microbubbles before intravenous injection improves their ultrasound-targeted delivery to skeletal muscle. *Small* **7**, 1227–35 (2011).

149. Burke, C. W. *et al.* Ultrasound-activated agents comprised of 5FU-bearing nanoparticles bonded to microbubbles inhibit solid tumor growth and improve survival. *Mol. Ther.* **22**, 321–328 (2014).

150. Kwan, J. J. *et al.* Ultrasound-Propelled Nanocups for Drug Delivery. *Small* **11**, 5305–5314 (2015).

151. Mannaris, C. *et al.* Gas-Stabilizing Gold Nanocones for Acoustically Mediated Drug Delivery. *Adv. Healthc. Mater.* **7**, 1800184 (2018).

152. Cochran, M. C., Eisenbrey, J., Ouma, R. O., Soulen, M. & Wheatley, M. A. Doxorubicin and paclitaxel loaded microbubbles for ultrasound triggered drug delivery. *Int. J. Pharm.* **414**, 161–70 (2011).

153. Shi, H. *et al.* Molecular imaging of telomerase and the enzyme activity-triggered drug release by using a conformation-switchable nanoprobe in cancerous cells. *Sci. Rep.* **8**, 16341 (2018).

154. Villar-Alvarez, E. *et al.* Gold Nanorod-Based Nanohybrids for Combinatorial Therapeutics. *ACS Omega* **3**, 12633–12647 (2018).

155. Yuan, P. & Song, D. MRI tracing non-invasive TiO_2-based nanoparticles activated by ultrasound for multi-mechanism therapy of prostatic cancer. *Nanotechnology* **29**, 125101 (2018).

156. Lee, J. *et al.* Theranostic gas-generating nanoparticles for targeted ultrasound imaging and treatment of neuroblastoma. *J. Control. Release* **223**, 197–206 (2016).

157. Marshalek, J. P. *et al.* Intracellular delivery and ultrasonic activation of folate receptor-targeted phase-change contrast agents in breast cancer cells in vitro. *J. Control. Release* **243**, 69–77 (2016).

158. White, B. D. *et al.* Nanoparticle Activation Methods in Cancer Treatment. *Biomolecules* **9**, 202 (2019).

159. Wang, X., Song, J., Liu, J. & Wang, Z. L. Direct-Current Nanogenerator Driven by Ultrasonic Waves. *Science (80-.).* **316**, 102–105 (2007).

160. Cucullo, L. *et al.* Very low intensity alternating current decreases cell proliferation. *Glia* **51**, 65–72 (2005).

161. Marino, A., Battaglini, M., De Pasquale, D., Degl'Innocenti, A. & Ciofani, G. Ultrasound-Activated Piezoelectric Nanoparticles Inhibit Proliferation of Breast Cancer Cells. *Sci. Rep.* **8**, 6257 (2018).

162. Allison, R. R. & Sibata, C. H. Oncologic photodynamic therapy photosensitizers: A clinical review. *Photodiagnosis Photodyn. Ther.* **7**, 61–75 (2010).

163. Wang, M., Abbineni, G., Clevenger, A., Mao, C. & Xu, S. Upconversion nanoparticles: synthesis, surface modification and biological applications. *Nanomedicine* **7**, 710–29 (2011).

164. HAYNES, W. M. *CRC handbook of chemistry and physics : a ready-reference book of chemical and physical data*. (2009).

165. Meng, Q. *et al.* Light-Activated Core–Shell Nanoparticles for Spatiotemporally Specific Treatment of Metastatic Triple-Negative Breast Cancer. *ACS Nano* **12**, 2789–2802 (2018).

166. Lucky, S. S. *et al.* Titania Coated Upconversion Nanoparticles for Near-Infrared Light Triggered Photodynamic Therapy. *ACS Nano* **9**, 191–205 (2015).

167. Dai, Y. *et al.* 808 nm near-infrared light controlled dual-drug release and cancer therapy in vivo by upconversion mesoporous silica nanostructures. *J. Mater. Chem. B* **5**, 2086–2095 (2017).

168. Huang, L. *et al.* Ultralow-Power Near Infrared Lamp Light Operable Targeted Organic Nanoparticle Photodynamic Therapy. *J. Am. Chem. Soc.* **138**, 14586–14591 (2016).

169. Vankayala, R., Kuo, C.-L., Nuthalapati, K., Chiang, C.-S. & Hwang, K. C. Nucleus-Targeting Gold Nanoclusters for Simultaneous In Vivo Fluorescence Imaging, Gene Delivery, and NIR-Light Activated Photodynamic Therapy. *Adv. Funct. Mater.* **25**, 5934–5945 (2015).

170. Jagdeo, J. R., Adams, L. E., Brody, N. I. & Siegel, D. M. Transcranial Red and Near Infrared Light Transmission in a Cadaveric Model. *PLoS One* **7**, e47460 (2012).

171. Qiu, M. *et al.* Novel concept of the smart NIR-light-controlled drug release of black phosphorus nanostructure for cancer therapy. *Proc. Natl. Acad. Sci. U. S. A.* **115**, 501–506 (2018).

172. Liu, J. *et al.* Gold Nanorods Coated with Mesoporous Silica Shell as Drug Delivery System for Remote Near Infrared Light-Activated Release and Potential Phototherapy. *Small* **11**, 2323–2332 (2015).

173. He, C., Liu, D. & Lin, W. Self-Assembled Core–Shell Nanoparticles for Combined Chemotherapy and Photodynamic Therapy of Resistant Head and Neck Cancers. *ACS Nano* **9**, 991–1003 (2015).

174. Occlusive Peripheral Arterial Disease - Heart and Blood Vessel Disorders - MSD Manual Consumer Version. Available at: https://www.msdmanuals.com/en-gb/home/heart-and-blood-vessel-disorders/peripheral-arterial-disease/occlusive-peripheral-arterial-disease. (Accessed: 10th January 2023)

175. Jing, X. *et al.* Role of hypoxia in cancer therapy by regulating the tumor microenvironment. *Mol. Cancer 2019 181* **18**, 1–15 (2019).

176. Gilkes, D. M., Semenza, G. L. & Wirtz, D. Hypoxia and the extracellular matrix: drivers of tumour metastasis. *Nat. Rev. Cancer* **14**, 430 (2014).

177. Piao, W. *et al.* Development of an azo-based photosensitizer activated under mild hypoxia for photodynamic therapy. *J. Am. Chem. Soc.* **139**, 13713–13719 (2017).

178. Wang, Y., Shang, W., Niu, M., Tian, J. & Xu, K. Hypoxia-active nanoparticles used in tumor theranostic. *Int. J. Nanomedicine* **14**, 3705 (2019).

179. Qian, C. *et al.* Light-Activated Hypoxia-Responsive Nanocarriers for Enhanced Anticancer Therapy. *Adv. Mater.* (2016). doi:10.1002/adma.201505869

180. Guan, M. *et al.* Multifunctional upconversion–nanoparticles–trismethylpyridylporphyrin–fullerene nanocomposite: a near-infrared light-triggered theranostic platform for imaging-guided photodynamic therapy. *NPG Asia Mater.* **7**, e205–e205 (2015).

181. Yue, C. *et al.* ROS-Responsive Mitochondria-Targeting Blended Nanoparticles: Chemo- and Photodynamic Synergistic Therapy for Lung Cancer with On-Demand Drug Release upon Irradiation with a Single Light Source. *Theranostics* **6**, 2352–2366 (2016).

182. Lu, K., He, C. & Lin, W. A Chlorin-Based Nanoscale Metal–Organic Framework for Photodynamic Therapy of Colon Cancers. *J. Am. Chem. Soc.* **137**, 7600–7603 (2015).

183. M. Solís-López, ... R.M. Ramírez-Zamora. Fenton Reaction - an overview | ScienceDirect Topics.

184. Kim, J. *et al.* Continuous O_2 -Evolving $MnFe_2O_4$ Nanoparticle-Anchored Mesoporous Silica Nanoparticles for Efficient Photodynamic Therapy in Hypoxic Cancer. *J. Am. Chem. Soc.* **139**, 10992–10995 (2017).

185. Espinosa, A. *et al.* Duality of Iron Oxide Nanoparticles in Cancer Therapy: Amplification of Heating Efficiency by Magnetic Hyperthermia and Photothermal Bimodal Treatment. *ACS Nano* **10**, 2436–2446 (2016).

186. Goodman, A. M. *et al.* Near-infrared remotely triggered drug-release strategies for cancer treatment. *Proc. Natl. Acad. Sci. U. S. A.* **114**, 12419–12424 (2017).

187. Yang, Y. *et al.* Near-infrared light-activated cancer cell targeting and drug delivery with aptamer-modified nanostructures. *Nano Res.* **9**, 139–148 (2016).

188. Chen, H. *et al.* Nanoscintillator-Mediated X-ray Inducible Photodynamic Therapy for In Vivo Cancer Treatment. *Nano Lett.* **15**, 2249–2256 (2015).

189. Kotagiri, N. *et al.* Radionuclides transform chemotherapeutics into phototherapeutics for precise treatment of disseminated cancer. *Nat. Commun.* **9**, 275 (2018).

190. Noto, V. *et al.* Effects of sodium ascorbate (vitamin C) and 2-methyl-1,4-naphthoquinone (vitamin K3) treatment on human tumor cell growth in vitro. I. Synergism of combined vitamin C and K3 action. *Cancer* **63**, 901–906 (1989).

191. Johannsen, M. *et al.* Clinical hyperthermia of prostate cancer using magnetic nanoparticles: Presentation of a new interstitial technique. *Int. J. Hyperth.* **21**, 637–647 (2005).

192. Bañobre-López, M., Teijeiro, A. & Rivas, J. Magnetic nanoparticle-based hyperthermia for cancer treatment. *Reports Pract. Oncol. Radiother.* **18**, 397–400 (2013).

193. Magforce: For Physicians. Available at: https://magforce.com/en/home/for_physicians/#clinical_trials. (Accessed: 8th September 2022)

194. Maier-Hauff, K. *et al.* Efficacy and safety of intratumoral thermotherapy using magnetic iron-oxide nanoparticles combined with external beam radiotherapy on patients with recurrent glioblastoma multiforme. *J. Neurooncol.* **103**, 317–324 (2011).

195. Hua, M.-Y. *et al.* The effectiveness of a magnetic nanoparticle-based delivery system for BCNU in the treatment of gliomas. *Biomaterials* **32**, 516–527 (2011).

196. Yang, H.-W. *et al.* Self-protecting core-shell magnetic nanoparticles for targeted, traceable, long half-life delivery of BCNU to gliomas. *Biomaterials* **32**, 6523–6532 (2011).

197. Nigam, S. & Bahadur, D. Dendrimer-conjugated iron oxide nanoparticles as stimuli-responsive drug carriers for thermally-activated chemotherapy of cancer. *Colloids Surfaces B Biointerfaces* **155**, 182–192 (2017).

198. Park, J. W., Bae, K. H., Kim, C. & Park, T. G. Clustered magnetite nanocrystals cross-linked with PEI for efficient siRNA delivery. *Biomacromolecules* **12**, 457–465 (2011).

199. Hu, S.-H., Liu, D.-M., Tung, W.-L., Liao, C.-F. & Chen, S.-Y. Surfactant-Free, Self-Assembled PVA-Iron Oxide/Silica Core-Shell Nanocarriers for Highly Sensitive, Magnetically Controlled Drug Release and Ultrahigh Cancer Cell Uptake Efficiency. *Adv. Funct. Mater.* **18**, 2946–2955 (2008).

200. Hu, S.-H., Chen, S.-Y., Liu, D.-M. & Hsiao, C.-S. Core/Single-Crystal-Shell Nanospheres for Controlled Drug Release via a Magnetically Triggered Rupturing Mechanism. *Adv. Mater.* **20**, 2690–2695 (2008).

201. Bringas, E. *et al.* Triggered release in lipid bilayer-capped mesoporous silica nanoparticles containing SPION using an alternating magnetic field. *Chem. Commun.* **48**, 5647 (2012).

202. Cai, K. *et al.* Magnetically Triggered Reversible Controlled Drug Delivery from Microfabricated Polymeric Multireservoir Devices. *Adv. Mater.* **21**, 4045–4049 (2009).

203. Thomas, C. R. *et al.* Noninvasive Remote-Controlled Release of Drug Molecules in Vitro Using Magnetic Actuation of Mechanized Nanoparticles. *J. Am. Chem. Soc.* **132**, 10623–10625 (2010).

204. Park, K. The drug delivery field at the inflection point: Time to fight its way out of the egg. *J. Control. Release* **267**, 2–14 (2017).

205. Vejpravová, J. P. *et al. Superparamagnetism of Co-Ferrite Nanoparticles*.

206. Mohapatra, J. *et al.* Size-dependent magnetic and inductive heating properties of Fe3O4 nanoparticles: Scaling laws across the superparamagnetic size. *Phys. Chem. Chem. Phys.* **20**, 12879–12887 (2018).

207. Poisoning in the Modern World: New Tricks for an Old Dog? - Google Books. Available at: https://books.google.co.uk/books?hl=en&lr=&id=nzj8DwAAQBAJ&oi=fnd&pg=PA77&dq=heavy+metal+oxidation+in+physiological+conditions&ots=RAURTCbjbR&sig=7jXivTfQib9X1oIo8taJQXFV0lA#v=onepage&q&f=false. (Accessed: 12th May 2022)

208. Rak, J. Mathematical model of induction heating. in 560046 (2017). doi:10.1063/1.4992729

209. Thébault, C. *et al.* Magneto-mechanical treatment of human glioblastoma cells with engineered iron oxide powder microparticles for triggering apoptosis. *Nanoscale Adv.* **3**, 6213–6222 (2021).

210. Amstad, E., Textor, M. & Reimhult, E. Stabilization and functionalization of iron oxide nanoparticles for biomedical applications. *Nanoscale* **3**, 2819–2843 (2011).

211. RAFT: Choosing the Right Agent to Achieve Controlled Polymerization. Available at: https://www.sigmaaldrich.com/GB/en/technical-documents/technical-article/materials-science-and-engineering/polymer-synthesis/raft-polymerization. (Accessed: 9th June 2022)

212. Mahmoudi, M., Sant, S., Wang, B., Laurent, S. & Sen, T. Superparamagnetic iron oxide nanoparticles (SPIONs): Development, surface modification and applications in chemotherapy. *Adv. Drug Deliv. Rev.* **63**, 24–46 (2011).

213. Introduction to Solid State Physics, 8th Edition | Wiley. Available at: https://www.wiley.com/en-us/Introduction+to+Solid+State+Physics%2C+8th+Edition-p-9780471415268. (Accessed: 9th June 2022)

214. Kim, D. H., Thai, Y. T., Nikles, D. E. & Brazel, C. S. Heating of aqueous dispersions containing MnFe2O4 nanoparticles by radio-frequency magnetic field induction. *IEEE Trans. Magn.* **45**, 64–70 (2009).

215. Cabrera, D., Camarero, J., Ortega, D. & Teran, F. J. Influence of the aggregation, concentration, and viscosity on the nanomagnetism of iron oxide nanoparticle colloids for magnetic hyperthermia. *J. Nanoparticle Res. 2015 173* **17**, 1–6 (2015).

216. Shah, R. R., Davis, T. P., Glover, A. L., Nikles, D. E. & Brazel, C. S. Impact of magnetic field parameters and iron oxide nanoparticle properties on heat generation for use in magnetic hyperthermia. *J. Magn. Magn. Mater.* **387**, 96–106 (2015).

217. Moad, G., Rizzardo, E. & Thang, S. H. Radical addition–fragmentation chemistry in polymer synthesis. *Polymer (Guildf).* **49**, 1079–1131 (2008).

218. Coote*, M. L. Ab Initio Study of the Addition−Fragmentation Equilibrium in RAFT Polymerization: When Is Polymerization Retarded? (2004). doi:10.1021/MA049444W

219. Hadadian, Y. *et al.* From Low to High Saturation Magnetization in Magnetite Nanoparticles: The Crucial Role of the Molar Ratios between the Chemicals. *ACS Omega* **7**, 15996–16012 (2022).

220. Synthesis and characterization of ultra-small superparamagnetic iron oxide nanoparticles thinly coated with silica. (2008). doi:10.1088/0957-4484/19/33/335601

221. GIUSTINI, A. J. *et al.* MAGNETIC NANOPARTICLE HYPERTHERMIA IN CANCER TREATMENT. *Nano Life* **01**, 17–32 (2010).

222. Cornia, A. *et al.* The Origin of Magnetic Anisotropy and Single-Molecule Magnet Behavior in Chromium(II)-Based Extended Metal Atom Chains. *Inorg. Chem.* **59**, 1763–1777 (2020).

223. Jia, D., Hamilton, J., Zaman, L. M. & Goonewardene, A. The time, size, viscosity, and temperature dependence of the Brownian motion of polystyrene microspheres. *Am. J. Phys.* **75**, 111 (2007).

224. Thompson, M. T. Simple Models and Measurements of Magnetically Induced Heating Effects in Ferromagnetic Fluids. *IEEE Trans. Magn.* **34**, 3755 (1998).

225. EASYHEAT ® 4.2 to 10 kW Induction Heating Systems.

226. Solary Magnetic Induction Heater Kit 1000W Hand Tool Set for Flameless Heat Induction Heat 1KW 220V : Amazon.co.uk: DIY & Tools. Available at: https://www.amazon.co.uk/Solary-Magnetic-Induction-Heater-Flameless/dp/B08MZJ12KM/ref=sr_1_1_sspa?crid=16DI9MIS92487&keywords=induction+heater&qid=1663091677&sprefix=induction+heater%2Caps%2C94&sr=8-1-spons&psc=1. (Accessed: 13th September 2022)

227. Deatsch, A. E. & Evans, B. A. Heating efficiency in magnetic nanoparticle hyperthermia. *J. Magn. Magn. Mater.* **354**, 163–172 (2014).

228. Kekalo, K., Baker, I., Meyers, R. & Shyong, J. Magnetic Nanoparticles with High Specific Absorption Rate at Low Alternating Magnetic Field. *Nano Life* **5**, 1550002 (2015).

229. Schild, H. G. Poly(N-isopropylacrylamide): experiment, theory and application. *Prog. Polym. Sci.* **17**, 163–249 (1992).

230. Masamichi Nakayama Teruo Okano and Françoise M. Winnik. Poly(N-isopropylacrylamide)-based Smart Surfaces for Cell Sheet Tissue Engineering | Sigma-Aldrich. *Mater. Matters* (2010).

231. Gangadhar Panambur, I. K. and S. B. & Aldrich Materials Science, 6000 N. Teutonia Milwaukee, W. 53209. NIPAM based Polymers | Sigma-Aldrich. Available at: https://www.sigmaaldrich.com/materials-science/polymer-science/nipam-polymers.html. (Accessed: 28th March 2018)

232. Schmaljohann, D. Thermo-and pH-responsive polymers in drug delivery. (2006). doi:10.1016/j.addr.2006.09.020

233. McCormick, C. L. & Lowe, A. B. Aqueous RAFT polymerization: Recent developments in synthesis of functional water-soluble (Co)polymers with controlled structures. *Acc. Chem. Res.* **37**, 312–325 (2004).

234. Cowie, J. M. G. (John M. G. & Arrighi, V. (Valeria). *Polymers : chemistry and physics of modern materials.* (CRC Press, 2008).

235. Yeole, N. Thiocarbonylthio Compounds. *Synlett* **2010**, 1572–1573 (2010).

236. Moad, G., Rizzardo, E. & Thang, S. H. Living Radical Polymerization by the RAFT Process – A Second Update. *Aust. J.*

Chem. **62**, 1402 (2009).

237. Seymour, R. B. Polymer chemistry: An introduction; Second edition (Stevens, Malcom P.). *J. Chem. Educ.* **68**, A185 (1991).

238. Bacskai, R. Structure of poly(maleic anhydride). *J. Polym. Sci. Polym. Chem. Ed.* **14**, 1797–1807 (1976).

239. Schwachula, G. Calculation of the copolymerization parameters in the ternary copolymerization system of styrene/m-divinyl-benzene/p-divinylbenzene. *J. Polym. Sci. Polym. Symp.* **53**, 107–112 (2007).

240. Mayo, F. R. & Lewis, F. M. Copolymerization. I. A Basis for Comparing the Behavior of Monomers in Copolymerization; The Copolymerization of Styrene and Methyl Methacrylate. *J. Am. Chem. Soc.* **66**, 1594–1601 (1944).

241. Tauer, K., Gau, D., Schulze, S., Völkel, A. & Dimova, R. Thermal property changes of poly(N-isopropylacrylamide) microgel particles and block copolymers. doi:10.1007/s00396-008-1984-x

242. and, H. Y. & Maeda*, Y. LCST and UCST Behavior of Poly(N-isopropylacrylamide) in DMSO/Water Mixed Solvents Studied by IR and Micro-Raman Spectroscopy. (2007). doi:10.1021/JP072438S

243. Jain, K., Vedarajan, R., Watanabe, M., Ishikiriyama, M. & Matsumi, N. Tunable LCST behavior of poly(N-isopropylacrylamide/ionic liquid) copolymers. *Polym. Chem.* **6**, 6819–6825 (2015).

244. Chen, H. & Fang, Y. *Synthesis and characterization of temperature and pH responsive Poly(N-isopropylacrylamide) copolymer*.

245. Crotonaldehyde data sheet. Available at: https://www.fishersci.com/store/msds?partNumber=AC427181000&productDescription=CROTONALDEHYDE+99%2B%25+AC+100ML&vendorId=VN00032119&countryCode=US&language=en. (Accessed: 16th August 2022)

246. ARMSTRONG GH & HARWOOD HJ. Copolymerization of methacrolein with styrene in the presence of ZnCl2. *J Polym Sci Part B Polym Lett* **8**, 627–630 (1970).

247. Anthony J. Convertine, ‡ *et al.* Direct Synthesis of Thermally Responsive DMA/NIPAM Diblock and DMA/NIPAM/DMA Triblock Copolymers via Aqueous, Room Temperature RAFT Polymerization†. (2006). doi:10.1021/MA0523419

248. Chiefari, J. *et al.* Living free-radical polymerization by reversible addition - Fragmentation chain transfer: The RAFT process. *Macromolecules* **31**, 5559–5562 (1998).

249. Yanjie Zhang *et al.* Effects of Hofmeister Anions on the LCST of PNIPAM as a Function of Molecular Weight†. (2007). doi:10.1021/JP0690603

250. Andreeva, I. V., Artemyeva, V. N., Nesterov, V. V. & Kukarkina, N. V. Methods of acrolein polymerization and investigation of structures of the polymers obtained. *J. Polym. Sci. Polym. Chem. Ed.* **17**, 3415–3424 (1979).

251. IUPAC. International Union of Pure and Applied Chemistry. Available at: http://publications.iupac.org/compendium/index.html. (Accessed: 29th July 2019)

252. Sneed, P. K. *et al.* Survival benefit of hyperthermia in a prospective randomized trial of brachytherapy boost ± hyperthermia for glioblastoma multiforme. *Int. J. Radiat. Oncol. Biol. Phys.* **40**, 287–295 (1998).

253. Lue, S. J., Chen, C.-H. & Shih, C.-M. Tuning of Lower Critical Solution Temperature (LCST) of Poly(N-Isopropylacrylamide-co-Acrylic acid) Hydrogels. *J. Macromol. Sci. Part B* **50**, 563–579 (2011).

254. Begum, R. *et al.* Fundamentals and applications of acrylamide based microgels and their hybrids: a review. *RSC Adv.* **9**, 13838–13854 (2019).

255. Herth, G., Schornick, G. & Buchholz, F. L. Polyacrylamides and Poly(Acrylic Acids). *Ullmann's Encycl. Ind. Chem.* 1–16 (2015). doi:10.1002/14356007.A21_143.PUB2

256. Stynes, G. D., Gengenbach, T. R., Kiroff, G. K., Morrison, W. A. & Kirkland, M. A. Thiol surface functionalization via continuous phase plasma polymerization of allyl mercaptan, with subsequent maleimide-linked conjugation of collagen. *J. Biomed. Mater. Res. - Part A* **105**, 1940–1948 (2017).

257. Svenson, A. & Carlsson, J. The thiol group of bovine serum albumin. High reactivity at acidic pH as measured by the reaction with 2,2'-dipyridyl disulphide. *Biochim. Biophys. Acta* **400**, 433–438 (1975).

258. Tokuyama, H., Onodera, M. & Ban, T. Selective temperature-swing adsorption of Pd(II) ions onto a poly(N-

isopropylacrylamide-co-allyl mercaptan) gel. *Sep. Purif. Technol.* **182**, 166–170 (2017).

259. Majorek, K. A. *et al.* Structural and immunologic characterization of bovine, horse, and rabbit serum albumins. *Mol. Immunol.* **52**, 174 (2012).

260. Rusmini, F., Zhong, Z. & Feijen, J. Protein immobilization strategies for protein biochips. *Biomacromolecules* **8**, 1775–1789 (2007).

261. Topală, T., Bodoki, A., Oprean, L. & Oprean, R. Bovine Serum Albumin Interactions with Metal Complexes. *Clujul Med.* **87**, 215 (2014).

262. Rodriguez-Abetxuko, A., Sánchez-deAlcázar, D., Muñumer, P. & Beloqui, A. Tunable Polymeric Scaffolds for Enzyme Immobilization. *Front. Bioeng. Biotechnol.* **8**, 830 (2020).

263. Chabner, B. A. & Roberts, T. G. Timeline: Chemotherapy and the war on cancer. *Nat. Rev. Cancer* **5**, 65–72 (2005).

264. Saab, R., Spunt, S. L. & Skapek, S. X. Myogenesis and rhabdomyosarcoma the Jekyll and Hyde of skeletal muscle. *Curr. Top. Dev. Biol.* **94**, 197–234 (2011).

265. Ognjanovic, S., Linabery, A. M., Charbonneau, B. & Ross, J. A. Trends in Childhood Rhabdomyosarcoma Incidence and Survival in the United States (1975–2005). *Cancer* **115**, 4218 (2009).

266. Pappo, A. S. *et al.* Survival after relapse in children and adolescents with rhabdomyosarcoma: A report from the Intergroup Rhabdomyosarcoma Study Group. *J. Clin. Oncol.* **17**, 3487–3493 (1999).

267. PDQ Pediatric Treatment Editorial Board. Childhood Rhabdomyosarcoma Treatment (PDQ®): Patient Version. *PDQ Cancer Inf. Summ.* (2002).

268. Glioblastoma Multiforme – Symptoms, Diagnosis and Treatment Options. Available at: https://www.aans.org/en/Patients/Neurosurgical-Conditions-and-Treatments/Glioblastoma-Multiforme. (Accessed: 14th August 2022)

269. Chemotherapy for breast cancer | Cancer Research UK. Available at: https://www.cancerresearchuk.org/about-cancer/breast-cancer/treatment/chemotherapy. (Accessed: 21st September 2022)

270. He, M.-K. *et al.* Hepatic artery infusion chemotherapy using mFOLFOX versus transarterial chemoembolization for massive unresectable hepatocellular carcinoma: a prospective non-randomized study. *Chin. J. Cancer* **36**, (2017).

271. Wang, J. & Zhang, B. Bovine Serum Albumin as a Versatile Platform for Cancer Imaging and Therapy. *Curr. Med. Chem.* **25**, 2938–2953 (2018).

272. Bovine Serum Albumin (BSA) - TCS Biosciences Ltd. Available at: https://www.tcsbiosciences.co.uk/bovine_serum_albumin.php?genre=pharma. (Accessed: 27th June 2022)

273. Miele, E., Spinelli, G. P., Miele, E., Tomao, F. & Tomao, S. Albumin-bound formulation of paclitaxel (Abraxane® ABI-007) in the treatment of breast cancer. *Int. J. Nanomedicine* **4**, 99 (2009).

274. Gradishar, W. J. Albumin-bound paclitaxel: a next-generation taxane. *http://dx.doi.org/10.1517/14656566.7.8.1041* **7**, 1041–1053 (2006).

275. Stinchcombe, T. E. Nanoparticle albumin-bound paclitaxel: a novel Cremphor-EL®-free formulation of paclitaxel. *https://doi.org/10.2217/17435889.2.4.415* **2**, 415–423 (2007).

276. Ganguly, A., Yang, H. & Cabral, F. Paclitaxel-dependent cell lines reveal a novel drug activity. *Mol. Cancer Ther.* **9**, 2914–23 (2010).

277. Jordan, M. A. & Wilson, L. Microtubules as a target for anticancer drugs. *Nat. Rev. Cancer* **4**, 253–265 (2004).

278. Jordan, M. A. & Wilson, L. Microtubules as a target for anticancer drugs. *Nat. Rev. Cancer 2004 44* **4**, 253–265 (2004).

279. Howat, S. *et al.* Paclitaxel: biosynthesis, production and future prospects. *N. Biotechnol.* **31**, 242–245 (2014).

280. Liebmann, J. E. *et al.* Cytotoxic studies of paclitaxel (Taxol) in human tumour cell lines. *Br. J. Cancer* **68**, 1104–1109 (1993).

281. Paclitaxel Albumin-stabilized Nanoparticle Formulation - National Cancer Institute. Available at: https://www.cancer.gov/about-cancer/treatment/drugs/nanoparticlepaclitaxel. (Accessed: 23rd July 2019)

282. Trynda-Lemiesz, L. Paclitaxel-HSA interaction. Binding sites on HSA molecule. *Bioorg. Med. Chem.* **12**, 3269–3275

(2004).

283. Karthikeyan, S. *et al.* Exploring the Binding Interaction Mechanism of Taxol in β-Tubulin and Bovine Serum Albumin: A Biophysical Approach. (2019). doi:10.1021/acs.molpharmaceut.8b00948

284. Drug: Paclitaxel - Cancerrxgene - Genomics of Drug Sensitivity in Cancer. Available at: https://www.cancerrxgene.org/compound/Paclitaxel/11/overview/ic50? (Accessed: 9th August 2022)

285. Vinblastine - Chemotherapy Drugs - Chemocare. Available at: https://chemocare.com/chemotherapy/drug-info/vinblastine.aspx. (Accessed: 28th February 2022)

286. Brito, D. A., Yang, Z. & Rieder, C. L. Microtubules do not promote mitotic slippage when the spindle assembly checkpoint cannot be satisfied. *J. Cell Biol.* **182**, 623–629 (2008).

287. Zu, Y. *et al.* Optimization of the preparation process of vinblastine sulfate (VBLS)-loaded folateconjugated bovine serum albumin (BSA) nanoparticles for tumor-targeted drug delivery using response surface methodology (RSM). *Int. J. Nanomedicine* **4**, 321 (2009).

288. Seetharamappa, J. & Kamat, B. P. Spectroscopic studies on the mode of interaction of an anticancer drug with bovine serum albumin. *Chem. Pharm. Bull. (Tokyo).* **52**, 1053–1057 (2004).

289. Drug: Vinblastine - Cancerrxgene - Genomics of Drug Sensitivity in Cancer. Available at: https://www.cancerrxgene.org/compound/Vinblastine/1004/by-tissue? (Accessed: 9th August 2022)

290. Metabolism of Paracetamol (Acetaminophen), Acetanilide and Phenacetin | Medicinal Chemistry | PharmaXChange.info. Available at: https://pharmaxchange.info/2012/08/metabolism-of-paracetamol-acetaminophen-acetanilide-and-phenacetin/. (Accessed: 2nd March 2022)

291. Moore, B. A. & Barnett, J. E. Oxford Clinical Psychology Military Psychologists ' Desk Reference. *Case Stud. Clin. Psychol. Sci. Bridg. Gap from Sci. to Pract.* 1–7 (2015). doi:10.1093/MED/9780199600830.001.0001/MED-9780199600830

292. Piperno, E. & Berssenbruegge, D. A. REVERSAL OF EXPERIMENTAL PARACETAMOL TOXICOSIS WITH N-ACETYLCYSTEINE. *Lancet* **308**, 738–739 (1976).

293. Mant, T. G. K., Tempowski, J. H., Volans, G. N. & Talbot, J. C. C. Adverse reactions to acetylcysteine and effects of overdose. *Br Med J (Clin Res Ed)* **289**, 217–219 (1984).

294. Daly, F. F. S., Fountain, J. S., Murray, L., Graudins, A. & Buckley, N. A. Guidelines for the management of paracetamol poisoning in Australia and New Zealand — explanation and elaboration. *Med. J. Aust.* **188**, 296–302 (2008).

295. Chiew, A. L., Gluud, C., Brok, J. & Buckley, N. A. Interventions for paracetamol (acetaminophen) overdose. *Cochrane Database Syst. Rev.* **2018**, (2018).

296. Missiaglia, E. *et al.* Genomic imbalances in rhabdomyosarcoma cell lines affect expression of genes frequently altered in primary tumors: an approach to identify candidate genes involved in tumor development. *Genes. Chromosomes Cancer* **48**, 455–467 (2009).

297. Hinson, A. R. P. *et al.* Human Rhabdomyosarcoma Cell Lines for Rhabdomyosarcoma Research: Utility and Pitfalls. *Front. Oncol.* **3**, (2013).

298. U-87 MG - HTB-14 | ATCC. Available at: https://www.atcc.org/products/htb-14. (Accessed: 14th August 2022)

299. MCF7 - HTB-22 | ATCC. Available at: https://www.atcc.org/products/htb-22. (Accessed: 14th August 2022)

300. Hep G2 [HEPG2] - HB-8065 | ATCC. Available at: https://www.atcc.org/products/hb-8065. (Accessed: 14th August 2022)

301. Wayback Machine. Available at: https://web.archive.org/web/20120417121807/http://www.sigmaplot.com/products/sigmaplot/Standard_Curves_Analysis.pdf. (Accessed: 9th August 2022)

302. Mund, M. E., Quarcoo, D., Gyo, C., Brüggmann, D. & Groneberg, D. A. Paracetamol as a toxic substance for children: aspects of legislation in selected countries. *J. Occup. Med. Toxicol.* **10**, (2015).

303. View of Evaluation of hepatotoxic effects of acetaminophen on HepG2 cells by parallel real-time monitoring in a multi-sensor analysis platform for automated cell-based assays. Available at: https://www.bioenergetics-communications.org/index.php/bec/article/view/heichler_2022/63. (Accessed: 27th September 2022)

304. Piel, S. *et al.* Cell-permeable succinate prodrugs rescue mitochondrial respiration in cellular models of acute acetaminophen overdose. *PLoS One* **15**, e0231173 (2020).

305. Kobayashi, H., Watanabe, R. & Choyke, P. L. Improving conventional enhanced permeability and retention (EPR) effects; what is the appropriate target? *Theranostics* **4**, 81–89 (2013).

306. Yang, Z. *et al.* Engineered bovine serum albumin-based nanoparticles with pH-sensitivity for doxorubicin delivery and controlled release. *Drug Deliv.* **27**, 1156–1164 (2020).

307. Yu, Z., Yu, M., Zhang, Z., Hong, G. & Xiong, Q. Bovine serum albumin nanoparticles as controlled release carrier for local drug delivery to the inner ear. *Nanoscale Res. Lett.* **9**, 1–7 (2014).

308. Zu, Y. *et al.* Optimization of the preparation process of vinblastine sulfate (VBLS)-loaded folate-conjugated bovine serum albumin (BSA) nanoparticles for tumor-targeted drug delivery using response surface methodology (RSM). *Int. J. Nanomedicine* **4**, 321–333 (2009).

309. Dahiya, V. & Pal, S. The effect of paracetamol on 5 fluorouracil and bovine serum albumin interaction: A biophysical study. *AIP Conf. Proc.* **1953**, 140012 (2018).

310. Milligan, T. P., Morris, H. C., Hammond, P. M. & Price, C. P. Studies on paracetamol binding to serum proteins. *Orig. Artic. Ann Clin Biochem* **31**, 492–496 (1994).

311. Agbanyim, A. N., Okoro, Oriakua & Glory C. The Effect of pH on the Binding Characteristics of Paracetamol to Bovine Serum Albumin. *Int. J. Sci. Res. Publ.* **6**, 598 (2014).

312. Yasuda, M. *et al.* BSA Adsorption and Immobilization onto Charged Monodisperse Polymer Nanoparticles. *J. Biosens. Bioelectron.* **06**, 1–8 (2015).

313. Dimerization of Bovine Serum Albumin As Evidenced By Particle Size and Molecular Mass Measurement :: Anton-Paar.com. Available at: https://www.anton-paar.com/corp-en/services-support/document-finder/application-reports/dimerization-of-bovine-serum-albumin-as-evidenced-by-particle-size-and-molecular-mass-measurement/. (Accessed: 15th August 2022)

314. 394332. Available at: https://pubmed.ncbi.nlm.nih.gov/394332/?format=pubmed. (Accessed: 27th September 2022)

315. Inde, Z., Forcina, G. C., Denton, K. & Dixon, S. J. Kinetic Heterogeneity of Cancer Cell Fractional Killing. *Cell Rep.* **32**, 107845 (2020).

316. Skeel, R. T. & Khlief, S. N. Handbook of Cancer Chemotherapy (Lippincott Williams & Wilkins Handbook Series). 875 (2011).

317. Zein, R., Sharrouf, W. & Selting, K. Physical Properties of Nanoparticles That Result in Improved Cancer Targeting. *Journal of Oncology* **2020**, (2020).

318. Brocato, T. A. *et al.* Understanding the Connection between Nanoparticle Uptake and Cancer Treatment Efficacy using Mathematical Modeling. *Sci. Rep.* **8**, (2018).

319. Eslaminejad, T., Nematollahi-Mahani, S. N. & Ansari, M. Glioblastoma Targeted Gene Therapy Based on pEGFP/p53-Loaded Superparamagnetic Iron Oxide Nanoparticles. *Curr. Gene Ther.* **17**, (2017).

320. Andreeva, I. V. *et al.* Polymerization of α-methacrolein and the structure of the polymers. *J. Polym. Sci. Part C Polym. Symp.* **16**, 1409–1421 (2007).

321. Xu, J., Liu, Y. & Hsu, S. Hydrogels Based on Schiff Base Linkages for Biomedical Applications. *Molecules* **24**, 3005 (2019).

322. Chirowodza, H., Weber, W., Hartmann, P. & Pasch, H. Surface-Initiated Reversible Addition Fragmentation Chain Transfer (RAFT) Polymerization of Styrene from Laponite Clay Surfaces. *Macromol. Symp.* **313**–**314**, 135–145 (2012).

323. Conzatti, G. *et al.* PNIPAM grafted surfaces through ATRP and RAFT polymerization: Chemistry and bioadhesion. *Colloids Surfaces B Biointerfaces* **151**, 143–155 (2017).

324. Subhan, M. A., Yalamarty, S. S. K., Filipczak, N., Parveen, F. & Torchilin, V. P. Recent Advances in Tumor Targeting via EPR Effect for Cancer Treatment. *J. Pers. Med.* **11**, (2021).

325. Chen, S., Chiang, C. li & Hsieh, S. Simulating physiological conditions to evaluate nanoparticles for magnetic fluid hyperthermia (MFH) therapy applications. *J. Magn. Magn. Mater.* **322**, 247–252 (2010).

326. Barbero, N., Barolo, C. & Viscardi, G. Cite This Article: Nadia Barbero, Claudia Barolo, and Guido Viscardi. *World J. Chem. Educ.* **4**, 80–85 (2016).

327. Nagy-Smith, K., Yamada, Y. & Schneider, J. P. Protein release from highly charged peptide hydrogel networks. *J. Mater. Chem. B* **4**, 1999–2007 (2016).

328. Tong, X., Lee, S., Bararpour, L. & Yang, F. Long-term Controlled Protein Release from Poly(ethylene glycol) Hydrogels by Modulating Mesh Size and Degradation. *Macromol. Biosci.* **15**, 1679 (2015).

329. Grossen, P., Witzigmann, D., Sieber, S. & Huwyler, J. PEG-PCL-based nanomedicines: A biodegradable drug delivery system and its application. *J. Control. Release* **260**, 46–60 (2017).

330. Garay, R. P., El-Gewely, R., Armstrong, J. K., Garratty, G. & Richette, P. Antibodies against polyethylene glycol in healthy subjects and in patients treated with PEG-conjugated agents. *http://dx.doi.org/10.1517/17425247.2012.720969* **9**, 1319–1323 (2012).

331. Moncalvo, F., Martinez Espinoza, M. I. & Cellesi, F. Nanosized Delivery Systems for Therapeutic Proteins: Clinically Validated Technologies and Advanced Development Strategies. *Front. Bioeng. Biotechnol.* **8**, 89 (2020).

332. Katagiri, K. *et al.* Magnetoresponsive On-Demand Release of Hybrid Liposomes Formed from Fe3O4 Nanoparticles and Thermosensitive Block Copolymers. *Small* **7**, 1683–1689 (2011).

333. Yildiz, T., Gu, R., Zauscher, S. & Betancourt, T. Doxorubicin-loaded protease-activated near-infrared fluorescent polymeric nanoparticles for imaging and therapy of cancer. *Int. J. Nanomedicine* **13**, 6961–6986 (2018).

334. Hu, S.-H., Chen, S.-Y. & Gao, X. Multifunctional Nanocapsules for Simultaneous Encapsulation of Hydrophilic and Hydrophobic Compounds and On-Demand Release. *ACS Nano* **6**, 2558–2565 (2012).

335. Huang, H.-Y. *et al.* Self-assembling PVA-F127 thermosensitive nanocarriers with highly sensitive magnetically-triggered drug release for epilepsy therapy in vivo. *J. Mater. Chem.* **22**, 8566 (2012).

336. Satarkar, N. S. & Zach Hilt, J. Hydrogel nanocomposites as remote-controlled biomaterials. *Acta Biomater.* **4**, 11–16 (2008).

337. Ruan, L., Chen, W., Wang, R., Lu, J. & Zink, J. I. Magnetically Stimulated Drug Release Using Nanoparticles Capped by Self-Assembling Peptides. *ACS Appl. Mater. Interfaces* **11**, 43835–43842 (2019).

338. Felfoul, O., Becker, A. T., Fagogenis, G. & Dupont, P. E. Simultaneous steering and imaging of magnetic particles using MRI toward delivery of therapeutics. *Sci. Rep.* **6**, 33567 (2016).

339. Waring, W. S. Novel acetylcysteine regimens for treatment of paracetamol overdose. *Ther. Adv. Drug Saf.* **3**, 305 (2012).

340. Jiang, Y., Li, Y., Richard, C., Scherman, D. & Liu, Y. Hemocompatibility investigation and improvement of near-infrared persistent luminescent nanoparticle ZnGa2O4:Cr3+ by surface PEGylation. *J. Mater. Chem. B* **7**, 3796–3803 (2019).

341. Propidium Iodide. Available at: https://www.thermofisher.com/order/catalog/product/P1304MP. (Accessed: 7th September 2022)

342. Nussbaum, G. H. *et al. AAPM REPORT NO. 27 HYPERTHERMIA TREATMENT PLANNING † REPORT OF TASK GROUP NO. 2 HYPERTHERMIA COMMITTEE* AAPM Members P. B. Dunscombe (Task Group Chairman)*. (1989).

343. Arigony, A. L. V. *et al.* The Influence of Micronutrients in Cell Culture: A Reflection on Viability and Genomic Stability. *Biomed Res. Int.* **2013**, 22 (2013).

344. Ma, P. & Mumper, R. J. Paclitaxel Nano-Delivery Systems: A Comprehensive Review. *J. Nanomed. Nanotechnol.* **4**, 1000164 (2013).

345. Galic, V. L., Herzog, T. J., Wright, J. D. & Lewin, S. N. Paclitaxel poliglumex for ovarian cancer. *Expert Opin. Investig. Drugs* **20**, 813–821 (2011).

346. Singer, J. W. Paclitaxel poliglumex (XYOTAX, CT-2103): a macromolecular taxane. *J. Control. Release* **109**, 120–126 (2005).

347. CHMP. Opaxio; INN: Paclitaxel poliglumex. (2009).

348. Loehr, M. *et al.* Cationic liposomal paclitaxel in combination with gemcitabine in patients with advanced pancreatic cancer: A phase II trial. *https://doi.org/10.1200/jco.2009.27.15_suppl.4526* **27**, 4526–4526 (2009).

349. Hua, M. Y. *et al.* Magnetic-nanoparticle-modified paclitaxel for targeted therapy for prostate cancer. *Biomaterials* **31**, 7355–7363 (2010).

350. Ursachi, V. C. *et al.* Paclitaxel-Loaded Magnetic Nanoparticles Based on Biotinylated N-Palmitoyl Chitosan: Synthesis, Characterization and Preliminary In Vitro Studies. *Molecules* **26**, (2021).

351. Guduru, R. & Khizroev, S. Magnetic field-controlled release of Paclitaxel drug from functionalized magnetoelectric nanoparticles. *Part. Part. Syst. Charact.* **31**, 605–611 (2014).

352. Zhu, Y., Liu, R., Huang, H. & Zhu, Q. Vinblastine-Loaded Nanoparticles with Enhanced Tumor-Targeting Efficiency and Decreasing Toxicity: Developed by One-Step Molecular Imprinting Process. *Mol. Pharm.* **16**, 2675–2689 (2019).

353. Huang, K. S., Yang, C. H., Wang, Y. C., Wang, W. T. & Lu, Y. Y. Microfluidic Synthesis of Vinblastine-Loaded Multifunctional Particles for Magnetically Responsive Controlled Drug Release. *Pharmaceutics* **11**, (2019).

354. Wang, W., Zhou, S., Sun, L. & Huang, C. Controlled delivery of paracetamol and protein at different stages from core–shell biodegradable microspheres. *Carbohydr. Polym.* **79**, 437–444 (2010).

355. Al-Nemrawi, N. K. & Dave, R. H. Drug Delivery Formulation and characterization of acetaminophen nanoparticles in orally disintegrating films. (2014). doi:10.3109/10717544.2014.936987

356. Behzadi, S. *et al.* Cellular Uptake of Nanoparticles: Journey Inside the Cell. *Chem. Soc. Rev.* **46**, 4218 (2017).

357. Sensenig, R., Sapir, Y., MacDonald, C., Cohen, S. & Polyak, B. Magnetic nanoparticle-based approaches to locally target therapy and enhance tissue regeneration in vivo. *Nanomedicine (Lond).* **7**, 1425 (2012).

358. Jeun, M., Kim, Y. J., Park, K. H., Paek, S. H. & Bae, S. Physical Contribution of Néel and Brown Relaxation to Interpreting Intracellular Hyperthermia Characteristics Using Superparamagnetic Nanofluids. *J. Nanosci. Nanotechnol.* **13**, 5719–5725 (2013).

359. 1st Law of Thermodynamics - Chemistry LibreTexts. Available at: https://chem.libretexts.org/Bookshelves/Physical_and_Theoretical_Chemistry_Textbook_Maps/Supplemental_Modules_(Physical_and_Theoretical_Chemistry)/Thermodynamics/The_Four_Laws_of_Thermodynamics/First_Law_of_Thermodynamics. (Accessed: 1st August 2019)

360. Kuhlman, D. A Python Book: Beginning Python, Advanced Python, and Python Exercises. (2009).

361. About. Available at: https://web.archive.org/web/20120420010049/http://www.python.org/about/. (Accessed: 21st August 2022)

362. PEP 206 – Python Advanced Library | peps.python.org. Available at: https://peps.python.org/pep-0206/. (Accessed: 21st August 2022)

363. Piñeiro-Redondo, Y. *et al.* The influence of colloidal parameters on the specific power absorption of PAA-coated magnetite nanoparticles. *Nanoscale Res. Lett.* **6**, 1–7 (2011).

364. Yoshida, T., Nakamura, T., Higashi, O. & Enpuku, K. Effect of viscosity on the AC magnetization of magnetic nanoparticles under different AC excitation fields. *J. Magn. Magn. Mater.* **471**, 334–339 (2019).

365. Smolkova, I. S. *et al.* Alternating magnetic field energy absorption in the dispersion of iron oxide nanoparticles in a viscous medium. *J. Magn. Magn. Mater.* **374**, 508–515 (2015).

366. Jr, L., De Biasi, E. & Vasquez Mansilla, M. Computational study on superparamagnetic hyperthermia with biocompatible SPIONs to destroy the cancer cells. *J. Phys. Conf. Ser. OPEN ACCESS* doi:10.1088/1742-6596/521/1/012015

367. Ruíz-Baltazar, A., Esparza, R., Rosas, G. & Pérez, R. Effect of the Surfactant on the Growth and Oxidation of Iron Nanoparticles. *J. Nanomater.* **2015**, (2015).

368. Beković, M., Trlep, M., Jesenik, M., Goričan, V. & Hamler, A. An experimental study of magnetic-field and temperature dependence on magnetic fluid's heating power. *J. Magn. Magn. Mater.* **331**, 264–268 (2013).

369. Wildeboer, R. R., Southern, P. & Pankhurst, Q. A. On the reliable measurement of specific absorption rates and intrinsic loss parameters in magnetic hyperthermia materials. *J. Phys. D. Appl. Phys.* **47**, 495003 (2014).

370. Barrera, G., Allia, P. & Tiberto, P. Temperature-dependent heating efficiency of magnetic nanoparticles for applications in precision nanomedicine. *Nanoscale* **12**, 6360–6377 (2020).

END

